



KIT SCIENTIFIC REPORTS 7627

# **Critical Heat Flux for Flow Boiling of Water at Low Pressure on Smooth and Micro-Structured Zircaloy Tube Surfaces**

Christoph Haas



Christoph Haas

**Critical Heat Flux for Flow Boiling of Water at Low Pressure  
on Smooth and Micro-Structured Zircaloy Tube Surfaces**

**Karlsruhe Institute of Technology**  
**KIT SCIENTIFIC REPORTS 7627**

# **Critical Heat Flux for Flow Boiling of Water at Low Pressure on Smooth and Micro-Structured Zircaloy Tube Surfaces**

by  
Christoph Haas

Report-Nr. KIT-SR 7627

Dissertation, Karlsruher Institut für Technologie (KIT)  
Fakultät für Chemieingenieurwesen und Verfahrenstechnik  
Tag der mündlichen Prüfung: 20.07.2012

### Impressum

Karlsruher Institut für Technologie (KIT)  
KIT Scientific Publishing  
Straße am Forum 2  
D-76131 Karlsruhe  
www.ksp.kit.edu

KIT – Universität des Landes Baden-Württemberg und  
nationales Forschungszentrum in der Helmholtz-Gemeinschaft



Diese Veröffentlichung ist im Internet unter folgender Creative Commons-Lizenz  
publiziert: <http://creativecommons.org/licenses/by-nc-nd/3.0/de/>

KIT Scientific Publishing 2012  
Print on Demand

ISSN 1869-9669  
ISBN 978-3-86644-923-7







# **Critical Heat Flux for Flow Boiling of Water at Low Pressure on Smooth and Micro-Structured Zircaloy Tube Surfaces**

zur Erlangung des akademischen Grades eines  
DOKTORS DER INGENIEURWISSENSCHAFTEN (Dr.-Ing.)

der Fakultät für Chemieingenieurwesen und Verfahrenstechnik des  
Karlsruher Instituts für Technologie (KIT)

genehmigte  
DISSERTATION

von  
Dipl.-Ing. Christoph Haas  
aus Tübingen

Hauptreferent: Prof. Dr.-Ing. Thomas Wetzel

Korreferent: Prof. Dr.-Ing. Thomas Schulenberg

Tag der mündlichen Prüfung: 20. Juli 2012



## Abstract

Flow boiling of a liquid is characterized by a high heat transfer from the heated surface into the fluid. However, the nucleate boiling regime is limited by the occurrence of the critical heat flux (CHF) leading to a possible thermal damage of the heated surface. Surface structure modifications can shift the CHF to higher heat energy input, thus increasing the safety and efficiency of the application.

This work focussed on the identification of suitable surface modifications for zircaloy cladding tubes used in nuclear reactors. The manufacturing was realized in cooperation with industry and scientific institutes and the produced surface textures are characterized by elevations in nano- and microscale, micro-channels, and porous or oxidized layers on the surface.

A new steam/water loop test facility for low pressures of 100-400 kPa (1-4 bar) with a vertical annular test section was installed for the critical heat flux experiments. Two different annular sizes were used, a 1.75 mm wide and a larger 4.25 mm wide gap. The water was flowing upwards through the annulus. The inner tube was directly heated by electric current over a length of 326 mm whereas the outer glass tube was unheated. Flow boiling at low pressures can be affected by flow instabilities. Therefore, an experimental stability investigation was examined in order to ensure CHF measurements at stable conditions.

The subsequent CHF measurements were performed for inlet subcooling conditions of 104-250 kJ/kg, outlet pressures of 115-300 kPa, and mass fluxes of 250-1000 kg/(m<sup>2</sup>s) for the smaller annulus and 250-400 kg/(m<sup>2</sup>s) for the larger annulus. Using the smaller annulus the axial CHF locations could vary in the upper half of the heated section, thus excluding a safe experimental operation for the surface structured tubes. In the larger annulus the CHF occurred always at the top end of the heated section. Therefore, the experiments with the surface structured tubes were examined in the larger annular geometry. The CHF results for the smooth surface tube showed very good agreement compared to literature data for similar experimental parameters. Furthermore, the measured results were compared to CHF predicting methods from literature.

The measurements at the lowest pressure of 120 kPa demonstrated almost no remarkable influence on CHF for all surface structured tubes compared to the smooth tube. The surface structures with elevations in nano- and micro-scale showed the same behavior and similar CHF values as the smooth tube for all applied conditions. Surfaces with micro-channels, porosity and cracks could lead to an increase in CHF of about 10 to 29% compared to the smooth tube for higher pressures.

Additionally, the flow boiling performance was observed by high-speed video visualization and the wetting behavior of the surface structures was measured by the Wilhelmy method. This force measurement method allowed the determination of fluid-surface interaction even for cylindrical geometries and surfaces with capillary texture. From the comparison of CHF results, wettability and flow boiling visualization could be concluded that capillary effects and/or increased number of nucleation sites on the surface could influence the critical heat flux.



## Kurzfassung

Beim Strömungssieden wird eine hohe Wärmeübertragung von der Heizfläche ins Fluid erreicht. Der Siedeprozess beim Blasensieden ist jedoch durch die kritische Wärmestromdichte (Critical Heat Flux-CHF) begrenzt. Beim Überschreiten der kritischen Wärmestromdichte kommt es zu einer plötzlichen Reduzierung des Wärmeübergangs und bei konstanter Heizleistung kann die Heizfläche durch die in der Folge stark ansteigenden Oberflächentemperaturen beschädigt werden. Eine Strukturierung der Oberfläche kann eine Erhöhung der kritischen Wärmestromdichte bewirken und somit die Sicherheit und die Effizienz der Anwendung steigern. In dieser Arbeit wurden geeignete Oberflächenstrukturen für Zircaloy-Hüllrohre, wie sie in Kernreaktoren verwendet werden, gesucht. Die Oberflächenstrukturen wurden in Kooperation mit Industriepartnern und Forschungsinstituten durch unterschiedliche Prozesse hergestellt und zeichneten sich durch Erhebungen im Nano- und Mikrometerbereich, Mikrokanäle, sowie poröse oder oxidierte Schichten aus.

Zur Untersuchung der kritischen Wärmestromdichte wurde eine Wasser/Dampf - Versuchsanlage für niedrige Drücke (100-400 kPa (1-4 bar)) aufgebaut. Die Teststrecke bestand aus einem vertikalen Ringspalt mit aufwärts strömendem Wasser. Zwei unterschiedliche Ringspaltgrößen mit 1,75 mm bzw. 4,25 mm Spaltbreite wurden untersucht. Das innere Rohr wurde über eine Länge von 326 mm direkt elektrisch beheizt während das äußere Glasrohr unbeheizt blieb. Da Zweiphasenströmungen bei niedrigen Drücken sehr anfällig für Strömungsinstabilitäten sind, wurde die Stabilität des Systems experimentell untersucht, um stabile Bedingungen bei den CHF Messungen zu gewährleisten. Die kritischen Wärmestromdichten wurden bei Eintrittsunterkühlungen von 100-250 kJ/kg, Drücken von 115-300 kPa und Massenstromdichten von 250-1000 kg/(m<sup>2</sup>s) für den kleinen Ringspalt und 250-400 kg/(m<sup>2</sup>s) für den großen Ringspalt gemessen. Aufgrund variierender axialer CHF Stellen im oberen Bereich der beheizten Strecke war der kleine Ringspalt für die Untersuchung der Oberflächenstrukturen ungeeignet. Der Wechsel zum größeren Ringspalt ermöglichte einen sicheren Einsatz der strukturierten Rohre, da hier der CHF ausschließlich am Ende der Teststrecke auftrat.

Die CHF Ergebnisse des glatten Rohrs zeigte eine sehr gute Übereinstimmung mit Literaturmessdaten bei vergleichbaren Versuchsbedingungen. Zusätzlich wurden die Messwerte mit bestehenden Berechnungsmethoden verglichen. Beim niedrigsten Druck von 120 kPa wurde die kritische Wärmestromdichte im Vergleich zum glatten Rohr bei allen Strukturen kaum beeinflusst. Oberflächenstrukturen mit Erhebungen im Nano- und Mikrometerbereich zeigten im ganzen Druckbereich ähnliches Verhalten und CHF Werte wie das glatte Rohr. Oberflächen mit Mikrokanälen, Porosität oder Rissen konnten die kritische Wärmestromdichte im höheren Druckbereich um 10-29% steigern.

Durch das Glasrohr konnte der Siedeprozess mit einer Hochgeschwindigkeitskamera aufgenommen werden. Mit dem Wilhelmy-Verfahren wurde eine Methode zur Charakterisierung der Benetzungseigenschaften gefunden, die auch eine Bestimmung der Fluid-Struktur Wechselwirkung an Oberflächen mit Kapillaren ermöglichte. Ein Vergleich der Erkenntnisse aus CHF Messung, Benetzungseigenschaften und Strömungsaufnahmen ließ darauf schließen, dass kapillare Effekte und/oder erhöhte Keimstellenanzahl bei diesen Strukturen zur Erhöhung der kritischen Wärmestromdichte führten.



## Danksagung

Die vorliegende Arbeit entstand während meiner Tätigkeit als Doktorand am Institut für Kern- und Energietechnik (IKET) des Karlsruher Instituts für Technologie (KIT).

Herrn Prof. Dr.-Ing. Thomas Wetzel, danke ich sehr für die fachlichen Anregungen zu dieser Arbeit und die Übernahme des Hauptreferats. Dem Leiter des Instituts, Herrn Prof. Dr.-Ing. Thomas Schulenberg, danke ich sehr für die Ermöglichung dieser Arbeit, die kompetente Betreuung und die Übernahme des Korreferats. Mein herzlicher Dank gilt meinem ehemaligen Gruppenleiter Herrn Dr.-Ing. Leonhard Meyer, der mich mit seiner fachlichen Betreuung und Diskussionsbereitschaft bei der Durchführung des Projekts sehr unterstützt hat. Herrn Dr.-Ing. Alexei Miassoedov danke ich sehr für das Weiterführen der Unterstützung und das entgegengebrachte Vertrauen.

Diese Arbeit wurde als Forschungsprojekt von der AREVA NP GmbH gefördert, für deren finanziellen Unterstützung und die Bereitstellung der Hüllrohre ich mich ebenfalls bedanken möchte. Herrn Andreas Möckel danke ich sehr für die persönliche und fachliche Unterstützung während des Projekts. Herrn Juris Kronenberg danke ich sehr für die fachlichen Diskussionen und Anregungen.

Besonders danken möchte ich auch allen Kollegen der Arbeitsgruppe, die beim Aufbau der Versuchsanlage COSMOS kräftig mitgewirkt haben und ohne deren Einsatz diese Arbeit nicht möglich gewesen wäre. Dieser Dank geht auch an die Mitarbeiter der mechanischen und elektrotechnischen Werkstätten auf deren Hilfe ich zurückgreifen konnte. Ein besonderer Dank geht auch an die Mitarbeiter der Institute und Firmen, die an den Oberflächenstrukturierungen beteiligt waren. Die unkomplizierte und hilfsbereite Zusammenarbeit und der Optimismus waren maßgeblich für die erfolgreiche Strukturierung der Zircaloy-Rohre.

Besonders danke ich auch allen Studenten, die als Hiwi oder im Rahmen von Praktika und Projekt-/Studien-/Bachelor- oder Diplomarbeiten wertvolle Beiträge für das Gelingen des Gesamtprojekts geleistet haben. Ebenso bedanke ich mich bei allen Kollegen am IKET für die wichtigen Kaffeepausen, die Hilfsbereitschaft und die freundliche Arbeitsatmosphäre.

Meinen Eltern danke ich besonders für den gegebenen Rückhalt während meiner gesamten Ausbildungszeit. Nicht zuletzt gilt mein herzlicher Dank Ulrike Pink, die mich während des Entstehens dieser Arbeit in allen Dingen unterstützt hat.

Karlsruhe, im Juli 2012

*Christoph Haas*





# Contents

<b>1</b>	<b>Introduction and Motivation</b>	<b>1</b>
<b>2</b>	<b>Fundamentals of Two-phase Flow Boiling</b>	<b>3</b>
2.1	Fundamental Equations and Characteristic Geometry Sizes	3
2.1.1	Hydraulic and Heated Equivalent Diameter	3
2.1.2	Mass Flux and Heat Flux	4
2.1.3	Inlet Subcooling, Vapor Mass Quality and Void Fraction	4
2.2	Two-phase Heat Transfer	6
2.3	Two-phase Pressure Drop	8
2.4	Two-Phase Flow Instabilities	9
2.4.1	Static Instability	9
2.4.2	Dynamic Instabilities	11
2.5	Relationship between Heat Transfer and Pressure Drop during CHF Experiment	11
2.6	Water and Steam Properties	12
<b>3</b>	<b>State of the Art</b>	<b>13</b>
3.1	Critical Heat Flux Experiments in Annuli	13
3.2	Theoretical Models for Critical Heat Flux	17
3.2.1	Critical Heat Flux Models for Pool Boiling	17
3.2.2	Critical Heat Flux Models for Flow Boiling	20
3.3	Measurements of CHF Considering Wettability and Surface Structure Influence	23
3.3.1	Pool Boiling Experiments	23
3.3.2	Flow Boiling Experiments	26
3.4	Link of Literature Findings to Present Work	27
<b>4</b>	<b>Test Facility for Experiments</b>	<b>29</b>
4.1	Experimental Setup	29
4.2	Test Section Design	32
4.2.1	Realization of Direct Electric Heating	32
4.2.2	Annular Geometry of the Test Section	35
4.3	Instrumentation and Accuracy	36
4.3.1	Temperature Measurement Module for Test Section	37
4.3.2	Power Measurement and Heat Flux	39
4.3.3	Mass Flow Measurement and Mass Flux	42
4.3.4	Temperature Calibration	43
4.3.5	Pressure Calibration	44
4.4	Loop Control and Data Acquisition	44

4.5	Safety System . . . . .	46
4.6	Procedure of Critical Heat Flux Measurements . . . . .	46
<b>5</b>	<b>Surface Structures and Characterization . . . . .</b>	<b>51</b>
5.1	Surface Structures on Zircaloy Cladding Tube . . . . .	51
5.1.1	Smooth Zircaloy Tube . . . . .	51
5.1.2	Nanoscale Roughness . . . . .	53
5.1.3	Hemispherical Roughness . . . . .	54
5.1.4	Micro-channel Structure . . . . .	55
5.1.5	Porous Layer Structure . . . . .	56
5.1.6	Oxidized Layer Structure . . . . .	59
5.2	Characterization of Surface Structures . . . . .	61
5.2.1	Wetting Behavior on Solid Surfaces . . . . .	61
5.2.2	Wilhelmy Method . . . . .	61
5.2.3	Measurements of the Wetted Length . . . . .	63
5.2.4	Topographical Measurements of Surfaces . . . . .	64
5.2.5	Measurements of Wetting Force and Dynamic Contact Angle . . . . .	67
5.2.6	Discussion of Wetting Behavior . . . . .	70
<b>6</b>	<b>Stability Analysis for the Test Section . . . . .</b>	<b>73</b>
6.1	Characteristic Pump Curves . . . . .	73
6.2	Stabilization Effect of Inlet Restriction . . . . .	74
6.3	Comparison of Unstable and Stable Critical Heat Flux . . . . .	76
6.4	Asymptotic Trend of Stable Critical Heat Flux . . . . .	78
6.5	The Way to Stabilize the CHF Measurements . . . . .	79
<b>7</b>	<b>Critical Heat Flux Measurements with Smooth Tube . . . . .</b>	<b>81</b>
7.1	Results of the Smooth Tube Experiments . . . . .	81
7.1.1	Influence of Mass Flux . . . . .	82
7.1.2	Reproducibility of Measurements . . . . .	84
7.1.3	Location of Critical Heat Flux Occurrence . . . . .	85
7.1.4	Influence of Inlet Subcooling . . . . .	88
7.1.5	Influence of Vapor Mass Quality . . . . .	89
7.1.6	Influence of Void Fraction . . . . .	92
7.1.7	Pressure Drop Behavior . . . . .	93
7.1.8	Influence of Outlet Pressure . . . . .	94
7.2	Comparison of Smooth Tube Results with Literature Data . . . . .	96
7.3	Comparison of Smooth Tube Results with Prediction Methods from Literature . . . . .	99
7.3.1	Correlation of Katto and Ohno . . . . .	100
7.3.2	Look-up Table for Critical Heat Flux . . . . .	101
7.3.3	Doerffer Correlations for Annuli . . . . .	105
7.3.4	Summary of Prediction Methods Comparison . . . . .	108

---

<b>8</b>	<b>Critical Heat Flux Measurements with Surface Structured Tubes</b>	<b>109</b>
8.1	Reproducibility of Measurements with Surface Structured Tubes	110
8.2	Categorization of Comparison Criteria	110
8.3	Results of Micro-channel Structure	110
8.4	Results of Nano-rough Structure	112
8.5	Results of Hemispherical Structure	112
8.6	Results of Porous Structures	114
8.7	Results of Oxidized Layer	115
8.8	Comparison of Structured Surface Results	116
8.9	Visualization of Two-phase Flow	119
8.9.1	Formation of Dry Patch at Critical Heat Flux	119
8.9.2	Flow Regime Comparison at Same Heat Input	122
<b>9</b>	<b>Conclusion of Surface Structure Influence</b>	<b>127</b>
<b>10</b>	<b>Summary</b>	<b>131</b>
10.1	Proposals for Future Work	133
<b>A</b>	<b>Piping and Instrumentation Diagram</b>	<b>135</b>
<b>B</b>	<b>Electric heating of Zircaloy tube</b>	<b>137</b>
<b>C</b>	<b>Tables of measurements</b>	<b>141</b>
	<b>Abbreviations and Symbols</b>	<b>145</b>
	<b>List of Figures</b>	<b>151</b>
	<b>List of Tables</b>	<b>154</b>
	<b>Bibliography</b>	<b>156</b>



# 1. Introduction and Motivation

Boiling of a liquid fluid is used for cooling and/or steam production in many technical applications, like power plants or electronic devices. There is an intense heat transfer from the heated surface to the saturated fluid caused by the phase change process of the fluid. The nucleate boiling process is limited by the critical heat flux (CHF), which is the highest heat flux that can be dissipated into a nucleate boiling system before the local transition to film boiling occurs. This transition at CHF implicates a fast increase of the surface temperature for a heating power driven system because of a significantly reduced heat transfer during the film boiling regime. This can lead to an irreversible thermal damage of the heated surface. Therefore, the knowledge of the critical heat flux is important for a safe operation of a boiling application.

Recent studies have shown that modifying the surface by roughening or micro-structural coating can improve the CHF, thus reaching higher applicable heat fluxes, which is of interest for safety and efficiency reasons.

The application of the current work is towards the flow boiling process and safety analysis of critical heat flux for nuclear reactors. The motivation and objectives of this project are to find feasible surface structures on zircaloy cladding tubes for enhancing the critical heat flux in flow boiling.

In Light Water Reactors (LWRs) uranium dioxide ( $\text{UO}_2$ ) fuel pellets are filled into the zircaloy cladding tubes. The tubes are grouped into fuel assemblies that are positioned in the reactor pressure vessel, so that the cladding is the outer layer of the fuel rods, standing between the coolant and the nuclear fuel. Subcooled water at high pressure enters the reactor vessel at the bottom and flows upwards cooling the outer surface of the cladding tubes. Energy is released due to the nuclear reaction of fissionable material in the fuel pellets and transferred through the cladding tube into the cooling water at the cladding outer surface. The water is heated up to saturation conditions in the boundary layer and starts to boil on the cladding surface. Thus, the cladding tube forms the mechanical structure for the nuclear heat source and provides the heat transfer interface to the boiling water. The boiling water flow in the reactor vessel has three main functionalities which are energy transport, cooling of the fuel rods, and moderation of neutrons. The transferred energy into the directly or indirectly produced steam at high pressure is converted into kinetic energy by expansion on the turbine. The electrical energy is then provided by the electrical generator.

As described above, the flow boiling processes on the surface of the cladding tube and particularly the limiting critical heat flux are the main focus of this project. This first step concentrates on the choice of suitable materials and manufacturing processes for surface modification and their behavior in flow boiling conditions for nearly atmospheric pressure. Clearly, the low pressure range reduces the complexity and the costs of the test facility. However, it should be noticed that pressures in LWRs are significantly higher: about 7 MPa (70 bar) in Boiling Water Reactors (BWR) and about 15 MPa (150 bar) in Pressurized Water Reactors (PWR).

Furthermore, the test section design used in the current work consists of a vertical annular assembly with a heated zircaloy cladding tube inside. Similarly to the fuel rods, the relevant surface for the flow boiling heat transfer is the outer surface of the cladding tube. On the other hand, a single tube surrounded by an

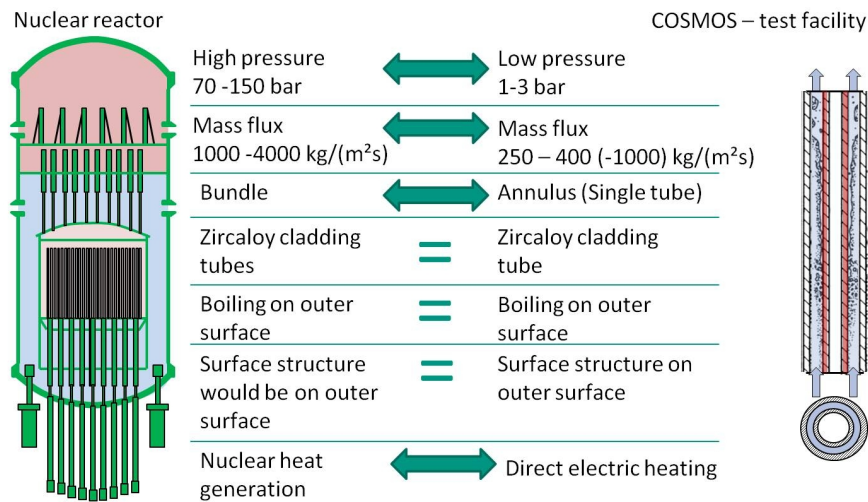


Figure 1.1.: Comparison of the main conditions realized in the current work to typical LWR conditions

unheated tube forming a uniformly narrow annulus differs from the flow hydrodynamic conditions through the bundle arrangement as in reactor case. The nuclear heat generation is simulated by a direct electrical heating of the zircaloy cladding tube. Figure 1.1 summarizes the main conditions realized in the current work compared to typical reactor conditions.

The tasks of the project were in particular

- to analyze the status of knowledge in this field with respect to experimental observations and thermo-hydraulic models.
- to design and to build a new thermo-hydraulic water/steam-test facility for experiments at low pressure.
- to design and to construct a vertical internally heated annular test section.
- to identify manufacturing processes and manufacturers for porous coatings and/or roughened surfaces on zircaloy tubes.
- to investigate experimentally the critical heat flux behavior of technically smooth and structured tubes.

This work presents the investigation of critical heat flux for flow boiling of water on smooth and micro-structured cladding tube surfaces at low pressures.

A brief introduction of the fundamentals of boiling heat transfer and two-phase flow is given in chapter 2 followed by a literature review on the topic in chapter 3. Chapter 4 presents the set-up of the experimental test facility and the test section design as well as the measurement instrumentation. The manufacturing of surface structures on the zircaloy cladding tube and the wetting behavior of the surfaces are described in chapter 5. Ensuring stable flow conditions is important for reliable critical heat flux determination. The experimental flow stability analysis for this test facility is described in chapter 6. Chapter 7 firstly presents the results of the critical heat flux measurements conducted with the smooth surface tube. Secondly, these results are compared with experimental data from literature and with values predicted by existing correlations. The results of the critical heat flux measurements performed for the structured surface tubes are compared to the smooth surface tube results in chapter 8. This chapter contains additionally the visualization of two-phase flow by high-speed imaging.

## 2. Fundamentals of Two-phase Flow Boiling

This chapter introduces necessary definitions and equations concerning two-phase flow systems with heat input. Then the characteristic behavior of heat transfer and pressure drop in such systems and flow instabilities which can affect the two-phase flow are presented. Furthermore, the importance of flow stabilization during a critical heat flux experiment is explained by considering the system operating points with increasing heat input. The last section shows the strong influence of pressure on the liquid-vapor density ratio of water for low pressures.

### 2.1. Fundamental Equations and Characteristic Geometry Sizes

The basic situation for the experiments presented in this work is flow boiling of water in a vertical internally heated annular test section. This section contains some fundamental equations and definitions which are used to describe such a two-phase system. These are the characteristic geometry sizes, the definitions of mass flux and heat flux, as well as the flow boiling parameters inlet subcooling, vapor mass quality and void fraction. Further detailed theoretical background of two-phase systems can be found in *Wallis* [101], *Baehr* [5] or *Hetsroni* [47], for instance.

#### 2.1.1. Hydraulic and Heated Equivalent Diameter

The hydraulic diameter expresses the relationship between the flow cross section  $A_{cross}$  and the wetted wall perimeter  $P_{wet}$ .

$$d_{hydr} = 4 \frac{A_{cross}}{P_{wet}} \quad (2.1)$$

The hydraulic diameter for an annulus is given by

$$d_{hydr,annulus} = 4 \frac{A_{cross}}{P_{wet}} = 4 \frac{\pi/4(d_o^2 - d_i^2)}{\pi(d_o + d_i)} = d_o - d_i \quad (2.2)$$

with the inner diameter  $d_i$  and the outer diameter  $d_o$  of the annulus as illustrated in Fig. 2.1.

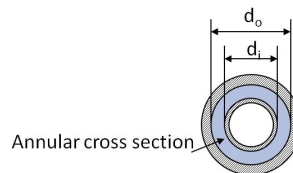


Figure 2.1.: Cross section of annular geometry

The heated equivalent diameter relates the flow cross section to the heated wall perimeter  $P_{heat}$ .

$$d_{he} = 4 \frac{A_{cross}}{P_{heat}} \quad (2.3)$$

Note, the heated equivalent diameter equals the hydraulic diameter in the case of a tube or an annulus heated from both sides since the wetted perimeter is identical to the heated perimeter. Therefore, the heated equivalent diameter is important for channels which are not uniformly heated over the wetted perimeter like annuli heated only from the inner or outer side. The heated equivalent diameter of an internally heated annulus is given by

$$d_{he,annulus-internally} = 4 \frac{A_{cross}}{P_{heat}} = 4 \frac{\pi/4(d_o^2 - d_i^2)}{\pi d_i} = \frac{(d_o^2 - d_i^2)}{d_i} \quad (2.4)$$

Characteristic dimensionless geometry quantities for the comparison of different channel sizes are formed by relating for example the length to the characteristic diameter. The  $L/d_{he}$ -ratio is important for the relationship between heat flux and vapor quality in a channel. The  $L/d_{hydr}$ -ratio is a characteristic ratio for considering the pressure drop, for instance.

### 2.1.2. Mass Flux and Heat Flux

Considering the related values *mass flux*  $G$  and *heat flux*  $\dot{q}$  allows to compare the flow and heating conditions between different system geometries.

The mass flux  $G$  is defined by dividing the mass flow rate  $\dot{M}$  by the cross sectional area  $A_{cross}$  of the flow. The same mass flux for different cross sections means that the fluid flows with the same velocity  $u$  if the density  $\rho$  is the same.

$$G = \frac{\dot{M}}{A_{cross}} = \frac{u \rho A_{cross}}{A_{cross}} = u \rho \quad (2.5)$$

The heat flux  $\dot{q}$  expresses the thermal area loading of the heated surface and is calculated by dividing the heating power  $\dot{Q}$  by the heated area  $A_{heat}$ .

$$\dot{q} = \frac{\dot{Q}}{A_{heat}} \quad (2.6)$$

### 2.1.3. Inlet Subcooling, Vapor Mass Quality and Void Fraction

The inlet subcooling can be derived by considering the energy equation between two axial position  $z_1$  and  $z_2$ , like it is depicted as an example in the draft of flow boiling in an internally heated annulus in Fig. 2.2. Neglecting kinetic and potential energy as well as heat loss, the steady state energy equation is given by

$$\frac{dH}{dt} = 0 = \dot{M} h_{l,1} + \dot{Q} - \dot{M} \left[ (1 - x_2) h_{l,2} + x_2 h_2'' \right] \quad (2.7)$$

where  $\dot{M}$  is the mass flow rate,  $\dot{Q}$  is the imposed heat energy,  $x_2$  is the vapor mass quality,  $h_{l,1} = h_l(p_1, T_{l,1})$  and  $h_{l,2} = h_l(p_2, T_{l,2})$  are the enthalpies of liquid, and  $h_2'' = h''(p_2)$  is the enthalpy of vapor at saturated condition.

If the liquid and vapor phases are in thermodynamic equilibrium at state (2), then the enthalpies refer to the saturation conditions. The energy equation for the thermodynamic equilibrium is then

$$0 = \dot{M} h_{l,1} + \dot{Q} - \dot{M} \left[ h_2' + x_{th,2} \Delta h_{v,2} \right] \quad (2.8)$$



where  $h'_2 = h' \langle p_2 \rangle$  is the saturation enthalpy of liquid and  $\Delta h_{v,2} = h'' \langle p_2 \rangle - h' \langle p_2 \rangle$  is the enthalpy of evaporation.  $x_{th,2}$  is the thermodynamic vapor mass quality at position  $z_2$ .

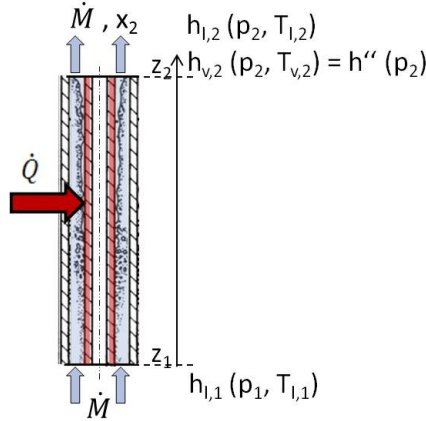


Figure 2.2.: Draft of flow boiling in internally heated annulus

The difference of the liquid inlet enthalpy at  $z_1 = z_{in}$  and the saturation enthalpy of the liquid at the outlet  $z_2 = z_{out}$  expresses the inlet subcooling condition given by

$$\Delta h_{in} = h' \langle p_{out} \rangle - h_{l,in} \langle p_{in}, T_{in} \rangle \approx h' \langle p_{out} \rangle - h_{l,in} \langle p_{out}, T_{in} \rangle \quad (2.9)$$

The pressure impact on the liquid enthalpy  $h_{l,in}$  in Eqn. (2.9) is very small. For instance, the liquid enthalpy of water for 45 °C and 120 kPa is 188.5 kJ/kg and the one for 45 °C and 1000 kPa is 189.3 kJ/kg. Thus, there is no significant error if the inlet subcooling is calculated by Eqn. (2.9) using the liquid enthalpy  $h_{l,in} \langle p_{out}, T_{in} \rangle$  referred to the outlet pressure instead of  $h_{l,in} \langle p_{in}, T_{in} \rangle$ . On the other hand, the inlet temperature  $T_{in}$  has a strong influence on the liquid enthalpy  $h_{l,in}$  which increases with increasing temperature. For instance, an increase in temperature from 45 to 80 °C at 120 kPa increases the liquid enthalpy from 188.5 to 335 kJ/kg. Consequently, for a constant outlet pressure the enthalpy difference has high values for low inlet temperatures, i.e high inlet subcooling ( $\Delta h_{in}(120 \text{ kPa}, 45^\circ \text{C}) = 250 \text{ kJ/kg}$ ), and small values for high temperatures, i.e low inlet subcooling ( $\Delta h_{in}(120 \text{ kPa}, 80^\circ \text{C}) = 104 \text{ kJ/kg}$ ).

Using Eqn. (2.8) and Eqn. (2.9) the thermodynamic vapor mass quality at the outlet is calculated as

$$x_{th,out} = \frac{\dot{Q}}{\dot{M} \Delta h_{v,out}} - \frac{\Delta h_{in}}{\Delta h_{v,out}} \quad (2.10)$$

Inserting the heat flux Eqn. (2.6) and mass flux Eqn. (2.5) into Eqn. (2.10) yields

$$x_{th,out} = \frac{\dot{q} \pi d_i L}{G \pi / 4 (d_o^2 - d_i^2) \Delta h_{v,out}} - \frac{\Delta h_{in}}{\Delta h_{v,out}} = \frac{4 \dot{q}}{G \Delta h_{v,out}} \frac{L}{d_{he}} - \frac{\Delta h_{in}}{\Delta h_{v,out}} \quad (2.11)$$

This expression of Eqn. (2.11) shows the importance of  $L/d_{he}$ -ratio for the relationship between thermodynamic vapor mass quality and heat flux for constant mass flux and pressure.

The void fraction expresses the relative area of the flow cross section which is filled with vapor and is related with the vapor quality according to

$$\frac{\dot{M}_v}{\dot{M}_l} = \frac{x \dot{M}}{(1-x) \dot{M}} = \frac{x}{1-x} \quad (2.12)$$

and

$$\frac{\dot{M}_v}{\dot{M}_l} = \frac{\rho_v u_v A_v}{\rho_l u_l A_l} = \frac{\rho_v u_v \varepsilon A}{\rho_l u_l (1 - \varepsilon) A} = \frac{\rho_v}{\rho_l} \frac{u_v}{u_l} \frac{\varepsilon}{(1 - \varepsilon)} \quad (2.13)$$

The combination of Eqn. 2.12 and Eqn. 2.13 gives the relationship

$$\frac{x}{1 - x} = \frac{\rho_v}{\rho_l} S \frac{\varepsilon}{(1 - \varepsilon)} \quad (2.14)$$

with the slip velocity ratio  $S$  defined by

$$S = \frac{u_v}{u_l} \quad (2.15)$$

The explicit expressions derived from Eqn. 2.14 for the relationship between void fraction and vapor quality are given by

$$\varepsilon = \frac{x}{(1 - x) \frac{\rho_v}{\rho_l} S + x} \quad (2.16)$$

and

$$x = \frac{\frac{\rho_v}{\rho_l} S \varepsilon}{1 - \varepsilon + \frac{\rho_v}{\rho_l} S \varepsilon} \quad (2.17)$$

## 2.2. Two-phase Heat Transfer

Boiling systems can be divided into pool boiling and flow boiling applications. An example of an everyday used pool boiling system is the cooking pot in the kitchen with the heat plate as the heated surface and the water as the boiling fluid in the pot. Fluid movement is only caused by free convection inside the pool.

Otherwise, a flow boiling system is characterized by an externally enforced fluid flow over the heated surface, for example by using a pump. A common flow boiling application is the cooling cycle in a refrigerator. The refrigerant flowing through the evaporator in the cooling chamber is evaporated by removing heat from the air environment in the cooling chamber.

The coolant flow through a nuclear reactor is the flow boiling application of interest for our investigations. Boiling of water at the outer surface of the fuel rods ascertains on the one hand a moderate surface temperature and on the other hand a high transfer rate of heat energy into the boiling fluid.

The boiling process yields a high heat transfer from the heated surface into the fluid because of the phase change from liquid to vapor. The required latent heat of vaporization is removed from the surface. Bubbles are generated in cavities on the surface, where they are growing before their departure into the liquid. This dynamic formation of bubbles leads to a cyclical moving of the thermal boundary layer on the surface intensifying the convection. Influencing parameters on the two-phase heat transfer are for instance pressure, mass flow, geometry, fluid and surface properties, and interaction between fluid and surface.

*Nukiyama* [78] introduced the characteristic boiling curve for a pool boiling system. Hence, the boiling curve is also called *Nukiyama-curve*. According to Eqn. (2.18) it describes the relationship between the heat flux  $\dot{q}$  transmitted from a heated surface into a boiling liquid and the wall temperature  $T_w$  or the wall superheat  $\Delta T_w$ . Thus, the boiling curve characterizes the variation of the heat transfer coefficient  $\alpha$ .

$$\dot{Q} = \alpha(T_w - T_{f,bulk}) = \alpha \Delta T_w \quad (2.18)$$

Figure 2.3 shows the boiling curve for a heating power controlled system. For instance nuclear or electric heating processes are systems with imposed heat flux. The characteristic curve is determined by increasing

the heat input and measuring the surface temperature. During a pool boiling experiment the fluid bulk temperature and system pressure are kept constant. In flow boiling, the constant parameters are mass flux, fluid inlet temperature and outlet pressure.

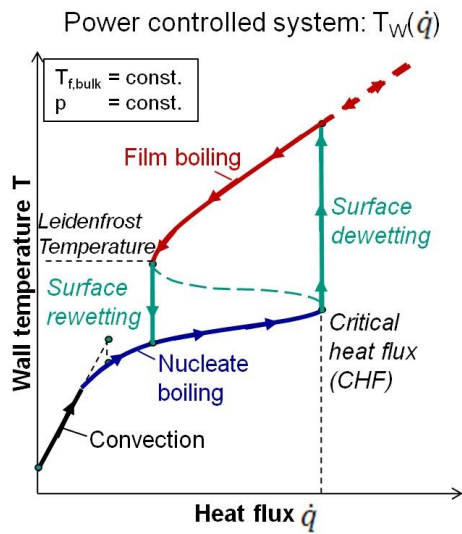


Figure 2.3.: Qualitative boiling curve for a heating power controlled system

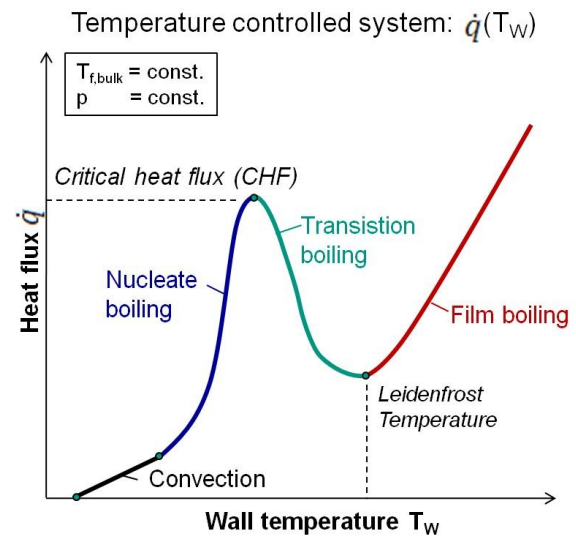


Figure 2.4.: Qualitative boiling curve for a surface temperature controlled system

For low power input the heat is transferred by convection from the heated surface into the liquid. The surface temperature increases fast because of the relatively poor convective heat transfer. With incipient boiling begins the region of nucleate boiling. The heat transfer is increased by the additional removal of the latent heat from the surface and the bubble dynamics which enforces the convection in the boundary layer. This boiling process is even intensified with increasing power. Consequently, the surface temperature increases only slightly which is noticeable in the decreased gradient of the curve.

However, the nucleate boiling region is limited by the critical heat flux (CHF). At this point, the surface locally dries out and vapor covers the dewetted surface at the CHF location. The imposed heat flux remains the same, but the covering vapor reduces dramatically the heat transfer in comparison with the nucleate boiling heat transfer. The consequence is a sudden jump of the surface temperature into the film boiling region. In film boiling the liquid boils at the interface to the superheated vapor covering the surface. Depending on the system conditions the surface temperature in film boiling can reach the melting temperature of the heater material causing thermal damage of the heating system. For most power driven systems the critical heat flux, also called 'burnout' is the limiting heat flux for the system operation and has to be avoided. Thus, the knowledge of the CHF for the specific system conditions is important for the safety of the application.

In the region of film boiling the heat transfer mechanism of radiation becomes more influencing. The transferred heat flux increases with temperature due to the proportional dependency on  $T^4$  of the radiation part. A boiling system could be operated in film boiling region at moderate surface temperature by using a fluid with a low saturation temperature.

The temperature curve for decreasing heating power from the stable film boiling region is different to the increasing power curve. The film boiling mechanism remains also for heat fluxes below the CHF remarkable in the high temperature difference. The lower limit of the film boiling curve is the so-called Leidenfrost point. Reaching this point the covering vapor blanket breaks down and the surface is rewetted by the liquid.

The heat transfer mechanism changes from film boiling to nucleate boiling, notable in the drop of the surface temperature caused by the high heat transfer of boiling liquid on the surface.

In short, the boiling curve of a heat flux controlled system shows a hysteresis with the critical heat flux as the upper limit of the nucleate boiling region for increasing heating power and the Leidenfrost point as the lower limit of the film boiling region for decreasing heating power. Both limits correspond to a sudden change in the boiling mechanism from nucleate to film boiling at the CHF caused by surface dewetting and reverse at the Leidenfrost point caused by surface rewetting.

In case of a temperature controlled system, illustrated in Fig. 2.4, it is possible to operate the system in the transition boiling region between nucleate and film boiling. Exceeding the surface temperature of the critical heat flux, the heat transfer coefficient decreases resulting in a lower transmitted heat flux. This decrease continues until the Leidenfrost point is reached.

For a power controlled system the transition region is unstable because of two co-existing stable operating modes in the nucleate and the film boiling section for the same heat flux. Therefore, the transition boiling region is plotted with a dashed line in Fig. 2.3.

### 2.3. Two-phase Pressure Drop

Figure 2.5 depicts qualitatively the pressure drop vs. mass flux curve of a two-phase flow system with heat input. The pressure drop curve for single-phase liquid flow continuously decreases with decreasing mass flux. However, the pressure drop vs. mass flux curve changes if there is heat input into the system. Decreasing the mass flux the test section pressure drop curve for a constant heat input follows the single-phase curve as long as there is no boiling. At the point called the Onset of Nucleate Boiling (ONB) the fluid begins to boil and a further decrease in mass flux causes a departure from the single-phase pressure drop curve. The reason is an increasing pressure drop caused by the increasing vapor fraction.

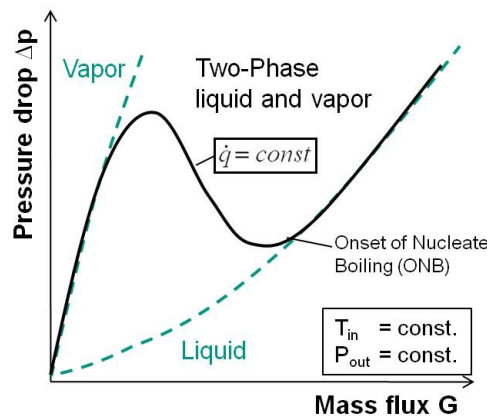


Figure 2.5.: Schematic pressure drop vs. mass flux curves for single and two-phase flow

Instead of decreasing continuously with the mass flux, the two-phase pressure drop curve passes a local minimum. At this point the curve changes from a positive to a negative slope. A further mass flow decrease intensifies the boiling and the pressure drop increases until a local maximum is reached. In this region the channel cross section is almost completely filled with vapor because of the high void fraction and the curve approaches the single-phase vapor curve.

From the momentum equation the two phase pressure can be expressed by the sum of three components which are frictional, gravitational and acceleration pressure drop. Considering the flow as steady state, homogeneous and one-dimensional the pressure drop components are given by the following equations [5]

Frictional pressure drop

$$-\left(\frac{dp}{dz}\right)_{friction} = \tau_{shear} \frac{P_{wet}}{A_{cross}} = \zeta \frac{\rho_{2ph}}{2} u^2 \frac{1}{d_{hydr}} = \zeta \frac{G^2}{2\rho_{2ph}} \frac{1}{d_{hydr}} \quad (2.19)$$

Gravitational pressure drop

$$-\left(\frac{dp}{dz}\right)_{gravitational} = [\varepsilon\rho_v + (1-\varepsilon)\rho_l] g \sin\gamma \quad (2.20)$$

Acceleration pressure drop

$$-\left(\frac{dp}{dz}\right)_{acceleration} = G^2 \frac{d}{dz} \left[ \frac{x^2}{\varepsilon\rho_v} + \frac{(1-x)^2}{(1-\varepsilon)\rho_l} \right] \quad (2.21)$$

The increasing two-phase pressure drop with decreasing mass flux at constant heat input in Fig. 2.5 is caused by the increasing vapor content. Since the density of vapor is lower than the one of liquid the two-phase mixture density is reduced. The resulting acceleration introduces an additional pressure gradient and moreover increases the frictional pressure drop for constant mass flux [5].

## 2.4. Two-Phase Flow Instabilities

Two-phase flow systems can be affected by instability and oscillation phenomena, which are classified in static and dynamic instabilities [16]. Static instabilities can cause a shift of the operating point to another steady state condition [15]. Dynamic instabilities are caused by inertia and feedback effects, like thermal, pressure or density oscillations [49]. These phenomena can lead to a premature critical heat flux which explains the extensive investigations performed on instability in two-phase processes as summarized for example in [16] - [32].

### 2.4.1. Static Instability

The region between the local extrema of the characteristic pressure drop curve in Fig. 2.6 has a negative slope. This region is susceptible to static instability, also termed as Ledinegg instability.

The minimum point is often termed in literature as the Onset of Flow Instability (OFI). It does not mean that the system flow is in every case unstable for mass fluxes below the OFI, but it defines the point where the region of possible flow instabilities begins. Otherwise, operating the system in the positive slope region of higher mass fluxes than the OFI ensures safety against static flow instability.

The static instability phenomenon occurs if the slope of the test section pressure drop curve is smaller (i.e. more negative) than the slope of the characteristic pump curve. The criterion for possible Ledinegg-instability is given by Eqn. (2.22).

$$\left(\frac{\partial \Delta p}{\partial G}\right)_{Testsection} < \left(\frac{\partial \Delta p}{\partial G}\right)_{Pump} \quad (2.22)$$

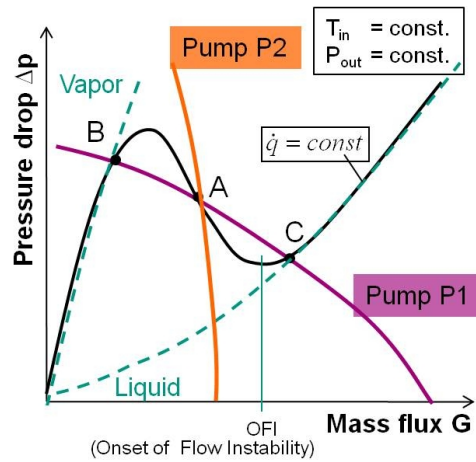


Figure 2.6.: Two-phase pressure drop curve and pump characteristic

Table 2.1.: Systematic classification of dynamic instabilities after Bouré et al. [16]

Class	Type	Mechanism
Fundamental dynamic instabilities	Acoustic oscillations	Resonance of pressure waves
	Density wave oscillations	Delay and feedback effects in relationship between flow rate, density and pressure drop
Compound dynamic instabilities	Thermal oscillations	Interaction of heat transfer variation and flow dynamics
	Parallel channel instability	Interaction between parallel channels
Compound dynamic instability as secondary phenomena	Pressure drop oscillations	Interaction between channel and compressible volume

The characteristic curve of pump P1 shows this unstable behavior for point A in Fig. 2.6. The slope of the pressure drop curve of the test section is steeper than the slope of the pump curve and the two curves share three intersection points. Induced by a disturbance the system state can change from the unstable point A to the point B. The resulting flow excursion is characteristically for Ledinegg-instability. Reaching point B the system conditions are suddenly in the region of low mass flow and high vapor content and consequently critical heat flux can be caused.

In contrast, the steeper characteristic curve of pump P2 has only one intersection point with the test section curve. Thus, the flow is stable for this system condition. Another stabilization precaution is the use of a throttle valve or orifice upstream of the boiling channel. Both effects are discussed later in more detail in chapter 6.

### 2.4.2. Dynamic Instabilities

Flow instabilities which are caused by inertia and feedback effects are termed as dynamic instabilities. The basic mechanism is the propagation of a wave through the boiling channel after a disturbance. For instance, a disturbance caused at the inlet reaches the exit after a certain delay time. The disturbance wave is then reflected and can cause a second disturbance at the point of origin. This mechanism can result in an oscillating behavior which depends on the propagation time the wave needs to pass the system. Typical dynamic instabilities in two-phase systems are acoustic wave, density wave, and pressure drop instabilities.

*Bouré et al.* [16] classified the dynamic instabilities in further categories of fundamental, compound, and compound as secondary phenomena which are listed in Tab. 2.1.

## 2.5. Relationship between Heat Transfer and Pressure Drop during CHF Experiment

This section shows how the two-phase pressure drop curve of chapter 2.3 is related to the heat transfer curve of chapter 2.2. Furthermore, the importance of flow stabilization against instabilities described in chapter 2.4 is explained by depicting the operating points of the boiling curve in the pressure drop diagram.

The critical heat flux is generally determined by increasing the heat input until the critical heat flux occurs while maintaining constant mass flow rate, fluid inlet temperature and outlet pressure. The resulting characteristic boiling curve is shown qualitatively in Fig. 2.7 b) for the local surface temperature  $T_{w,z}$  at the axial position  $z$  as function of heat flux at constant mass flux  $G^*$ , fluid inlet temperature  $T_{in}$  and outlet pressure  $p_{out}$ . Numbers from 1 to 5 denote the local tube temperatures for various heat inputs from the onset of boiling (1) to the temperature jump at the CHF (5).

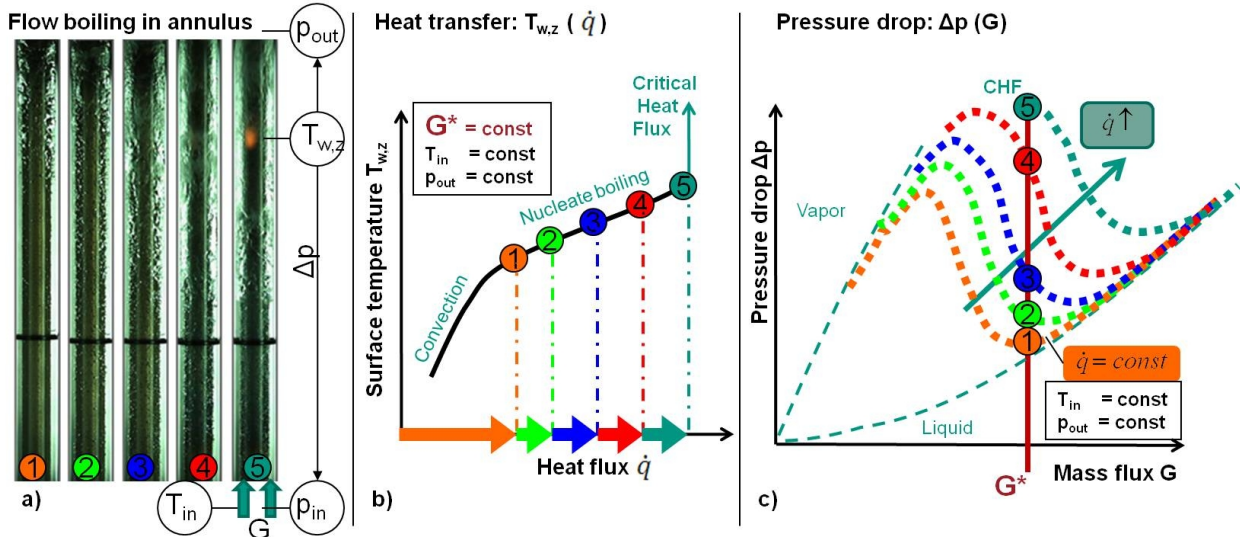


Figure 2.7.: a) Flow boiling in channel with increasing heat input, b) Characteristic boiling curve: Surface temperature depending on heat input, c) Characteristic pressure drop curves for different constant heat inputs

The pictures of the test section in Fig. 2.7 a) show the intensified flow boiling in the annular channel with increasing heat input. The location of significant void production is shifted upstream and the vapor content in the mixture increases. The location where the temperature rise occurs at the critical heat flux is obvious in picture (5): the red surface point is caused by glowing.

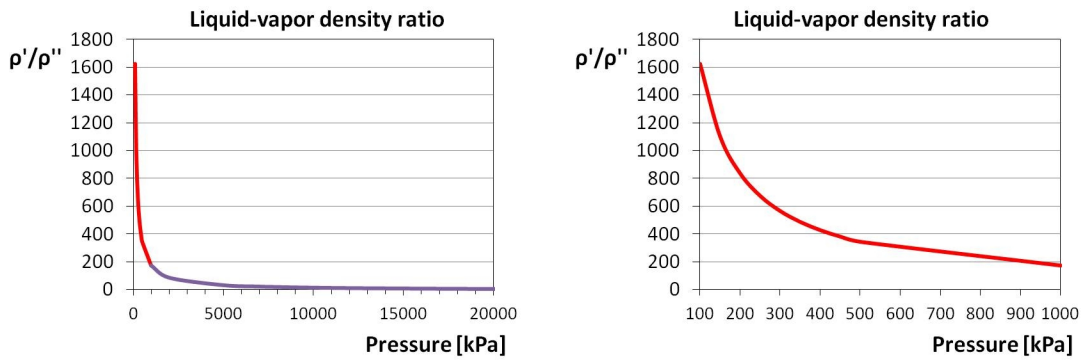


Figure 2.8.: Pressure dependency of density ratio between liquid and vapor phase of saturated water

Figure 2.7 c) shows the characteristic pressure drop curves for the selected heat inputs (1)-(5). The method to determine the characteristic pressure drop curve is to decrease the mass flow rate while maintaining constant heat input, fluid inlet temperature and outlet pressure. Therefore, each pressure drop curve corresponds to a constant heat input, but is related to the variation of mass flux.

In order to find the operating points of diagram b) in diagram c), the pressure drop curves for the specific heat inputs at the same inlet temperature and outlet pressure, have to be known. Drawing a vertical line in diagram c) at the constant mass flux  $G^*$  of diagram b) defines the operating points (1)-(5) by the intersection points with the pressure drop curves at the specific heat flux. This means that in case of the measurement of a stable critical heat flux, the stable flow conditions have to be ensured for any operating point of the vertical line at mass flux  $G^*$  until the stable CHF occurs.

In short, each point of the boiling curve describing the heat transfer is related to a point of the pressure drop curve indicating the sensitivity to instabilities. Note, the boiling curve in diagram b) has no information about the system susceptibility for instabilities.

## 2.6. Water and Steam Properties

Fluid properties such as density, viscosity, surface tension, enthalpy and others depend on pressure and temperature. In the case of boiling water, the two existing phases of liquid water and vapor (steam) have each different properties and dependencies. With the transition between the states of matter some properties are changing abruptly. These differences between the phases can be expressed by the ratio of the properties. For instance the density ratio is an important factor for the two phase system affecting the vapor volume fraction (Eqn. (2.16)).

The influence of pressure on the properties of water and steam is particularly significant for low pressures. Figure 2.8 shows the pressure dependency of the density ratio of the liquid phase ( $\rho'$ ) and the vapor phase ( $\rho''$ ) at saturation conditions.

The density ratio decreases dramatically from about 1600 to 170 in the low pressure range between 100 and 1000 kPa (1-10 bar). Considering the low pressure range more closely in the diagram on the right of Fig. 2.8, the negative gradient is very steep between 100 and 300 kPa (1-3 bar). In the higher pressure range from 1000 to 20000 kPa (10-200 bar) the ratio decreases more slowly from 170 to 3. Other fluid properties like viscosity, saturation temperature or surface tension show also a higher influence of pressure in the low pressure region.



### 3. State of the Art

This chapter contains a review on literature related to the present work. The first section describes experimental conditions and observations for investigations of critical heat flux in internally heated annuli at low pressures. The next section introduces theoretical models for describing the phenomena of critical heat flux in pool boiling and flow boiling systems. The third section presents experimental work performed for investigating surface structure or wettability effects on the critical heat flux.

#### 3.1. Critical Heat Flux Experiments in Annuli

Experiments of boiling heat transfer and critical heat flux for forced convective flow boiling with regard to the conditions in nuclear reactors and steam generators are generally conducted with tube, annular or rod bundle test section geometries. Extensive studies were performed, however particularly for high pressure, high flow conditions and most of them were examined with tubes. Reviews on CHF for these conditions are given in [54], [24], [22], [27], [64], for instance. Critical heat flux at low flow, low pressure conditions is important with respect to accident conditions of boiling water reactors [22], [25]. Nevertheless, available experimental data and prediction methods are limited.

This section contains firstly a short comparison between CHF in tube and annular conditions followed by a summary of critical heat flux experiments for flow boiling in annuli focusing on low pressure conditions.

The general parametric trends of CHF in annuli in comparison to CHF in a reference tube of 8 mm diameter are discussed by *Doerffer et al.* (1994) [30]. The authors collected experimental data considering the general effects of pressure, mass flux, vapor quality, gap size,  $L/d_{he}$ -ratio, and curvature. However, their data cover only high pressures from 980 to 14100 kPa (9.8-141 bar). Thus, the effects for pressures below 1000 kPa (10 bar) are not included in this study.

*Pressure:* For pressures higher than 3000 kPa (30 bar) the CHF decreases with increasing pressure for both geometries. CHF in annuli are smaller than in the 8 mm-tube, particularly in the lower pressure region of the considered range. The difference in CHF between annuli and tube decreases with increasing pressure. For lower pressures than 3000 kPa (30 bar) *Doerffer et al.* [30] assumed a constant influencing factor of  $\dot{q}_{CHF,annulus} = 0.9 \dot{q}_{CHF,tube}$ .

*Vapor mass quality:* Regarding the effect of vapor mass quality on the CHF for annuli the CHF decreases in the negative and low positive vapor mass quality region. The decreasing trend diminishes and the CHF values are almost constant for higher qualities. Compared to the 8 mm-tube the CHF values in annuli are smaller for the same quality and similar conditions. The differences in CHF are higher for positive than for negative vapor mass qualities.

*Mass flux:* The effect of mass flux is similar for both geometries: increasing CHF with increasing mass flux in the low quality region. Furthermore, *Doerffer et al.* [30] report a decreasing influence on CHF for increasing mass flux in the higher positive quality region which is observed for both geometries.

*Geometry:* The influence of gap size showed an increasing trend of CHF with increasing gap size from 1 to 4 mm, a maximum in the range of 4-6 mm and a decreasing tendency for gaps larger than 6 mm. According

to *Doerffer et al.* [30] the decrease in CHF with decreasing gap size in the region of 1-4 mm might be caused by vapor bridging the gap and therefore provoking the CHF at lower heat fluxes.

*Doerffer et al.* [30] observed that the curvature effect is insignificant comparing the CHF data of annuli with the same gap size but different inner and outer diameter at similar  $L/d_{he}$  ratio, mass flux, and pressure. However, only few data complied with these requirements. Furthermore, they reported a generally higher CHF for externally than for internally heated annuli.

Based on their parametric study *Doerffer et al.* [30] developed a correlation for CHF in annuli using the 1986 CHF look-up table for tubes of *Groeneveld et al.* [42]. The CHF is calculated for a tube with 8 mm diameter for the given conditions and corrected by three factors corresponding to the observed effects of pressure, vapor mass quality and gap size.

*Mishima et al.* (1987) [75] investigated the difference in CHF between round tubes, annuli and rectangular channels at low pressures. A geometry effect was more remarkable for low and intermediate mass velocities. Similar to *Doerffer et al.* [30] they observed lower CHF in geometries with unheated wall than in tubes at same vapor mass quality. The existence of an unheated wall causes a non-uniform distribution of liquid film according to the authors. They assumed that a substantial amount of liquid remained on the unheated wall. The reduced vapor mass quality at CHF is approximated by following equation

$$x_{CHF,channel} = x_{CHF,tube} \frac{P_{heat}}{P_{wet}} \quad (3.1)$$

where  $P_{heat}$  and  $P_{wet}$  are the heated and wetted perimeter of the channel. This effect is supposed to become smaller for higher mass fluxes.

Furthermore, *Mishima et al.* [75] presented experimental data of a benchmark project of the Japanese Society of Mechanical Engineers (JSME). CHF experiments with the same geometrical annular test section design and parameter conditions have been conducted at several universities and institutions. Since the original report from 1967 [98] was written in Japanese this summary refers to the presented data and comments in *Mishima et al.* [75]. The annular test sections had a heated length of 300 mm, an inner diameter of 10 mm and an outer diameter of 19 mm. The experimental parameters were outlet pressure of 100 kPa (1 bar), low inlet subcoolings of 19, 61, and 124 kJ/kg, and high mass fluxes between 500 and 5000 kg/(m<sup>2</sup>s).

Although applying the same experimental conditions the experimental data of the different institutions differed significantly. The measured CHF values for the highest applied subcooling of 124 kJ/kg were quite close. However, the CHF results of some institutions for the lowest subcooling at 19 kJ/kg were about 50% lower at the same conditions. It has been reported that the discrepancy in the data could be related to flow instability because of varied pump characteristics and inlet throttling conditions. However, this circumstances were not satisfactorily discussed according to *Mishima et al.* [75].

In another work *Mishima et al.* (1985) [76] investigated experimentally the influence of flow instabilities on the CHF for water flow in a tube at atmospheric pressure. Their results showed that the CHF at low flow and low pressure conditions was influenced by various instabilities resulting in remarkably lower CHF values for unstable than for stable flow conditions.

*Fiori and Bergles* (1968) [36] performed CHF experiments in annular and tube geometry at low pressure. Using an outer glass tube for the internally heated annulus, they visualized the flow regime and the occurrence of CHF by photographs and video tapes. They conducted experiments with outlet pressures of 148-600 kPa (1.48-6 bar), mass fluxes of 542-1722 kg/(m<sup>2</sup>s) and inlet subcoolings of 23-221 kJ/kg. The

inner stainless steel tube had an outer diameter of 7.92 mm and 0.89 mm wall thickness. The heated length varied between 179 and 254 mm. The outer glass tubes had inner diameters of 12.55 and 13.61 mm. Since there was no burnout protection system installed each CHF experiment led to the destruction (burnout) of the inserted tube.

*Fiori and Bergles* [36] identified visually slug or froth flow prior to CHF in subcooled flow boiling. Slug flow was also determined for flow boiling in the tube geometry using an electric resistant probe. They observed the formation of a very localized dry patch at CHF according to following mechanism: The liquid film under a passing vapor clot breaks at this location and the temperature rises due to the dry out. If the subsequently liquid slug is not sufficiently quenching the dry patch then the temperature rises and the circular patch glows. The patch expands rapidly over the entire circumference and melts the metal.

*Fiori and Bergles* [36] developed a model considering the unstable situation of cyclical dry out and quenching of the surface at CHF. However, the authors pointed out that the model could not be used generally since flow structure information such as slug frequency or radius of the initial dry spot was needed and basic theoretical models for these phenomena were not available. Nevertheless, the model regards the evolution of the temperature rise at the surface implicating surface properties such as conductivity of the material. This is a difference to the hydrodynamic models. According to their model wall thickness and wall material should influence the CHF. Increased wall thickness and thermal conductivity would increase CHF.

*Rogers et al.* (1982) [85] conducted CHF experiments for three different annular gap sizes. The directly heated inner Inconel-718 tube was 480 mm long and had an outer diameter of 13.1 mm and a wall thickness of 1.25 mm. The unheated outer glass tubes had inner diameters of 22, 25, and 30.2 mm. *Rogers et al.* [85] presented experimental CHF data for a mass flux range from 60 to 650  $kg/(m^2s)$ , inlet subcooling conditions of 180, 265, and 389  $kJ/kg$  and a constant outlet pressure of 156  $kPa$ . The results showed that CHF occurred at higher values, the larger the annular gap was. The authors distinguished between a low mass flux region  $G < 180, kg/(m^2s)$  and a high mass flux region  $G > 180 kg/(m^2s)$ . A linear relationship between critical heat flux and mass flux for a given inlet subcooling was observed for the higher mass flux region. Increased subcooling led to higher CHF values for mass fluxes between 180 and 650  $kg/(m^2s)$ . Furthermore, the difference in CHF between the different subcooling conditions increased with increasing mass flux.

*Rogers et al.* [85] compared their results with four different empirical correlations of *Knoebel et al.* [59], *McAdams et al.* [72], *Menegus* [73], and *Katto* [52]. All correlations significantly overpredicted the experimental CHF. The authors emphasized that using empirical correlations all important variables have to be exactly in the range for which the correlation was developed for.

Since the tested correlations were inadequate to describe their experimental data, *Rogers et al.* [85] developed for each tested annular geometry an individual empirical correlation depending on mass flux and inlet subcooling condition. A general use of these correlations is not possible.

*El-Genk et al.* (1988) [33] investigated CHF for water in vertical annuli at low flow and low pressure. The inner stainless steel tube with an outer diameter of 12.7 mm and a wall thickness of 0.89 mm was heated directly over a length of 500 mm. The outer tube was made of Pyrex and was unheated. Three annular geometries were tested with inner diameters of the outer tubes of 20, 21.84, and 25.4 mm.

They conducted experiments for subcooled inlet conditions between 182 and 312  $kJ/kg$ , mass fluxes from zero flow to 260  $kg/(m^2s)$ , and a constant outlet pressure of 118  $kPa$  (1.18 bar). The CHF values for the two smaller annuli were in a similar range. In contrast, the CHF for the largest annulus was notably

higher. Moreover, a subcooling effect was only noticeable for the largest annulus for mass fluxes higher than  $150 \text{ kg}/(\text{m}^2\text{s})$ . In this range the CHF increased with increasing subcooling.

According to their visual observations a two-phase flow transition occurred at CHF from annular to annular-mist flow for the smallest annulus and from slug-churn to churn-annular flow for the two larger annuli. *El-Genk et al.* [33] developed separate empirical correlations for both flow pattern transitions at CHF conditions. However, these correlations are inadequate for general use since they are only valid in the small parameter range of the experimental data.

*Schoesse et al.* (1997) [90] measured CHF for flow boiling in an vertical internally heated annulus at low flow and low pressure conditions. The test section consisted of an inner stainless steel tube with an outer diameter of 10 mm, a wall thickness of 1.2 mm and a heated length of 1000 mm. The outer tube with an inner diameter of 22 mm was made of Pyrex glass for flow observation. The experimental conditions were mass fluxes of  $20\text{-}280 \text{ kg}/(\text{m}^2\text{s})$ , inlet subcoolings of  $30\text{-}218 \text{ kJ}/\text{kg}$  and a constant outlet pressure of 128 kPa (1.28 bar).

The authors differed between a lower and a higher mass flux range. For mass fluxes lower than  $140 \text{ kg}/(\text{m}^2\text{s})$  they observed at CHF conditions flooding and chugging at the exit. These fluctuations were not noticeable for mass fluxes higher than  $140 \text{ kg}/(\text{m}^2\text{s})$ . The two phase flow pattern was characterized by transitions from bubble flow to churn flow to annular flow over the heated length of the channel. In the annular flow regime they distinguished between pulsated annular flow where liquid is periodically accelerated through the channel and stable annular-mist flow with a continuous annular flow pattern.

*Chun et al.* (2001) [25] performed CHF experiments in an annular test section for a wide range of pressures from 570 to 15010 kPa (5.7-150.1 bar). The mass flux varied between 200 and  $650 \text{ kg}/(\text{m}^2\text{s})$  and the inlet subcooling conditions covered a range from 85 to  $413 \text{ kJ}/\text{kg}$ . The inner Inconel-600 tube with an outer diameter of 9.54 mm was heated indirectly over a length of 1842 mm. The wall thickness was not reported. The inner diameter of the outer tube was 19.4 mm. The two-phase flow pattern was not visually observable.

CHF occurrence was detected by a continuous temperature increase at one of the embedded thermocouples on the outer surface of the heated tube. CHF occurred always at the top end of the heated section.

The authors reported that the CHF increased with pressure, reached a maximum in the pressure range of 2000-3000 kPa (20-30 bar), and decreased with further increase in pressure. However, this effect was particularly observed for CHF at higher mass fluxes ( $500\text{-}650 \text{ kg}/(\text{m}^2\text{s})$ ) and high subcoolings. For the lower mass fluxes ( $200\text{-}500 \text{ kg}/(\text{m}^2\text{s})$ ) the rapid increase in the low pressure region was hardly observed or not observed at all.

An interesting observation was the pressure dependency of the thermodynamic vapor mass quality at CHF. For a low mass flux of  $200 \text{ kg}/(\text{m}^2\text{s})$  the quality increased continuously from about 0.2 at 570 kPa to 0.4 at 15010 kPa whereas the quality for the high mass flux of  $650 \text{ kg}/(\text{m}^2\text{s})$  remained almost constant between 0.1 and 0.2 over the complete range of pressure.

*Chun et al.* [25] compared their experimental results with the correlations of *Doerffer et al.* [30], *Bowring* [17], and *Janssen and Kervinen* [48]. The *Doerffer* correlation using the 1986 look-up-table of *Groeneveld et al.* [42] significantly overpredicted the CHF values for the lower pressure range. However, the predicted values on base of the improved look-up-table of 1995 [40] showed better performance. This demonstrates that the accuracy of the *Doerffer* correlation strongly depends on the accuracy of the used look-up-table for tubes. The *Bowring* correlation showed satisfying agreement with the experimental data in the complete experimental range whereas the *Janssen and Kervinen* correlation overpredicted the lower

pressure data. In summary, all three correlations tended to overestimate (slightly or significantly) CHF for lower pressures than 10000 kPa (100 bar).

The summary of the geometry parameters and experimental conditions for the above described investigations of critical heat flux in annuli at low pressure conditions is presented in Tab. 3.1. Moreover, the experimental parameters of the present work (COSMOS) are added at the bottom of the table.

Table 3.1.: Literature for CHF in annuli at low pressure and experimental parameter range

Data source	L	d <sub>i</sub>	d <sub>o</sub>	d <sub>hydr</sub>	d <sub>he</sub>	L/d <sub>he</sub>	G	p	Δh <sub>in</sub>
	mm	mm	mm	mm	mm		kg/(m <sup>2</sup> s)	kPa	kJ/kg
JSME data in Mishima et al. [75]	300	10	19	9	26.1	11.5	528 -4958	100	19 124
Fiori and Bergles [36]	179 -254	7.92	12.55 -13.61	4.62 -5.69	11.9 -15.5	15 -21.3	542 -1722	148 -600	23 -221
Rogers et al. [85]	480	13.1	22 -30.2	8.9 -17.1	23.85 -56.5	8.5 -20.2	60 -648	156 156	180 -389
El-Genk et al. [33]	500	12.7	20 -25.4	7.3 -12.7	18.8 -38.1	13.1 -26.6	19.3 -258	118	182 -312
Schoesse et al. [90]	1000	10	22	12	38.4	26.0	20 -280	128	30 -218
Chun et al. [25]	1842	9.54	19.4	9.86	29.9	61.6	198 -645	570 -15000	85 -353
COSMOS small an. present work	326	9.5	13	3.5	8.3	39.3	250 -1000	115 -300	100 -250
COSMOS large an. present work	326	9.5	18	8.5	24.6	13.2	250 -400	120 -300	104 -250

## 3.2. Theoretical Models for Critical Heat Flux

This section presents some theoretical approaches from literature for describing the mechanism of critical heat flux occurrence. Most theoretical CHF models were developed for saturated pool boiling systems and consider particularly the hydrodynamic aspects of the boiling system. The first part describes existing models for pool boiling conditions and the second part considers theoretical descriptions of CHF mechanisms for flow boiling.

### 3.2.1. Critical Heat Flux Models for Pool Boiling

*Kutadeladze* (1949) [63] developed a model for pool boiling CHF based on the hydrodynamic effect of the destruction of a local two-phase flow close to the surface. Reaching a critical velocity in the vapor phase the CHF is initiated. *Kutadeladze* [63] proposed the following equation with factor  $K=0.16$  from experimental data.

$$\frac{\dot{q}_{CHF}}{\Delta h_v \rho_v^{1/2} [\sigma g (\rho_l - \rho_v)]^{1/4}} = K \quad (3.2)$$

*Zuber* (1959) [110] considered a model of vapor jets above nucleation sites and liquid flow towards the surface between the jets. For increasing heat flux the space between vapor jets and liquid flow diminishes causing an unstable condition. Consequently, vapor patches are formed and collapsed on the surface. Using the Taylor and Helmholtz instability *Zuber* [110] developed an equation of the same form as Eqn. (3.2) of *Kutadeladze* [63] but with a constant  $K=0.131$ .

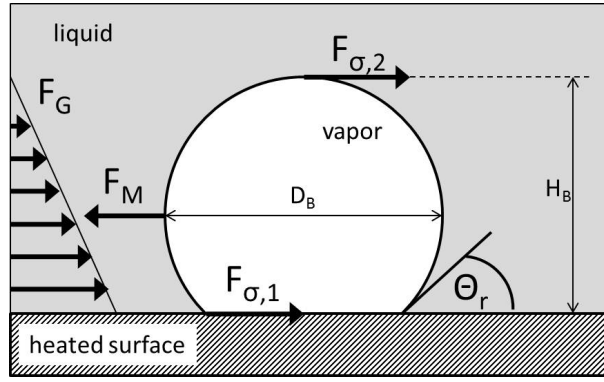


Figure 3.1.: Single bubble attached to heated surface as basic situation for the model of *Kandlikar* [51]

*Chang* (1961) [23] also obtained a similar equation to Eqn. (3.2) considering the forces acting on a rising bubble. CHF is induced when the rising vapor is carried back to the surface expressed by a critical value of Weber number. *Chang* [23] proposed the factor  $K=0.098$  for a vertical surface and  $K=0.13$  for a horizontal surface.

*Lienhard and Dhir* (1973) [67] further modified the model of *Zuber* [110] including geometry and size.

*Haramura and Katto* (1983) [46] extended the model of *Zuber* [110] considering the formation of small vapor jets in a liquid macrolayer under a bubble.

*Rohsenow and Griffith* (1956) [87] considered a blockage of liquid flow to the heated surface by vapor bubbles over the surface. They proposed the following equation for CHF

$$\frac{\dot{q}_{CHF}}{\Delta h_v \rho_v} = C_{m/s} \left( \frac{g_{loc}}{g} \right)^{1/4} \left[ \frac{\rho_l - \rho_v}{\rho_v} \right]^{0.6} \quad (3.3)$$

where  $C_{m/s}$  is a dimensional coefficient of  $C_{m/s}=0.012$  m/s, and  $g_{loc}$  and  $g$  are the local and standard gravitational accelerations, respectively.

The above described models only consider the hydrodynamic aspects for a two phase system. According to *Kandlikar* (2001) [51] there is a need of including fluid-surface interaction. Therefore, he developed a theoretical model for predicting the critical heat flux in saturation pool boiling including surface-liquid interaction. *Kandlikar* [51] identified the receding contact angle to be the important parameter for the fluid-surface interaction at CHF. The basic background of the model is described in the following.

The considered situation in the model of *Kandlikar* [51] is shown in Fig. 3.1 with a sketch of a single bubble attached to a heated surface. Evaporation of a bubble causes a momentum force parallel to the heated surface acting against gravity and surface tension forces. This force pulls the bubble interface into the surrounding liquid. If the momentum force  $F_M$  due to evaporation exceeds the retaining forces of surface tension  $F_{\sigma,1}$  and  $F_{\sigma,2}$  and the gravitational force  $F_G$  then the CHF is initiated by expanding the dried out zone. The force balance is given by

$$F_M = F_{\sigma,1} + F_{\sigma,2} + F_G \quad (3.4)$$

Due to the evaporation the produced vapor causes a change in momentum resulting in a force acting at the interface. The interface is considered in the model as a 2-dimensional plane with height  $H_B$  and a unit

width. Expressing the momentum change by the evaporating mass flow rate and the vapor velocity yields

$$F_M = \left( \frac{\dot{q}_I}{\Delta h_v} \right)^2 \frac{1}{\rho_v} H_B \quad (3.5)$$

where  $\dot{q}_I$  is the heat flux at the interface.

The surface tension force  $F_{\sigma,1}$  acts on the three-phase contact line of liquid, vapor and solid phases at the bubble base. At the top portion of the bubble acts the surface tension force  $F_{\sigma,2}$  between the liquid and the vapor phase. These forces are given for unit length normal to the plane by

$$F_{\sigma,1} = 1 \sigma \cos \theta_r \quad (3.6)$$

$$F_{\sigma,2} = 1 \sigma \quad (3.7)$$

with the fluid surface tension  $\sigma$ , and the receding contact angle  $\theta_r$ .

The force due to gravity depends on the heater surface orientation given by the inclination angle  $\gamma$  and the hydrostatic pressure on a surface of height  $H_B$  and unit width.

$$F_G = \frac{1}{2} g (\rho_l - \rho_v) H_B H_B 1 \cos \gamma \quad (3.8)$$

The terms of the individual forces of Eqns. (3.5), (3.6), (3.7), and (3.8) are inserted into Eqn. (3.4). Furthermore, the bubble diameter is expressed considering the wave-length of Taylor instability of a vapor film on the heated surface. The heat flux at the interface  $\dot{q}_I$  is related by *Kandlikar* [51] to the removed heat from an influenced surface area around the bubble as it was already proposed by *Han and Griffith* [45]. The resulting equation for the model of *Kandlikar* [51] for saturated pool boiling including the fluid-surface interaction by the receding contact angle is given by

$$\frac{\dot{q}_{CHF}}{\Delta h_v \rho_v^{1/2} [\sigma g (\rho_l - \rho_v)]^{1/4}} = \left( \frac{1 + \cos \theta_r}{16} \right) \left[ \frac{2}{\pi} + \frac{\pi}{4} (1 + \cos \theta_r) \cos \gamma \right]^{1/2} \quad (3.9)$$

Thus, the model of *Kandlikar* [51] results in a similar form as Eqn. (3.2) but the factor on the right side is expressed in dependency of receding contact angle. The model is developed for surface orientations between horizontal and vertical. Higher inclination angles (heated surface facing downward) would lead to flow hydrodynamics and the heater size would be of importance. Furthermore, subcooling effects are not directly considered in the model.

*Kolev* [60] developed a model to predict both, the heat transfer and the critical heat flux with a single model. The author considered the microscale phenomena of the nucleate boiling heat transfer process of turbulence generation in the boundary layer due to bubble growth and bubble departure. *Kolev* [60] used foregoing models for bubble departure diameter, active nucleate site density and distance between nucleation sites. The empirical correlation of *Wang and Dhir* [102] is inserted for calculating the active site density  $n_{act}$  with the following proportional relationship

$$n_{act} \propto n_{cav} (1 - \cos \theta) / D_{B,crit}^6 \quad (3.10)$$

with number of micro-cavities per unit surface area  $n_{cav}$ , static contact angle  $\theta$ , and a critical bubble diameter

expressed by a function of local superheating expressed by

$$D_{B,crit} \approx \frac{T_{sat}}{T_w - T_{sat}} \frac{4\sigma}{\rho'' \Delta h_v} \quad (3.11)$$

From Eqn. (3.10) results that increasing contact angle leads to an increased number of active sites. Furthermore, an increased number of micro-cavities on the surface increases the number of active sites.

*Kolev* [60] introduced a time-averaged fluctuation velocity for the mechanism of heat transfer by turbulence in the boundary layer. The heat flux is related to the ratio  $\Delta\tau_w/\Delta\tau_d$  of waiting time  $\Delta\tau_d$  between departure and bubble activation and time  $\Delta\tau_d$  needed for the growth from activated critical diameter to bubble departure size.

With increasing temperature difference the nucleate site density increases as well. This causes a decrease in bubble diameter and therefore a decrease in bubble departure time. At a certain temperature difference the heat flux reaches a maximum which is considered to be the critical heat flux. This behavior is very interesting since the CHF is derived directly from the nucleate boiling heat transfer mechanism of the model. The CHF depends on the static contact angle since the used expression of the nucleate site density is a function of it. According to the model, the CHF increases with decreasing contact angle. On the other hand, CHF would decrease if the amount of microcavities on the surface is increased as shown qualitatively in *Kim et al.* [57].

*Kolev* [60] found good agreement in both, the heat transfer and critical heat flux, when applying his model to reference data from literature in saturated pool boiling of water.

### 3.2.2. Critical Heat Flux Models for Flow Boiling

Critical heat flux and boiling heat transfer under force convective conditions were extensively investigated because of the flow boiling application in nuclear reactors and steam generators. Methods to predict critical heat flux are empirical correlations, mechanistic models or look-up-tables. These methods are mostly recommended for operating conditions of Boiling Water or Pressurized Water Reactors. Nevertheless, most experimental data and correlations refer to CHF in tube geometries. An overview of CHF and predicting methods concerning reactor conditions is given by *Cheng and Müller* [24].

Several empirical correlations have been reported for different conditions of pressure, mass flux, local quality, tube diameter and fluid. These correlations are only valid in the given parameter ranges of the correlated experiments. Empirical correlations covering wide parameter ranges are given for example by *Doroshchuk et al.* [31], *Kon'kov* [61] or *Katto and Ohno* [55].

Look-up-tables (LUT) for critical heat flux predict the CHF for tubes as a function of pressure, mass flux and thermodynamic vapor mass quality. The tables are developed for a normalized tube diameter from large data banks of experimental data. Variations in geometry and other conditions to the normalized case are corrected by additional factors. The advantage of the look-up-tables is the wide application range of parameters and the simple application. However, the accuracy depends on the availability of sufficient experimental data in the respective parameter range. Moreover, the correction factors have to reproduce the correct trends.

Similar to the theoretical models for CHF in pool boiling most flow boiling CHF models consider only the hydrodynamic aspect. A review on CHF modeling is given by *Katto* [54], for instance.

*Weisman and Pei* (1983) [104] developed a CHF model according to the near-wall bubble crowding theory. The model considers a bubble layer between the heated surface and the liquid core. The bubble crowding



near the surface prevents the cold liquid from reaching the heated wall at a certain critical void fraction in the layer. The void fraction is defined by the balance of the outward vapor flow and the inward liquid flow at the bubbly layer-liquid core interface. This basic *Weisman-Pei* model was extended and improved in subsequent work by *Ying and Weisman* (1986) [106] and *Weisman and Ileslamlou* (1988) [103].

Since the *Weisman-Pei* model [104] was developed and tested for flow boiling in tubes *Lim and Weisman* (1990) [68] modified the model to predict CHF in internally heated annular geometry. The authors found an empirical correction factor depending on the diameter ratio of the annulus for correcting the predicted CHF value using the *Weisman-Pei* model [104] for a round tube of the same heated equivalent diameter  $d_{he}$  (Eqn. (2.4)) according to

$$\dot{q}_{CHF,annulus} = (1.46 - 0.27 \frac{d_o}{d_i}) \dot{q}_{CHF,tube}(d_{he}) \quad (3.12)$$

with  $d_i$  and  $d_o$  being the inner and outer diameter of the annulus, respectively. The correction procedure showed good agreement in comparison with literature data for pressures of 6800-15500 kPa (68-155 bar).

The liquid sublayer dryout theory of *Lee and Mudawar* (1988) [65] describes the dryout of a thin liquid sublayer underneath an intermittent vapor blanket. Helmholtz-instability is the basic mechanism of initiating dry out at the interface between macrolayer and vapor blanket. The length of the vapor blanket is determined by the Helmholtz critical wave length. The model implicates three empirical constants to evaluate the temperature of the liquid entering the sublayer and to calculate the layer thickness.

*Katto* (1992) [53] improved and extended the model for the use of other fluids than water and for lower pressure by inserting a single empirical vapor velocity coefficient depending on Reynolds number, density ratio and void fraction instead of the three empirical constants.

*Celata et al.* (1994) [19] compared four correlations and three models with several experimental data with regard to fusion reactor requirements, i.e. relatively low pressure range (100 to 8400 kPa), high mass fluxes (2000 to 90000 kg/(m<sup>2</sup>s)), and high subcooling conditions. As expected by *Celata et al.* [19] the models of *Lee and Mudawar* [65] and *Weisman and Ileslamlou* [103] show unsatisfactory performance for low pressure data since these models have empirical coefficients and are developed for pressures above 7000 kPa. According to *Celata et al.* [19] the main reason for the inaccuracy at low pressure is the assumption of a small vapor layer in the wall region while the core liquid flow remains its velocity profile. This assumption is invalid for two-phase flow at CHF in low pressures. The *Katto* [53] model showed better performance, however about 50% of the data could not be calculated with the model because of a required layer void fraction below 0.7 in the model. This upper limit defines the validity range of the assumed homogeneous flow in the bubble layer according to *Katto* [53].

*Celata et al.* [20] improved the foregoing models of *Lee and Mudawar* [65] and *Weisman and Ileslamlou* [103] by eliminating the empirical factors. They developed a procedure to evaluate the layer thickness and the temperature of the liquid entering the sublayer by considering the temperature distribution across the tube section.

The basic situation of the theoretical model of *Celata et al.* [20] is a subcooled liquid core flow in a vertical tube as it is depicted in Fig 3.2. Boiling takes place in a liquid superheated layer at the heated tube wall. Small vapor bubbles coalesce to elongated vapor blankets in the near wall region. Underneath this vapor blanket exists a very thin liquid microlayer. CHF occurs if the microlayer is evaporated during the

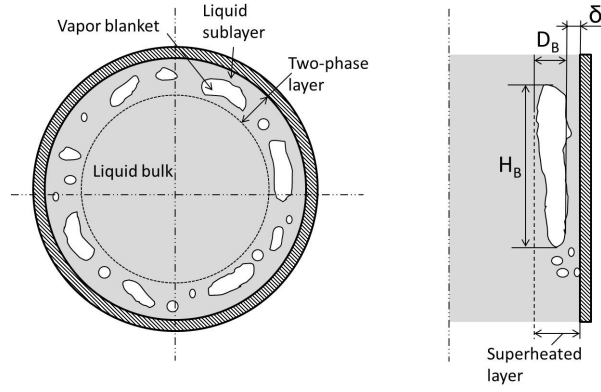


Figure 3.2.: Subcooled core flow with liquid superheated layer as basic situation for model of *Celata et al.* [20]

passage time of the vapor blanket yielding

$$\dot{q}_{CHF} = \frac{\rho_l \delta \Delta h_v}{\tau} = \frac{\rho_l \delta \Delta h_v}{H_B} U_B \quad (3.13)$$

with initial microlayer thickness  $\delta$ , liquid density  $\rho_l$ , latent heat of evaporation  $\Delta h_v$  and the passage time  $\tau = H_B/U_B$  calculated by the length  $H_B$  and velocity  $U_B$  of the vapor blanket.

Similar to the model development of *Lee and Mudawar* [65] and *Katto* [53], the vapor blanket length is obtained by considering the critical wave length of Helmholtz instability at the vapor-liquid interface. The velocity of the blanket is determined by the force balance between buoyancy and drag forces. See *Celata et al.* [20] for the detailed equations.

Since a focus of the present work is on the influence of fluid-surface interaction, the determination of the vapor blanket thickness in the model of *Celata et al.* [20] is further considered. The vapor blanket thickness is assumed to be equal to a bubble diameter at departure. The authors used the model of *Staub* [95] to calculate the diameter  $D_B$  given by

$$D_B = \frac{32 \sigma f \langle \theta \rangle \rho_l}{\zeta G^2} \quad (3.14)$$

where  $\zeta$  is the friction factor and  $f \langle \theta \rangle$  is a function depending only on the contact angle  $\theta$ . *Staub* [95] recommended a value of 0.02-0.03 for  $f \langle \theta \rangle$  for water and *Celata et al.* [20] used  $f \langle \theta \rangle = 0.03$ .

Surface roughness used for the calculation of friction factor  $\zeta$  is proposed to be  $0.75 D_B$ . Thus, the only term of the model which includes any fluid-surface interaction is the blanket thickness  $D_B$  in Eqn.(3.14). However, this diameter is used for calculating the vapor blanket velocity as well as the initial thickness  $\delta$  of the superheated microlayer.

*Celata et al.* [20] tested their model with 1888 experimental data points of CHF in subcooled flow boiling for tubes in the parameter range of  $100 \leq p \leq 8400$  kPa,  $0.3 \leq d \leq 25.4$  mm,  $2.5 \leq L \leq 610$  mm,  $1000 \leq G \leq 90000$  kg/(m<sup>2</sup>s),  $25 \leq \Delta T_{sub} \leq 255$  K.

The results showed good agreement with the experimental data and a better performance than the *Katto* [53] model for this parameter range. Approaching saturation conditions ( $x_{th} \approx 0$ ) the model underpredicts the CHF. The authors pointed out that the assumptions in the development of the model are only valid for subcooled conditions.

### 3.3. Measurements of CHF Considering Wettability and Surface Structure Influence

Recently *Poniewski and Thome* (2008) [84] published a book with a new state-of-the-art on the specific topic of nucleate pool boiling for different fluids on micro-structured surfaces. They describe different structuring processes for modifying surfaces. Examples for industrially manufactured structured surfaces after *Poniewski and Thome* [84] are shown schematically in Fig. 3.3. These structures are preferably produced on copper or copper-alloy tubes and they are usually applied for boiling or condensation of refrigerants.

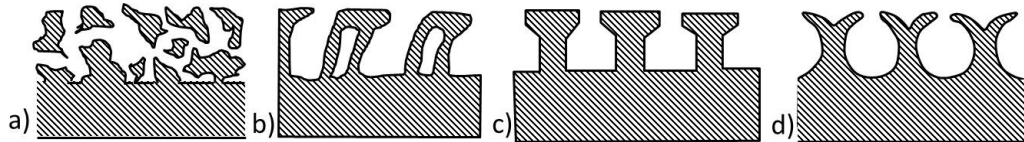


Figure 3.3.: Industrially manufactured micro-structured surfaces after [84]: a) High Flux (UOP) - sintered particles; b) Thermoexcel-E (Hitachi) - cut and bent over fins; c) Turbo-B (Wolverine Tube) - compressed and knurled fins; d) Gewa-TXY (Wieland-Werke) - split and compressed fins.

Other surface modifications are sintered powder, thermally sprayed, mesh, metal fibrous and combined structures. Thermally sprayed layers can be produced by plasma spraying, electric arc spraying and flame spraying. The authors ascribe good mechanical properties and good adhesion to these layers. They are all used to make porous coatings, but it is difficult to achieve a good porosity with open pores.

For the fabrication of fibrous structures, single metal fibers (i.e. of copper, steel, nickel or aluminum) are produced in a range of 10 to 100  $\mu\text{m}$  in diameter and 1 to 10 mm in length. The thin fibers of a set length and diameter are formed to a flat layer. As a next step the fibers are sintered and pressed for adjusting thickness and porosity. Then the layer is fixed onto the base surface by welding or soldering. Advantages of such structures are the possibility of setting structural parameters (i.e. thickness, porosity), high porosity with open pores.

Surface structures typically show smaller initial superheating, higher heat transfer coefficient and increased stability of boiling process compared to technically smooth surfaces. The majority of experiments with sintered powder structures confirm that an optimum layer thickness for maximum heat transfer coefficient at given conditions can be found. Better results of heat transfer coefficients for pool boiling are generally obtained for thin layers. The technique of sintered powders does not have industrial applications on large scale yet, except for the High Flux tube.

CHF investigations in pool boiling and flow boiling systems focusing on the effect of surface structure and/or surface wettability are presented in the following.

#### 3.3.1. Pool Boiling Experiments

*Malysenko and Styrikovich* (1989) [70] performed pool boiling experiments with porous layers on sheets with an area of 10mm x 40mm for pool boiling of water and ethanol, mainly at atmospheric pressure. Sintered powder technique and plasma spraying were used to produce nichrome (NiCr) and corundum ( $\text{Al}_2\text{O}_3$ ) porous coatings. The authors distinguish between three kinds of boiling inside a porous covering, shown in Fig. 3.4.

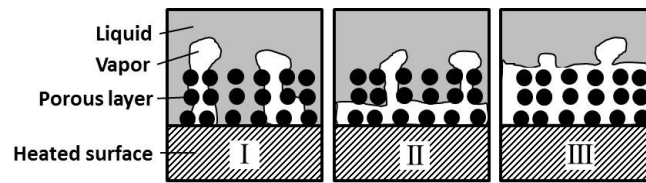


Figure 3.4.: Kinds of boiling inside a porous layer after Malyshenko [70]

- I Nucleate I: Areas of vapor do not coalesce and the liquid remains in contact with the base surface.
- II Nucleate II: The liquid layer is pushed upwards but is still within the porous layer.
- III Film: Continuous vapor film fills the porous coating.

Depending on the region of the boiling curve heat transfer coefficients for porous coatings were determined 5 to 15 times higher than for a technically smooth surface. Critical heat flux for nucleate boiling crisis and film boiling crisis were few times higher than measured for smooth surface.

*You et al.* (2004) [107] summarized investigations of heat transfer and critical heat flux on microporous surfaces in pool and flow boiling for highly wetting fluids like FC-72, FC-87 and R-123. Porous coated surfaces were found to increase significantly the CHF, about 100%, on flat surfaces in pool boiling.

Horizontal cylindrical tubes with smooth and microporous coated surfaces were tested by *Chang and You* (1997) [21] in saturated pool boiling of FC-87 and R-123. Heat transfer was enhanced, however, CHF was similar to smooth tube. This behavior is different to the investigations on flat surfaces. The authors assume that the increased void fraction due to the raising bubbles from the bottom surface prevent the liquid from rewetting the surface.

*Fong et al.* (1999) [37] investigated the influence of surface roughness on transient CHF for a zircaloy tube in pool boiling. The experiments were performed with tubes of 19.5 mm outer diameter, 0.76 mm wall thickness, and 450 mm length. The tube was orientated horizontally in a liquid pool of water at saturated conditions at atmospheric pressure. The power was increased rapidly with 75kW/s to a set point, held for 2 seconds and then was turned off. This procedure was repeated with stepwise increased set points. The boiling regime during the heat increase was observed by video camera. CHF was identified visually when film boiling was observed for a specific power set point.

The roughness of the tubes was modified by glass-peening the outer surface with different glass bead sizes. Compared to the smooth (un-peened) surface the observed critical heat flux was increased up to a maximum of 57%, i.e. from 0.86 MW/m<sup>2</sup> to 1.35 MW/m<sup>2</sup>. Considering the large-scale average roughness values like average height difference or root-mean-squared deviation, the authors found no correlation with the CHF-values. However, the authors found a correlation between a surface roughness exponent and the CHF-values. The roughness exponent is derived by plotting the average height difference against the distance of evaluated roughness measurement points. The exponent corresponds to the gradient in the small distance region. See *Fong et al.* [37] for more details.

*Fong et al.* [37] assumed that the improvement is related to the changes in contact angle. They suggest that the micro-topological features of the rough surfaces are fractal over the relevant dimensions of forming vapor bubbles. The induced cavities can act as nucleation sites providing increased heat transfer. Furthermore, the increased CHF values could result from a change in contact angle with increased fractal surface roughness. However, *Fong et al.* [37] did not measure any contact angle for these surface.

Modified surfaces on zircaloy plates in pool boiling of water were investigated by *Ahn et al.* (2010) [3]. The zircaloy-4 surfaces were modified by anodic oxidation. The polished and cleaned plates were anodized with different exposure times between 0 and 600s in a hydrofluoric acid solution. Due to the electrochemical reaction the material oxidized at the interface. For certain materials and process parameters the produced oxide layer consists of an ordered nano/microscale structure.

Additionally, they measured the static contact angle of a sessile drop on the surfaces. With increasing anodization time the contact angle decreased. The measured static contact angles ranged from  $49.3^\circ$  for the untreated surface to near  $0^\circ$  with surface spreading.

*Ahn et al.* [3] performed pool boiling experiments with water at saturated conditions using the zircaloy plates with different topography and wettability. The boiling heat transfer curves were almost identical for all samples. However, the critical heat fluxes were increased for the treated samples in comparison to the smooth surface. With decreasing contact angle CHF increased and reached significantly higher values for contact angles below  $10^\circ$ .

The authors compared their results with experimental data of *Diesselhorst*(1977) [29] and with predicted values of the model of *Kandlikar* [51] according to Eqn.(3.9). The measured and the theoretical values show the qualitatively similar tendency of increasing CHF with decreasing contact angle. For contact angles below  $10^\circ$  the experimental values of *Ahn et al.* [3] are further increasing with decreasing contact angle down to  $0^\circ$  whereas the predicted curve becomes flat.

*Kim et al.* (2007) [56] performed critical heat flux experiments with a thin wire in saturated pool boiling of water and nanofluids. The stainless steel wire with a diameter of 0.381 mm and a length of 120 mm was installed horizontally in a pool boiling facility. Three different particle materials were used: alumina ( $\text{Al}_2\text{O}_3$ ), zirconia ( $\text{ZrO}_2$ ), and silica ( $\text{SiO}_2$ ). Low concentrated water based nanofluids with volume qualities of 0.001%, 0.01%, and 0.1% were prepared for each particle material. CHF was measured for pool boiling in pure deionized water pool as well as in the different nanofluids. Observed glowing of the wire and/or the sudden change in the electrical resistance defined the CHF. Compared with the CHF for pool boiling in water, the nanofluids showed enhancement of CHF for all concentrations and materials. The increase in CHF was between 11.5% and 52% for 0.001-vol%, 15% and 75% for 0.01-vol%, and 20% and 80% for 0.1-vol% nanoparticle concentration.

SEM-pictures of the wires after boiling in pure water or nanofluids showed that the surface structure changes due to the boiling in nanofluids. The wire surface boiled in pure water remained smooth, whereas the boiling in nanofluids formed an irregular porous layer on the surface. This layer influenced the boiling performance through changes in surface area, roughness and wettability [56]. Flat surfaces of 45 mm length and 5 mm width were boiled in pure water and nanofluids in order to characterize the surface structure and wettability since the curvature and the thin diameter made the wire inconvenient for characterization methods. CHF measurements for the flat surface were not conducted. The static contact angle was measured by a sessile drop on the flat surface at  $22^\circ\text{C}$  at air. The contact angle was similar when using pure water or nanofluid as drop liquid. However, the modified surface structure by nanofluid boiling decreased the static contact angle significantly. The static contact angle on the water boiled surface was about  $80^\circ$  and the one on the nanofluid boiled surface was between  $8$  and  $36^\circ$ .

*Kim et al.* [56] concluded that the CHF enhancement was caused by the modification of the surface due to the deposition of nanoparticles forming a porous layer. The improved wettability characterized by the decreased static contact angle is assumed to be an important parameter for the increased CHF. The authors

discussed different existing mechanistic models with regard to wettability influence. They found supporting links for the observed CHF increase with increasing wettability in the hot/dry spot theory of *Theofanous et al.* [99] and the bubble interaction theory of *Kolev* [60].

### 3.3.2. Flow Boiling Experiments

*Ammerman and You* (2001) [4] measured critical heat flux on microporous surfaces for flow boiling of FC-87 in a small horizontal square channel with a cross-sectional side length of 2 mm and a heated length of 80 mm. The bottom side of the channel was heated. The CHF was increased between 14 and 36% in comparison to the smooth surface. The enhancement is smaller than for pool boiling (up to 100%). According to the authors the difference is caused by the limited liquid amount in the narrow channel geometry used in the flow boiling experiments.

*Stein* (2004) [96] investigated critical heat flux of flow boiling on surfaces with porous sinter structure. The experiments of CHF-determination were conducted with low mass fluxes of 24-300 kg/(m<sup>2</sup>s), pressure range of 120-700 kPa and varied inlet subcooling of 15-50 K. The test section was a directly electric heated vertical tube in two different lengths (127mm, 450mm). For each length a technical smooth and two inner porous coated tubes were used with the same layer thickness of 300 μm, but different particle sizes (30-40 μm, 60-80 μm). Tube and coating material were both of Inconel 600. These experiments showed increasing and decreasing effects of the porous layer effect on the CHF in comparison to the smooth surface. Similar observations were already reported in previous experiments of *Schroeder-Richter et al.* (1996) [91]. The critical heat flux on the shorter tube with a L/d-ratio of 14.1 was positively effected by the porous structure with an increase up to 80% depending on the experiment parameters. For the longer tube (L/d=50) the CHF was generally reduced in comparison to the smooth tube, but this effect diminishes with increasing pressure. The author assumed that there was, on the one hand, a positive effect of porous coatings caused by capillary forces which feed the heated surface with liquid, and an increment of the number of nucleation sites. On the other hand, he mentioned a negative effect of an increased entrainment depending on the coating parameters and the tube length. *Stein* [96] recommended in his work porous layers with particle diameters of 20-30 μm, layer thickness of 5-6 times the particle diameter and a porosity of 60-70% for improving critical heat flux in the investigated parameter range.

*Sarwar et al.* (2007) [89] investigated the influence of porous coatings on flow boiling CHF of water in vertical tubes at atmospheric pressure. Stainless steel tubes of 10.92 mm inner diameter, 0.89 mm wall thickness, and 230 mm heated length were coated on the inner surface. The coatings were prepared with three different particle powders: Al<sub>2</sub>O<sub>3</sub> (<10 μm), Al<sub>2</sub>O<sub>3</sub> (<1 μm), TiO<sub>2</sub> (<5 μm). The particle suspensions of isopropyl alcohol and epoxy were sprayed on the inner surface of the tube. Afterwards the coating was dried and heat treated in a furnace. The thickness of the coating layers was 50 μm for each particle size and additionally 20 μm for Al<sub>2</sub>O<sub>3</sub> (<10 μm).

CHF was determined for low mass fluxes of 100-300 kg/(m<sup>2</sup>s), outlet pressure of 101.3 kPa and inlet temperature subcoolings of 50 and 75 K. Compared to the smooth tube results, the coating with Al<sub>2</sub>O<sub>3</sub> (<1 μm) particles, called nanoporous layer, had similar CHF values. The coating of Al<sub>2</sub>O<sub>3</sub> (<10 μm), however showed the best performance for the investigated parameter range and increased the CHF about 25%. *Sarwar et al.* [89] reported higher CHF values for the thicker porous layer when comparing the 50 μm and 20 μm coatings of Al<sub>2</sub>O<sub>3</sub> (<10 μm). The authors assumed that the porous coatings enhance the CHF by increasing the nucleation site density.

*Sarwar et al.* [89] performed wettability tests with the coated tubes. They defined a wettability index as a characteristic value for the capability of keeping water in the porous layers. Therefore, the tubes were weighed in dry conditions and after soaking with water. The weight difference per surface area of the tubes was 0.062, 0.050, and 0.037 kg/m<sup>2</sup> for the 50 μm coatings of Al<sub>2</sub>O<sub>3</sub> (<10 μm), TiO<sub>2</sub> (<5 μm), and Al<sub>2</sub>O<sub>3</sub> (<1 μm), respectively.

Observing the behavior of a sessile drop on the dry porous coatings of Al<sub>2</sub>O<sub>3</sub> (<10 μm) and TiO<sub>2</sub> (<5 μm), the authors found relatively high contact angles (around 90°). However, the liquid drop spread on the surface when putting the drop on the porous surface with water entrapped in the porous layer.

### 3.4. Link of Literature Findings to Present Work

The observations of flow boiling at low pressure showed that such systems are sensitive to flow instabilities. Therefore, the flow stability in the test facility was experimentally investigated in order to establish stable flow conditions for the applied parameter range. Early CHF models considered only hydrodynamic aspects for describing the critical heat flux. However, some recent models consider the fluid-surface interaction as an important factor. Experimental investigations showed effects on CHF using for example porous layers, finned surfaces, deposition of nano-particles, rough surfaces and variation in contact angle by oxidized surfaces. Consequently, possible similar surface modifications were tested to be realized on zircaloy tubes. Furthermore, a focus was set on finding suitable methods to characterize the fluid-surface interaction and the topography for structured surfaces. Experimental data for critical heat flux in internally heated annuli at low pressure are sparsely available in literature and the experiments were conducted only with technically smooth tubes. The experimental results of the present work can expand the experimental data range for smooth tubes and introduce the CHF behavior of surface structured tubes for flow boiling of water at low pressure in an internally heated annular geometry.





## 4. Test Facility for Experiments

The experimental investigations of critical heat flux for flow boiling on micro-structured surfaces were introduced at the Institute of Nuclear and Energy Technologies (IKET) in cooperation with AREVA NP by this starting project. After having defined the working tasks of the project and having planned the main components and the piping of the water loop, this PhD-work started when the basic apparatuses had been ordered. During this project, the experimental setup was installed as an all new test facility including detail planning, build-up, instrumentation, test section design and construction, commissioning as well as programming software for loop control, data acquisition and evaluation.

Resulting from the detail planning, the piping and instrumentation diagram (P&I diagram), shown in appendix A, is the backbone for the hardware assembling, instrumentation, electrical installation and loop control. Furthermore, the specifications of measurement devices and safety requirements were defined in this process. Chapter 4.3 describes the measurement devices and their accuracy for the parameters of main interest.

One of the most important tasks was the design and construction of the test section for the flow boiling experiments using an original cladding tube. The geometry and the zircaloy material were a challenge for the connection to the electric heating power as well as for the manufacturing processes of the surface structures. The details of the test section design are described in chapter 4.2.

In addition, a further challenge was the realization of the surface temperature measurement due to the electric current and the narrow inner diameter of 8.2 mm of the zircaloy tube. The measurement module, specially designed and manufactured for this application, is explained in chapter 4.3.1.

The following chapter 4.1 begins with the description of the experimental setup explaining the general assembly and the basic parameters of the water loop.

### 4.1. Experimental Setup

The test facility COSMOS (Critical-heat-flux On Smooth and MOdified Surfaces) was assembled at the Institute of Nuclear and Energy Technologies (IKET) of the Karlsruhe Institute of Technology (KIT) during this work. COSMOS is a water loop for thermo-hydraulic experiments of two-phase heat transfer and critical heat flux at low pressure. Figure 4.2 shows pictures of the test facility and the test section and in Fig. 4.1 can be seen a 3D-CAD image of the loop construction. The fluid flow through the loop is explained in the following on basis of the process flow diagram in Fig. 4.3.

Deionized water, as the working fluid, is circulated through the test loop by a *pump*. Passing a flow meter (F), the water flows through a *preheater* where the fluid temperature is adjusted to a defined temperature for the test section inlet. A *filter* is mounted in a bypass to the *preheater* which is closed during the experiments, but it can be opened to clean the water. *Control valve* V1 is installed between the *preheater* and the *test section* inlet for flow regulation and stabilization. Closing the valve spool increases the pressure before the valve because of the increased flow resistance of the reduced cross-section. Inside the *test section*, the fluid flows upwards through the annular gap between the inner and outer tube. The inner tube is heated directly

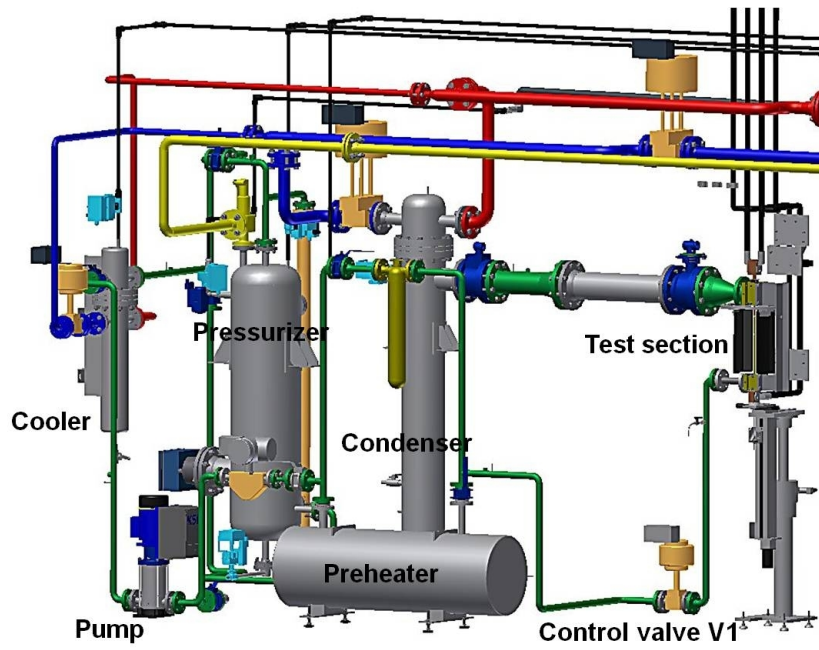


Figure 4.1.: 3D-CAD image of the test facility COSMOS



Figure 4.2.: Pictures of the COSMOS test facility (left) and the test section (right)

by electric current (AC) supplied by a *transformer*. Supplying sufficient heating power, the water boils at the outer surface of the inner tube. Consequently, the fluid is heated from a subcooled liquid state at the inlet to a two-phase state of vapor and liquid at the outlet. The two-phase mixture enters a *condenser* where the vapor is recondensed. Afterwards, the liquid fluid passes a connected *pressurizer* used to regulate the system pressure during the experiment. The following *cooler* decreases the temperature to a value lower than the test section inlet temperature before the water is pumped again through the loop.

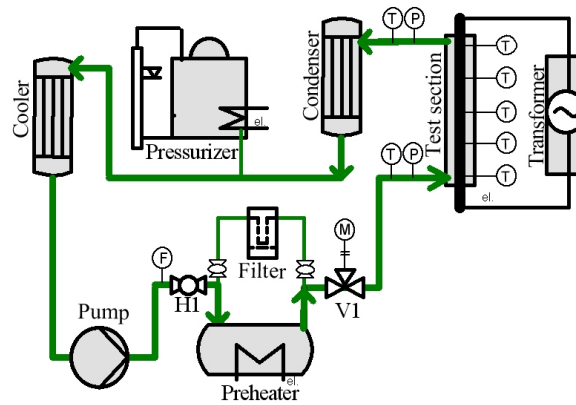


Figure 4.3.: Process flow diagram of COSMOS thermo-hydraulic test facility

COSMOS is a low pressure loop with a maximum pressure at the test section outlet of 400 kPa (4 bar). The components between the pump and the regulation valve V1 operate up to a maximum pressure of 700 kPa (7 bar), thus, ensuring the possibility to throttle at valve V1 even for the highest outlet pressure. Table 4.1 lists the general applicable ranges of the process parameters for the test facility. The applied parameter range of the experiments can be found in the result chapter 7.

Table 4.1.: General process parameters of test facility COSMOS

Mass flow	0.01 - 0.1	kg/s
Outlet pressure	1.2 - 4.0	bar
Inlet temperature	45 - 120	°C
Electric heating power	3 - 75	kW

Additionally, a secondary cooling cycle is necessary to operate the condenser and the cooler. This loop has been neglected in the process flow diagram in Fig. 4.3, but it is depicted in the P&I-diagram in appendix A. The heat energy imposed into the primary water loop is first transferred into the secondary cooling loop and then dissipated into the environment. Therefore, a pump circulates a mixture of water and glycol through the main cooling pipe which is split at the cold side into two branches feeding the condenser and the cooler. Recombined at the hot side the coolant flows through an air cooler outside the building. Three flow regulation valves are installed in the cooling loop, one in the main stream and each one before the condenser and the cooler. The flow rate, and therefore the cooling power, is regulated manually by the operator.

## 4.2. Test Section Design

The test section for the flow boiling investigations is designed as an internally heated vertical annulus. The fluid flows upward in the annular gap between two coaxial tubes. Prior to this work the basic requirements for the test section, listed in Tab. 4.2, have been established in the planning phase of the project. During this work, the whole development process of the test section from the conception to the application in the experiments has been realized.

Table 4.2.: Basic requirements for the test section concept

1	Use of an original zircaloy cladding tube
2	Direct heating by AC electric current
3	Vertical coaxial annular geometry with inner heated tube
4	Outer diameter of 13 mm for the annular gap (Inner diameter of 9.5 mm is given by the zircaloy tube)
5	Interchangeability of the test tube
6	Possibility to observe the boiling process

Figure 4.4 shows a vertical section of the test section on the left. The relevant parts are designated in the draft and, as far as visible, also in the photograph of the mounted test section on the right. According to requirement 5, the complete test section is modularly designed for exchanging the test tubes. Dismantling, cleaning, changing the tube and reassembling the test section takes approximately 4 hours.

The water enters the inlet part at four sides and is then directed upwards into an unheated annular part. The lower copper part of the inner test tube is centered in the inlet part by a ring with four spacers. The ring is made of the thermoplastic material PEEK (Polyether ether ketone) which also insulates against electrical contact between both parts. The glass tube is sealed by an O-ring and centered by a PEEK-ring in the inlet part. The heated section begins where the fluid enters the annular channel formed by zircaloy tube and the glass tube. Flowing upwards the fluid boils at the surface of the inner heated tube. This heated part has a length of 326 mm and the microstructures are manufactured over this length in case of a structured test tube. Reaching the outlet part the two-phase fluid exits the channel into a larger space where the flow velocity is reduced. Leaving the outlet part horizontally in direction of the condenser, the vapor and liquid phases separate from each other. The glass tube and the upper copper lead are as well centered and sealed in the outlet part. Outside of the test section, flexible cables of the power supply are connected to the bottom and top end of the inner tube assembly. The inlet part is fixed and positioned relative to the outlet part at a stiff structure.

Indeed, the presented test section design in Fig. 4.4 is the result of various improvement steps resulting from the experiences during manufacturing, mounting, commissioning and experimental conduction. Details about the construction and technical drafts of the single parts can be found in the reports of *Knobloch* [58] and *Zinn* [109]

### 4.2.1. Realization of Direct Electric Heating

The greatest challenge during the conceptual design of the test section was the realization of requirement 1 and 2 of the list in table 4.2, and even more the combination of both. Using a part of an original cladding

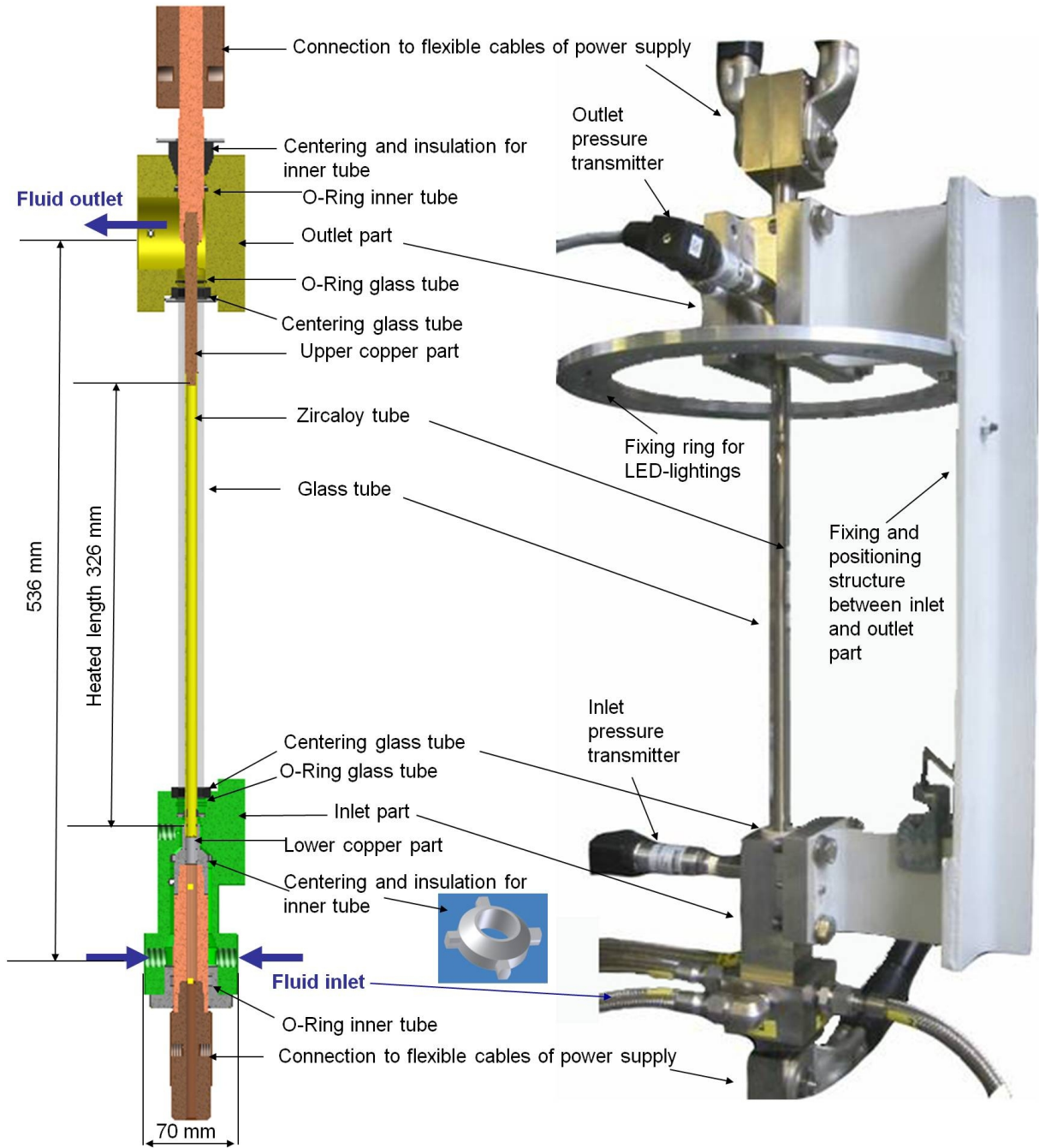


Figure 4.4.: Test section design

tube for nuclear fuel rods, fixes the material and the geometry for the inner tube. With an inner diameter of 8.2 mm and an outer diameter of 9.5 mm, the tube wall thickness of 0.65 mm is rather thin.

The material is zircaloy-4 containing 97 % zirconium, and is applied in the reactor because of its low neutron absorption cross section and its good corrosion resistance against deionized water. Zircaloy is affine to oxygen forming a natural nano-thin protective layer, however, this effect makes it very difficult to connect zircaloy with other materials. This zircaloy tube is furthermore the basic material for the structured test tubes whereas the surface coating material can be different from zircaloy. For more details about the materials and structure properties see chapter 5.

Direct electric heating has been chosen for mainly two reasons. First, the heat impact on the tube immediately stops with the absence of electric current, if the power is shut off. Second, the combination of heater and heated tube in one simplifies the exchange of the test tubes (requirement 5). The implementation of a heater element and temperature measurement devices inside a test tube for indirect heating would be more complex and costly.

AC power was chosen for the direct electric heating of the zircaloy tube in order to avoid an eventual electrolysis process of water at the electrodes when direct current (DC) is applied. However, the alternating current generates an electromagnetic field. The magnetic field strength increases with the current intensity and decreases proportional to the reciprocal value of the radial distance to the current-carrying tube. This relationship is expressed by

$$H_{magn} = \frac{I}{2\pi r} \quad (4.1)$$

where  $H_{magn}$  is the magnetic field strength,  $I$  is the electric current and  $r$  is the radial distance.

The low voltage of maximum 45 V at the test section is nonhazardous to humans obviating special safety precautions for the test facility. On the other hand, the higher intensity of current enforces the magnetic field strength according to Eqn (4.1).

Having a relatively high electrical resistivity for metals of approximately  $7.4 \cdot 10^{-7} \Omega m$ , which is similar to that of stainless steel, the zircaloy tube is well-suited for direct heating by electric current (requirement 2). Since the cross sectional area of the heated zircaloy tube is constant over the length, it is assumed to have a uniform axial power profile, meaning that the same heat energy is transferred from every surface location. The temperature profile of the electrical heated zircaloy tube in air atmosphere was examined in the master thesis of *Coerdts* [26]. The main results of this study are described in appendix B.

In order to release the heating energy only over a specific length of the annular channel, it was necessary to realize a changeover to another material with lower resistivity. Well known for its low resistivity ( $1.7 \cdot 10^{-8} \Omega m$ ), copper is an appropriate metal to form the unheated part of the test section. However, the connection of both materials is difficult. Welding or brazing of both materials was infeasible and the thin wall thickness of the zircaloy tube excluded the solution to tap a thread. A practical solution was found by connecting the parts with interference fits.

The changeover at the upper end was constructed with a copper rod pressed over a length of 9.5 mm into the inside of the zircaloy tube. Thus, the upper part is closed and sealed by the copper. With the same outer diameter the changeover is formed smooth for not disturbing the upward flow. In contrast, the inside of the tube at the bottom end had to be accessible for the temperature measurement module which is described in next chapter 4.3.1. Thus, the bottom copper part is formed as a bushing and pressed again over a length of 9.5 mm, but onto the outside of the zircaloy tube. Figure 4.5 shows a technical draft of the three single parts and a picture of the connected parts forming the test tube.

Due to the difference in the thermal expansion between zircaloy and copper, the over-sized diameters and tolerances for both press fits have to be chosen carefully. On the one hand, a good contact for the electric flux and the sealing must be guaranteed for the whole applied temperature range. On the other hand, the operation of the pressing has to be practicable and nondestructive for the tubes. The last requirement is particularly precarious for the coated and micro-structured tubes.

The different thermal expansion are used for conducting the interference fit. The upper copper part is shrunk in liquid nitrogen at  $-196\text{ }^{\circ}\text{C}$  and the lower copper part is enlarged in an electric furnace at  $300\text{ }^{\circ}\text{C}$  before being connected with the zircaloy tube by pressing. The processing of the interference fit was first tested with a sample and then consequently improved with each set.

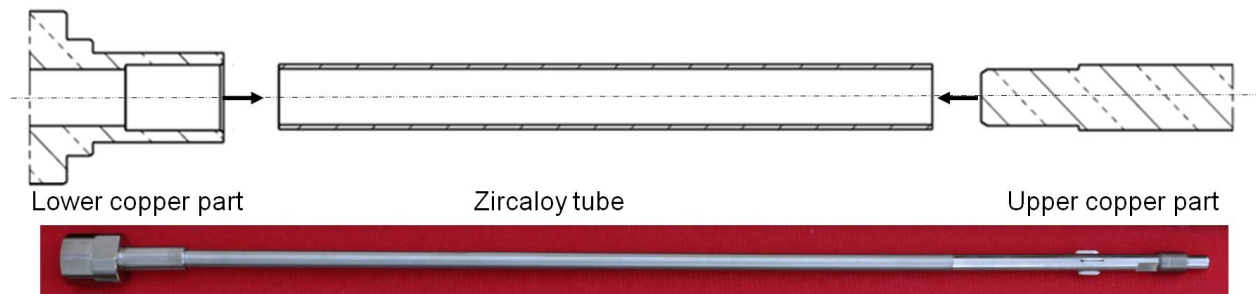


Figure 4.5.: Test tube with lower and upper interference between the zircaloy tube and nickel-plated copper parts.

At both endings the interference parts are bolted to further copper parts leading out off the test section. Flexible cables from the transformer are connected to these parts, thus forming the electrical power supply chain. All the copper parts installed in the test section are nickel-plated for corrosion protection in deionized water. The nickel layer was manufactured by electroless nickel plating and has a layer thickness of about  $30\text{ }\mu\text{m}$ .

Centering devices in the inlet and outlet parts adjust the concentricity between the glass tube and the test tube, see Fig. 4.4. Manufactured of PEEK-material, they additionally work as electrical insulators separating the inner current carrying parts from the surrounding parts.

#### 4.2.2. Annular Geometry of the Test Section

The unheated outer tube with an outer diameter of 20 mm is manufactured of quartz glass allowing observation of the flow boiling process. Giving an inner diameter of 13 mm in requirement 4, the annulus is designed with a narrow gap width of 1.75 mm between the inner heated and the outer unheated tube.

Geometry models for the thermohydraulic system of a light water reactors can be for example a bundle of several tubes, a single tube or an annular arrangement [64]. In the very first project concept, a bundle arrangement of four tubes had been proposed for a test section in a high pressure test facility [18]. For example, such a 2x2 rod bundle arrangement as shown in Fig 4.6 on the left was used in experiments of *Shin and Chang* [92]. Focusing then primarily on the feasibility to manufacture surface coatings on zircaloy and their general boiling behavior, the complexity and costs have been reduced by two decisions. Firstly, the test facility was downscaled to low pressure ranges only slightly higher than atmospheric pressure. And secondly, the geometry was reduced to an annular test section with a single heated tube. The outer diameter of the small annular concept was defined prior to this work and probably extracted from the planned bundle

geometry by laying a circle around the rod covering the minimum gap width of the bundle as illustrated in Fig. 4.6.

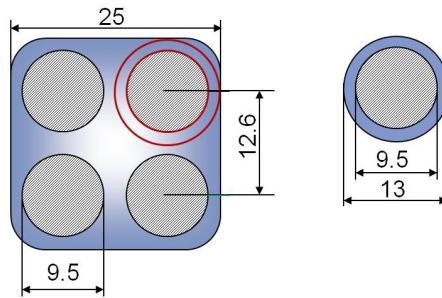


Figure 4.6.: Left: bundle arrangement of planned test section with four rods; right: annular geometry with single rod

The commissioning, stability analysis and critical heat flux experiments for the technical smooth and micro-channel structured tubes have been carried out for the narrow annulus. However, an essential conclusion from these extensive investigations was the extension of the experimental range for a larger annular gap. Prevention of thermal damage of the structured surfaces and comparability with literature data have been the decisive factors. These effects concerning the narrow channel are described and discussed in the result section in chapter 7.1.3. With an inner diameter of the outer glass tube of 18 mm, the larger annulus has a gap of 4.25 mm. This geometry was chosen for practical reasons given by the existing test section design and for using similar parameters as comparable experiments of *Rogers et al.* [85] in literature.

### 4.3. Instrumentation and Accuracy

This section describes the instrumentation of the test section and the loop. Different measurement devices are installed at specific positions in the test loop in order to control the system state and to determine the relevant parameters for the experiments. A special measurement module was designed for detecting the surface temperatures of the heated tube in the test section. This module is presented in the first part. The second part describes loop instrumentation and the measurement accuracy.

The measurement parameters of main interest are

- 
- Mass flow ( $\dot{M}$ )
  - Fluid temperature (T) at inlet and outlet of the test section
  - Pressure (p) at inlet and outlet of the test section
  - Heating power ( $\dot{P}_{el}$ )
  - Visualization of two-phase flow
- 

The mass flow is measured with a coriolis mass flow measuring system Promass80E of Endress+Hauser. The fluid temperature and pressure in the loop are determined with K-type thermocouples and Omega PXM209 (0 - 6 bar) absolute pressure transducers, respectively. Relative pressure transducers of the type Omega PX4202 (0 - 2.5 bar) measure the pressure at the inlet and the outlet of the test section. The imposed heating power is determined by an AC wattmeter (0 - 80 kW) from Redur.

The precision of the measurement devices is important for the evaluation of the measured data. Relevant devices were checked in calibration tests to determine the measurement accuracy. Table 4.3 lists the achieved accuracies from the methods described in this section.



Table 4.3.: Accuracy of measurements

Measured quantity	Symbol	Range		Accuracy	
Pressure	p	100 - 300	kPa	1.2	kPa
Temperature	T	20 - 220	°C	0.15	K
Power	$P_{el}$	0 - 80	kW	0.5	% <sup>*)</sup>
Heat flux	$\dot{q}$	0 - 3	MW/m <sup>2</sup>	3.2	% <sup>*)</sup>
Mass flow	$\dot{M}$	0 - 1	kg/s	0.25	% <sup>*)</sup>
Mass flux	G				
small annulus		250 - 1000	kg/(m <sup>2</sup> s)	4.8	% <sup>*)</sup>
large annulus		250 - 400	kg/(m <sup>2</sup> s)	3.4	% <sup>*)</sup>

<sup>\*)</sup> % of measured value

#### 4.3.1. Temperature Measurement Module for Test Section

The wall temperature measurement of the heated inner tube is important for detecting the temperature jump at the critical heat flux. If one of the measured temperatures passes a preset temperature limit, then the fast shut off of the heating is triggered in order to avoid thermal damage of the tube.

A reasonable concept of measuring directly the outer surface temperature was not found. The main reasons are the presence of surface structures on the outer surface of the modified tubes and the intention of not disturbing the fluid flow and the boiling process. Infrared temperature determination is inapplicable because the outer glass tube and the water in the ring gap are impermeable for infrared radiation.

Therefore, the temperature is measured by thermocouples at the inside of the test tube. However, the narrow inner tube diameter of 8.2 mm demanded a special design of the measurement module to place ten to twelve thermocouples inside the test tube. The temperature should be determined at different axial positions for having several points for the CHF-detection along the heated length and, moreover, the axial temperature profile is of interest. Furthermore, the measurement system had to be applicable for all of the test tubes. The direct electric heating of these tubes required the need of electric insulation of the measurement system.

Figure 4.7 shows a picture of the designed measurement module. It consists of maximum six measuring heads each equipped with two thermocouples with a sheath diameter of 0.36 mm. This module is inserted from the bottom into the inner tube of the test section assembly. Furthermore, the measurement module can be moved automatically up and down inside the tube. For this purpose, it is connected to a positioning stage driven by a stepping motor which is regulated by the control program. The actual positions of the measuring heads are determined by a position sensor.

The measuring tip of the thermocouple is positioned in axial grooves in the PEEK measuring heads. Formed as a spring ring, the measuring head presses the thermocouples against the inner tube surface. The ring material PEEK has good properties of high temperature stability, good electrical insulation and low thermal conductivity. The individual measuring heads are positioned on stainless steel connecting parts as depicted in Fig. 4.8. These parts are screwed together to the configuration of the temperature measurement module, like it is shown in Fig. 4.7. The relative azimuthal position and the axial distances between the measuring heads are adjustable. For instance, an often used assembly was the axial positioning of the measuring heads at 15, 170, 240, 290, and 320 mm from the bottom end of the heated length ( $L_{heat} = 326$  mm). The thermocouple strands are led out of the test section through the inside of the connecting parts.

Sheathed NiCr-Ni thermocouples (K-type) with a diameter of 0.36 mm manufactured by the thermometry

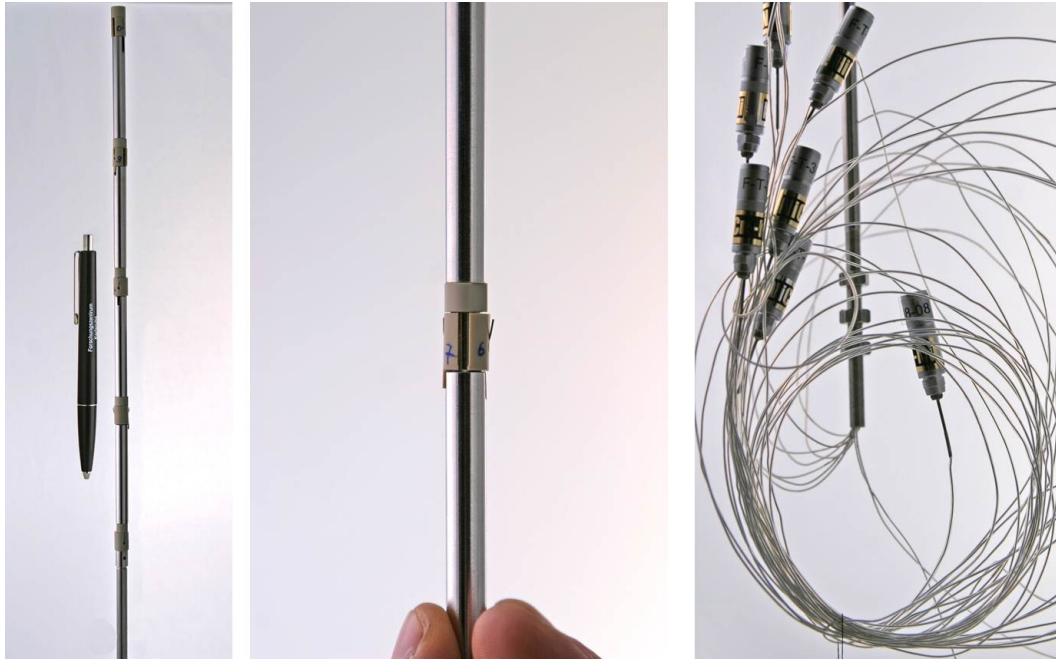


Figure 4.7.: Measurement module to determine the wall temperature from the inside of the tube

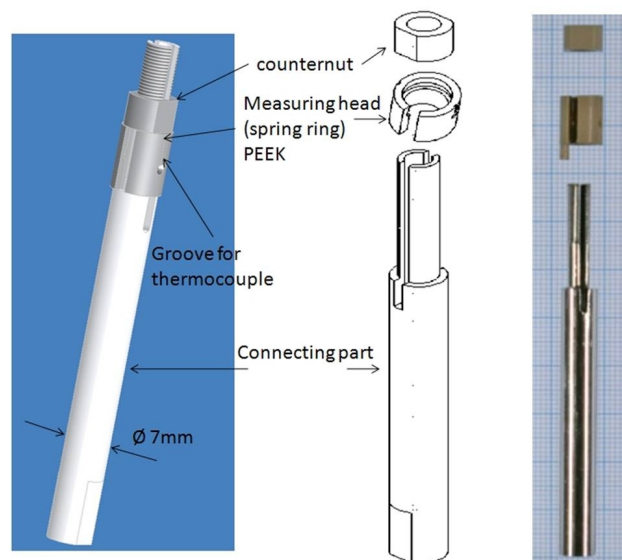


Figure 4.8.: Design of the measuring head, part of the module for wall temperature measurement

workshop of KIT are used for the temperature measurement. The principle mounting of such a thermocouple is shown in Fig. 4.9. The welded connection point of two thin wires of different materials forms the measurement point. These wires are surrounded by an electrically insulating layer of mineral oxid powder and sheathed by a stainless steel sheath.

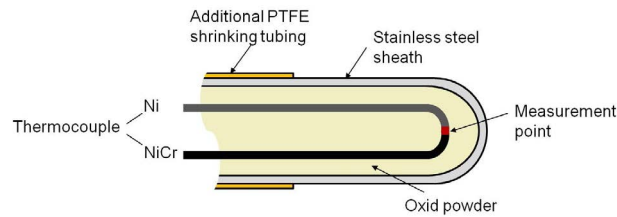


Figure 4.9.: Principle mounting of a thermocouple which is sealed and isolated from sheath

Since the test tube is current-carrying, additional precautions are necessary to avoid electrical contact between the thermocouple sheaths. Lets consider two thermocouples A and B each pressed with the sheath of the measurement tip against the current-carrying test tube at two different axial positions. Between these positions is a voltage difference. If there exists a contact point between the sheaths of thermocouple A and B, then the circuit is closed and electric current flows through the sheaths. Thus, the stainless steel tubing of the thermocouple is electrically heated leading to a mistaken temperature measurement and moreover, the thermocouple could be damaged. Consequently, each thermocouple is additionally sheathed by a very thin insulating shrink tubing of PTFE except of the measuring tip. Furthermore, the signal amplifiers must have a galvanic separation between input and output.

#### 4.3.2. Power Measurement and Heat Flux

The electrical power applied to the test section is an important measurement parameter because it corresponds to the heat input into the boiling system and determines the critical heat flux when the temperature rise occurs. Electric current flows directly through the inner tube of the test section annulus generating heat due to the specific electrical resistance of the zircaloy material.

The power is supplied by a transformer of Ruhstrat with a thyristor power controller of AEG (Type: 1A-400-280HF RL1) able to shut down the power very fast. The transformer converts the primary two-phase alternating current (AC) power supply from 400 V and 200 A at 50 Hz to 45 V and 1650 A as maximum values for the secondary single phase AC circuit. Accordingly, the maximum power input is 74.25 kW. Figure 4.10 shows a schematic draft of the test section power supply.

The heating power can be adjusted between 2.4 and 74.25 kW with incremental steps of approximately 0.1 kW. The thyristor controller cuts off parts of the sinusoidal current to regulate the power, like it is depicted in Fig. 4.11. Using AC power involves the measurement of root mean square (rms) values of the voltage, current intensity or power. Consequently, an adequate transducer has to be capable to determine correctly the rms value of the cut-off signals.

The input quantities for measuring the electrical power  $P_{el}$  are voltage  $U$  and current intensity  $I$  according to

$$P_{el} = UI \quad (4.2)$$

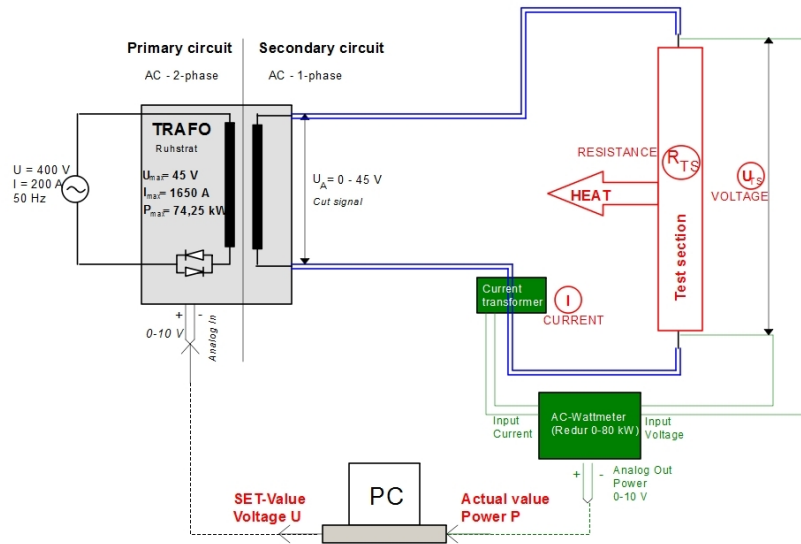


Figure 4.10.: Schematic draft of test section power supply

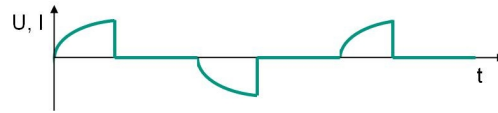


Figure 4.11.: Sketch of a cut sinusoidal voltage or current signal

The uncertainty can be calculated with the help of the total derivative as described in [81]. Applied on Eqn. (4.2) gives

$$dP_{el} = \left| \frac{\delta P_{el}}{\delta U} \right| dU + \left| \frac{\delta P_{el}}{\delta I} \right| dI \quad (4.3)$$

Evaluating the partial derivations and the deviation intervals result in

$$\Delta P_{el} = I \Delta U + U \Delta I \quad (4.4)$$

Dividing Eqn. (4.4) by Eqn. (4.2) gives the relative deviation of

$$\frac{\Delta P_{el}}{P_{el}} = \frac{\Delta U}{U} + \frac{\Delta I}{I} \quad (4.5)$$

The electrical power is measured by an AC wattmeter (0 - 80 kW) from Redur. The voltage signal is tapped directly by two shielded cables from the copper connections outside the test section. Voltage losses in the copper connections and sensing cables are neglected ( $\Delta U \approx 0$ ). A current transformer reduces the current intensity from high values (0-1650 A) to a low ampere range of 0-5 A which is transmitted to the wattmeter. The specified accuracy of the current transformer is 0.2% of the measured value. Thus, the relative deviation of the electric power from the input signals results in

$$\frac{\Delta P_{el,input}}{P_{el,input}} = \frac{\Delta I}{I} = 0.2\% \quad (4.6)$$

The relative uncertainty for the transformation of the input signals to the output signal is specified as 0.3% for the wattmeter.

$$\frac{\Delta P_{el,output}}{P_{el,output}} = 0.3\% \quad (4.7)$$

The relative deviation of the complete power measurement chain can be derived by connecting the deviation in the input signal with the uncertainty of wattmeter. The total deviation of the output value from the origin value is given by

$$\Delta P_{el,total} = P_{el,output} - P_{el} \quad (4.8)$$

With the deviations  $\Delta P_{el,input} = P_{el,input} - P_{el}$  and  $\Delta P_{el,output} = P_{el,output} - P_{el,input}$  follows for Eqn. (4.8)

$$\Delta P_{el,total} = (\Delta P_{el,output} + P_{el,input}) - (P_{el,input} - \Delta P_{el,input}) = \Delta P_{el,output} + \Delta P_{el,input} \quad (4.9)$$

Dividing Eqn. (4.9) by the measured output value gives

$$\frac{\Delta P_{el,total}}{P_{el,output}} = \frac{\Delta P_{el,output}}{P_{el,output}} + \frac{\Delta P_{el,input}}{P_{el,output}} = \frac{\Delta P_{el,output}}{P_{el,output}} + \frac{\Delta P_{el,input}}{P_{el,input} + \Delta P_{el,output}} \quad (4.10)$$

Since  $\Delta P_{el,output} \ll P_{el,input}$  follows

$$\frac{\Delta P_{el,input}}{P_{el,input} + \Delta P_{el,output}} \approx \frac{\Delta P_{el,input}}{P_{el,input}} \quad (4.11)$$

and the relative deviation of the measured electric power is calculated with the values from Eqns. (4.6) and (4.7) as

$$\frac{\Delta P_{el,total}}{P_{el,output}} \approx \frac{\Delta P_{el,output}}{P_{el,output}} + \frac{\Delta P_{el,input}}{P_{el,input}} = 0.3\% + 0.2\% = 0.5\% \quad (4.12)$$

Thus, the summarized relative deviation for the measured power signal results in 0.5% of the measured value.

For proving the reliability of the heating power we double-checked the measurement by two different approaches. First, voltage and current were measured additionally by two multimeter of the type Fluke 45. The calculated power from the displayed values was compared to the measured value of the wattmeter. These multimeter are also capable to integrate a cut signal. Second, the heat energy was calculated from the energy equation for single-phase flow of water for the measurement conditions. Knowing the mass flow and the fluid temperature and pressure at the inlet and outlet, the required heat input  $\dot{Q}$  to increase the temperature from the inlet temperature to the higher outlet temperature can be calculated from the energy balance

$$\dot{Q} = \dot{M}(h_{l,out} - h_{l,in}) + \dot{Q}_{loss} \quad (4.13)$$

where  $\dot{M}$  is the mass flow rate,  $h_{l,in}$  and  $h_{l,out}$  are the specific liquid enthalpies at the inlet and outlet and  $\dot{Q}_{loss}$  is the dissipated heat.

The heat loss through the glass tube to the environment was considered in the master thesis of *Coerdts* [26] and found to be insignificant compared to the heat input into the fluid. The calculated heat loss was in the low Watt region of approximately 10 W which is negligible in relationship to the kW-values of the heating. The single-phase heating could only be performed for higher mass flow rates and relatively low power input compared with the CHF values in the experiments. Otherwise, there would be boiling at the heated surface making the energy equation more complex.

Table 4.4 lists an excerpt of the comparison and shows a good agreement between the different measurements methods. The measured values of the wattmeter and the Fluke multimeter are very similar. The calculated power from the energy equation is slightly lower, but in the same range. Note, that the heat loss was neglected in the calculation. As mentioned above the heat loss through the glass tube is very low. However, the fluid flows in the upper part of the channel over the unheated upper copper part with a length of about 100 mm before reaching the temperature measurement point. A slight decrease in the liquid temperature in this upper part could explain the slightly lower values. In summary, the comparison shows that the wattmeter gives reliable measurement values of the heating power.

Table 4.4.: Comparison of different power measurement methods

$P_{el,wattmeter}$	$U_{Fluke}$	$I_{Fluke}$	$P_{el,Fluke}$	$\dot{M}$	$T_{in}$	$T_{out}$	$p$	$\dot{Q}_{energy-equ}$
<b>kW</b>	<b>V</b>	<b>A</b>	<b>kW</b>	<b>g/s</b>	<b>°C</b>	<b>°C</b>	<b>kPa</b>	<b>kW</b>
<b>3.0</b>	6.83	431.80	<b>2.95</b>	59.6	48.6	60.2	121.4	<b>2.89</b>
<b>5.0</b>	8.94	554.20	<b>4.95</b>	79.6	45.9	60.3	122.2	<b>4.79</b>
<b>6.9</b>	10.56	649.40	<b>6.86</b>	100.3	46.9	62.8	125.3	<b>6.67</b>

The heat flux is calculated by dividing the measured heating power by the heated surface according to Eqn.(2.6). Expressing the heated surface by the heated length  $L$  and the inner diameter of the annulus  $d_i$  Eqn.(2.6) can be written as

$$\dot{q} = \frac{P_{el}}{\pi d_i L} \quad (4.14)$$

The relative deviation is derived from Eqn. (4.14) in the same procedure as described for the electric power from Eqn. (4.3) to Eqn. (4.5) and is given by

$$\frac{\Delta \dot{q}}{\dot{q}} = \frac{\Delta P_{el}}{P_{el}} + \frac{\Delta d_i}{d_i} + \frac{\Delta L}{L} \quad (4.15)$$

As shown above the relative uncertainty of the measured heating power is  $\frac{\Delta P_{el}}{P_{el}}=0.5\%$ . Variation in the heated length can result from the cut of the base tube and the transition lengths of the interference fits to copper parts at both ends. The estimated length variation between the tubes is  $\Delta L=2$  mm. The surface structures have a maximum thickness of  $100 \mu\text{m}$ , thus increasing the outer diameter of the inner tube about maximum  $\Delta d_i=0.2$  mm. The heat flux was calculated for each tube with a diameter  $d_i=9.5$  mm and a length of  $L=326$  mm in Eqn. (4.14). The resulting relative uncertainty in heat flux from Eqn. (4.15) is 3.22% for both annuli.

#### 4.3.3. Mass Flow Measurement and Mass Flux

The fluid mass flow through the test loop is determined by a coriolis mass flow measuring system Pro-mass80E of Endress+Hauser. The accuracy is specified as 0.25% of the measured value. The location of the flow meter (F) between the pump and the preheater is shown in the process diagram in Fig. 4.3. Note, that the mass flow measurement gives the overall fluid mass circulation through the loop as the result. Consequently, the local velocities of the two-phase flow in the test section are inaccessible by this measurement. The increasing vapor content accelerates the flow in the heated section due to the lower density of vapor.

Moreover, flow fluctuations in the test section caused by static instabilities during the stability analysis were also undetectable for the flow meter, because of the big volume of the preheater and the distance to the test section.

The mass flux is calculated according to Eqn. (2.5) by dividing the measured mass flow rate by the flow cross section area. Inserting the cross section area of an annulus in Eqn. (2.5) yields

$$G = \frac{\dot{M}}{\frac{\pi}{4}(d_o^2 - d_i^2)} \quad (4.16)$$

with mass flow  $\dot{M}$  and inner and outer diameter of the annulus  $d_i$  and  $d_o$ . The total derivative of Eqn. (4.16) is given by

$$dG = \left| \frac{\delta G}{\delta \dot{M}} \right| d\dot{M} + \left| \frac{\delta G}{\delta d_o} \right| dd_o + \left| \frac{\delta G}{\delta d_i} \right| dd_i \quad (4.17)$$

Similar to the procedure for Eqn.(4.3)-(4.5) the partial derivations of Eqn.(4.17) are evaluated and the resulting equation is divided by Eqn. (4.16). The relative deviation for the mass flux is then

$$\frac{\Delta G}{G} = \frac{\Delta \dot{M}}{\dot{M}} + 2 \frac{d_o \Delta d_o}{(d_o^2 - d_i^2)} + 2 \frac{d_i \Delta d_i}{(d_o^2 - d_i^2)} \quad (4.18)$$

The relative deviation of mass flow is given by  $\frac{\Delta \dot{M}}{\dot{M}}=0.25\%$ . The uncertainty of  $\Delta d_o=0.1$  mm for the inner diameter of the outer tube is very precise for a glass tube. The small annular geometry consists of an inner and outer diameter of 9.5 and 13 mm. The inner technical smooth tube is produced with an outer diameter tolerance of  $\Delta d_{i,smooth}=0.05$  mm. Since only smooth tubes were tested in the small annular test section the relative deviation in Eqn. (4.18) is calculated with  $\Delta d_{i,smooth}=0.05$  mm and results in 4.8%. On the other hand, the smooth tubes as well as the different surface structured tubes were assembled in the large annular test section. The outer diameter of the glass tube is 18 mm for the large annulus with the same deviation of  $\Delta d_o=0.1$  mm. The surface structures have a maximum thickness of 100  $\mu\text{m}$ , thus increasing the outer diameter of the inner tube about maximum  $\Delta d_i=0.2$  mm. The same inner diameter of  $d_i=9.5$  mm was used for calculating the mass flux for all test tubes. Thus, the relative deviation for all tested tubes in the large annulus results in 3.4% according to Eqn. (4.18).

#### 4.3.4. Temperature Calibration

The calibration of the thermocouples for the fluid temperature at the inlet and outlet as well as for the surface temperature of the inner tube was conducted with the calibration system of AMETEK type ATC-650 B. The thermocouples and the PT100 reference sensor (type: STS-100 A 901) were positioned in a heated copper cylinder.

The general configuration from the measurement tip of the thermocouple to the recorded signal was the same for the calibration as for the measurements in the experiments. Thus, the complete measurement chain of thermocouple, compensating cable, amplifier, signal cable and data recorder was considered. Consequently, all parts of the measurement chain which can be influenced by disturbances were included in the calibration.

The heating control of the calibration system stabilized the reference sensor temperature within a maximum variation of 0.03 K of the preset calibration temperature. The calibration system defined the condition as stable after maintaining constant the temperature in this variation range for 10 minutes. Subsequently, the

#### 4. Test Facility for Experiments

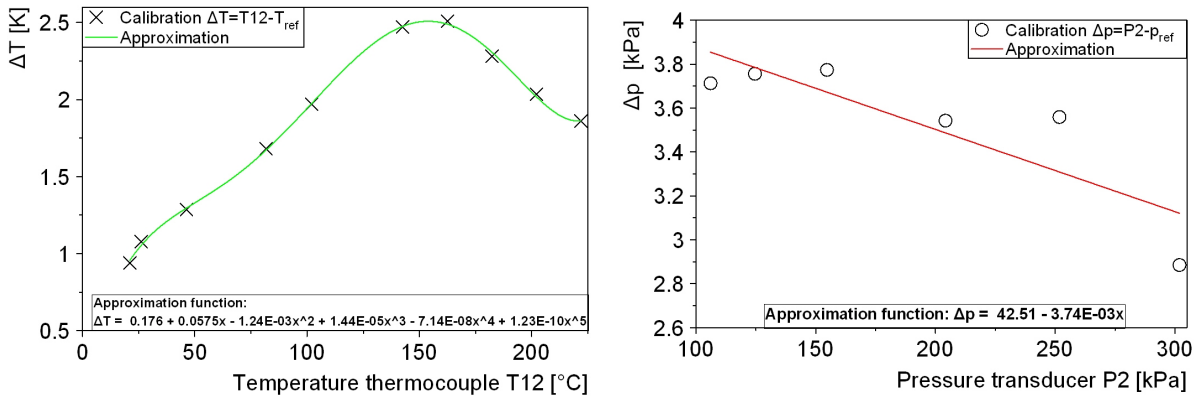


Figure 4.12.: Measurement points and approximation curve for the calibration of thermocouple T12 (left) and pressure transducer P2 (right)

data were recorded for approximately 5 minutes. Then, the difference of the calculated mean value and the value of the reference sensor was plotted against the sensor value as shown in Fig. 4.12. The approximation curve for these data was evaluated for each thermocouple. Thus, the measured thermocouple temperatures can be corrected in the calibration range with the help of the approximation curves.

The achievable absolute accuracy of the temperature calibration depends on the uncertainty of the reference sensor ( $\pm 0.02 K$ ), the adjustment of the calibrator heating ( $\pm 0.03 K$ ) and the deviation of the approximation curves from the measured data (max.  $\pm 0.1 K$ ). The sum of these deviations leads to an accuracy of  $\pm 0.15 K$  for the calibrated temperature range from  $20^\circ C$  to  $220^\circ C$ . The surface temperature of the heated tube during flow boiling varied between  $120^\circ C$  and  $220^\circ C$  depending on actual heat input, mass flow and local pressure.

#### 4.3.5. Pressure Calibration

The pressure transducers are sensing the hydrostatic pressure of the water head, if the test facility is filled with water. Therefore, the pressure calibration was conducted for the test loop filled only with air. A reference pressure transducer of the type Kistler (4045A5) with a piezoresistive amplifier (4603B) was additionally installed for the calibration. The system pressure was increased by adding stepwise compressed air into the loop. The pressure data were recorded for each pressure step and they were evaluated in the same procedure as described above for the temperature calibration. The calibration range was between 100 and 300 kPa and the linear approximation for the outlet pressure transducer P2 is shown exemplary in Fig. 4.12. With an estimated uncertainty of the reference system of ( $\pm 0.9 kPa$ ) and the deviation of the approximation curves from the measured data (max.  $\pm 0.3 kPa$ ) resulted an accuracy of  $\pm 1.2 kPa$  for the pressure measurement in the calibrated range.

#### 4.4. Loop Control and Data Acquisition

The control system consists of an interacting chain of software and hardware components from graphical user interfaces of the control program to the measuring or regulating device in the loop. The PC running the controlling program is connected to the automation and synchronizations platform PXI 1042 from National



Instruments as the controller interface. This platform provides plug-in boards for the input and output signal cables which are connected with the specific measurement or regulation devices in the loop.

For controlling the COSMOS test facility, the PXI platform handles and synchronizes a total of 47 input and 8 output signals as well as 10 relay switches with an applied sampling frequency of 100 Hz. Figure 4.4 shows the schematic configuration of loop control and measurement chain on the left-hand side.

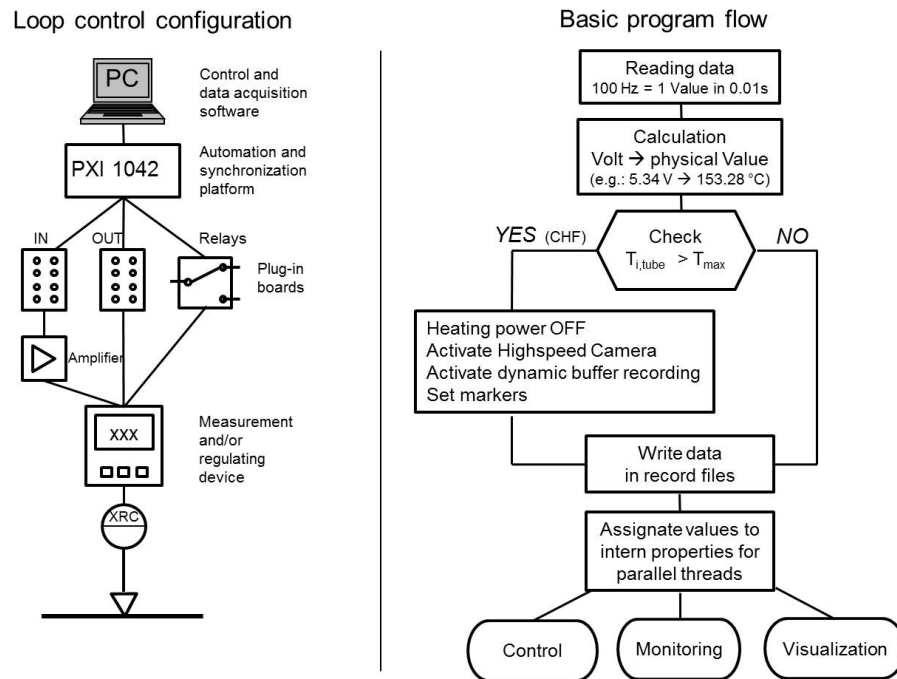


Figure 4.13.: Left: Configuration of measurement and control chain. Right: Scheme of main thread of the control program

The control and data acquisition software was all new developed for this application programming in Visual Basic Studio 2005 Environment. The software function is to visualize, record, and control the processing parameters during the test facility operation. Several tasks have to be active at the same time. Therefore, the program is built up in parallel threads. The main thread, shown in Fig. 4.4 on the right-hand side, reads in the signal data and calculates the physical from the voltage values. The tube temperature values are first checked if one exceeds the set maximum value. The other measurement values are checked for certain events, like over-pressure or minimum flow rate, in monitoring subroutines of a second thread.

In case of over-temperature, meaning CHF-detection, the output signal going to the transformer is immediately interrupted by switching automatically a relay connection. Additionally, the program activates the output trigger for the high-speed camera and sets time markers signaling CHF-detection and camera triggering for the records. The read data is then written into recording files and assigned to intern properties providing the values for the other threads.

A noteworthy specialty of the program is the ring buffer writing the data into a dynamic array covering 70 s of the records. The CHF event activates the recording of the buffer into a separate file containing the measured data of 60 s before and 10 s after the CHF. This method simplifies the evaluation of the CHF point.

The other parallel threads process the read data mainly for the visualization showing diagrams, for example of the heating power, tube temperature or mass flow. Most relevant for the operation control is the plot

of the process diagram indicating the numeric values according to their loop location.

Furthermore, the control program provides a graphical interface for controlling the specific loop operating devices, like pump, heaters or valves. The set values of the program are transferred by the PXI platform and send as output voltage signals to the specific device.

### 4.5. Safety System

Safety precautions for raised pressure and temperature are taken at important positions of the test rig. The safety system works in different steps. First, there is a visual and acoustic warning if a temperature or pressure exceeds a certain limit. Second, if the pressure or temperature rises above a maximum limit then the test section power supply and in some cases also the heaters in preheater and pressurizer are shut down. And third, a pressure relief valve installed at the pressurizer opens at the maximum pressure of 4 bar venting over-the-roof.

Other events triggering the shutdown of heaters are low water level in the pressurizer and a minimum mass flow. All the mechanical and software safety installations were tested during an inspection by an approved test center (TÜV).

The protection against thermal damage of the test tube surface is important, but on the other hand the determination of critical heat flux is of interest in the experiments. The temperature measurement module (section 4.3.1) equipped with thermocouples detects the inner wall temperature of the test tube at different positions. When the critical heat flux occurs and one of the wall temperatures exceeds a temperature limit, then the electrical power supply is shut down fast.

Additionally, two of the twelve thermocouples measuring the tube temperature are connected to external temperature controls. These independent monitoring devices shut the transformer off even if the data acquisition system and the control program are inactive.

### 4.6. Procedure of Critical Heat Flux Measurements

This section describes the typical procedure for the operation of a critical heat flux experiment. In short, the measurement procedure for a CHF experiment is a stepwise increase in heating power at constant inlet temperature, outlet pressure, and mass flow rate until detecting a rise of the tube temperature above a preset limit.

The target parameter set of inlet temperature, outlet pressure, and mass flow rate is defined prior to the experiment. Influenced parameters by the power increase are for instance the pressure drop across the test section, the fluid outlet temperature, and the temperature of heated tube. Figure 4.14 shows the time dependent signals of the constant, the operated and the influenced experimental parameters for a typical experimental run of a critical heat flux experiment.

The first measurements with the smooth tube in the small annulus have been time consuming as it was unknown how the system behaves and at which power input values the CHF occurs. Knowing the behavior and the range of CHF, the experiments of the large annulus and the surface structures could be conducted with a sophisticated procedure. The experimental operation for each parameter set consisted of different parts which were parameter setting, degassing, CHF measurements, and flow boiling videos, as it is depicted in Fig. 4.15.

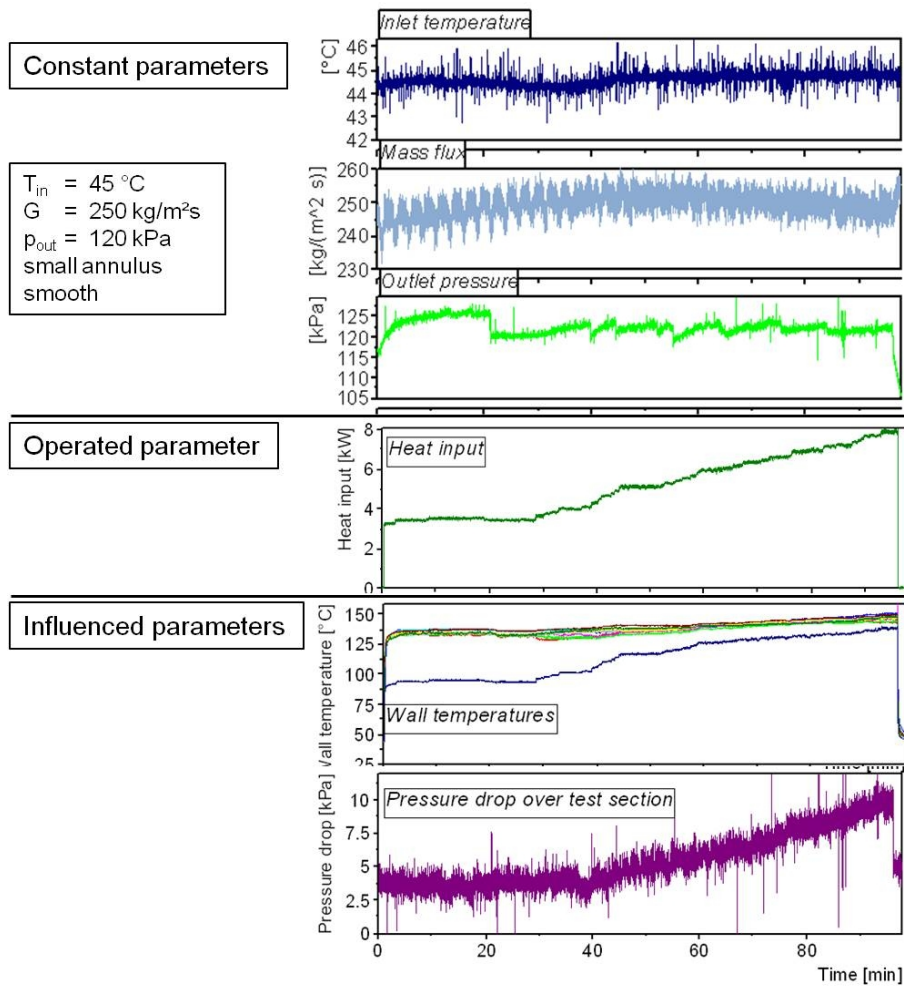


Figure 4.14.: Example of important parameters during critical heat flux experiment

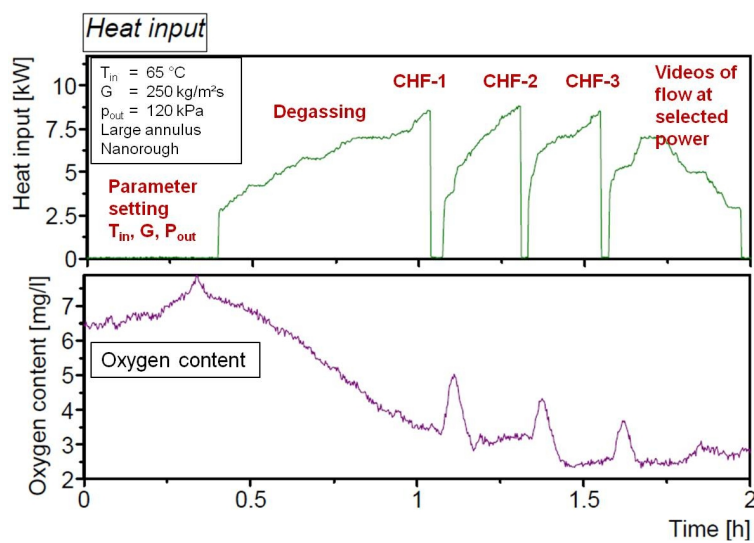


Figure 4.15.: Time depending power input and oxygen content for a typical operation of a critical heat flux experiment

Firstly, the target conditions for the constant parameters are adjusted. The mass flow depends on the pump rotation speed and the settings of valve V1 (see Fig. 4.3 for the loop positions). Increasing the rotation speed increases the flow rate. Closing valve V1 increases the pressure drop across the valve and consequently, the flow rate is reduced according to the pump characteristic curve. Moreover, the pressure drop across the throttle valve upstream of the test section is important for ensuring stable flow conditions as it is explained later in chapter 6.2. The heating control of the preheater regulates the preset water temperature for the test section inlet. In this early stage, the outlet pressure can be increased by heating up the water in the pressurizer and it can be further adjusted by either adding pressurized air into the pressurizer or venting at one of the air valves.

After having adjusted the target conditions, the next part is degassing the loop water. The solubility of air in water decreases with increasing temperature and decreasing pressure. For instance, the oxygen content for 100 % oxygen saturation of water at 1 bar and 25 °C is about 9 mg/L and at 90 °C it is about 2 mg/L [62]. If the water enters with a high gas content into the test section, then a gas phase is produced because of the decreasing solubility in the heated water. Consequently, an additional gas phase of soluble gas in the water increases the void fraction. Therefore, the loop water is degassed prior to the CHF measurement. The heating power of the test section is increased to a value below CHF, but high enough for boiling in the channel. The power input is kept in this range until the oxygen content is decreased to a constant value as it is shown in Fig. 4.15. The gas content is controlled by measuring the oxygen content. The oxygen content during the CHF measurements was between 2 and 4 mg/L depending on the system and pressure conditions.

Parallel to the degassing process, the secondary cooling loop for the condenser and the cooler is started giving the system time to adjust stable conditions.

Approaching a constant oxygen content and stable system conditions, the power input is further increased in small steps of about 0.1 kW until detecting the first critical heat flux. The parameter set of inlet temperature, outlet pressure and mass flow rate is kept constant during the power increase. The inlet temperature is regulated automatically by the heating control of the preheater. However, the mass flow rate and the outlet pressure have to be adjusted by the operator. Particularly, the outlet pressure has to be adjusted frequently. On the one hand, the increasing vapor content leads to an increasing system pressure. The pressure can be decreased by either venting at the pressurizer or increasing the flow rate of the cooling cycle. On the other hand, the intensified boiling process increases the pressure in the test section, as it is explained in chapter 2.3. Therefore, the flow rate has to be adjusted occasionally by varying the pump rotation speed or the setting of valve V1.

The temperature of the inner heated tube increases slightly with increasing heating power. As explained in section 4.3.1 the tube temperature is measured by thermocouples at the inside of the inner tube at different axial positions. The temperature limit is kept about 10-15 K above the actual highest tube temperature. The CHF is defined if one of the tube temperatures exceeds the temperature limit. Then, the power input into the test section is automatically shut off for preventing damage of the tube. Moreover, the CHF event triggers the record of an extra data file as well as the high speed camera record.

Shutting off the test section heating power stops the vapor production. Consequently, the system pressure drops because of the missing vapor volume in the condenser and water is shifted from the pressurizer into the condenser. The oxygen content of the water in the pressurizer is higher than the one of the water flowing permanently through the boiling channel. This effect causes the peaks in the oxygen content in Fig. 4.15 as soon as the power is shut off at CHF.

The test section heating power is then increased fast to boiling conditions below CHF in order to establish again stable operation conditions in the loop after the disturbance by the shut off at CHF. Having adjusted the target constant parameters conditions, the CHF measurement is repeated in the same manner as explained above. Usually two repetition measurements have been conducted. After the last repetition, the heating power is increased once more to boiling conditions below the CHF. Then, the power is decreased at the constant target parameters and high speed videos of the flow boiling process are tapped at various selected power inputs.

This measurement procedure for one set of parameters could be conducted in about 2 - 4 hours depending on the parameter conditions.



## 5. Surface Structures and Characterization

This chapter presents firstly the surface structure modifications of the zircaloy tube by suitable manufacturing processes. A challenge for finding suitable surface structures was posed by the base tube geometry and in particular the material zircaloy. The manufacturing of the different surface modifications was realized in cooperation with industry and scientific institutes. Furthermore, the wettability behavior of these structures was characterized by applying the Wilhelmy method. This method and the wettability results are described in the second part of this chapter. Additional surface characteristics of some structures could be determined by measuring the surface topography.

### 5.1. Surface Structures on Zircaloy Cladding Tube

The objective of defined micro-structures on the tube surface is to increase the critical heat flux for flow boiling of water on the structured surface in comparison to the technical smooth tube surface. Surface modifications like porous layers, finned surfaces, deposition of nano-particles, rough surfaces and oxidized surfaces showed effects on critical heat flux and heat transfer in various investigations as described in chapter 3. As influencing parameters were mentioned number of active nucleation sites, surface area, contact angle, and capillary forces, for instance.

With regard on the flow boiling process in nuclear reactors additional requirements for the surface modifications were demanded. The surface structures shall be produced directly on an original zircaloy cladding tube with a maximum layer thickness of  $100\ \mu\text{m}$ . Moreover, sufficient coating adhesion strength and layer durability for flow boiling are required and the materials should be suitable for reactor conditions.

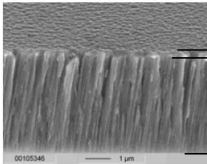

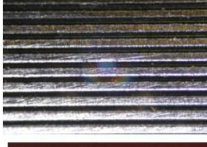


Nevertheless, the main focus of this work was to find generally feasible surface modification processes for the zircaloy tube similar to applied structures on other materials in literature. Table 5.1 gives an overview on the modified surfaces described in detail in the following sections.

#### 5.1.1. Smooth Zircaloy Tube

The base tube for the experiments and the surface modification is an original cladding tube for nuclear fuel rods. The material is zircaloy-4 containing 97% zirconium (Zr) and additional components of mainly tin (Sn) and iron (Fe). In the technical application the fuel rods have a length of over 4 m. We used a part of this tube with a length of 0.345 m because of practical reasons concerning the manufacturing of the structures and the installation into the test facility. The zircaloy tube has an inner diameter of 8.2 mm and an outer diameter of 9.5 mm. Hence, the tube wall thickness is 0.65 mm. This tube geometry is applied in pressurized water reactors (PWR).

Zircaloy has a low neutron absorption cross section of 0.18 barn (iron 2.4 barn, nickel 4.5 barn). Furthermore, it has a good corrosion resistance in water and steam because of a natural passivating layer. These are some main reasons why zircaloy is used as cladding tube material. The nano-thin protective layer is formed

Table 5.1.: Overview on surface structures

Structure name:		Layer thickness:	Manufacturing process:
Nanoscale roughness		100 nm 5 μm	Physical Vapor Deposition (PVD)
Hemispherical structure		30 μm	Electroforming
Microchannel		100 μm	Mechanical
Porous layer		50 and 100 μm	Powder sintering
Oxidation layer		100 μm	Temperature treatment

immediately if zirconium is in contact to oxygen atmosphere. Even a very low oxygen content is sufficient for this process. This effect makes it very difficult to combine zircoloy with other materials.

The zircaloy tubes used for this investigation were disposed by AREVA NP and the cladding tube manufacturer had been AREVA ANF GmbH Duisburg. The manufacturing process of the cladding tubes is a pilgering process. In a second step the outer surface is belt grinded. The surface structure after grinding shows micro-grooves running crosswise to the axial direction. Figure 5.1 shows light microscope pictures of the tube surface after the pilgering on the left and the final belt grinding on the right. The technically smooth tube used in this work as the reference surface is defined as the tube with the surface condition after grinding. The basic characteristics of the smooth tube are summarized in Tab. 5.2.

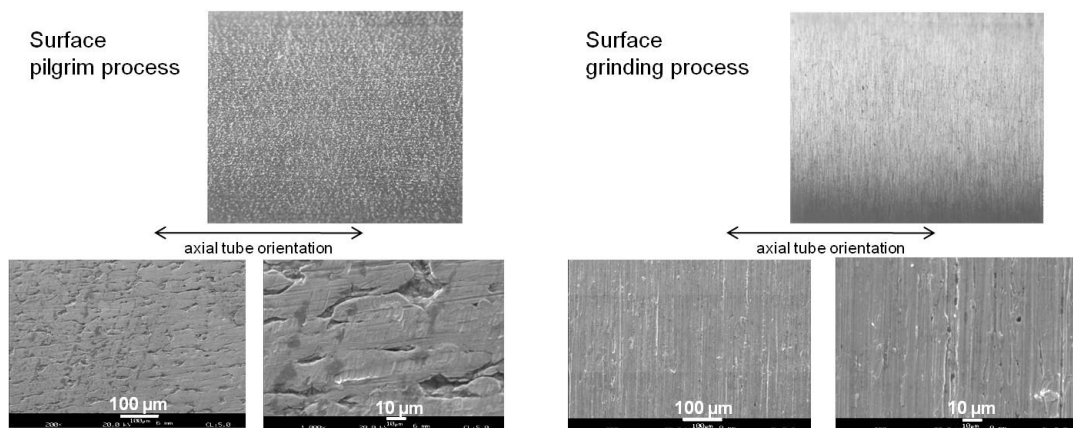


Figure 5.1.: Tube surface after pilgering (left) and grinding process (right). Pictures taken by AREVA NP with light microscope (upper) and SEM (lower).



Table 5.2.: Zircaloy tube with technically smooth surface

Name	smooth
Description	Original cladding tube for fuel rods Base tube for surface modification Reference tube for experiments Micro-grooves crosswise to axis
Manufacturer	AREVA, ANF GmbH Duisburg
Manufacturing process	Pilgering and grinding
Material	Zircaloy-4

### 5.1.2. Nanoscale Roughness

A surface structure of nanoscale roughness can be manufactured by physical vapor deposition (PVD) process. This coating process is a method to create thin layers onto a surface by evaporating the coating material. PVD is a common industrial coating process for functional surfaces like for instance coated boring or milling tools. It can be conducted with almost all metal materials and also in addition of reactive gases like oxygen or nitrogen.

The Institute for Applied Materials (IAM-AWP) at the KIT has a processing technique for coating layers with a nanoscale roughness on the surface. The common functional layers are very thin in the range of several 100 nm. Therefore, it covers the surface with a smooth layer maintaining the base roughness. With increasing thickness, the coating begins to form nanoscale elevations on the surface which are created by crystal growth in the layer. The roughness of the ground surface still remains, but is now overlaid by nanoscale elevations. Thus, the nanoscale modification could be combined also with other structures as an overlaid roughness.

With zirconium as the coating material the layer is of the same material as the main component of zircaloy containing 97 % of zirconium. The required thickness for a nano-rough zirconium layer is 5  $\mu\text{m}$ , whereas the rough structure profile is in the range of 100 nm.

The manufacturing process was tested by coating two silicon wafers, one with a 0.1  $\mu\text{m}$  thin smooth surface and the other one with a 5  $\mu\text{m}$  layer forming the nanoscale roughness. The wafers were characterized using a scanning electron microscope (SEM). The SEM-pictures in Fig. 5.2 illustrate clearly the difference in surface structure between the smooth and rough layer. The layer fracture in Fig. 5.2 on the right side shows the buildup of the nanoscale elevations by crystal growth.

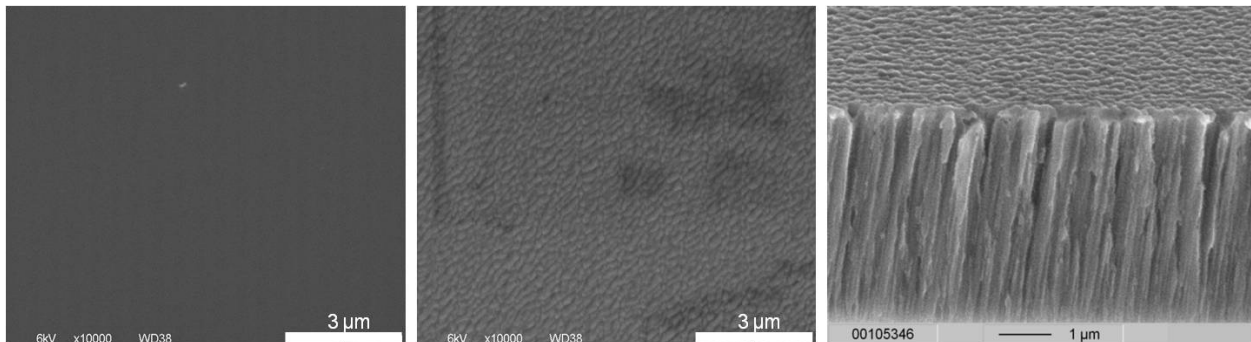


Figure 5.2.: SEM pictures of PVD coated wafer. Left: smooth 0.1  $\mu\text{m}$  layer; Middle: 5  $\mu\text{m}$  layer with nanoscale roughness; Right: Fracture appearance of 5  $\mu\text{m}$  layer with nanoscale roughness

Table 5.3 gives an overview on the nanorough PVD surface coating. Two zircaloy tubes of 345 mm and a reference sample of 100 mm coated with a 5  $\mu\text{m}$  nanoscale rough zirconium layer were manufactured at IAM-AWP in January 2009.

Table 5.3.: Nanoscale roughness on zircaloy tube

Name	Nano-rough
Description	Creation of nanoscale elevations by crystal growth Roughness of basic tube is overlaid
Manufacturer	Institute for Applied Materials (IAM-AWP), Karlsruhe Institute of Technology
Manufacturing process	Physical vapor deposition (PVD)
Basic tube material	Zircaloy-4
Coating material	Zirconium
Total layer thickness	5 $\mu\text{m}$
Height of structure profile	about 100 nm

### 5.1.3. Hemispherical Roughness

Topocrom GmbH in Stockach, Germany, has developed a method for coating surfaces with a hemispherical structure of hard chromium layers. The surface topography defined by layer thickness and number of the hemispheres per area can be varied according to the requirement. The height of hemispheres depends on the thickness and the number density is distinguished between open and closed structures. Isolated hemispheres on the surface are characteristic for an open structure, whereas the hemispheres on a closed structure are contacting the neighboring ones.

Technical applications using Topocrom coatings are for instance coated cylinders of paper print machines to enhance the surface wetting or coated pipes for concrete pumps to enhance the surface resistance.

Hemispherical elevations are produced by a special electroplating process with chrome. Nuclei are created on a base smooth chrome layer by a particular current operation during electroplating. The electrical field is focused at these small pins leading to an increased deposition of material and thus, the elevations are growing to a hemispherical structure. Figure 5.3 shows a light microscope picture of a closed hemispherical structure coated on the zircaloy tube. Table 5.4 summarizes the surface structure facts.



Figure 5.3.: Light microscope picture of hemispherical structure

Table 5.4.: Hemispherical structure on zircaloy tube

Name	Hemispherical structure
Description	Growth of hemispherical elevations by selective deposition Stochastic distribution of hemispheres on surface Parameters: layer thickness and number density
Manufacturer	Topocrom GmbH, Stockach
Manufacturing process	Electroplating
Base tube material	Zircaloy-4
Coating material	Chrome
Total layer thickness	30 $\mu m$
Height of structure	5-7 $\mu m$
Number density	Closed structure

Topocrom GmbH tested successfully the coating process on a sample of the zircaloy tube. However, the manufacturer reported that electroplating chrome on the zircaloy base material turned out to be very difficult. A nickel strike layer on the surface, which could only be combined with the zircaloy material by special processing, was necessary for good adhesion of the coating.

After having identified the suitable process parameters two zircaloy tubes of 345 mm and a reference tube of 100 mm were coated with a closed hemispherical structure of chrome in April 2009.

#### 5.1.4. Micro-channel Structure

Micro channel structures for improving heat transfer are used for example in micro heat exchangers, micro reactors or heat pipes. For these applications the high ratio of surface area to fluid volume is one of the important advantages.

Micro channels can be manufactured by various processes like turning, erosion, milling or etching. The cross section form depends on the manufacturing technique and is generally round or rectangular. A typical rectangular micro channel geometry is around 50-200  $\mu m$  in depth and width.

The Institute for Micro Process Engineering (IMVT) at KIT has experience in manufacturing micro channels with several materials, geometries and processes. The milling process was successfully tested at the IMVT with a 50 mm long sample of the zircaloy tube shown in Fig. 5.4. The channels are manufactured parallel to the tube axis. Processing the structure into the base material is a great advantage because there is no need of extra coating material. Table 5.5 lists the description of the micro-channel structure on the zircaloy tube.

However, the manufacturing of micro-channels onto the test tube with a length of 400 mm required additional preparatory work. The tube had to be fixed in position during the milling process because even a slight bending would cause a variation in depth of the channel. Therefore, two supporting devices with prism forms have been designed and manufactured by the IMVT.

During the manufacturing process in a CNC machine, the milling tool is directed axially on the vertex of the tube, see Fig. 5.4 a. Then the tube is turned automatically with a preset angle and the next channel is processed. Subsequently, the channel edges have to be smoothed manually.

The IMVT manufactured three zircaloy tubes with the same channel geometry of 200  $\mu m$  width and 66  $\mu m$  depth and a total number of about 100 channels. The manufactured tubes of 400 mm were cut to the

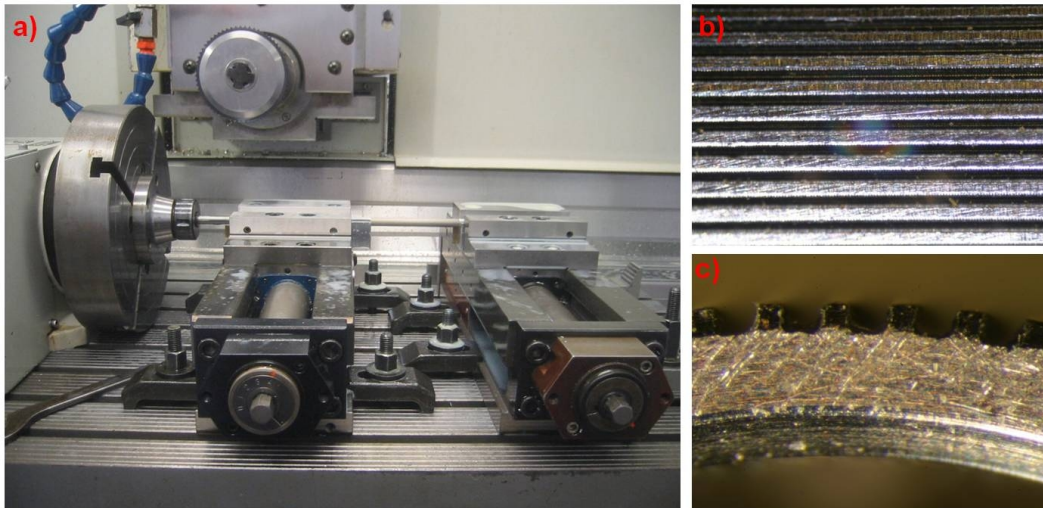


Figure 5.4.: a) Micro-channel manufacturing on zircaloy tube in CNC machine; b) Top view on channel structure; c) Cross sectional view on channel structure

Table 5.5.: Micro-channel structure on zircaloy tube

Name	Micro-channel
Description	Microscale channels in axial direction Rectangular channel cross section Mechanically processed into base tube material
Manufacturer	Institute for Micro Process Engineering (IMVT) Karlsruhe Institute of Technology (KIT)
Manufacturing process	Milling
Base tube material	Zircaloy-4
Number of channels	100
Channel depth	66 $\mu\text{m}$
Channel width	200 $\mu\text{m}$
Fin width	80 $\mu\text{m}$

length of 345 mm receiving a reference part of 55 mm for each tube. The micro channel structures on the zircaloy tubes were finished by the IMVT in July 2010.

### 5.1.5. Porous Layer Structure

Porous surface structures were already investigated in pool and flow boiling applications as mentioned in chapter 3.3. Wet powder sintering is a possible manufacturing process for porous layers with good adhesion properties. Further processes for porous layers are for instance plasma spraying, electric arc spraying, and flame spraying. In the wet powder sintering process a suspension of water and powder is sprayed as a covering film onto the surface. The liquid is removed during the following heat treatment at temperatures near the melting point. The result is a porous layer of bonded particles with a good adhesion to the coated surface.

The Institute for Manufacturing Technology and Advanced Materials (IFAM) of Fraunhofer-Institute in Dresden is experienced in manufacturing sinter layers with several materials. For example the porous



Figure 5.5.: Left: homogeneous porous layer; Middle: Cracks on layer show insufficient adhesion; Right: Melted layer caused by slightly higher local temperature

structures for the boiling investigations of *Stein* [96] and *Goldschmidt* [38], have been manufactured at IFAM.

However, coating a zircaloy surface required various preliminary tests to investigate the parameters of spraying, sintering, layer adhesion and layer shrinking. These tests were conducted with small samples of the zircaloy tube. Two inconel 625 powders with different particle sizes have been tested. Inconel is a nickel based alloy with additional components of mainly chromium and molybdenum.

Inconel 625 Powder-1:  $d_{50} \approx 8 \mu m$

Inconel 625 Powder-2:  $d_{50} \approx 25 \mu m$

Water based binder dissolution and metal powder are mixed to a sprayable suspension. For applying the spraying layer evenly, it is important to have a homogeneous suspension. The coarser powder-2 with a median particle size of  $25 \mu m$  was difficult to spray because it could block the nozzle. Therefore, the finer powder-1 with a particle size of about  $8 \mu m$  was selected for practical reasons.

The heat treatment must be carried out in a reducing atmosphere, because of the high oxygen affinity of zirconium. First steps were made in hydrogen atmosphere, but in spite of low residual moisture content in the hydrogen, it was enough to build an oxide layer on the surface limiting the adhesion. Therefore the sintering process was conducted in high vacuum atmosphere.

Further tests were made to optimize the sintering temperature conditions in order to reach good adhesion and layer porosity. The sintering temperature is one of the most sensitive parameters, because there is only a narrow temperature range of  $\pm 5 K$  for obtaining a porous layer with good adhesion. The combination of zircaloy and inconel is characterized by an eutectic point of Zr and Ni at  $960^\circ C$ . The best sintering results were obtained with a temperature of  $970^\circ C$ . On the one hand, a lower temperature leads to an insufficient melting zone between zircaloy and inconel and the coating layer shows insufficient adhesion and cracks. On the other hand, a higher temperature melts the layer causing the loss of porosity. Figure 5.5 shows these three cases for the porous inconel layer on the zircaloy tube.

After having completed the pretests the next step was coating the zircaloy tubes for the flow boiling experiments with two different layer thickness targets of  $50 \mu m$  and  $100 \mu m$ . Six test tubes of 345 mm, three of each layer thickness, and five reference tubes of 100 mm length have been coated in total and were finished in May 2009. Each porous coating was conducted with the tube and the reference part in the same process. The process parameters were the same as in the pretests using the finer inconel powder-1. Table 5.6 contains a summary of the porous coating manufacturing.

The absolute layer thickness, shown in Tab. 5.7, was determined by measuring the outer diameter at

Table 5.6.: Porous structure on zircaloy tube

Name	Porous-50 and Porous-100
Description	Porous layer of sintered inconel powder Melting zone with Zircaloy for layer adhesion Difficult to achieve homogenous porosity
Manufacturer	Institute for Manufacturing Technology and Advanced Materials (IFAM), Fraunhofer-Institute, Dresden
Manufacturing process	Wet powder-sintering
Base tube material	Zircaloy-4
Coating material	Inconel 625
Powder size (median)	8 $\mu m$
Total layer thickness	50 $\mu m$ and 100 $\mu m$

several positions before and after sintering. The results show that the layer thickness remains the same after the sintering process. Therefore, the target layer thickness of the sintered product can be set by spraying a layer of the same thickness onto the green part.

Table 5.7.: Determination of porous coated layer thickness with micrometer screw and metallographic micrograph

tube-no.	micrometer screw		micrograph reference sample	comments on 345 mm tube
	coated	sintered	sintered	
	[ $\mu m$ ]	[ $\mu m$ ]	[ $\mu m$ ]	
Thickness target: 50 $\mu m$				
4	53	53	70	homogeneous surface
6	51	53	30	partly melted areas
7	52	50	30	partly melted areas
Thickness target: 100 $\mu m$				
2	105	99	no ref	homogeneous surface
3	94	95	102	cracks on surface
10	99	97	100	homogeneous surface

Additionally the metallographic micrographs of the reference tube were evaluated. These pictures provide closer information about the real porous thickness, because it can be distinguished between the melting and the porous zone. However, the polished cut image is only from a single position of the reference tube. Some SEM images of the fracture appearance of the porous layer are shown in Fig. 5.6. On the left side and in the middle are pictures of well manufactured porous layers. The image on the right side shows the melt down of the porosity by producing too much liquid phase because of a slightly higher local temperature during the sintering process.

The homogeneity of the porous layer can be further characterized by the superficial appearance of the surface (Fig. 5.5). A uniform light gray surface color indicates a good homogeneity. Areas with low porosity, i.e. melted layer areas, have a darker or metallic appearance and areas with insufficient adhesion show cracks on the surface. White patches can remain on the coating from the binder dissolution.

Manufacturing a homogeneous porosity over the complete zircaloy tube turned out to be very difficult. Two of the coated and sintered 345 mm tubes (tube no. 6 and 7) with a target thickness of 50  $\mu m$  have partly melted zones on the surfaces (Tab. 5.7). Therefore, only one of the three coated tubes remained for the boiling experiments with a homogenous porous coating. In case of the 100  $\mu m$  porous coating, one tube (no. 3) showed cracks in the layer, but two 345 mm tubes (no. 2 and 3) had a homogenous appearance.

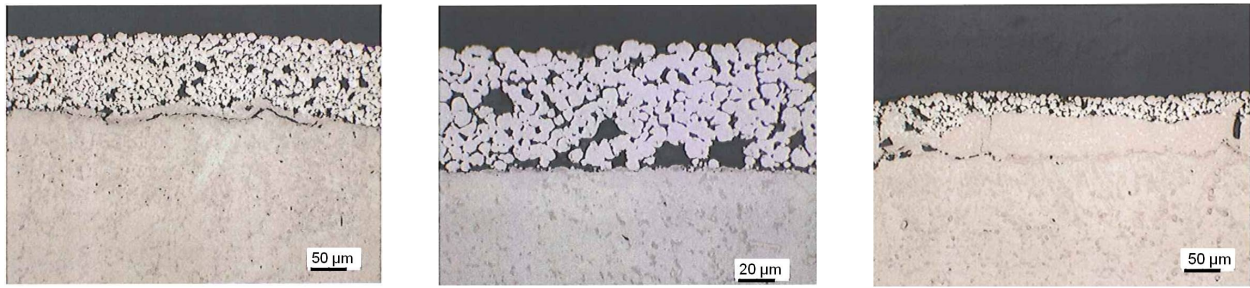


Figure 5.6.: SEM Fracture appearance images taken by IFAM. Left: 100  $\mu\text{m}$  porous layer (ref-tube no.3); Middle: 50  $\mu\text{m}$  porous layer (ref-tube no.4); Right: Melted layer caused by slightly higher local temperature (ref-tube no.6)

### 5.1.6. Oxidized Layer Structure

A thick oxidation layer can be created on the zircaloy surface, if it is in permanent contact with oxygen at a high temperature. The built-up of the oxidation layer shows a fine porosity. This circumstance gave rise to the idea to produce on purpose a thick oxidized layer on the surface. An advantage is that the basic tube material is used to create the layer. On the other hand, the oxidized material  $\text{ZrO}_2$  has a lower thermal conductivity than the metallic zircaloy.

The manufacturing of the oxidized tubes was coordinated by AREVA NP Laboratory in Erlangen. Two zircaloy tubes with a total length of 460 mm were oxidized in the laboratory and finished in January 2010.

With a heat treatment process in an electric furnace a thick oxidized layer is produced on the surface. The layer is growing on the surface due to the oxidation of the tube material  $\text{Zr}$  to  $\text{ZrO}_2$ . In order to achieve a thick layer the tube was kept for about one month in the furnace at 550 °C in air atmosphere. During the heat treatment the oxidized layer was built up to a homogeneous thickness of  $90 \pm 4 \mu\text{m}$ .

A difficulty is the possible deformation of the tube due to the heat treatment. The maximum bending of the two oxidized 460 mm long tubes resulted in 0.45 mm and 0.55 mm. Furthermore, the inside of the tube had to be prevented against oxidation. Therefore, the tube was filled with inert gas and closed by welded caps. Table 5.8 summarizes the description of the oxidized tube.

Table 5.8.: Oxidized layer structure on zircaloy tube

Name	Oxidized
Description	Thick oxidized layer of $\text{ZrO}_2$ on the surface Layer growth by oxidation of base tube material Dense surface with cracks - Inside fine porosity
Manufacturer	Laboratory of AREVA NP GmbH, Erlangen
Manufacturing process	Temperature treatment
Basic tube material	Zircaloy-4
Coating material	$\text{ZrO}_2$
Total layer thickness	90 $\mu\text{m}$

After the manufacturing process the oxidized layer was characterized by SEM images taken by the Technical Center of AREVA NP. The oxidized zircaloy tube shown in Figure 5.7 has a light brown color. Figure 5.8 shows that the outer surface of the oxidized layer is rather dense and has the same topography of micro-grooves crosswise to the tube axis as the technically smooth tube (Fig. 5.1). There are no visible open

## 5. Surface Structures and Characterization

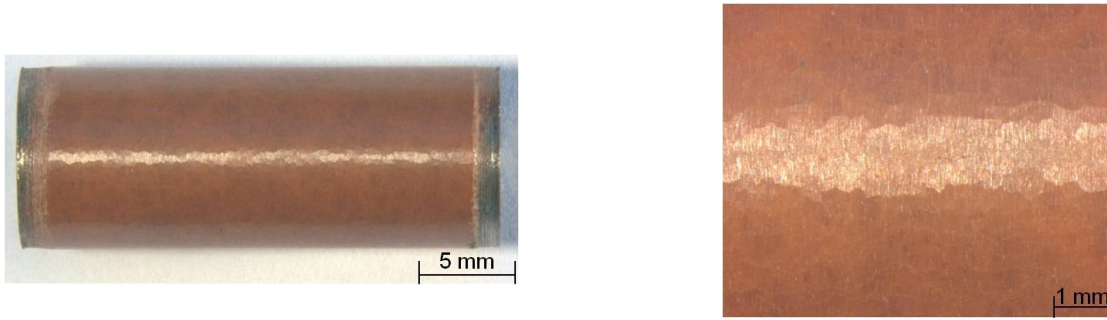


Figure 5.7.: Zircaloy tube with light brown oxidized layer of  $90\ \mu\text{m}$  thickness (Pictures from AREVA NP Technical Center)

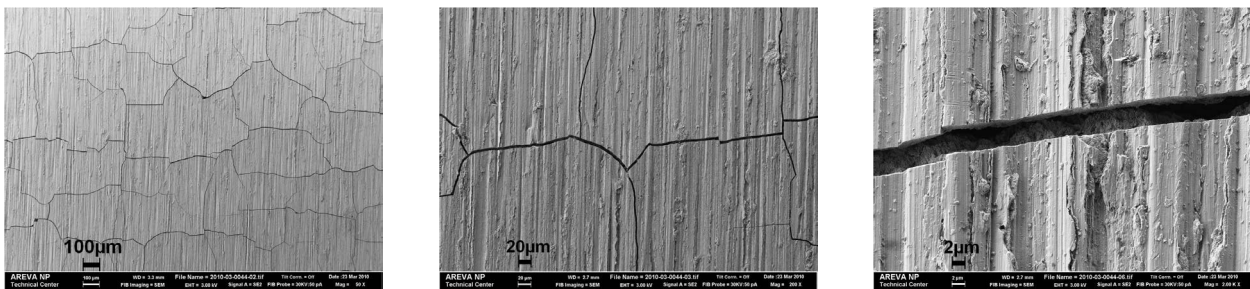


Figure 5.8.: SEM images of oxidized layer surface which is divided into polygonal sections by cracks (Pictures from AREVA NP Technical Center)

pores on the surface of the layer. However, the oxidized layer is not a completely closed layer, but shows instead regular polygonal sections which are separated by cracks of about  $1$  to  $2\ \mu\text{m}$  width as apparent in Fig. 5.8. The separated sections have a length and width of about  $200$ - $300\ \mu\text{m}$ .

These vertical cracks into the layer are also visible in the polished cut image in Fig. 5.9 on the left. Ending inside the layer the cracks do not reach the bottom of the layer. Short horizontal cracks inside the layer are also visible in the same image. These short cracks and the top view on a mechanically spalled area in Fig. 5.9 (middle and right) indicate the very fine porosity inside the oxidized layer.

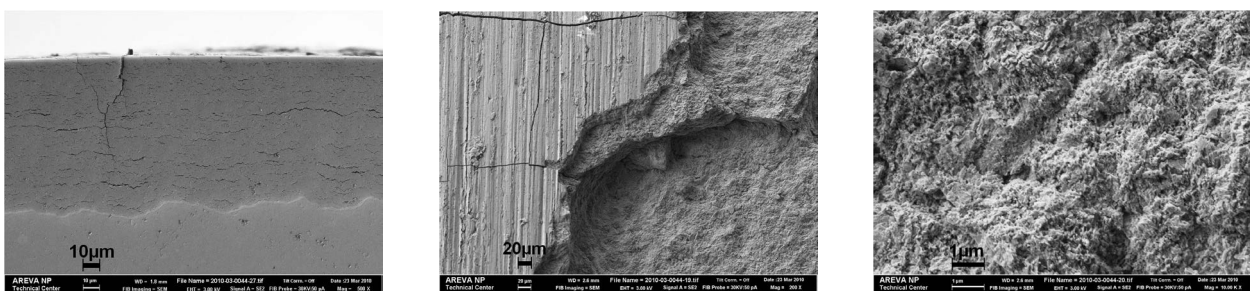


Figure 5.9.: SEM images of polished cut of oxidized layer (left) and top view on a mechanically spalled area (middle and right) (Pictures from AREVA NP Technical Center)



## 5.2. Characterization of Surface Structures

The wetting behavior of the fluid on the surface is an important parameter for the mechanisms of bubble creation and CHF ([51], [29], [66]). In order to characterize the fluid-structure interaction the wetting behavior of water on the structured surface zircaloy samples was considered. A brief introduction of surface wetting and the Wilhelmy measurement method are first described in this chapter before presenting the measurements of wetted length and wetting behavior of the tube samples. Additionally, the topographical profiles of particular surface structures are compared with the wetted length results.

### 5.2.1. Wetting Behavior on Solid Surfaces

Considering a drop on a solid surface the contact angle is formed at the three-phase line (triple line) between solid, liquid and gas phase. A contact angle of  $\theta=0^\circ$  means total wetting of the surface by the liquid, a contact angle of  $\theta=180^\circ$  means that the liquid is non-wetting on the surface and the contact angles between  $0^\circ < \theta < 180^\circ$  refer to partial wetting conditions.

In order to characterize the interaction between a solid surface and a fluid the static or dynamic contact angles are often considered. A sophisticated theoretical background on wetting phenomena and measurement methods is given in [28] or [10], for instance.

There are several methods for measuring the contact angle. A common method is the sessile drop method. The basic principle is to put a liquid drop on the surface and to measure visually the contact angle at the triple line. Although appearing simple the measurement could be quite complex because it depends on time, surface roughness, preparation, drop volume, and evaluation method, for instance. The quasi-stationary contact angle of the drop on the surface is defined as the static contact angle.

The dynamic contact angles can be measured by increasing or decreasing the drop volume continuously. With increasing drop volume the contact angle exceeds the static contact angle and finally moves with a constant advancing angle  $\theta_a$ . If the drop volume is decreased, then the contact angle decreases as well until the contact line moves back with a constant receding angle  $\theta_r$ . The difference between both angles  $\theta_a$  and  $\theta_r$  defines the dynamic contact angle hysteresis.

The sessile drop method is suitable for flat objects and relatively smooth surfaces. However, the reference samples for the surface structure characterization were produced on a zircaloy tube sample in the same manufacturing process as the tubes for the test section. The curvature of the cylindrical sample can deform the shape of a sessile drop on the tube surface. Moreover, the liquid drop invades surface structures with micro-channels or porous layer. Consequently, the sessile drop method is inappropriate for determining the contact angle on the tube samples.

A suitable method for determining the dynamic contact angle allowing both the use of a tube and capillary texture on the surface was found in the Wilhelmy method. The measurement principle is explained in the following.

### 5.2.2. Wilhelmy Method

A KRÜSS *K100C* Tensiometer shown in Fig. 5.10 was used to measure the wetting force and the dynamic contact angle with the Wilhelmy method. It is based on the relationship between contact angle, surface tension, wetted length, and Wilhelmy force. This force results from the interaction between the liquid and the solid surface and can be measured when the solid object immerses or leaves the liquid. If the wetted



Figure 5.10.: Krüss Tensiometer K100C with mounted smooth tube at balance

length and the surface tension are known, then the contact angle can be calculated from the measured Wilhelmy or wetting force by following equation

$$\cos\theta = \frac{F_{wet}}{L_{wet} \sigma} \quad (5.1)$$

where  $\theta$  is the contact angle,  $F_{wet}$  the wetting force,  $L_{wet}$  the wetted length, and  $\sigma$  the surface tension of the liquid.

The advancing contact angle results from the measured force when the object immerses the liquid. The receding contact angle refers to the force when the object is withdrawn as illustrated qualitatively in Fig. 5.11. The forces acting on the object are gravitational, wetting and buoyant forces and the sum of these forces gives the total force according to

$$F_{total} = F_G + F_{wet} - F_{buoyancy} \quad (5.2)$$

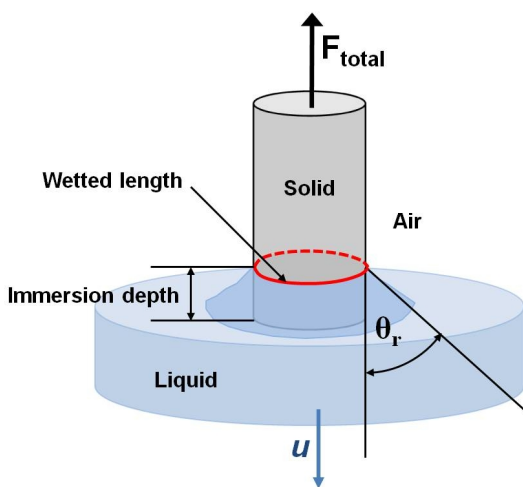


Figure 5.11.: Schematic draft of receding contact angle measurement with Wilhelmy method

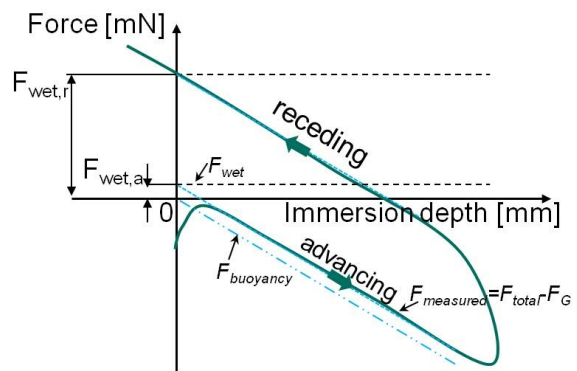


Figure 5.12.: Qualitative force measurement over immersion depth for force tensiometry

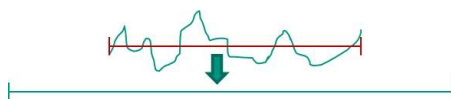


Figure 5.13.: Development from base profile length to effective length

The object is fixed at the tensiometer balance and tarred for removing the effect of weight ( $F_G$ ). Thus, the measured force  $F_{measured}$  corresponds to the relationship between wetting and buoyant force. The liquid pool is raised with constant velocity and the measurement is triggered when the solid object contacts the liquid surface. During the immersion of the object into the fluid the force against immersion depth curve is recorded as it is depicted in Fig. 5.12. Due to the increasing buoyancy force the measured force is linearly decreasing if the object geometry remains constant. After reaching a predefined immersion depth the liquid pool is lowered for determining the force corresponding to the receding angle. The required wetting forces result from extrapolating the linear curve sections to zero immersion depth where the buoyancy force is zero. These wetting forces are used for calculating the advancing and the receding contact angle with Eqn. (5.1). Generally, a measured force of 0 mN corresponds to an contact angle of  $90^\circ$ , a positive force ( $>0$ ) corresponds to an contact angle between 0 and  $90^\circ$ , and a negative force ( $<0$ ) corresponds to an contact angle between 90 and  $180^\circ$ . The measured forces as well as the contact angles are average values over the perimeter and/or over the immersed depth.

According to Eqn. (5.1) the wetted length and the surface tension have to be known for determining the contact angle. Both values can be determined applying the same measurement method. Using an object of known geometry (Wilhelmy-plate or Du Noüy-ring) made of a solid material with high surface energy as platinum the surface tension can be measured. The cos-term on the left in Eqn. (5.1) equals unity since the contact angle on platinum is  $0^\circ$ . The tensiometer software already provides a large data base of surface tensions for various fluids.

Using a highly wetting fluid with known surface tension the wetted length can be determined. As mentioned above the wetted length is a required quantity for the determination of the contact angle with the Wilhelmy method. Since the structured surface tubes have different surface profiles the wetted length has to be determined for each sample. These measurements are presented in the next section.

### 5.2.3. Measurements of the Wetted Length

The wetted length is the length of the triple line between the solid, liquid and gas phases. In case of a vertical and bottom closed tube entering a liquid pool as depicted in Fig. 5.11, the wetted length equals the effective length of the outer tube perimeter. Effective perimeter means that the topographical profile of the surface is taken into account. The sketch in Fig. 5.13 shows the difference between the base profile length and the effective or stretched length.

The wetted length can be determined by using a fluid with low free surface energy, like n-heptan. This fluid spreads on the solid surface with a contact angle of  $0^\circ$ . Thus, the cos-term on the left side in Eqn. (5.1) equals unity and the wetted length results from the measured force and the known surface tension.

The wetted length of the different tube samples are illustrated with bars in Figure 5.14. The mean value of at least 5 repetitions is denoted above each bar and the small error bar indicates the corresponding standard deviation. The first bar refers to the technically smooth zircaloy tube. Compared to the geometrical perimeter of a circle of  $P_{geom}=29.85$  mm, calculated with the outer tube diameter of 9.5 mm, the measured

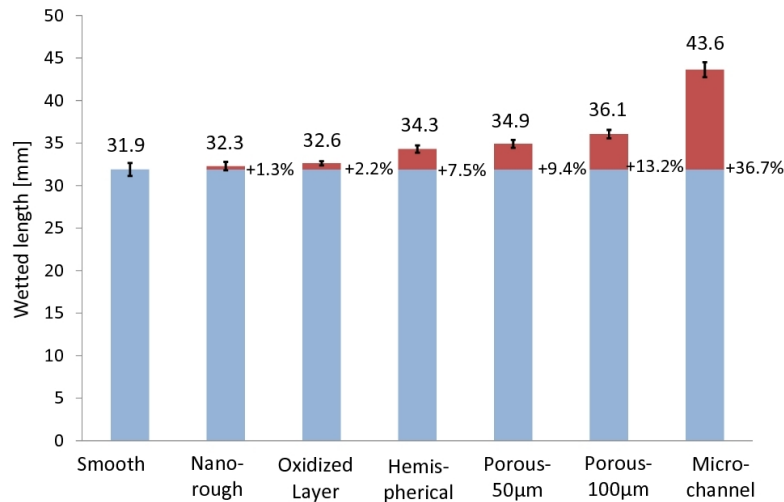


Figure 5.14.: Wetted lengths of surface structured tubes compared to smooth tube

wetted length of 31.9 mm is already 6.9% higher. The wetted or effective length is longer because the surface roughness is taken into account. Hence, using the geometrical perimeter for determining the contact angle with Eqn. (5.1) would give a different result.

The red parts of the bars visualize the difference in wetted length between the structured-surface tubes and the smooth tube. The percentage value is given on the right side of each bar. The mean values of wetted length of all surface structured samples are higher than the one of the smooth tube. However, the values of the nano-rough and oxidized layer structures are in the deviation range of the smooth tube. The hemispherical profile leads to an increase of 7.5% of the effective perimeter. The 50µm and 100µm porous layers increase the wetted length about 9.4% and 13.2%, respectively. The most significant enlargement of the perimeter was measured with 36.7% for the micro-channel structure. Since the surface structure characteristic remains similar over the length of each tube, the percentage increase in wetted length due to the surface modification expresses also the increase in surface area which is in contact with the fluid.

#### 5.2.4. Topographical Measurements of Surfaces

The wetted length is a required and important quantity for the contact angle determination using the Wilhelmy method. Therefore, the wetted length measurements with the tensiometer were compared to other topographical determination methods as far as applicable for the particular surface. A chromatic white light sensor and a 3-D light microscope were used for reference measurements. The methods and the comparing results are explained in the following.

With chromatic white light (CWL) sensor technique a 3D-image of the surface topography can be produced and analyzed getting information about roughness, texture and surface area, for instance. The topography measurements of the tube surfaces were conducted in cooperation with the Institute for Applied Materials - Material Process Technology (IAM-WPT) at the Karlsruhe Institute of Technology. The MicroProf®100 of Fries Research and Technology (FRT) with the chromatic white light sensor FRT CWF600 was used for the topography measurements. The optical sensor technology allows a complete non-

destructive measurement. The resolution is  $1\ \mu\text{m}$  in lateral and  $6\ \text{nm}$  in vertical direction. A positioning device was designed to position the test tube on the instrument table. Figure 5.15 shows the topography apparatus and an extra designed positioning device consisting of a traversing rail with two slides in which the test tube is chucked. The positioning device design and the measurement principle and results are described in the project thesis of *Knobloch* [58] and *Philipps* [83].

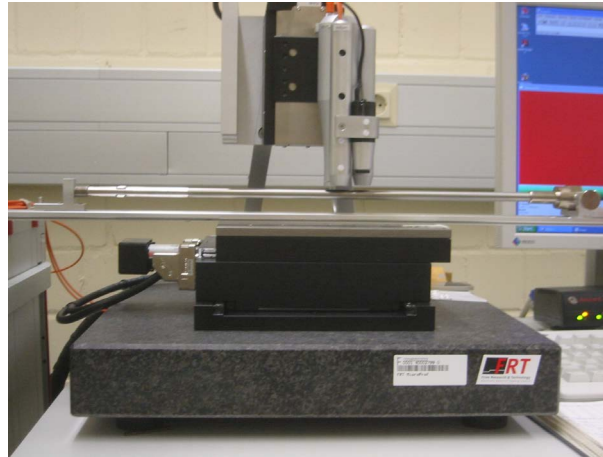


Figure 5.15.: Installation of the positioning device with a test tube in the topography apparatus

This measuring method was applicable for the technically smooth and the micro-channel structured surfaces. Figure 5.16 shows two different section details of the 3D-image of the technical smooth surface. The micro-groove texture orientated cross-wise to the tube axis due to the belt grinding manufacturing process, as described in section 5.1.1, is clearly visible in these pictures. Figure 5.16 illustrates the rectangular geometry of the micro-channel structure from the chromatic white light measurements.

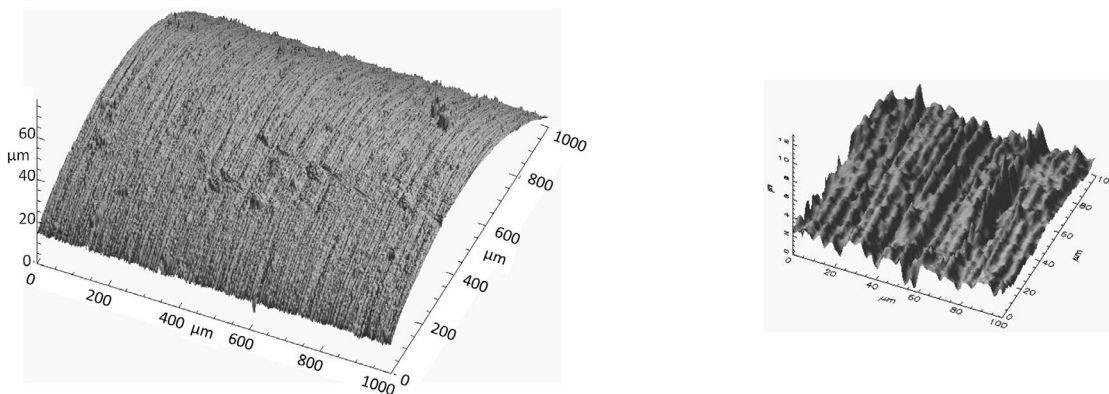


Figure 5.16.: 3D topographical images of smooth zircaloy tube determined by chromatic white light sensor technique

The surface structure characteristics for the smooth and micro-channel tubes derived from the topographical measurements are summarized in the following.

**Characteristics of technical smooth tube:**

- Micro-grooves orientated cross-wise to tube axis.
- Mean values groove geometry are
  - width of  $4.89 \pm 1.6\ \mu\text{m}$ ,
  - depth of  $0.61 \pm 0.35\ \mu\text{m}$ .

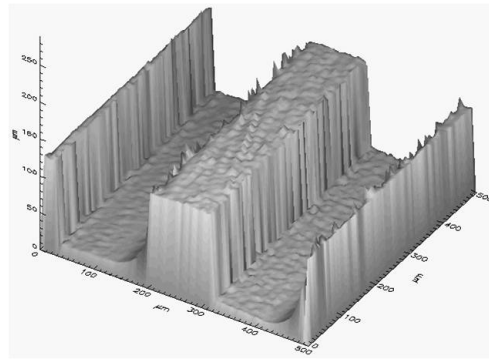


Figure 5.17.: 3D-image of micro-channel structure using chromatic white light sensor technique

**Characteristics of micro-channel structure:**

- Rectangular micro-channels orientated in tube axis.
- Mean values of the channel geometry are
  - channel width of  $208 \pm 9 \mu m$ ,
  - channel depth of  $66 \pm 15 \mu m$ ,
  - fin width of  $80 \pm 11 \mu m$ .

The CWL sensor technique was inapplicable for the other structures because of different reasons. The lateral resolution was too low for imaging the nano-rough structure. The inner layer build-up is important for the porous layers, however, only superficial information is available with the CWL measurement system. The hemispherical structure produced reflections at the edges of the hemispheres giving misleading height results.

In case of the hemispherical structure a light microscope Olympus BX61 with an integrated automatic vertical positioning of the sample table allowed 3D-imaging of the surface texture. A 3D-profile is generated in numerical postprocessing of a series of images at different focal depths. The single microscope images have only sections of the sample in focus. The measurement technique is called Extended Focal Imaging (EFI). Combining the in-focus regions of the single images with the positioning measurement a height map can be produced which gives the 3D topographical information. However, the vertical resolution of about  $0.5 \mu m$  is rather low compared to the chromatic white light sensor. A 2D-profile of the hemispherical structure extracted from the 3D-image of the light microscopic image is shown in Fig. 5.18. More details about the equipment and the measurements are described in the project thesis of *Philipps* [83]. The following summary presents the characteristic sizes of the hemispheres on the surface.

**Characteristics of hemispherical surface:**

- Closed structure of stochastically distributed hemispheres.
- Mean values of single hemispheres are
  - diameter of  $15.6 \pm 3 \mu m$ ,
  - height of hemispheres of  $2.2 \pm 1.2 \mu m$ .

The effective perimeters of the smooth, the hemispherical and the micro-channel tube samples were calculated using the topographical information of the surface texture. 2D-profiles at several location cross-wise to the tube axis were evaluated from the CWL measurements for the smooth and the micro-channel structures and from the 3D light microscope images for the hemispherical structure. The measured effective lengths correspond only to sections of the perimeter. Therefore, the entire effective perimeter was calculated by multiplying the sectional effective lengths with the ratio of  $360^\circ$  and the angle of the evaluated circular

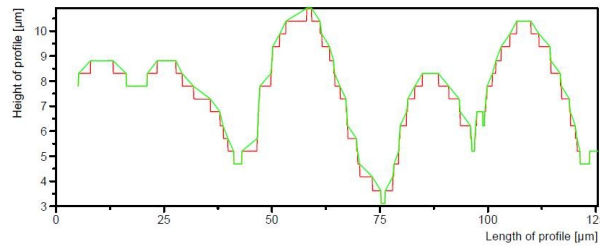


Figure 5.18.: 2D profile of hemispherical structure using light microscope

Table 5.9.: Comparison of perimeter results between tensiometer and topographical measurements

	Tensiometer	Topography
	$L_{wet}$	$L_{topography}$
Structure	mm	mm
Smooth	31.9	31.7
Micro-channel	43.6	43.5
Hemispherical	34.3	34.7

sector.

Table 5.9 contains the comparison between the resulting effective perimeters from the topographical measurements and the wetted lengths from the tensiometer measurement described in section 5.2.3. The comparison shows a good agreement of the effective lengths in spite of different measurement techniques. The tensiometer results of the wetted length used for the contact angle determination are therefore confirmed even for structures with capillaries like the micro-channel tube. The comparison emphasizes the good application of a simple and nondestructive method to determine the average effective perimeter by using the Wilhelmy method. Even porous structures can be characterized by this wetted length measurement.

### 5.2.5. Measurements of Wetting Force and Dynamic Contact Angle

The wetting behavior of water on the structured tube samples was characterized by applying the Wilhelmy method explained in section 5.2.2. The resulting characteristic values are the wetting forces and the dynamic contact angles.

The sample preparing of cleaning with hydrochloric acid, acetone and deionized water and subsequent drying, as well as the measurement conditions, see Tab. 5.10, have been the same for each tube sample. The measurement procedure involved two cycles: a first one in which the dry surface was immersed into the liquid and then removed back, and a second one repeating the measurement with the wet surface. The experimental procedure of the wettability tests is described in more detail in the project thesis of *Philipps* [83].

Table 5.10.: Conditions of tensiometer measurements

Fluid	Water
Fluid temperature	30 °C
Immersion velocity	4 mm/min

Figure 5.19 shows the measured wetting forces acting on the dry surface in the first measurement cycle. The advancing forces of 0.88 and 1.22 mN for the micro-channel and the porous-100 structures tower above

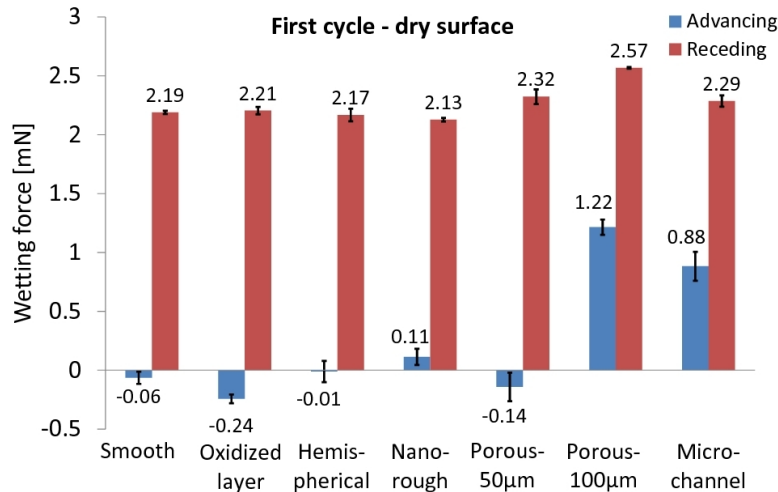


Figure 5.19.: Wetting force for advancing and receding behavior on dry surface in first measurement cycle

the ones for other structures with values between -0.24 and 0.11 mN. The porous-100 structure also has the highest receding force of 2.57 mN followed by the porous-50 (2.32 mN) and micro-channel (2.29 mN) structure. The other structures have values between 2.13 and 2.21 mN. The higher forces for the micro-channel and porous-100 structures are caused by additional capillary effect. The liquid is drawn into the capillaries when the solid object immerses the liquid and it is kept in the capillaries when the object leaves the liquid pool.

It is interesting that the porous-50 structure has insufficient capillary effect to draw the liquid into the pores which is noticeable in the small advancing force compared to the porous-100 structure. The value of the advancing force is even slightly lower than the one of the smooth tube. On the other hand, the receding force is similar to the micro-channel structure indicating that the liquid is kept in the surface texture.

Figure 5.20 shows the advancing and receding forces of the second measurement cycle for the wetted surface after the first cycle. The smooth surface behavior is almost unaffected compared to the first cycle. Whereas the oxidized, nano-rough and hemispherical surface structures demonstrate an increase in the advancing force in the second cycle. It is supposed that these surface structures are capable to remain more liquid in the texture than the smooth tube. The receding forces of the second cycle are almost identical to the ones of the first cycle for all samples. This is not surprising since the receding force is always measured on a formerly wetted surface.

The porous layer and the micro-channel structure indicate an increased advancing force. The bounded liquid in these structures leads to similar measurement values at the balance for the immersion as well as the withdrawing process. The tensiometer displayed no values for the second cycle for the porous-100 structure.

The measured wetting forces are used for calculating the contact angles. The wetted perimeter and the surface tension are further relevant factors according to Eqn. (5.1). A higher force means a lower contact angle for constant wetted length and surface tension. The surface tension is constant in this case since the fluid temperature was kept at 30 °C for all measurements. However, the particular wetted lengths from Fig. 5.14 in section 5.2.3 have to be inserted for each structure.



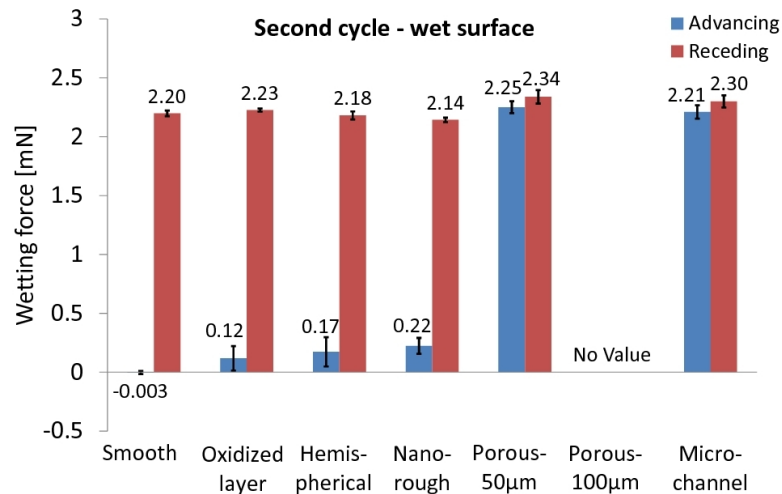


Figure 5.20.: Wetting force for advancing and receding behavior on wet surface in second measurement cycle

Figure 5.21 shows the resulting contact angles for the first and Fig. 5.22 for the second measurement cycle. The general behavior of the structures wettability explained for the wetting force is also expressed by the contact angle. The influence of the wetted length is noticeable in the values of the receding contact angle of the micro-channel structure. In spite of higher receding wetting force in Fig. 5.19 the receding contact angle of the micro-channel structure is with  $42^\circ$  significantly higher than for the other structures because of the increased perimeter of the channel structure.

The wetting behavior of the technically smooth zircaloy surface is characterized by a large advancing

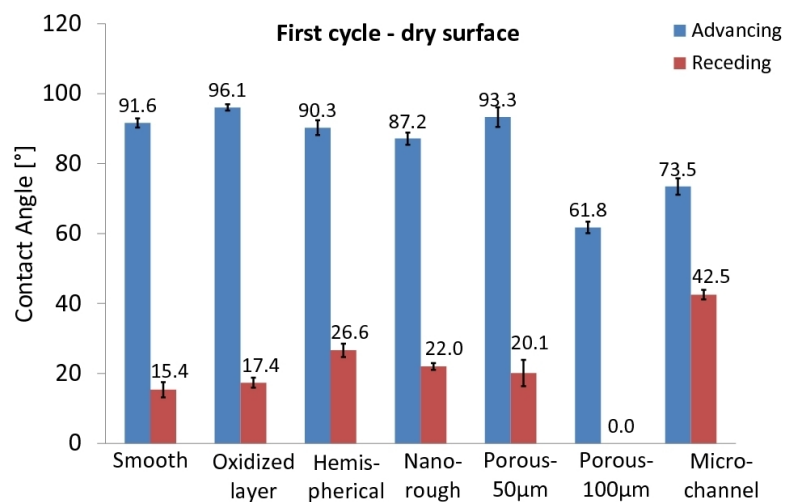


Figure 5.21.: Advancing and receding contact angle of first measurement cycle with dry surface

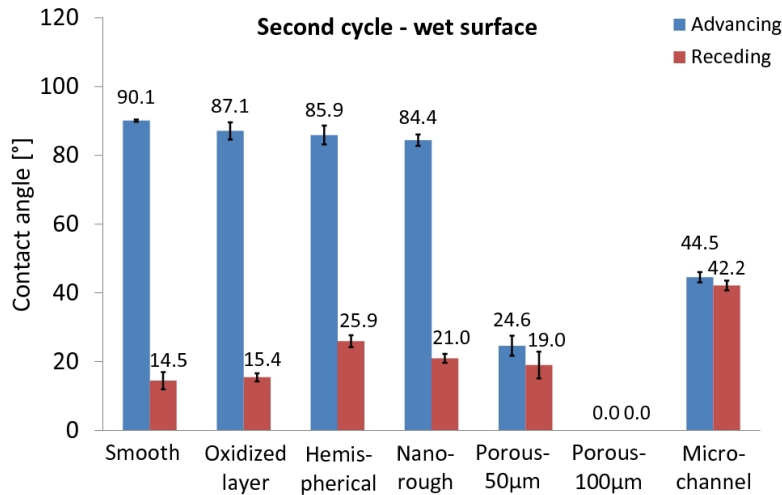


Figure 5.22.: Advancing and receding contact angle of second measurement cycle with wet surface

and a low receding contact angle of about  $90.6^\circ$  and  $15.4^\circ$ , respectively. Thus, the dynamic contact angle hysteresis is rather high with  $75^\circ$ . The tube samples of oxidized layer, hemispherical, nano-rough, and porous-50 surface structures also have an advancing contact angle between  $87.2^\circ$  (nano-rough) and  $96.1^\circ$  (oxidized layer) on the dry surface.

Comparing the advancing contact angles of the first cycle in Fig. 5.21 with the ones of the second cycle in Fig. 5.22, the advancing contact angle of the oxidized layer is decreased about  $9^\circ$  from  $96.1^\circ$  to  $87.1^\circ$ . This is a higher decrease than observed for the smooth, hemispherical or nano-rough surface structures with differences of  $1.5^\circ$ ,  $4.4^\circ$ , and  $2.8^\circ$ . This is an indication of the capability to keep liquid in the cracks of the oxidized layer texture, see section 5.1.6. The porous-50 surface structure shows this effect obviously with a decrease in the advancing contact angle from  $93.3^\circ$  in the first to  $24.6^\circ$  in the second cycle.

*Sarwar et al.* [89] observed a similar behavior for a sessile drop on porous coatings. They found relatively high contact angles (around  $90^\circ$ ) on the dry surface. However, the drop spreads on the surface when putting the drop on a surface with water entrapped in the porous layer.

The porous-50, porous-100, and micro-channel structures are capable to remain a significant amount of liquid in the surface texture. This behavior is noticeable in the similar values of advancing and receding contact angles for the second measurement cycle in Fig. 5.22.

### 5.2.6. Discussion of Wetting Behavior

The measurement of the dynamic wetting behavior depends on the velocity. The dependency on velocity was measured for the smooth tube and increased velocities up to 100 mm/min in the project thesis of *Philipps* [83]. The advancing contact angle remained almost unvaried at about  $90^\circ$ . However, the receding contact angle showed an increase from  $15^\circ$  at 4 mm/min to  $35^\circ$  at 100 mm/min. The general objective of the wettability measurements was a comparison of the fluid-structure interaction between the different surface structures. Therefore, the same slow velocity of 4 mm/min for the pool movement was chosen for

all measurements. The uncertainty of tensiometer measurement was estimated to be less than 1% of the measured value [83].

Contact angle measurements from literature are difficult to compare because of different measurement techniques and the influence of surface roughness and texture on the contact angle [93]. Only few comparable contact angle measurements of water on technically smooth metal surfaces were found in literature. *Bernardin et al.* [13] investigated the static contact angle for water droplets on an aluminum surface. They determined a relatively constant contact angle of about  $90^\circ$  in the pressure range from 101.3 to 827.4 kPa and surface temperatures below  $120^\circ\text{C}$ . *Kamura et al.* [50] measured a static contact angle via sessile drop method for a water drop on a zircaloy plate of  $80^\circ$  at  $25^\circ\text{C}$  and high pressure of 14000 kPa. Furthermore, they determined contact angles for aluminum and stainless steel. The authors found only a small effect of pressure on the contact angle. They report a slight decrease from  $90^\circ$  to  $80^\circ$  with increasing pressure from 830 to 14000 kPa for the stainless steel surface. *Bernardin et al.* observed no influence of pressure in the lower pressure range between 100 and 830 kPa.

Furthermore, the contact angle depends on temperature. Both, *Bernardin et al.* [13] and *Kamura et al.* [50], reported a small or no decrease of the contact angle with increasing temperature below temperatures of  $120^\circ\text{C}$  [13] and  $150^\circ\text{C}$  [50] and a considerable almost linear decreasing effect for temperatures above these values. *Petke and Ray* [82] found a similar behavior for water on polymeric surfaces observing a low temperature region ( $5\text{-}100^\circ\text{C}$ ) with almost constant contact angle and a high temperature region ( $100\text{-}160^\circ\text{C}$ ) with a drastically decrease in contact angle. A theoretical model for the temperature dependency was presented by *Adamson* [1] relating the molecular surface adsorption of a solid to the contact angle of a liquid on the solid.

The measured dynamic advancing contact angle of  $91.6^\circ$  ( $30^\circ\text{C}$ , 100 kPa) for the technical smooth zircaloy surface with the tensiometer of the present work is slightly higher than the measurement of  $80^\circ$  ( $25^\circ\text{C}$ , 14000 kPa) of *Kamura et al.* [50] with the sessile drop method on the zircaloy plate. However, the advancing angle is generally greater than the static contact angle and the contact angle decreases slightly with increasing pressure.

The present measurements of the fluid-structure interaction were conducted at  $30^\circ\text{C}$  and atmospheric pressure. In the flow boiling process, however, the fluid is at saturation temperature in the boundary layer of the surface. An increase of liquid temperature for the tensiometer measurement was inapplicable for the present tensiometer assembly since the gas phase could not be tempered. Condensing liquid at the tube would give misleading values. Nevertheless, the temperature regulation of the gas phase in the tensiometer is principally possible with appropriate equipment.

Table 5.11 lists some more differences between the flow boiling system of the CHF measurements and the applied conditions for the wettability characterization using the Wilhelmy method. Furthermore, the surface boundary layer could be affected by discontinuous slug flow, entrainment, and droplet deposition during the flow boiling process. Thus, it is difficult to relate both situations. *Sadisavan et al.* [88] discussed that although numerous CHF investigations pointed out the importance of wettability, it is not clear whether a contact angle is appropriate for use in boiling application or which contact angle should be considered.

Nevertheless, the Wilhelmy method could be applied in the current investigations as a simple and non-destructive method to measure the effective perimeter and the general wetting behavior of the different micro-structured tube samples. Even surface structures with capillaries like the micro-channel or porous layer surfaces could be characterized.

Table 5.11.: Differences in boundary conditions between flow boiling system and applied tensiometer measurements

Condition	Flow boiling	Tensiometer measurement
Fluid temp.	$T_{sat}$	303 K
Surface temp.	$> T_{sat}$	303 K
Pressure	120-300 kPa	101.3 kPa
Gas atmosphere	Vapor	Air
Fluid velocity	$\geq 0.25$ m/s for 250 kg/(m <sup>2</sup> s) $\geq 0.4$ m/s for 400 kg/(m <sup>2</sup> s) Depending on flow rate, local vapor content and distribution and slip velocity ratio, among others.	4 mm/min ( $6.7 \times 10^{-5}$ m/s)  Constant and slow immersion velocity

However, the absolute contact angle values of surface structures with capillaries should not be directly compared with values of other measurement methods since the capillary force is implicitly counted into the contact angle value of the Wilhelmy method. In order to compare the fluid-structure interaction of samples with similar geometrical diameter but surface structures capable to remain liquid in the texture (porosity, channels or cracks) the wetting forces should be compared rather than the calculated contact angles from these values. An additional measurement with the formerly wetted surface gives further information about the capability to entrap water in the surface texture.

## 6. Stability Analysis for the Test Section

Two-phase boiling systems can be affected by flow instabilities. For instance, *Mishima et al.* [76] observed that flow boiling of water in a tube at low pressure could be affected by various instabilities. The CHF due to unstable flow conditions occurred at remarkably lower values than the CHF at stable flow conditions. Moreover, narrow channels are sensitive to flow instabilities because of their high two-phase pressure drop which can cause variations in the fluid properties during the flow through the channel [77]. Flow instability phenomena in small diameter and micro channel geometries were subject of the investigations of *Zhang et al.* [108] or *Bergles et al.* [11], for example. Characteristic two-phase pressure drop curves and flow excursion instability of water flow in different narrow rectangular channels at low pressure were measured by *Whittle et al.* [105]. *Stoddard et al.* [97] investigated the minimum point of the pressure drop vs flow rate curve and the CHF for horizontal annuli with small gap widths.

The investigations of the present project started with a small annular gap configuration of 1.75 mm formed by an inner and outer diameter of the annulus of 9.5 mm and 13 mm, respectively. Pretests in this small annular geometry without any stabilizing precautions showed that the flow boiling process was highly affected by instabilities. A pulsating flow boiling process could be observed in case of unstable flow conditions. These oscillations caused the occurrence of a premature critical heat flux at a much lower power input than for stable conditions.

*Katto* criticized in [54] that experiments on the CHF near atmospheric pressure are often subject to insufficient throttling conditions upstream of the test section. As already mentioned in section 3.1, the JSME conducted a benchmark study of low pressure CHF measurements in the same annular test section geometry examined by different institutions [75]. Although applying the same experimental conditions there was a scatter in the data between the institutions, particularly for low subcoolings. *Mishima et al.* [75] assumed that the discrepancy could be related to flow instability because of varied pump characteristics and inlet throttling conditions.

Therefore, the objective of the experimental stability analysis, described in this chapter, in [44] and in the master thesis of *Coerdts* [26], was to suppress sufficiently the flow instabilities in order to ensure stable measurement results in the CHF experiments of this work.

### 6.1. Characteristic Pump Curves

Two different pumps were used for the investigations. A rotary pump of the type Movitec from KSB was installed to determine the characteristic pressure drop vs. mass flux curve from single-phase to two-phase flow. However, the operation range of this pump is limited by a minimum flow rate of 0.06 kg/s or a mass flux of 1000 kg/(m<sup>2</sup>s) for the narrow annulus. Therefore, we used a gear pump of the type VGS120 from VERDERgear to cover the lower mass flux region. Furthermore, the CHF experiments were conducted with this pump because it is less susceptible to static flow instability.

Figure 6.1 shows the relationship between pressure drop and mass flux for the rotary and the gear type pump. For each curve with constant pump rotation speed  $n$ , the pressure drop in the system was increased by

closing the throttle valve V1 stepwise. Valve V1 is installed upstream of the test section like it is indicated in Fig 4.3 or Fig 4.1.

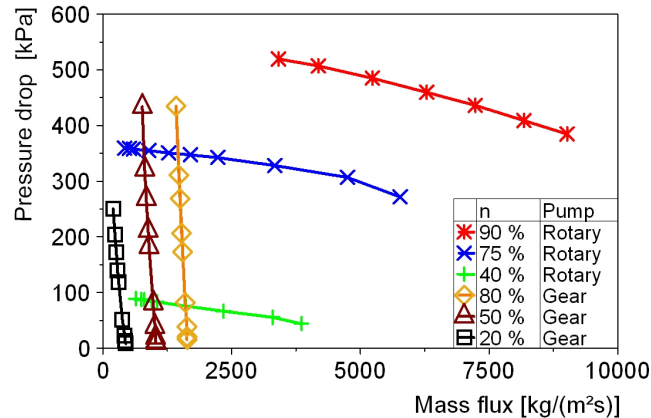


Figure 6.1.: Characteristic curves of the rotary and the gear type pump

The curves of the rotary pump illustrate clearly that the mass flux depends strongly on the system pressure drop for this pump type. A slight increase in the pressure drop causes a significant decrease in flow rate. In contrast, the mass flux of the gear type pump is almost independent of the system pressure drop.

In short, the rotary pump covers a wide range of mass flux, but has a small negative slope. The gear pump has a steep slope instead, but covers only a narrow flow rate region.

The influence of the pump characteristics on the stability of the system is explained in chapter 2.3. According to the Ledinegg criterion in Eqn. (2.22) the system becomes unstable if the slope of the pressure drop curve is more negative than the slope of the pump curve, like it is shown schematically in Fig. 2.5. Using the gear type pump with its stiff characteristics enhances the stability.

Another well-known precaution to suppress flow instabilities is the installation of a throttle valve upstream of the inlet. The method of throttling and how it affects the two-phase flow stability is explained in the following.

## 6.2. Stabilization Effect of Inlet Restriction

Ledinegg-instabilities can be avoided by installing a throttle valve close to the heated section inlet. Figure 6.2 demonstrates how a throttle valve affects the stability of the two-phase system. The flow rate is decreased by reducing the speed of the rotary pump while the throttle valve V1, see Fig. 4.3, was kept in a half closed position. The characteristic pressure drop curve of the test section (square symbols) shows the two-phase behavior like it is explained in the introduction section 2.3.

With decreasing mass flux the two-phase pressure drop curve (10kW) departs from the single phase curve (0kW) and slightly increases with further decreasing mass flux. The curve marked with x represents the pressure drop curve of the throttle valve kept in a fixed position (54% open). The pressure drop decreases continuously with decreasing flow rate. The combination of both curves is plotted with square symbols with inner crosses.

The operating point of the system is defined by the intersection of the pressure drop curve of the system and the characteristic curve of the pump (dashed line). These points are marked in Fig. 6.2 with a circle

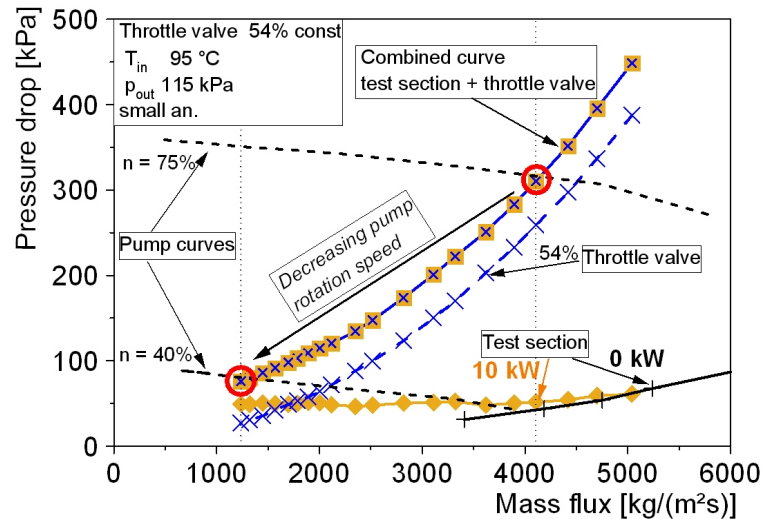


Figure 6.2.: Combined pressure drop curve of test section and throttle valve when the pump rotation speed is decreased at a fixed throttle valve setting

for the relative pump rotation speeds of 40% and 75%. The throttle valve impact on the system stability is a shift of positive slope region to lower mass fluxes. However, the influence diminishes for low flow rates because of the decreasing pressure drop at the throttle.

In contrast, the throttle effect increases if the mass flux is decreased by closing the throttle valve at a constant pump rotation speed, see Fig. 6.3. The pressure drop at the throttle increases and the combined curve (square symbols with inner crosses) is similar to the characteristic curve of the pump at constant rotation speed. The system operating points are marked with circles for three different mass fluxes. The dashed curves at these selected points represent the characteristic curves of the throttle, if the valve were kept fixed at these settings, like it is the case explained for Fig. 6.2. These characteristic curves show a steeper slope when the throttle valve is further closed. Consequently, the stiffness of the system is increased.

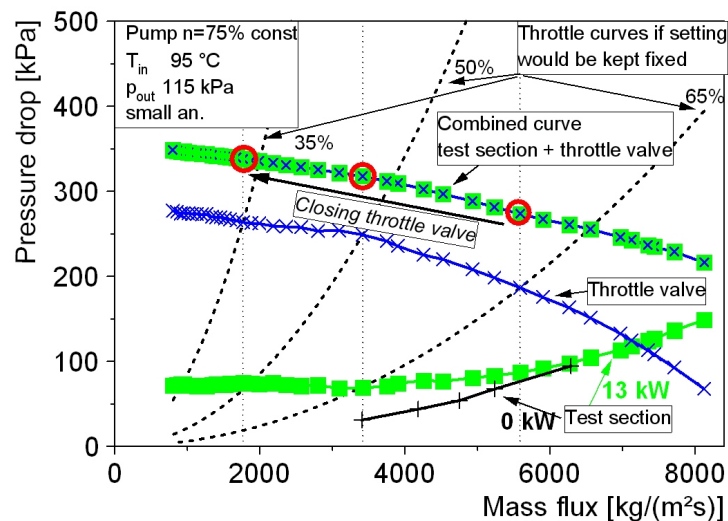


Figure 6.3.: Combined pressure drop curve of test section and throttle valve when the throttle valve is closed at constant pump rotation speed

In summary, an additional pressure drop by a throttle at the inlet shifts the positive slope region of the

pressure drop curve in the range of lower mass fluxes. With a positive slope of the combined curve, the flow is stabilized against static instabilities.

The following section presents measured pressure drop curves of the test section for stable and unstable flow conditions. In case of the stable conditions, the pressure drop curve was determined using the second method according to Fig. 6.3 of closing the valve V1 at the test section inlet to ensure a sufficient throttle effect even for the low mass flux region.

### 6.3. Comparison of Unstable and Stable Critical Heat Flux

The pressure drop across the internally heated annulus for decreasing mass flux was measured in order to characterize the two-phase flow behavior of the test section. Figure 6.4 shows the resulting characteristic curves which are typical for two phase flow in a heated tube or channel [71], [105].

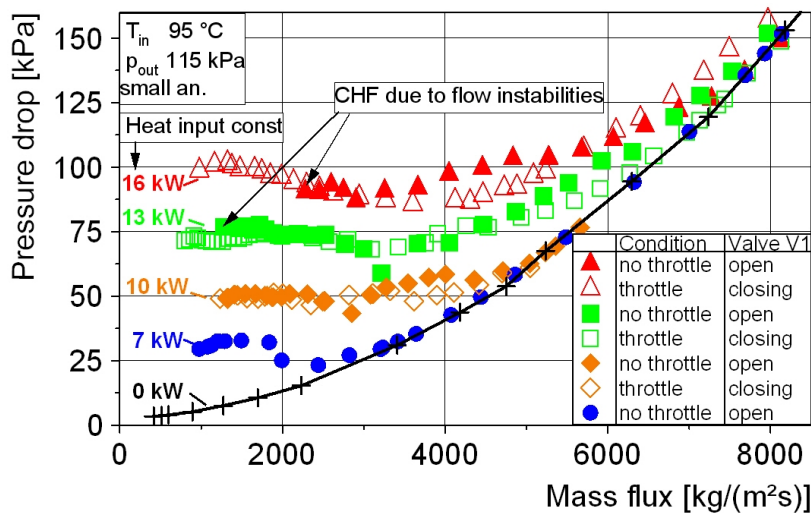


Figure 6.4.: Two-phase pressure drop across the test section in dependency on mass flux for different constant heat input

The pressure drop curves were determined for unstable and stable conditions. For each curve the mass flux was decreased while the heat input into the system was kept constant at values of 7, 10, 13, and 16 kW. The fluid inlet temperature was at  $95 \pm 1$  °C and the outlet pressure was maintained at  $115 \pm 5$  kPa. The system had time to adapt to the new condition after the flow rate was changed to the next lower value. The curves plotted with closed symbols in Fig. 6.4 refer to the experiments at unstable conditions and the open symbols indicate the stable experiments.

For the investigation at unstable conditions, the flow rate was decreased by closing stepwise the hand valve H1 at a constant pump rotation speed. The control valve V1 was set completely open. The loop positions of H1 and V1 are indicated in the process diagram in Fig. 4.3. The pressure drop at H1 does not have sufficient stabilization effect on the test section flow because of the distance and the large surge volume of the preheater between the valve and the test section inlet.

The stable experiments were conducted by closing stepwise the control valve V1 like it is explained for Fig. 6.3 in the section above.



The experimental data were evaluated for each constant valve setting. The data points plotted in Fig. 6.4 are the arithmetic mean values of the pressure drop over the mean values of mass flux. At every valve setting, the pressure drop measurement points for a corresponding mass flux in the range of the mean value  $\pm 5 \text{ kg}/(\text{m}^2\text{s})$  were taken into account.

The curve with + symbols in Fig. 6.4 represents the characteristic curve for single liquid flow (0 kW) in the annulus. The pressure drop decreases continuously with decreasing mass flux. With incipient boiling, the pressure drop curves with power input depart from the single phase curve with decreasing mass flux. The slope changes from positive to negative at the minimum point. The region with a negative slope is susceptible to Ledinegg-instability as explained in section 2.3.

Figure 6.4 shows clearly that for higher heat input the departure from the single phase curve is, of course, shifted to higher flow rates. Accordingly, the minimum point is also shifted to the range of higher mass fluxes. This means, that an increase in heating power causes an augmentation in susceptibility to unstable flow. This is important, because the CHF experiments are conducted at constant mass flux increasing step-wise the heating power. In this case, the system stability for the constant mass flux has to be ensured for the complete range of heat input until the critical heat flux occurs. This relationship between the increasing heat input and the operating points in the pressure drop-mass flux curve is shown in section 2.5.

The heat input of 13 kW and 16 kW was sufficient to cause an unstable CHF in the mass flux range covered by the rotary pump. The premature CHF occurred at a mass flux of 1276 and 2279  $\text{kg}/(\text{m}^2\text{s})$  for the heating power of 13 and 16 kW, respectively.

In contrast, the curves with inlet throttle in Fig. 6.4 show clearly that the system was stabilized. The mass flux could be reduced to values below the unstable CHF without any unstable flow occurrences. However, the CHF at stable flow conditions could not be reached because the mass flow decrease was stopped at the recommended minimum flow rate of 0.062 kg/s (1000  $\text{kg}/(\text{m}^2\text{s})$ ) for the small annular geometry) for the used rotary pump.

Therefore, the completion of the pressure drop curve to lower mass fluxes until the stable CHF occurs was carried out with the gear type pump. Figure 6.5 shows the entire characteristic curve to the stable CHF for a constant heat input of 16 kW. The error bars indicate the standard deviation from the mean. The stable CHF at a heat input of 16 kW occurred at a mass flux of 691  $\text{kg}/(\text{m}^2\text{s})$ . Thus, the mass flux of the unstable CHF is a factor 3.3 higher than the corresponding mass flux of the stable CHF for these conditions. The stable curve passes the local maximum at low mass flow and the CHF occurs in the region with a positive slope.

Figure 6.6 shows the time dependent curves of the inlet and outlet pressure and the wall temperature eight seconds before the unstable CHF occurred. At time zero, the CHF was detected by the local wall temperature rise and the heat input was immediately shut down within less than 0.1 seconds. The temperature rise at the local CHF position is remarkably fast and would cause thermal damage of the tube without the fast shut down of the power input.

The system condition of Fig. 6.6 corresponds to the operating point at the mass flux of 2279  $\text{kg}/(\text{m}^2\text{s})$  of the unstable curve in Fig. 6.5. The inlet pressure was oscillating before CHF with a frequency and amplitude of about 2 Hz and 20 kPa, respectively. A fluctuating flow was observable in the test section for these conditions. The operating point for a mass flux of about 2280  $\text{kg}/(\text{m}^2\text{s})$  at a power input of 16 kW lies already in the negative slope region of the pressure drop curve, see Fig. 6.5. The sudden drop in the inlet pressure before CHF, as shown in Fig. 6.6 at time -0.3s, indicates the transition to another operating mode

## 6. Stability Analysis for the Test Section

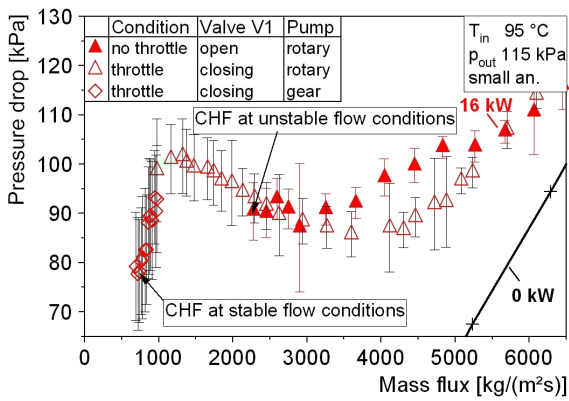


Figure 6.5.: Pressure drop across the test section for 16 kW until stable CHF occurred

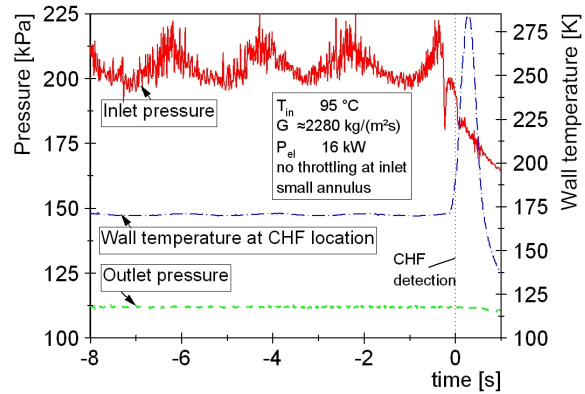


Figure 6.6.: Time dependent curves of inlet and outlet pressure and wall temperature before CHF at unstable flow conditions

causing the CHF.

### 6.4. Asymptotic Trend of Stable Critical Heat Flux

Different critical heat flux experiments for the same parameter set, but with variation of the inlet throttle pressure drop were conducted in order to prove that the throttling is sufficient and a stable CHF value is reached. Contrary to the pressure drop measurements, the procedure of each CHF measurement was keeping constant the mass flux, the inlet temperature and the outlet pressure while the heating power was increased until the CHF was detected.

The experimental parameters were a mass flux of  $250 \text{ kg}/(\text{m}^2\text{s})$ , an inlet temperature of  $95 \text{ }^\circ\text{C}$ , and an outlet pressure of  $120 \text{ kPa}$ . Figure 6.7 shows the CHF measurements in dependency of the pressure drop at the inlet throttle valve V1, see Fig. 4.3 for valve position.

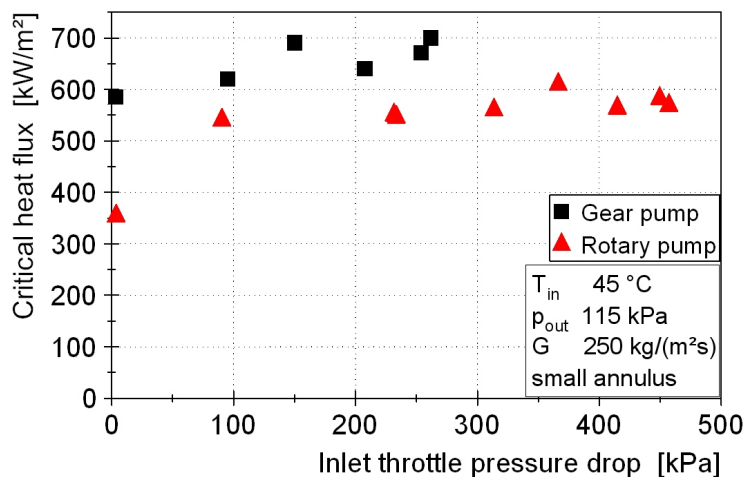


Figure 6.7.: Influence of pressure drop at inlet throttle valve V1 on the CHF

Black squares indicate the measurement results of the gear type pump. Without throttling, i.e. pressure drop zero at the throttle valve, the CHF occurred at  $585 \text{ kW}/\text{m}^2$ . On the other hand, the mean value of the

throttled CHF measurements is  $650 \pm 44 \text{ kW/m}^2$ . Thus, the CHF without throttling was 90% of the stable CHF for the gear type pump. The gear type pump was indeed not completely eliminating the flow fluctuations for operating conditions near the CHF. Consequently, a throttle valve is still necessary to stabilize the flow although the pump characteristic curve is steeper than test section pressure drop curve.

The same measurement procedure at the same parameters was conducted for the rotary pump shown with red triangles in Fig. 6.7. Note, that we operated the rotary pump with a mass flow of  $0.015 \text{ kg/s}$  ( $250 \text{ kg/(m}^2\text{s)}$ ) under the recommended minimum mass flow rate of  $0.062 \text{ kg/s}$  ( $1000 \text{ kg/(m}^2\text{s)}$ ) for this rotary pump. The unstable CHF occurred at a heat flux of  $353 \text{ kW/m}^2$  showing notably an oscillating flow before CHF. With increasing pressure drop at the throttle, the CHF values follow an asymptotic trend, see Fig. 6.7. This asymptotic CHF behavior was discussed by *Lowdermilk et al.* [69]. The mean value for the stable CHF for throttle pressure drops between 300 and 450 kPa was at  $577 \pm 10 \text{ kW/m}^2$ . Thus, the premature CHF without throttling occurred at 61% of the stable value for the rotary pump.

Furthermore, the stable value of the rotary pump is lower than the stable value of the gear pump type in spite of the same parameter conditions. The reason for this difference could not be explained. The lower value for the rotary pump may result from the operation below the designed working range. Nevertheless, the results show the significant difference between the unstable CHF and the stable CHF values and the asymptotic trend with increasing throttle pressure drop.

## 6.5. The Way to Stabilize the CHF Measurements

This section summarizes the relevant conclusions to ensure stable flow conditions from the discussion above. Typical for a two-phase flow boiling system is a characteristic s-shaped pressure drop vs. mass flux curve with a local minimum and maximum. The negative slope region between the extrema is sensitive to instabilities. If the power is kept constant and the mass flux is decreased, then a premature CHF can already occur at a higher mass flux due to instabilities. On the other hand, if the mass flux is constant and the power is increased, then the premature CHF can already occur at a lower heat flux due to instabilities.

The occurrence of static instability depends on the characteristic pump curve. The Ledinegg criterion describes the system susceptibility to static instabilities. If the pump curve is flatter than the negative slope region of the pressure drop curve, then there exist more intersection points meaning more possible operating points. Thus, the system is unstable for these conditions. The stiffer the pump curve, the more stable the system.

An additional pressure drop by throttling upstream of the boiling section enhances flow stability. The combined curve of the pressure drop at the throttle valve and the pressure drop at the test section shows a shift of the positive slope region to lower mass fluxes. However, the throttling has to be sufficient to guarantee the positive slope for the applied conditions of heat flux and mass flux. Both effects of a steep pump curve and an additional throttle pressure drop are depicted qualitatively in Fig. 6.8.

Increasing the additional pressure drop upstream of the test section leads to an asymptotic trend of the CHF value. In other words, after a certain value a further increase of the throttle pressure drop does not lead to more stabilization. The stable CHF-value is defined by this asymptotic value.

Based on the stabilization investigations, the CHF experiments described in the following result section were conducted with the gear type pump and with sufficient inlet restriction. It is noteworthy that the

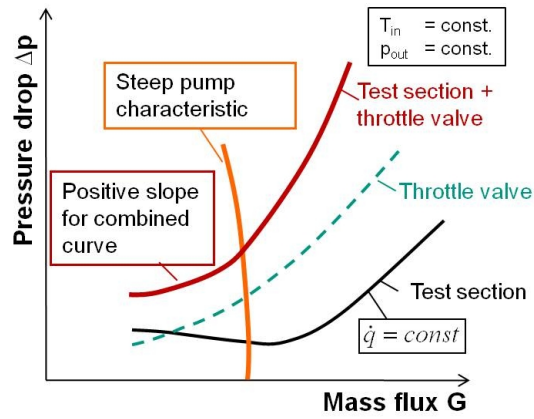


Figure 6.8.: Influence of steep pump curve and pressure drop at inlet throttle on two-phase system with constant heat input

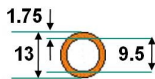
following single points of the CHF results have all the effort of flow stabilization discussed in this chapter in the background.

## 7. Critical Heat Flux Measurements with Smooth Tube

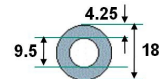
The critical heat flux experiments were conducted in a vertical, internally heated annular test section for different mass flux, inlet temperature, and outlet pressure conditions. Mass flux, inlet temperature and outlet pressure were kept constant while the heating power was increased in small increments until the CHF occurred.

Two annular geometries were used, called small and large annulus, with gap sizes of 1.75 and 4.25 mm, respectively. Firstly, the investigation concept included only the use of the small annular geometry. Therefore, the commissioning and the first measurement series were conducted with this annulus. However, the change to a larger annulus was required because of mainly two reasons: safety against thermal damage of the tubes and comparable conditions to literature data. The background of these reasons is explained later in this chapter. Geometry details and characteristic ratios of the small and the large annular test sections are presented in Tab. 7.1.

Table 7.1.: Comparison of the geometry details between the small and large annulus



Small annulus



Large annulus

Outer diameter	$d_o$	13	<	18	mm
Inner diameter	$d_i$	9.5	=	9.5	mm
Annular gap width	$s$	1.75	<	4.25	mm
Heated length	$L$	326	=	326	mm
Cross section area	$A_{cross} = \frac{\pi}{4}(d_o^2 - d_i^2)$	61.85	<	183.6	mm <sup>2</sup>
Wetted perimeter	$P_{wet} = \pi(d_o + d_i)$	70.7	<	86.4	mm
Hydraulic diameter	$d_{hydr} = 4 \frac{A_{cross}}{P_{wet}} = d_o - d_i$	3.5	<	8.5	mm
Length to hydraulic diameter	$L/d_{hydr}$	93.1	>	38.4	
Heated perimeter	$P_{heat} = \pi d_i$	29.85	=	29.85	mm
Heated area	$A_{heat} = \pi d_i L$	9730	=	9730	mm <sup>2</sup>
Heated equivalent diameter	$d_{he} = 4 \frac{A_{cross}}{P_{heat}} = \frac{d_o^2 - d_i^2}{d_i}$	8.3	<	24.6	mm
Length to heated equivalent diameter	$L/d_{he}$	39.3	>	13.2	

The first part of this chapter presents the measurement results of the technically smooth tube. Then, the results are compared with literature data and with existing prediction methods.

### 7.1. Results of the Smooth Tube Experiments

This section contains the critical heat flux results for the smooth tube and describes the measurement characteristics and influencing parameters. Tables 7.2 and 7.3 show the parameter range of the experiments

## 7. Critical Heat Flux Measurements with Smooth Tube

using the small and the large annulus, respectively. Both annular geometries are considered in parallel in the following.

Table 7.2.: Experimental parameter range for smooth tube in small annular geometry

Annulus	Surface	$p_{out}$	$T_{in}$	$\Delta h_{in}(p, T)$	G
-	-	kPa	°C	kJ/kg	kg/(m <sup>2</sup> s)
Small	Smooth	115	45	250	250, 400, 600, 1000
			65	167	250, 400, 600, 1000
			80	104	250, 400, 600, 1000
		140	45	270	400, 600
		200	60	250	400, 1000
		300	73	250	400, 1000

Table 7.3.: Experimental parameter range for smooth tube in large annular geometry

Annulus	Surface	$p_{out}$	$T_{in}$	$\Delta h_{in}(p, T)$	G
-	-	kPa	°C	kJ/kg	kg/(m <sup>2</sup> s)
Large	Smooth	120	45	250	250, 400
			65	167	250, 400
			80	104	250, 400
		150	73	167	250, 400
		200	80	167	250, 400
		250	88	167	250, 400
		300	94	167	250, 400

### 7.1.1. Influence of Mass Flux

Figure 7.1 shows the measured electric heating power at CHF-detection as a function of mass flow rate for both annuli. The plotted values refer to three different inlet temperatures (45, 65, and 80 °C) at an outlet pressure kept in the range between 110 and 121 kPa. The applied mass flow rates were 15, 25, 36, and 60 g/s for the small annulus and 46 and 73 g/s for the large annulus. The imposed heating power at CHF for the applied parameters was between 6 kW and 27.5 kW.

In order to compare the heat input and flow conditions in different test section geometries, the related values *critical heat flux* and *mass flux* are generally considered. The mass flux is defined as mass flow rate per cross sectional area of the flow according to Eqn. (2.5). The outer and inner diameter of 13 and 9.5 mm for the small annulus form a cross section area of 61.85 mm<sup>2</sup>. The large annulus has the same inner diameter but an increased outer diameter of 18 mm leading to a three times greater cross section of 183.6 mm<sup>2</sup>. Consequently, a three times higher mass flow rate is necessary for reaching the same mass flux in the large annulus as in the small one. Cross section drafts with the corresponding diameters are shown in Tab. 7.1.

The critical heat flux is calculated according to Eqn. (2.6) by dividing the critical heating power by the heating area. Therefore, the critical heat flux expresses the maximum thermal area loading of the heated surface before the local transition to film boiling occurs. The heated area of the inner tube is 9700 mm<sup>2</sup>

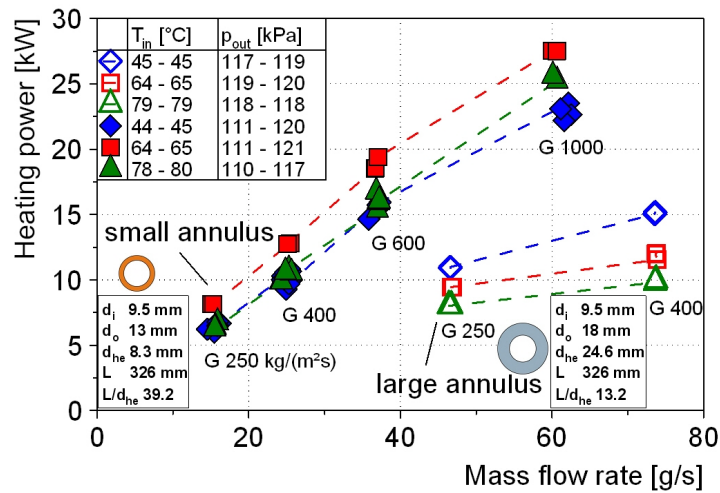


Figure 7.1.: Heat input at CHF against mass flow rate for smooth tube in small and large annulus at 110-121 kPa

given by a heated length of 326 mm and an outer diameter of the inner tube of 9.5 mm. Since only the inner tube, which remains the same, is heated, the heated surface area is identical for both annuli.

The relationship between the calculated critical heat fluxes by Eqn. (2.6) and mass fluxes by Eqn. (2.5) for the measured values from Fig. 7.1 are shown in Fig. 7.2 and 7.3 for the small and large annulus, respectively. The critical heat fluxes for the small annulus increase from 0.62 and 2.84 MW/m<sup>2</sup> with mass fluxes of 250, 400, 600, and 1000 kg/(m<sup>2</sup>s). The increase is almost linearly for the mass fluxes between 250 and 600 kg/(m<sup>2</sup>s). The CHF values for the large annulus range from 0.82 to 1.55 MW/m<sup>2</sup> for mass fluxes of 250 and 400 kg/(m<sup>2</sup>s). The higher mass fluxes of 600 and 1000 kg/(m<sup>2</sup>s) were unachievable for the large annulus using the installed gear type pump because of a limited mass flow rate.

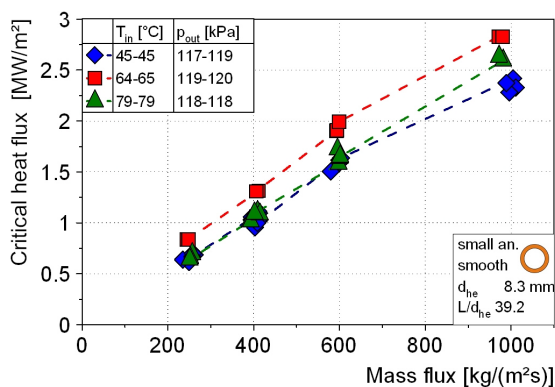


Figure 7.2.: All CHF-results at constant outlet pressure (110-121 kPa) for smooth tube in small annulus

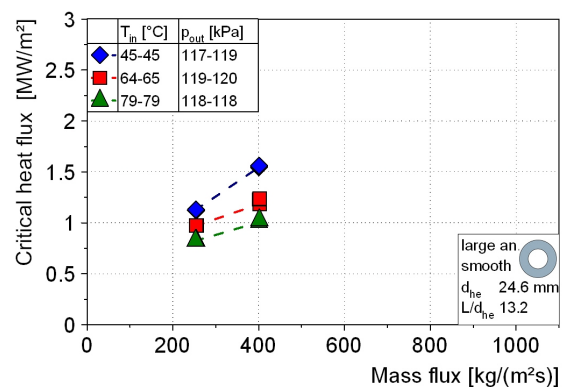


Figure 7.3.: All CHF-results at constant outlet pressure (117-120 kPa) for smooth tube in large annulus

The CHF results for the small annulus are in a similar range as those for the larger annulus. According to Eqn. (2.5) a smaller mass flow rate is necessary for the small annulus to reach the same mass flux as for the

large annulus because of the smaller cross section. Nevertheless, the CHF-values for both annuli are close for the applied conditions. This behavior is also obvious in Fig 7.1.

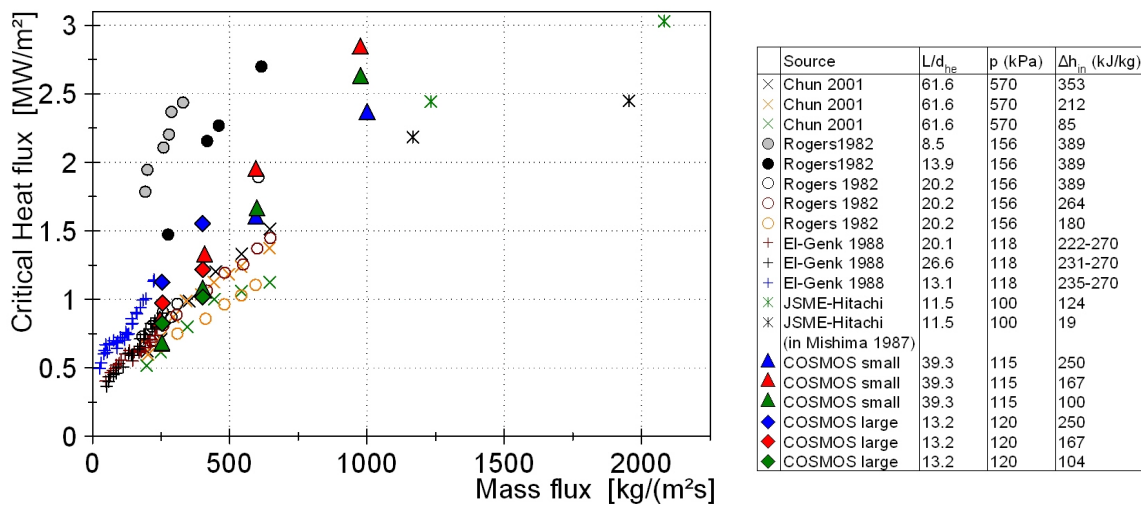


Figure 7.4.: Comparison of CHF results with literature data

An increase in CHF with mass flux is generally reported in literature. This behavior is similar to CHF in tubes [30]. For instance, *Rogers et al.* [85], *Chun et al.* [25] and *El-Genk et al.* [33] measured the CHF in dependency of mass flux for flow boiling in annular geometries at low pressures. Figure 7.4 puts the measured values of the present work in correlation to their CHF data. A direct comparison between the values is not possible because of differences in test section sizes (length to heated equivalent diameter ratio  $L/d_{he}$ ) as well as in the experimental parameters. Nevertheless, the own measured data are in accordance with the tendencies and the value region of the literature data.

### 7.1.2. Reproducibility of Measurements

Each CHF experiment is conducted for a parameter set of inlet temperature, mass flux, inlet throttling, and outlet pressure. These parameters are defined prior to the operation and are kept constant during the power increase until the CHF occurs. Particularly the outlet pressure has to be adjusted permanently with increasing heat input.

Figure 7.5 shows the CHF-results for eleven individual measurements at the same parameter set of mass flux at  $400 \text{ kg}/(\text{m}^2\text{s})$ , inlet temperature at  $45 \text{ }^\circ\text{C}$ , and outlet pressure at  $115 \text{ kPa}$ . The variation ranges of the parameters at CHF for the different measurements are  $45.0 - 46.2 \text{ }^\circ\text{C}$ ,  $111 - 119 \text{ kPa}$ , and  $395 - 413 \text{ kg}/(\text{m}^2\text{s})$  for inlet temperature, outlet pressure, and mass flux, respectively. The measured critical heat fluxes are between  $0.96$  and  $1.12 \text{ MW}/\text{m}^2$  with an arithmetic mean value of  $1.05 \text{ MW}/\text{m}^2$  depicted with a green square symbol in Fig. 7.5.

In the presented case the standard deviation in heat flux is  $0.04 \text{ MW}/\text{m}^2$  and the maximum deviation from the mean is  $0.09 \text{ MW}/\text{m}^2$ . These deviations are also quite representative for other parameter sets. Considering all conducted experiments the standard deviation is  $0.06 \text{ MW}/\text{m}^2$  and the maximum deviation is  $0.1 \text{ MW}/\text{m}^2$ . In summary, the measurement repetitions are well adjustable and reproducible in the deviation ranges given in Tab. 7.4.



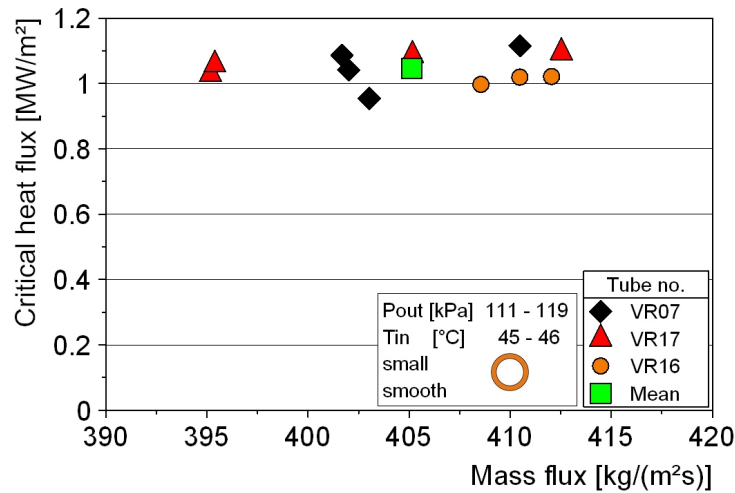


Figure 7.5.: CHF measurements for different tubes at the same parameter set

Table 7.4.: Deviations of experimental parameters for all conducted experiments

Parameter	Symbol	Std. deviation	Max. deviation
Mass flux	$G$	$\pm 5 \text{ kg}/(\text{m}^2\text{s})$	$\pm 15 \text{ kg}/(\text{m}^2\text{s})$
Inlet temperature	$T_{in}$	$\pm 0.4 \text{ K}$	$\pm 1 \text{ K}$
Outlet pressure	$p_{out}$	$\pm 5 \text{ kPa}$	$\pm 10 \text{ kPa}$
Critical heat flux	$\dot{q}_{CHF}$	$\pm 0.06 \text{ MW}/\text{m}^2$	$\pm 0.1 \text{ MW}/\text{m}^2$

The measurements in Fig 7.5 have been conducted using three different tubes of the technically smooth surface. The data points for each tube (called VR07, VR17, and VR16) are indicated in Fig 7.5 with different symbols showing that the CHF-values are similar. Thus, the experiments were reproducible for different tubes of the same surface condition. Furthermore, the experiments were conducted by two operators and at different dates and day times.

### 7.1.3. Location of Critical Heat Flux Occurrence

The axial CHF location is important for the consideration of local conditions at CHF as well as for the temperature rise detection for the safety shut off. A variation in the axial CHF position was a challenge during the experiments with the small annular geometry. Figure 7.6 shows the axial positions of the CHF occurrence for the small annulus in the left diagram. The y-axis refers to the heated length of the inner zircaloy tube. The heat input into the upward fluid flow begins at  $y = 0 \text{ mm}$  and ends at  $y = L_{heat} = 326 \text{ mm}$ . The locations of CHF detection are shown in dependency of mass flux for the three inlet temperatures at an outlet pressure of 115 kPa. Obviously, the locations are distributed for all mass fluxes in the upper half of the heated length between 150 and 326 mm. The distribution appears to be randomly without any schematic order. In other words, there exist several possible axial locations of CHF occurrence for the same parameter set of mass flux, inlet temperature, and outlet pressure.

The critical heat flux detection was defined if one of the measured temperatures rises about 10-15 K above the actual surface temperature. The measurement module is inserted into the inner tube of the annulus for detecting the temperature jump as described in chapter 4.3.1. The module consists of five to six measuring heads each pressing two thermocouples against the inner tube wall.

## 7. Critical Heat Flux Measurements with Smooth Tube

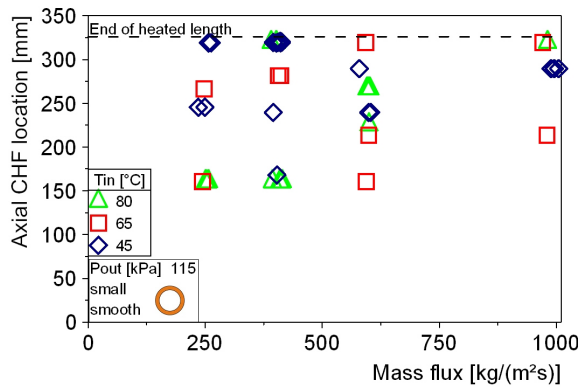


Figure 7.6.: Axial position of CHF detection in dependency of mass flux and inlet temperature for outlet pressure of 115 kPa

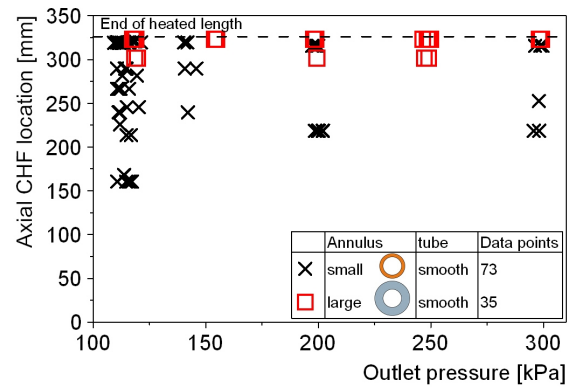


Figure 7.7.: Axial CHF position for all measurements of smooth tube in small (73 data points) and large (35 data points) annulus

During the first experiments the module was mounted to have equidistant measuring positions of 70 mm along the tube axis. In consequence of the observed variation in CHF location the measuring positions had to be changed to prevent damage of the tube and the measurement module. Therefore, five measurement heads were positioned in the upper half of the tube with distances of about 30-40 mm and one measurement head was positioned near the beginning of heated length. A typical positioning of the measuring heads was at 0, 160, 225, 265, 295, and 320 mm of the heated length. Nevertheless, the variation of the CHF location remained a difficulty.

The CHF is initiated at small local spot on the tube surface for the experimental parameters and test section geometry of these investigations. The surface temperature rises at this location due to the drastically reduced heat transfer by the vapor covering the dried out patch. The CHF location covers only a small section of the heated perimeter at the axial CHF position. Figure 7.8 shows a smooth test tube after several experiments in the small annular test section with typical oxidized CHF positions distributed in the upper half. In summary, the temperature rise begins at a small spot which can vary in the axial and azimuthal position on the heated surface even for the same parameter set.

If the CHF occurs between the axial or azimuthal thermocouple positions, then the hot spot expands until it reaches the next thermocouple and the heating is shut off. The temperature of the hot zone reached values leading to surface oxidation. Thus, the surface showed tempering colors from blue to black at this location. In some high-speed videos glowing could be observed at the hot spot. The time span from glowing to rewetted surface conditions at zero heating power was within approximately 500 ms. The temperature rising rate at the detecting thermocouple could achieve 300-400 K/s or even more.

The expansion of the hot zone before reaching a detecting thermocouple endangered the tube. On the one hand, the surface is oxidized at the CHF patch and the tube can bend due to the thermo-mechanical impact. On the other hand, the high temperature can damage the measurement module inside the tube, particularly the measuring heads of PEEK. Furthermore, the glowing of the material has to be avoided for the tubes with surface structures, particularly the porous structures. Due to the thermal influence the surface structure at the CHF location could be changed. Thus, a further application of the tube for comparable measurements is excluded because of the modified surface conditions.

The extremely localized CHF is consistent with observation of *Fiori and Bergles* [36] for CHF in internally heated vertical annulus at low pressure. Since they did not have installed a burnout protection system

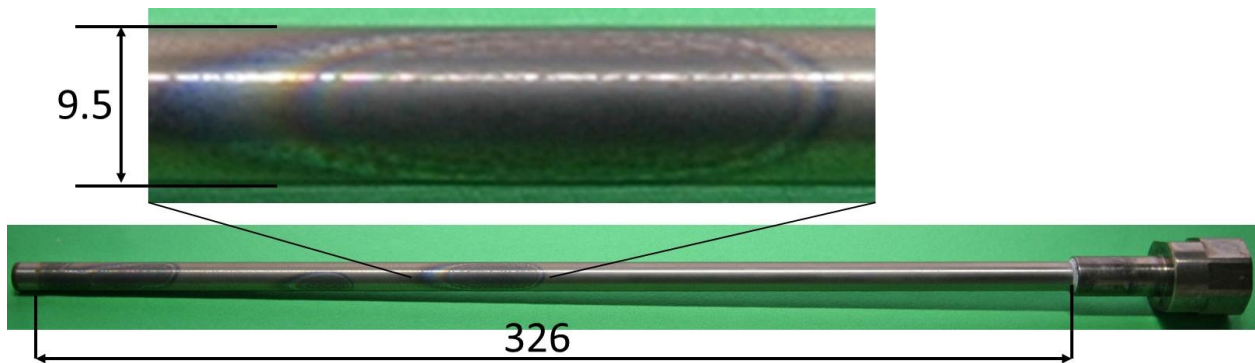


Figure 7.8.: Test tube used in experiments with small annulus showing visible oxidized CHF locations distributed in the upper half

the individual CHF experiments ended in failure of the test section due to CHF. They observed glowing at a local hot patch which then expanded rapidly (1-2 seconds) over the entire circumference and melted the metal. Furthermore, they noticed very small pin-holes in the burnout area. The zircaloy surface showed also small oxidized dots on the surface after intensive boiling. These small spots are assumed to refer to nucleation sites where the surface is temporarily dried out under the bubble during the periodic bubble growth and departure cycle.

*El-Genk et al.* [33] and *Rogers et al.* [85] used larger annular geometries for their investigations of flow boiling in vertical annuli near atmospheric pressure. The authors of both works reported that the CHF occurred always at the top end of the heated section. Therefore, the test section assembly was modified in order to install an outer tube with a greater inner diameter of 18 mm instead of 13 mm. This size was chosen for having a  $L/d_{he}$ -ratio of 13.2 comparable to an annular configuration of *Rogers et al.* [85] with  $L/d_{he} = 13.9$ .

The right diagram in Fig. 7.7 illustrates the comparison of the CHF-locations between the large and the small annulus for all measurements conducted with the smooth tube. The axial CHF locations are plotted against the applied outlet pressure. The cross symbols indicate the locations of 73 individual measurements for the small annulus and the square symbols indicate 35 data points for the large annulus. It is evident that the CHF was detected always on the top end of the heated section for the large annulus, whereas the data points of small annulus are distributed in the upper half as described above.

*Schoesse et al.* [90] observed a CHF location distribution using an annular gap of 6 mm which is even greater than the large annulus of the present work. However, their test section was about three times longer with a heated section of 1000 mm. *Schoesse et al.* identified flow pattern transitions from bubble flow to churn/pulsated annular flow to annular flow over the heated length. For the higher mass fluxes of their investigation about  $280 \text{ kg}/(\text{m}^2\text{s})$  and higher inlet subcoolings ( $\Delta T_{sub} > 25 \text{ K}$ ) the CHF location occurred near the top end of the heated section in churn or pulsated annular flow. With decreasing subcooling the transition point of churn/pulsated annular flow to stable annular flow is shifted to lower axial positions. The CHF could occur either in the lower axial region of churn/pulsated annular flow or in the stable annular flow region at the top of the heated length. This behavior is similar to the observation of CHF occurrence in the small annulus of the present work.

The void fraction is an important factor for the flow pattern development in the annular channel. Considering Eqn. (2.11) the exit vapor quality increases either with increase in length or decrease in gap size

while remaining constant mass flux, heat flux and inlet subcooling. The  $L/d_{he}$ -ratio of 26 of *Schoesse et al.* is between the large annulus  $L/d_{he}=13.9$  and the small annulus  $L/d_{he}=39.2$  of the present work. Thus, increasing the heated length for the present large annulus could lead to a distribution in CHF-position as observed for the small annulus or in the work of *Schoesse et al.* [90].

#### 7.1.4. Influence of Inlet Subcooling

Decreasing the inlet temperature leads to an increased inlet subcooling and affects that more energy is required to heat the fluid up to saturation temperature for evaporation. The CHF experiments were conducted applying three different inlet temperatures 45, 65, and 80 °C for each mass flux at constant outlet pressure of 120 kPa. Table 7.5 contains the resulting inlet subcooling conditions calculated by Eqn. (2.9) as described in chapter 2.1.3.

Table 7.5.: Inlet subcooling conditions for the three different inlet temperatures at 120 kPa

$p_{out}$ kPa	$T_{in}$ °C	$T_{sat}$ °C	$\Delta T_{sub}$ K	$h_{l,in}$ kJ/kg	$h'_{out}$ kJ/kg	$\Delta h_{in}$ kJ/kg
120	45	104,8	59,8	189	439	250
120	65	104,8	39,8	272	439	167
120	80	104,8	24,8	335	439	104

Figures 7.9 and 7.10 illustrate the influence of subcooling on critical heat flux for the small and large annulus, respectively. The CHF-values are plotted against the inlet temperatures for the different applied mass fluxes. The CHF-values of the large annulus in Fig. 7.10 are continuously increasing with decreasing inlet temperature. The gradient for the higher mass flux of 400 kg/(m<sup>2</sup>s) is slightly steeper than the one of 250 kg/(m<sup>2</sup>s). The CHF-results for the small annulus show a different behavior in Fig. 7.9. A maximum can be observed at the medium subcooled condition at  $T_{in} = 65$  °C. This dependency on the inlet temperature is similar for all measured mass fluxes.

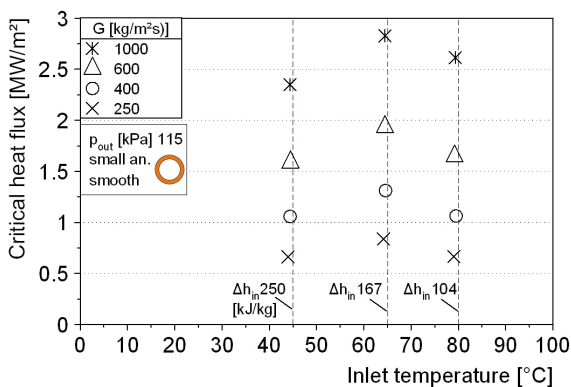


Figure 7.9.: CHF against inlet temperature at 115 kPa for smooth tube in small annulus

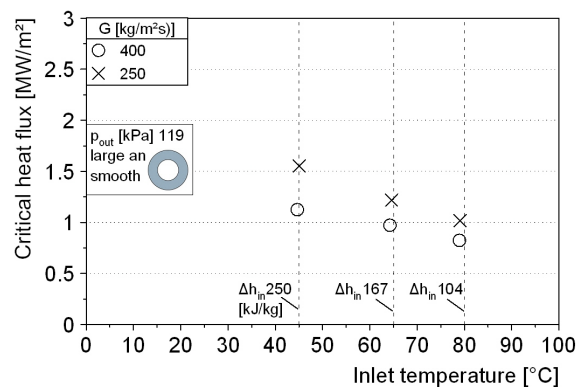


Figure 7.10.: CHF against inlet temperature at 119 kPa for smooth tube in large annulus

Having investigated similar gap sizes and  $L/d_{he}$ -ratios as the larger annulus of the present work *Rogers et al.*[85] reported a similar behavior for their measurements of mass fluxes between 180 and 650 kg/(m<sup>2</sup>s) as described for the larger annulus. Increased subcooling led to increased CHF values and the effect is more

significant for the higher mass fluxes. They observed a diminishing effect of subcooling for the low mass fluxes around  $200 \text{ kg}/(\text{m}^2\text{s})$  meaning that the CHF-values become similar for all subcooling conditions at the same mass flux.

*Schoesse et al.* [90] observed almost constant CHF values with increasing inlet temperature followed by an increase in CHF near saturation conditions at the inlet for a mass flux of  $270 \text{ kg}/(\text{m}^2\text{s})$ . Lower mass fluxes ( $50\text{-}110 \text{ kg}/(\text{m}^2\text{s})$ ) showed almost constant values for all inlet subcoolings.

With decreasing subcooling less heat flux is necessary for vapor generation which has an decreasing effect on the critical heat flux. On the other hand, an increased vapor content reduces the mixture density and accelerates the two-phase flow in the channel which leads to an increasing effect on the CHF. *Fiori and Bergles* report that the critical heat flux is not continuously decreasing with decreasing subcooling, particularly at low pressures and low mass fluxes because of a higher throughput velocity resulting from increased void fraction. Instead, the CHF curves become flat and can even increase with decreasing subcooling at low subcoolings. The flow in the small annulus is more affected by increased velocity since the vapor mass quality at CHF is higher than for the large annulus as will be shown in the next section. The combination of both opposed effects could lead to the behavior observed for the small annulus in Fig. 7.9.

#### 7.1.5. Influence of Vapor Mass Quality

The inlet subcooling condition described in the previous section is one of the important parameters which can be adjusted and kept constant during the experiment. Regarding Eqn. (2.11) clarifies that a variation in inlet subcooling affects the vapor mass quality, and therefore the void fraction, for constant heat flux, mass flux, pressure and geometry. Instead of the inlet conditions (subcooling) the local conditions (void or vapor quality) at CHF are often considered when comparing or correlating the CHF. However, in the practical application the local conditions depend on the inlet conditions and the channel geometry.

The relationship between critical heat flux and thermodynamic vapor mass quality is shown in Fig. 7.11. The mean values of exit thermodynamic vapor quality are plotted for both annuli, small and large, in the same diagram. Generally the vapor mass qualities at CHF are smaller for the large annulus than the ones for the small annulus. The CHF-values for the large annulus are in the negative and very low vapor quality region between  $-0.02$  and  $0.03$ . The curves of both mass fluxes are overlapping and have the same decreasing trend. The values for the small annulus are at higher exit qualities between  $0.05$  and  $0.16$ . The critical heat flux is first constant with increasing vapor quality and even increases for qualities about  $0.15$  or higher. The curves for each inlet mass flux are clearly separated.

Considering the exit vapor quality allows to compare the general conditions between the measurements in these specific test section geometries of small and large annulus. The vapor quality referred to the CHF-position is important for describing the local conditions at CHF. In case of the large annulus the exit quality equals the quality at CHF because the CHF occurred always at the end of the heated section. Using the small annulus the CHF-location could vary in axial position as depicted in Fig. 7.6 in section 7.1.3.

Figure. 7.12 illustrates the vapor quality calculated by inserting in Eqn. (2.11) the heated length of the particular CHF position. The data points are indicated with different symbols corresponding to the three inlet temperatures and they are framed additionally for each mass flux. Compared to the CHF versus exit vapor quality plot in Fig. 7.11 the CHF values are more distributed in range of vapor quality between  $0.02$  to  $0.15$  in Fig. 7.12. Nevertheless, the almost constant relationship between CHF and vapor quality for each mass flux remains similar.

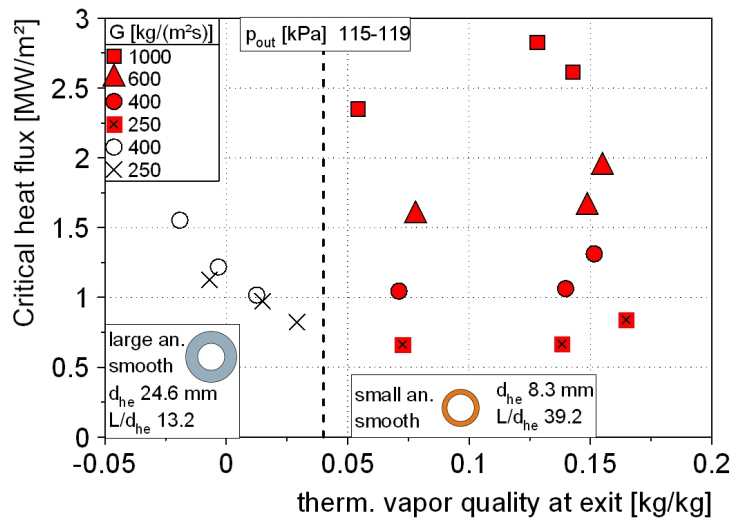


Figure 7.11.: CHF against exit vapor mass quality for small and large annulus at 115-119 kPa

Like it is described in chapter 7.1.3, the CHF location refers to the position of the thermocouple detecting the temperature jump. However, the initial occurrence point can be located between the axial measurement positions. Consequently, the calculated value at the position of detection can differ from the vapor quality at the CHF origin. A variation in CHF position of  $\pm 20$  mm leads to a deviation in vapor mass quality of  $\pm 0.013$  as indicated with error bars in Fig. 7.12.

The liquid temperature, measured at the exit, was always identical to saturation conditions at CHF for the small annulus. Therefore, the thermodynamic quality values are all in the positive region. In contrast, the liquid temperature could be still below the saturation temperature in some cases for the large annulus indicated by negative thermodynamic vapor qualities in Fig. 7.11. As described in chapter 2.1.3 it is assumed for calculating the thermodynamic vapor quality with Eqn. (2.10) that the liquid and the vapor phase are in thermodynamic equilibrium state.

More realistic vapor quality values result by taking the measured liquid outlet temperatures  $T_{l,out}$  into account. The vapor quality is calculated with Eqn. 2.7 remaining the liquid enthalpy at the outlet as a function of outlet temperature and pressure  $h_{l,2} = h_{l,out}(p_{out}, T_{l,out})$ . Note, for  $T_{l,out} = T_{sat}$  the resulting vapor mass quality is the thermodynamic vapor mass quality. The CHF versus vapor mass quality calculated with the measured outlet temperatures is shown in Fig. 7.13. The resulting vapor mass qualities are all in the positive quality region even for the cases with subcooled liquid temperatures at the exit. However, the vapor qualities are very small with values of approximately  $x = 0.001$  for the former negative qualities.

Doerffer *et al.* [30] investigated the difference between CHF in tube and annular geometries. Therefore, they collected experimental CHF data from literature for CHF in internally heated annuli. However, the data cover only the high pressure range between 980 and 14100 kPa. The region of CHF values in dependency of thermodynamic vapor mass quality for the data collection of Doerffer *et al.* [30] is illustrated in Fig. 7.14. Furthermore, 292 data points for CHF in annuli at low pressure conditions from 100 to 600 kPa are plotted with x-symbols. The CHF values are from the present work and from literature of Fiori and Bergles [36], JSME data ( $T_{in} 70^\circ\text{C}$ ) in Mishima *et al.* [75], El-Genk *et al.* [33], and Chun *et al.* [25].

Characteristic curves for CHF in a 8mm tube from the 2006 CHF look-up-table (LUT) of Greoneveld *et al.* [41] are exemplary plotted for a mass flux of 300 kg/(m²s) and three different pressures of 100, 1000, and 10000 kPa. The curves show the typical trend of decreasing CHF values in the low quality region and a

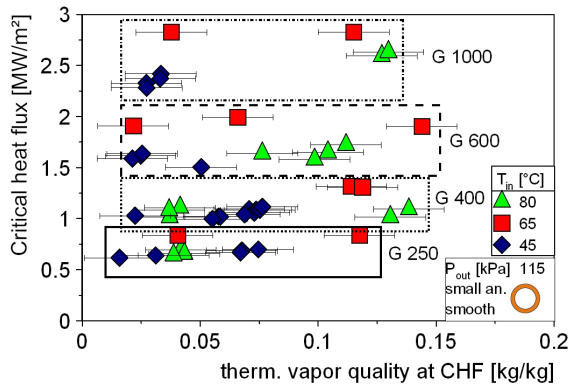


Figure 7.12.: CHF against vapor quality at CHF for smooth tube in small annulus at outlet pressure of 115 kPa

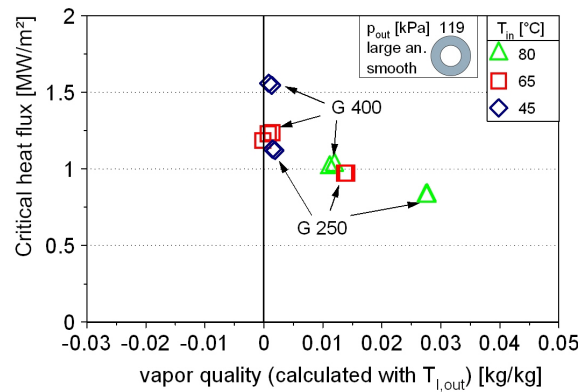


Figure 7.13.: CHF against vapor quality calculated with measured outlet temperature  $T_{l,out}$  for smooth tube in large annulus at 119 kPa

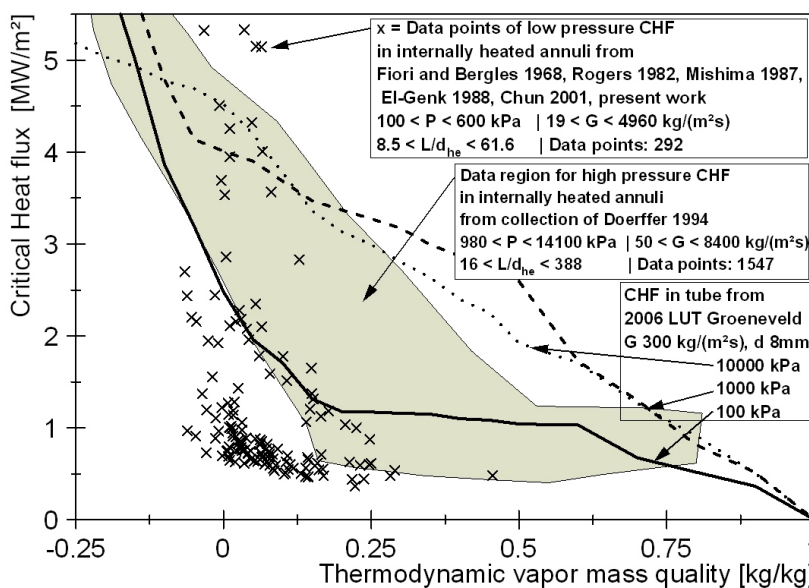


Figure 7.14.: Comparison of low pressure (100-600 kPa) and high pressure (980-14100 kPa) CHF behavior for internally heated annuli

decrease in slope or even constant values with further increasing vapor mass quality. It is noteworthy that the characteristic CHF versus vapor quality curve is strictly valid for fixed conditions of mass flux, pressure, and characteristic geometry size. Nevertheless, the regions of the annuli data demonstrate the same tendencies although corresponding to wide ranges of these parameters. Comparing the CHF in annuli with the CHF in a 8 mm tube at similar conditions *Doerffer et al.* [30] reports a generally lower CHF for the annular geometry. They observed a greater difference in CHF value for positive than for negative vapor mass qualities.

Both pressure regions for CHF in annuli have a similar shape but the low pressure region is shifted to lower vapor mass qualities. This behavior is also noticeable for the characteristic curves for CHF in the tube. Furthermore, the CHF curve of 100 kPa changes in the small positive vapor quality region from a decreasing trend to almost constant CHF values. This tendency corresponds to the behavior of decreasing CHF for the large annulus in the negative and very low vapor quality region and almost constant CHF for the small annulus for higher vapor qualities in Fig. 7.11.

The pressure effect on the void fraction is assumed to be one of the influencing parameters for the shift of the CHF region to lower vapor mass qualities. The vapor volume fills a larger fraction of the tube or channel cross section for lower pressures than for higher pressures at similar vapor mass qualities because of a drastic increase in density ratio between liquid and vapor with decreasing pressure, particularly for pressures  $<1000$  kPa (see Fig. 2.8). This effect is discussed in the next section.

### 7.1.6. Influence of Void Fraction

The flow pattern development across the channel length and the mechanisms leading to critical heat flux are affected by the void fraction in the channel. The void fraction expresses the relative vapor area in the flow cross section and is a function of vapor mass quality, density ratio and slip velocity ratio according to Eqn. (2.16) in section 2.1. The density ratio depends on the fluid and the pressure. Thus, the void fraction is also affected by pressure. The dependency of void fraction on vapor mass quality and pressure is shown for an assumed slip velocity ratio of  $S=1$  in Fig. 7.15 and  $S=10$  in Fig. 7.16.  $S=1$  means that the vapor and the liquid phases have the same velocity (Eqn. (2.15)). For  $S=10$  the vapor phase flows ten times faster than the liquid phase.

Figure 7.15 demonstrates that the void fraction increases rapidly in the low quality range. The slope becomes steeper with decreasing pressure. The reason of high void fractions even at low vapor mass quality for low pressures is the high density difference between liquid and vapor for water at low pressure. As shown in Fig. 2.8 in chapter 2.6 the density ratio ( $\rho'/\rho''$ ) of saturated liquid ( $\rho'$ ) and vapor ( $\rho''$ ) decreases significantly from 1600 to 170 between 100 and 1000 kPa.

The second influencing parameter in Eqn. (2.16) is the slip velocity ratio. Increasing vapor velocity causes decreasing void fraction. Therefore, the void values at the same vapor quality are lower for  $S=10$  in Fig. 7.16 than for  $S=1$  in Fig. 7.15. Moreover, the increase in slip ratio has a stronger decreasing effect on the higher pressure than on the lower pressure curves.

The calculated local void fractions at CHF for the present measurements are additionally plotted in Fig. 7.15 and 7.16. The vapor mass quality values at CHF used for the void calculation of the large annulus are the ones calculated with the measured outlet temperature as explained in the previous section for Fig. 7.13. Due to the low pressure condition the void values are rather high even for very low mass qualities. The void fraction for the CHF values of the large annulus are in the steeply increasing part of the curve with values between 0.30 and 0.98 for  $S=1$  and between 0.08 and 0.81 for  $S=10$ . The void fraction values for the small annulus data are all very high in the range from 0.97 to 0.99 for  $S=1$  and from 0.80 to 0.95 for  $S=10$ . The real void fractions could not be measured for the experiments of the present work.

*Evangelisti and Lupoli* [35] investigated the void fraction for flow boiling of water in an internally heated vertical annulus at atmospheric pressure. The inner and outer diameter of the annulus were 7 and 15 mm and the heated length was 500 mm. The void fraction was measured by a gamma-ray densitometer. They calculated the slip velocity ratio by inserting the measured void fraction and the calculated thermodynamic vapor quality into Eqn. (2.14) for values of the positive thermodynamic quality region. The slip ratio increases from 5 to 15 with vapor mass qualities from 0.01 to 0.04 for a mass flux of  $600 \text{ kg}/(\text{m}^2\text{s})$  and a heat flux of  $0.63 \text{ MW}/\text{m}^2$ . An increase in mass flux to  $1416 \text{ kg}/(\text{m}^2\text{s})$  affected a slight increase in slip ratio. In the negative thermodynamic quality region they assumed a slip velocity ratio of  $S=2-4$ . The results of *Evangelisti and Lupoli* demonstrate that the exemplary taken slip ratio of  $S=10$  in Fig. 7.16 is in a realistic range.



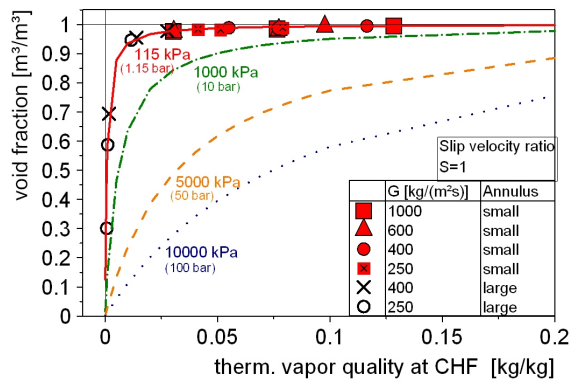


Figure 7.15.: Void fraction against mass quality for slip velocity ratio  $S=1$  for smooth tube in small and large annulus

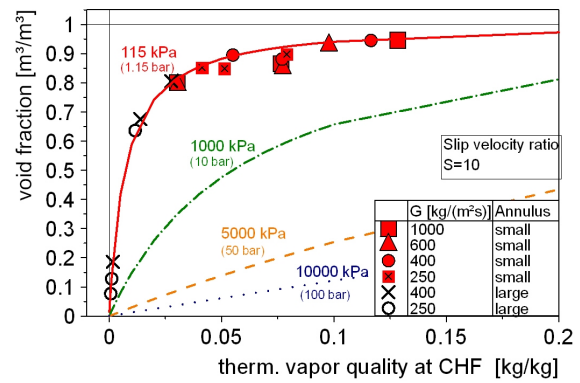


Figure 7.16.: Void fraction against mass quality for slip velocity ratio  $S=10$  for smooth tube in small and large annulus

Nevertheless, it is important to note that this slip ratio is only used for showing the qualitative influence of the slip ratio on the void fraction without any measured or calculated background.

At local zero thermodynamic vapor quality *Evangelisti and Lupoli* [35] measured a void fraction of about 0.65 for the mentioned conditions ( $600 \text{ kg}/(\text{m}^2\text{s})$  and  $0.63 \text{ MW}/\text{m}^2$ ) for flow boiling conditions below critical heat flux. *Rogers et al.* [85] measured the void fraction by a gamma-ray densitometer at CHF for flow boiling in internally heated annular test sections at low pressure. Detailed measurement results are missing, however they mentioned high void fractions at CHF, up to 0.8, even for subcooled conditions at the test section exit.

In summary, high void fractions are characteristically for flow boiling and CHF in annuli at low pressure even for low or negative thermodynamic vapor mass qualities due to the influence of pressure on the density ratio. This phenomenon influences the CHF versus vapor mass quality curve as shown in Fig 7.14 and makes the system sensitive to flow instabilities as explained in chapter 6 by causing a high pressure drop as will be shown in the following.

### 7.1.7. Pressure Drop Behavior

The two-phase pressure drop increases with increasing vapor content. The low density of vapor reduces the mixture density causing an acceleration of the flow according to Eqn. (2.5). The characteristic two-phase pressure drop behavior of a boiling channel is explained in chapter 2.3.

Fig. 7.17 shows the pressure drop across the test section as a function of heat input for different mass fluxes at a fixed outlet pressure of 115 kPa. The diagrams on top and the bottom left one depict the pressure drop in the small annulus each for a different inlet temperature of 45, 65, and  $80^\circ\text{C}$ , respectively. The pressure drop for the flow in the small annulus is highly affected by the boiling process.

At zero heat input we have single phase liquid pressure drop. With increasing heat input the boiling process is intensified leading to a parabolic behavior of the curves. With decreasing mass flux the onset of boiling is shifted to lower power input. Thus, the two-phase pressure drop for low mass fluxes increases already at lower heat inputs than for higher mass fluxes. However, this effect decreases with increasing inlet temperature. The pressure drop behavior for the highest inlet temperature of  $80^\circ\text{C}$  is independent of the applied inlet mass fluxes. The pressure drop curves become generally steeper with increasing inlet temperature.

## 7. Critical Heat Flux Measurements with Smooth Tube

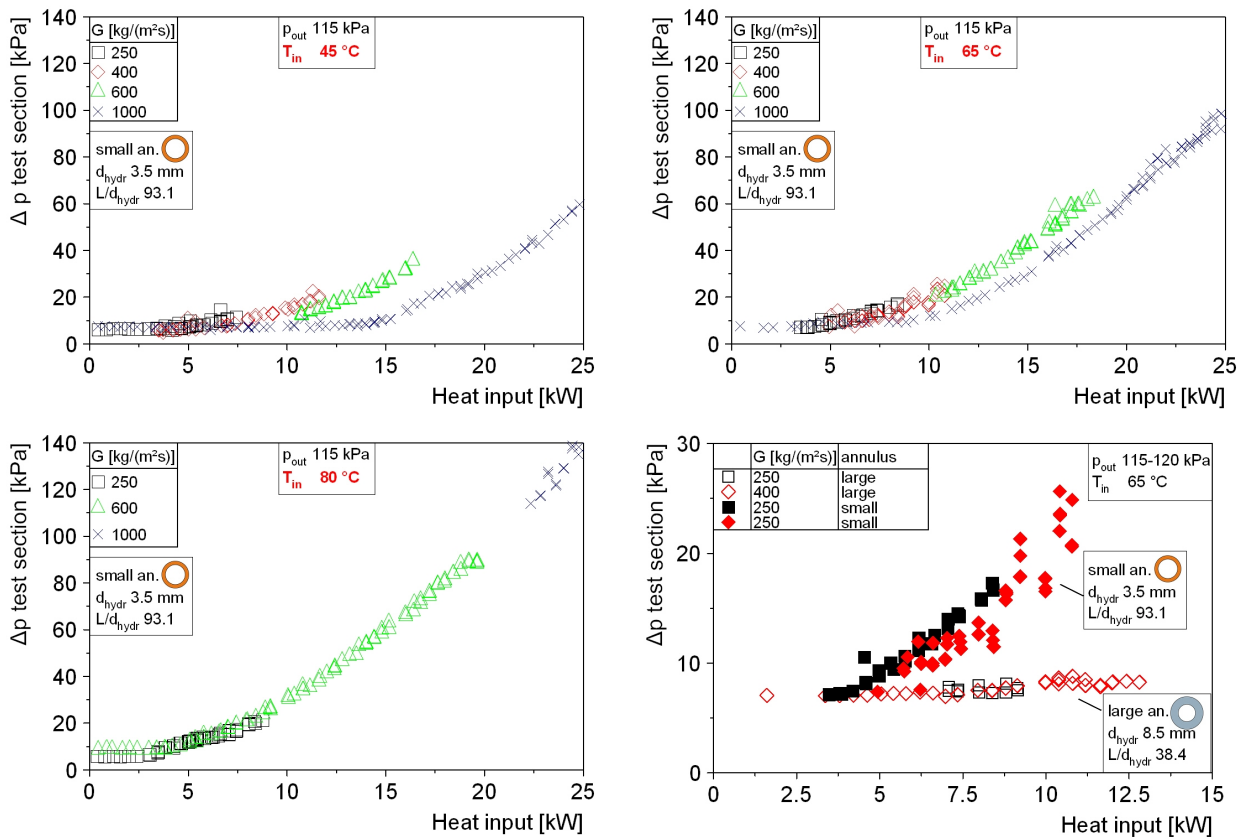


Figure 7.17.: Pressure drop across test section against heat input for smooth tube. *top left, top right and bottom left:* Small annulus at outlet pressure 115 kPa and inlet temperatures of 45, 65, and 80 °C, respectively; *Bottom-right:* Small and large annulus at outlet pressure 115 kPa and inlet temperature of 65 °C

The diagram bottom right in Fig. 7.17 compares the two-phase pressure drop between the small and the large annulus for mass fluxes of 250 and 400 kg/(m<sup>2</sup>s) at an inlet temperature of 65 °C and an outlet pressure of 115 kPa. In contrast to the small annulus, the heat input effect on the pressure drop is only small for the large annulus in the observed range of mass flux and heat input.

As described in chapter 2.3 the two-phase pressure drop consists of three components: frictional, gravitational and acceleration pressure drop. Considering Eqn. (2.11) shows that a smaller heated equivalent diameter leads to higher vapor mass quality at same heat input. Therefore, the void in the small channel is already higher at same heat flux leading to an increased two-phase pressure drop. Furthermore, the small annular gap has an increased frictional pressure drop compared to the large annulus for the same flow velocity. Inserting the hydraulic diameter for an annulus Eqn. (2.2) into Eqn. (2.19) gives a proportional relationship of frictional pressure drop to  $\frac{1}{d_{hydr}} = \frac{1}{d_o - d_i}$ . Thus, a smaller gap size causes a higher frictional pressure drop.

The combination of higher void at same heat flux and increased frictional pressure drop due to the gap size explains why the pressure drop in the small annulus is significantly higher than in the large annulus.

### 7.1.8. Influence of Outlet Pressure

The system pressure affects the fluid properties. For instance, the density ratio between liquid and vapor is strongly affected by pressure variation in the low pressure range (Fig. 2.8). This effect causes decreasing void fraction with increasing pressure at same vapor mass quality as described in section 7.1.6. Other properties like viscosity or surface tension are also stronger influenced by lower pressures than by higher

pressures. Furthermore, increasing pressure leads to increased saturation temperature and a decrease in enthalpy of evaporation.

Therefore, experiments were performed for different outlet pressures in order to determine the pressure influence on CHF in the narrow low pressure range between 115 and 300 kPa. The pressure effect on CHF for a particular test section geometry can be systematically investigated by conducting experiments for various outlet pressures, but keeping constant the mass flux and inlet subcooling conditions. Consequently, the inlet temperature has to be adapted for each outlet pressure in order to adjust a constant inlet subcooling enthalpy difference according to Eqn. (2.9).

Figure 7.18 illustrates the outlet pressure influence on the CHF for the smooth tube in the small annulus. The measurements were made for mass fluxes of 400 and 1000 kg/(m<sup>2</sup>s) at outlet pressures of 115, 200, and 300 kPa and a constant subcooling of  $\Delta h_{in}=250$  kJ/kg.

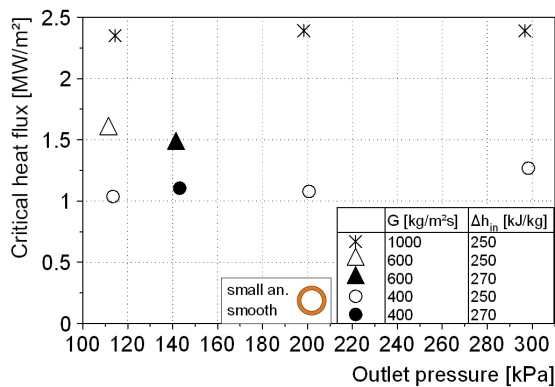


Figure 7.18.: CHF against outlet pressure at subcooling of 250-270 kJ/kg for smooth tube in small annulus

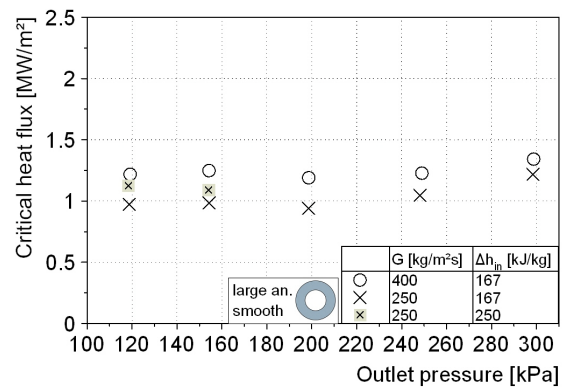


Figure 7.19.: CHF against outlet pressure at subcooling of 167 and 250 kJ/kg for smooth tube in large annulus

The CHF-results for the mass flux of 1000 kg/(m<sup>2</sup>s) show similar values of about 2.34 MW/m<sup>2</sup> for the measured outlet pressures between 115 and 300 kPa. The results for 400 kg/(m<sup>2</sup>s) are in the identical range of about 1.1 MW/m<sup>2</sup> for the pressures of 115 and 200 kPa. The CHF at 300 kPa shows an increasing tendency with a value of 1.27 MW/m<sup>2</sup>. Additional measurement points for the mass fluxes of 400 and 600 kg/(m<sup>2</sup>s) at an outlet pressure of 140 kPa and a subcooling of 270 kJ/kg are also plotted in Fig. 7.18. They show the same trend of unnoticeable pressure influence in the low pressure region.

The outlet pressure influence on the CHF for the large annulus is shown in Fig 7.19. The measurements were conducted for mass fluxes of 250 and 400 kg/(m<sup>2</sup>s) at outlet pressures of 115, 150, 200, 250, and 300 kPa and constant subcooling of 167 kJ/kg. The pressure influence on the CHF-values is similar to the behavior in the small annulus. There is insignificant variation of the CHF for outlet pressures between 115 and 200 kPa and a trend of increasing CHF between 200 and 300 kPa. Two additional measurement points for the same higher subcooling of 250 kJ/kg as in the small annulus at a mass flux of 250 kg/(m<sup>2</sup>s) and outlet pressures of 115 and 150 kPa confirm the invariable trend of CHF for low pressures.

In summary, a similar influence of outlet pressure on the CHF was observed for different mass fluxes and inlet subcoolings for both annuli. The CHF-values are almost constant for outlet pressures between 115 and 200 kPa and show an increase in the range between 200 and 300 kPa. Due to the observed pressure behavior,

the CHF experiments with surface structured tubes were also performed for various outlet pressures at constant inlet conditions referring to the measurements shown in Fig 7.19.

Most literature data for CHF in internally heated annuli at low pressure were conducted for only one fixed pressure. A systematical comparison between the data considering the pressure influence was not possible because of differences in the other variables of mass flux, inlet subcooling and geometry. *Chun et al.* [25] investigated the pressure influence on CHF systematically over a wide pressure range. However, the lowest pressure of 570 kPa is already higher than the considered range of 115-300 kPa of the present work. For mass fluxes of 500-650 kg/(m<sup>2</sup>s) they report a rapid CHF increases with pressure followed by a maximum in the pressure range of 2000-3000 kPa and a decrease with further pressure increase up to 15010 kPa. The rapid increase in the low pressure region was not observed or only small for lower mass fluxes 200-500 kg/(m<sup>2</sup>s).

## 7.2. Comparison of Smooth Tube Results with Literature Data

Experimental data for critical heat flux in annuli at low pressure conditions are scarce in literature. Moreover, the available data mostly differ in various experimental parameters making it difficult to compare the results systematically. Important variables for comparing different experimental conditions are test section geometry, inlet subcooling, mass flux, outlet pressure, fluid, surface material and surface structure. No suitable literature data was found for a direct comparison with the CHF results for the small annulus. With the necessary change to a larger annulus, the geometry was selected in order to provide comparable conditions to experiments of *Rogers et al.* [85].

The experimental parameters of inlet subcooling, outlet pressure and mass flux are in the similar range as shown in Tab. 7.6. *Rogers et al.* [85] conducted CHF experiments for three different inlet subcooling conditions at a constant outlet pressure of 156 kPa. As shown in section 7.1.8 the CHF is independent of the outlet pressure between 120 and 150 kPa. Thus, the CHF-values between the present work (COSMOS) and *Rogers et al.* [85] can be compared without considering a pressure effect.

Table 7.6.: Comparison of experimental conditions between *Rogers et al.* [85] and present work (COSMOS)

General conditions			Experimental parameters				
	COSMOS	Rogers et al	COSMOS		Comp.	Rogers	
Test section	Annulus	Annulus	$P_{out}$	kPa	120	≈	156
Heated part	Internally	Internally	G	kg/(m <sup>2</sup> s)	250, 400	=	180-600
Inner tube	Zircaloy	Inconel	$\Delta h_{in}$	kJ/kg		>	389
Outer tube	Glass	Glass			250	≈	265
Fluid	Water	Water			167	≈	180
					104	<	

*Rogers et al.* [85] performed CHF measurements for water using three different annuli. The diameter of the inner tube remained at 13.1 mm while the outer diameter was varied between 22, 25, and 30.2 mm. The heated length of 480 mm is factor 1.5 longer as the zircaloy tube in the present work. Table 7.7 contains the geometry details and the comparison between the test sections of *Rogers et al.* [85] and the large annulus of COSMOS. The smallest annulus (TS no.1) of *Rogers et al.* [85] is similar in heated equivalent diameter  $d_{he}$  and hydraulic diameter  $d_{hydr}$ . The medium annulus (TS no.2) is larger in the characteristic diameters, but has a comparable  $L/d_{he}$ -ratio. The largest annulus (TS no.3) differs in all geometry characteristics.

Table 7.7.: Comparison of geometry sizes between test sections of *Rogers et al.* [85] and present work (COSMOS)

Geometry	$d_i$	$d_o$	$s$	$d_{hydr}$	$d_{he}$	$d_o/d_i$	L	$L/d_{hydr}$	$L/d_{he}$
	mm	mm	mm	mm	mm		mm		
COSMOS small an.	9.5	13	1.75	3.5	8.3	1.37	326	93.1	39.2
COSMOS large an.	9.5	18.0	4.25	8.5	24.6	1.89	326	38.4	13.2
Rogers no. 1	13.1	22.0	4.45	8.9	23.9	1.68	480	53.9	20.2
Comp. with large an.	>	>	=	=	=	<	>	>	>
Rogers no. 2	13.1	25.0	5.95	11.9	34.6	1.91	480	40.3	13.9
Comp. with large an.	>	>	>	>	>	=	>	=	=
Rogers no. 3	13.1	30.2	8.55	17.1	56.5	2.31	480	28.1	8.5
Comp. with large an.	>	>	>	>	>	>	>	<	<

*Rogers et al.* [85] developed empirical correlations for each test section characterized by  $L/d_{he}$ . The least-square correlations describe their CHF-results as a function of mass flux, inlet subcooling and empirical coefficients of the form given in Eqn. (7.1)

$$\dot{q}_{CHF} = C_1 - C_2 G + (C_3 G - C_4) \frac{\Delta h_{in}}{\Delta h_v} \quad (7.1)$$

with  $G$  in  $[\text{kg}/(\text{m}^2\text{s})]$  and  $\dot{q}_{CHF}$  in  $[\text{W}/\text{cm}^2]$ . The empirical coefficients and the parameter range for the correlations are listed in Tab. 7.8

Table 7.8.: Empirical coefficients and parameter range for correlation of *Rogers et al.* [85] in Eqn. (7.1)

Coefficients for correlation						Parameter range		
no.	$L/d_{he}$	$C_1$	$C_2$	$C_3$	$C_4$	$P_{out}$	$G$	$\Delta h_{in}/h_v$
1	20.2	63.61	0.0329	1.781	279.7	$\approx 160 \text{ kPa}$	$\leq 650 \text{ kg}/(\text{m}^2\text{s})$	$\leq 0.175$
2	13.9	74.86	0.0329	2.251	112.5	$180 \leq$	$0.081 \leq$	$= 8.5, 13.9, 20.2$
3	8.5	92.06	0.203	3.894	-6.567			

Figure 7.20 shows the comparison of the measured CHF values of the present work with the experimental data for test section no. 2 of *Rogers et al.* [85]. The CHF values are plotted against mass flux for each inlet subcooling condition. In this case the ratio of heated length to heated equivalent diameter is similar for both test sections with  $(L/d_{he})_{Rogers} = 13.9$  and  $(L/d_{he})_{Cosmos} = 13.2$ . Since *Rogers et al.* presented in [85] only the measured values for the highest inlet subcooling, the experimental results for the other conditions were reproduced by applying their correlation (Eqn. (7.1)). These values are denoted in the legend with (Corr=Exp). The given rms-error of the predicted CHF values is below 5% for each correlation.

Figure 7.20 demonstrates that the experimental values of both works are matching very well. On the one hand, the values at similar experimental inlet subcooling conditions of both works at 250-265 kJ/kg and 167-180 kJ/kg are almost identical. And on the other hand, the influence of subcooling and mass flux is complemented reasonably by the higher subcooling of 389 kJ/kg of *Rogers et al.* [85] and the lower subcooling of 104 kJ/kg of COSMOS. Furthermore, the CHF for the lowest subcooling condition of COSMOS is also predicted correctly by the empirical correlation of *Rogers et al.* [85]. This subcooling ( $\Delta h_{in}=104 \text{ kJ}/\text{kg}$  at 120 kPa:  $h_{in}/h_v=0.048$ ) is below the parameter range for which the correlation was developed, see Tab. 7.8. Thus, the reliability of the own measured values is confirmed by this comparison of similar experimental conditions and same  $L/d_{he}$  ratio.

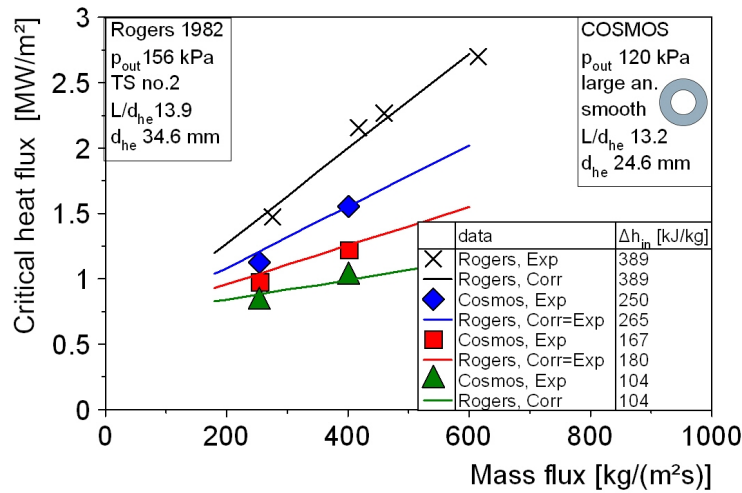


Figure 7.20.: Comparison of measured values with experimental data of *Rogers et al.*[85] for similar  $L/d_{he}$  of 13.9 (Rogers) and 13.2 (COSMOS)

The importance of the  $L/d_{he}$  ratio for the comparison of CHF-data in different test section geometries becomes more clearly if the relationship between thermodynamic vapor mass vapor quality  $x_{th}$  and heat flux  $\dot{q}$  in Eqn. (2.11) is considered:  $x_{th} \propto \dot{q}L/d_{he}$  for the same parameter set of inlet subcooling  $\Delta h_{in}$ , mass flux  $G$  and outlet pressure  $p_{out}$  ( $h_v(p_{out})$ ). In other words, the similar CHF-values of COSMOS and *Rogers et al.* [85] mean that  $x_{th}$  was also similar at the CHF location at the exit because of the same experimental conditions and test sections with similar  $L/d_{he}$ .

For CHF in tubes, it is known that the influence of  $L/d_{he}$  diminishes for longer tubes. It is important to note that for tubes the different characteristic length to diameter ratios are identical:  $\left(\frac{L}{d_{he}} = \frac{L}{d_{hydr}} = \frac{L}{d}\right)_{tube}$  since  $(d_{he} = d_{hydr} = d)_{tube}$ . For instance, *Bergles* [12] investigated the length to diameter effect for CHF in small tube diameter of 2.4 mm at low pressure of 200 kPa. The CHF decreased with increasing  $L$  for  $L/d < 35$  and became almost constant for  $L/d > 35$ . *Groeneveld et al.* [42] account for the  $L/d$  effect with a correction factor for  $L/d \leq 80$  in their CHF look-up-table.

Figure 7.21 compares the COSMOS results with the measured CHF data for the test section no. 1 of *Rogers et al* [85]. As shown in Tab. 7.7 the test section geometries are similar in heated equivalent diameter, however, the heated length of *Rogers et al.* [85] is factor 1.5 longer. Considering the comparable inlet subcoolings of 250-265 kJ/kg and 167-180 kJ/kg, the CHF values of COSMOS are noticeably higher than ones of *Rogers et al* [85]. This comparison shows that the CHF decreases with increasing length at the same  $d_{he}$  which is similar to the effect described above for short tubes in the investigations of *Bergles* [12]. Thus, the CHF for this annular size depends on the length in this range of  $L/d_{he}$ .

The influence of  $L/d_{he}$  is also obvious in Fig. 7.22 showing the CHF results for the different annular geometries of *Rogers et al.* [85] and the present work at similar inlet subcooling conditions of  $\Delta h_{in} = 250$ -265 kJ/kg. As mentioned above, the CHF decreases with increasing  $L/d_{he}$ . However, this trend apparently changes in the range of  $L/d_{he}=20.2$ . The CHF-values for the small annulus of the COSMOS experiments with  $L/d_{he}=39.2$  are similar to the values of *Rogers et al.* [85] with  $L/d_{he}=20.2$ . Moreover, the  $L/d_{he}$  influence seems to be independent of mass flux. The observed behavior in Fig. 7.22 give rise to the assumption that for annuli at low pressure the  $L/d_{he}$  effect becomes insignificant for ratios around  $L/d_{he}=20.2$ . However, this should be confirmed by further data of various  $L/d_{he}$  at constant conditions of  $G$ ,  $p_{out}$ , and  $\Delta h_{in}$ .

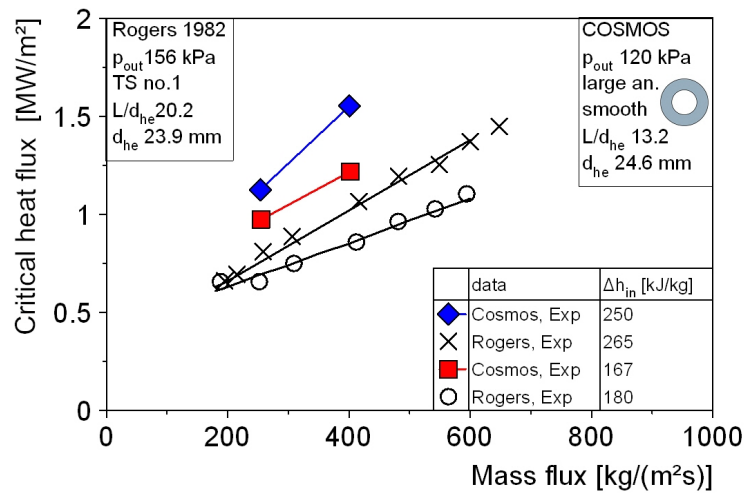


Figure 7.21.: Comparison of CHF measurements between COSMOS and Rogers for similar  $d_{he}$  but different  $L/d_{he}$

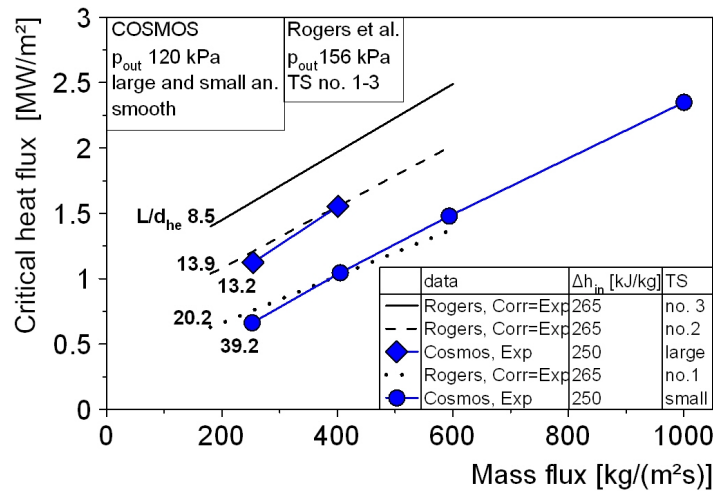


Figure 7.22.: Influence of  $L/d_{he}$  variation on CHF for constant inlet sub-cooling condition of 250-265 kJ/kg

### 7.3. Comparison of Smooth Tube Results with Prediction Methods from Literature

The experimental results of the smooth tube in the large annulus at 120 kPa were compared with different correlations from literature. In a first step the recommended calculation instructions given by the VDI-Wärmeatlas [94] (Hbc) have been examined. Four separate regions depending on system pressure and mass flux are considered in VDI-Wärmeatlas. Correlations of *Doroshchuk et al.* [31] or *Kon'kov* [61] are recommended for the high pressure - high mass flux region (2900-20000 kPa (29-200 bar) and 500-5000 kg/(m<sup>2</sup>s)). In the high pressure - low mass flux region (2900-20000 kPa and 0-500 kg/(m<sup>2</sup>s)) the correlation of *Katto and Ohno* [55] should be applied. This correlation is also the choice for both mass flux regions in the low pressure region (100-2900 kPa (1-29 bar)). The 1995 CHF look-up table of *Groeneveld et al.* [40] is additionally recommended for the low pressure - low mass flux region (100-2900 kPa and 0-500 kg/(m<sup>2</sup>s)).

These correlations are valid for vertical tubes with upward flow. In case of an annular flow cross section,

the VDI-Wärmeatlas distinguishes in [94] (Hbc,2.2) between three types of heat input: a) heating of the outer tube, b) heating of the inner tube, c) heating of both tubes. The authors recommend to use the outer diameter  $d_o$  of the annulus for the calculation independent of externally (a) or internally (b) heating conditions.

The experimental conditions of the present work correspond to the low pressure - low mass flux region (100-2900 kPa and 0-500 kg/(m<sup>2</sup>s)). Therefore, the CHF was calculated by applying the *Katto&Ohno* [55] correlation as well as the look-up tables of *Groeneveld et al* [42],[40],[41]. The calculation methods and the predicted results are presented in the following sections.

Furthermore, the CHF correlations of *Doerffer et al.* [30] were applied for predicting the CHF. These correlation methods base on the 1986 look-up table of *Groeneveld et al.* [42] and were developed for the particular case of internally heated annular geometries.

### 7.3.1. Correlation of Katto and Ohno

*Katto and Ohno* [55] developed a generalized correlation for CHF in vertical uniformly heated tubes for the application of various fluids. The basic equation for this correlation is given by

$$\dot{q}_{CHF} = \dot{q}_{CHF,sat} (1 - K_i x_{th,in}) \quad (7.2)$$

where  $\dot{q}_{CHF,sat}$  is the critical heat flux for saturated inlet conditions,  $x_{th,in} = (h_{l,in} - h')/\Delta h_v$  is the thermodynamic vapor quality at the inlet, which is negative for subcooled conditions, and  $K_i$  is a correlated subcooling parameter.

The CHF for saturated conditions is calculated according to the following relationship

$$\dot{q}_{CHF,sat} = \frac{\dot{q}_i^*}{G \Delta h_v} \quad (7.3)$$

The value of  $\dot{q}_i^*$  is given for five different cases in dependence of three dimensionless parameters  $\sigma^*$ ,  $l^*$ , and  $\rho^*$  which are defined as

$$\sigma^* = \frac{\sigma \rho_l}{G^2 L} \quad (7.4)$$

$$l^* = \frac{L}{d_{char}} \quad (7.5)$$

$$\rho^* = \frac{\rho_v}{\rho_l} \quad (7.6)$$

The five equations for  $\dot{q}_i^*$  are

$$\begin{aligned} \dot{q}_1^* &= C (\sigma^*)^{0.043} \frac{1}{l^*} \\ \dot{q}_2^* &= 0.1 (\rho^*)^{0.133} (\sigma^*)^{1/3} \frac{1}{1+0.0031l^*} \\ \dot{q}_3^* &= 0.098 (\rho^*)^{0.133} (\sigma^*)^{0.433} \frac{(l^*)^{0.27}}{1+0.0031l^*} \\ \dot{q}_4^* &= 0.234 (\rho^*)^{0.513} (\sigma^*)^{0.433} \frac{(l^*)^{0.27}}{1+0.0031l^*} \\ \dot{q}_5^* &= 0.0384 (\rho^*)^{0.6} (\sigma^*)^{0.173} \frac{1}{1+0.28(\sigma^*)^{0.233}l^*} \end{aligned}$$

The subcooling parameter  $K_i$  is also a function of the parameters  $\sigma^*$ ,  $l^*$ , and  $\rho^*$  and is calculated for three cases



$$K_1 = \frac{1.043}{4C(\sigma^*)^{0.043}}$$

$$K_2 = \frac{5}{6} \frac{0.0124 + 1/l^*}{(\rho^*)^{0.133} (\sigma^*)^{1/3}}$$

$$K_3 = 1.12 \frac{1.52(\sigma^*)^{0.233} + 1/l^*}{(\rho^*)^{0.6} (\sigma^*)^{0.173}}$$

The dimensionless parameter  $C$  in the equations of  $\dot{q}_1^*$  and  $K_1$  is

$$C = 0.25 \quad \left| \begin{array}{l} \text{for } l^* < 50 \\ \text{for } 50 \leq l^* \leq 50 \\ \text{for } l^* > 150 \end{array} \right.$$

$$C = 0.25 + 9 \cdot 10^{-4} (l^* - 50)$$

$$C = 0.34$$

The application of the above mentioned equations is separated by *Katto and Ohno* [55] into two different pressure regions which are represented by the density ratio of vapor and liquid. The first region is defined by  $\rho^* = \frac{\rho_v}{\rho_l} \leq 0.15$  and the second by  $\rho^* = \frac{\rho_v}{\rho_l} > 0.15$

$\rho^*$	$\dot{q}^*$	$K_i$
$\rho^* \leq 0.15$	$\dot{q}_1^* \leq \dot{q}_2^*$ : $\dot{q}^* = \dot{q}_1^*$ , $K_1 \geq K_2$ : $K_i = K_1$	
	$\dot{q}_1^* > \dot{q}_2^*$ and $\dot{q}_2^* \geq \dot{q}_3^*$ : $\dot{q}^* = \dot{q}_2^*$ , $K_1 < K_2$ : $K_i = K_2$	
	$\dot{q}_1^* > \dot{q}_2^*$ and $\dot{q}_2^* < \dot{q}_3^*$ : $\dot{q}^* = \dot{q}_3^*$	
$\rho^* > 0.15$	$\dot{q}_1^* \leq \dot{q}_4^*$ : $\dot{q}^* = \dot{q}_1^*$ , $K_1 \geq K_2$ : $K_i = K_1$	
	$\dot{q}_1^* > \dot{q}_4^*$ and $\dot{q}_4^* \geq \dot{q}_5^*$ : $\dot{q}^* = \dot{q}_4^*$ , $K_1 < K_2$ and $K_2 \leq K_3$ : $K_i = K_2$ ,	
	$\dot{q}_1^* > \dot{q}_4^*$ and $\dot{q}_4^* < \dot{q}_5^*$ : $\dot{q}^* = \dot{q}_5^*$ , $K_1 < K_2$ and $K_2 > K_3$ : $K_i = K_3$	

The *Katto&Ohno* [55] correlation was applied for the conditions of inlet subcoolings of 250, 167, and 104 kJ/kg, mass fluxes from 250 to 1000 kg/(m<sup>2</sup>s), and outlet pressure of 120 kPa. As recommended in *VDI-Wärmeatlas* [94] (Hbc,2.2) the outer diameter of the annulus ( $d_o=18$  mm for the large annulus) was inserted as  $d_{char}$  in Eqn. (7.5) for taking the internally heated annular geometry into account.

Figure 7.23 shows the calculated values for the *Katto&Ohno* [55] correlation in comparison with the measured CHF results. The correlation highly over-predicts the experimental CHF-results for the applied conditions. The calculated values are more than 500% higher than the measured values. Thus, the *Katto&Ohno* [55] correlation for tubes using the outer diameter of the annulus is inapplicable for this internally heated annular geometry at the present low pressure - low mass flux conditions. The same poor prediction resulted when using the highest pressure of the experiments of 300 kPa in the correlation.

### 7.3.2. Look-up Table for Critical Heat Flux

The CHF look-up table (LUT) is basically a normalized data bank predicting the CHF for a vertical 8 mm water-cooled tube as a function of pressure  $p$ , mass flux  $G$  and thermodynamic vapor mass quality  $x_{th}$ :

$$\dot{q}_{CHF,8}(d = 8mm, G, p, x_{th})$$

The first LUT version of *Groeneveld et al.* from 1986 [42] has been extended and improved with the up-dated versions of 1995 CHF look-up table [40] and 2006 CHF look-up table [41].

It is distinguished between two methods of applying the look-up-table [39]. The first method, called direct substitution method (DSM), is based on constant local conditions. The CHF for the point in question characterized by ( $x_{th}$ ,  $G$ ,  $p$ ) is found directly in the table for a tube diameter of 8 mm via interpolation. However, this method requires the knowledge of the thermodynamic quality at CHF. For instance, the DSM can be used to compare measured CHF data with the values of the look-up table.

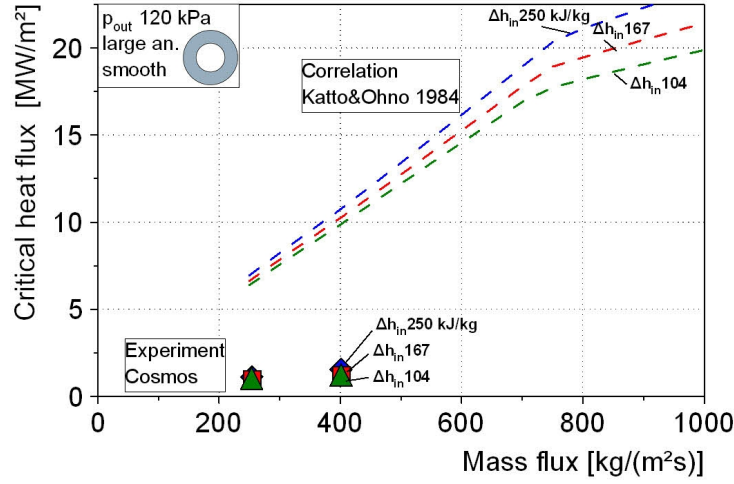


Figure 7.23.: Comparison of results for smooth tube in large annulus at 120 kPa with calculated values of the Katto&Ohno-correlation [55]

The second method of CHF prediction, called heat balance method (HBM), is based on constant inlet condition. The thermodynamic vapor quality and the corresponding CHF are calculated iteratively. With this method it is possible to predict the CHF for given geometry and system conditions.

The CHF value from the LUT for the specific case of 8 mm tube diameter is corrected by factors in order to apply the method for other geometries and conditions. These correction factors are listed in LUT1986 [42] or more recently in [43]. The annular geometry is taken into account by factor  $f_1$  according to Eqn. (7.7) and using the heated equivalent diameter  $d_{he}$  in [mm] as proposed by *Groeneveld et al.* [42] and applied by *Park et al.* [80], for instance. The exponent of  $-\frac{1}{2}$  is given in [41].

$$\dot{q}_{CHF,f1} = \dot{q}_{CHF,8} f_1 = \dot{q}_{CHF,8} \left( \frac{d_{he}}{8} \right)^{-\frac{1}{2}} \quad (7.7)$$

The effect of heated length is corrected by multiplying the CHF value with factor  $f_4$  of [42] given in Eqn. (7.8)

$$\dot{q}_{CHF,f4} = \dot{q}_{CHF,8} f_4 = \dot{q}_{CHF,8} \exp \left( \frac{d_{hydr}}{L} \exp(2\varepsilon_{hom}) \right) \quad (7.8)$$

for  $5 \leq \frac{L}{d_{hydr}} \leq 80$  and with the homogeneous void fraction  $\varepsilon_{hom}$  according to Eqn. (2.16) with  $S=1$ .

In summary, the critical heat flux with corrections for diameter and length effects is calculated by

$$\dot{q}_{CHF} = \dot{q}_{CHF,8} f_1 f_4 \quad (7.9)$$

Figure 7.24 shows the resulting curves and the different correction steps for the DSM evaluation using the LUT2006 [41]. The critical heat flux is plotted against the thermodynamic vapor quality. The length correction factor  $f_4$  in Eqn.(7.8) depends on the void fraction in order to include a diminishing length effect for low qualities approaching  $x_{th}=0$  [43, 42]. The factor is constant for subcooled conditions ( $x_{th} \leq 0$ ) because of inserted zero void fraction. In case of low pressures the void fraction increases drastically in the range of very low vapor qualities because of the high density difference between vapor and liquid. This effect causes the step in the corrected curve with  $f_4$  at zero quality in Fig. 7.24.

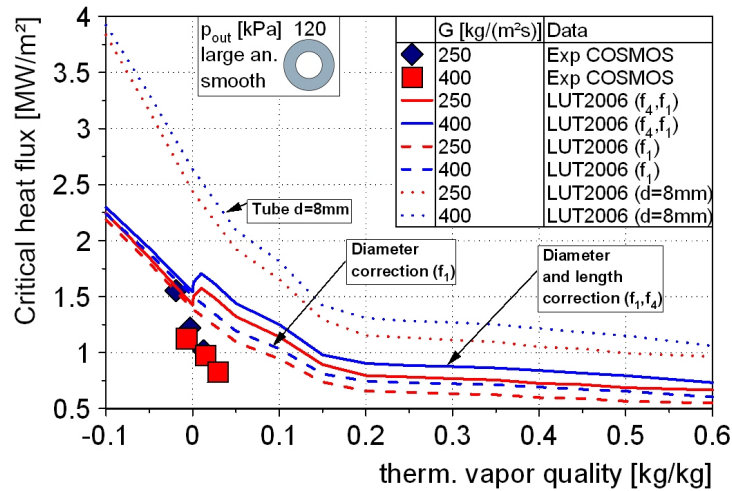


Figure 7.24.: Comparison of experimental data and results from look-up tables of *Groeneveld et al.* from 2006 [41] using direct substitution method and correction factors for diameter and length effects

Table 7.9.: Comparison of experimental data and results from look-up tables of *Groeneveld et al.* from 1986 [42], 1995 [40], and 2006 [41] using the direct substitution method

G	$T_{in}$	Experiment		LUT1986		LUT1995		LUT2006	
		$x_{th}$	$\dot{q}_{exp}$	$\dot{q}_{LUT}$	$\frac{\Delta\dot{q}}{\dot{q}_{exp}}$	$\dot{q}_{LUT}$	$\frac{\Delta\dot{q}}{\dot{q}_{exp}}$	$\dot{q}_{LUT}$	$\frac{\Delta\dot{q}}{\dot{q}_{exp}}$
kg/(m²s)	°C	kg/kg	kW/m²	kW/m²	%	kW/m²	%	kW/m²	%
250	45	-0.007	1125	1746	55	1603	42	1486	32
	65	0.015	973	1906	96	1590	63	1553	60
	80	0.029	824	1910	132	1409	71	1466	78
400	45	-0.019	1553	2233	44	1927	24	1694	9
	65	-0.003	1218	1993	64	1813	49	1570	29
	80	0.012	1017	2241	120	1884	85	1696	67

In contrast, the experimental values covering the range around zero quality are continuously decreasing with increasing quality. Nevertheless, a length effect on the CHF has to be accounted as it is discussed in the comparison with the measured values of *Rogers et al.* [85] in section 7.2. Except of the described step, the predicted curves and the measured values show a qualitatively similar decreasing tendency with increasing vapor quality. However, the calculated curves are shifted to higher vapor quality.

Table 7.9 compares the experimental results and the DSM values from the different CHF look-up tables of *Groeneveld et al.* from 1986 [42], 1995 [40], and 2006 [41]. LUT1986 gives the worse prediction with 44 to 132% higher values than the experimental results. The LUT2006 shows the best performance, but is still over-predicting the CHF of 29 to 78% with an exception of 9% at  $G=400$  kg/(m²s) and  $x_{th}=-0.019$  because of the change in the predicted curve due to the length correction, see Fig. 7.24.

The calculation instruction for predicting the critical heat flux with the heat balance method is explained in the following.

- The first step is to calculate a starting vapor mass quality  $x_{th,i}$  by inserting an estimated heat flux into Eqn. (2.10).

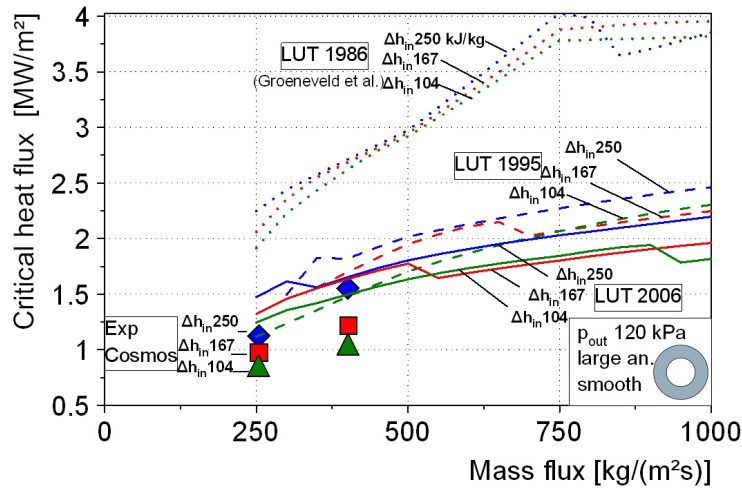


Figure 7.25.: Comparison of experimental data and results from look-up tables of *Groeneveld et al.* from 1986 [42], 1995 [40], and 2006 [41] using the heat balance method

- Then the CHF for a 8 mm tube is evaluated from the LUT by 3-dimensional interpolation in direction of  $G$ ,  $x_{th,i}$ , and  $p$ .
- For accounting the annular geometry the value is corrected by factor  $f_1$  according to Eqn. (7.7).
- The effect of heated length is considered by factor  $f_4$  from Eqn. (7.8).
- The quality for the next step  $x_{th,i+1}$  is now calculated with Eqn. (2.10) inserting the actual predicted CHF value and the procedure is repeated.
- This evaluation is conducted iteratively until the CHF value converges.

The 3-dimensional interpolation and iteration of the look-up table was programmed in Matlab and calculated for the large annulus geometry and the conditions of inlet subcoolings of 250, 167, and 104 kJ/kg, mass fluxes from 250 to 1000 kg/(m<sup>2</sup>s), and an outlet pressure of 120 kPa.

The results for the different LUTs of *Groeneveld et al.* from 1986 [42], 1995 [40], and 2006 [41] using the heat balance method (HBM) are shown in Fig. 7.25. The steps in the individual curves are caused by factor  $f_4$  when the conditions change from negative to positive thermodynamic vapor quality as it was described above. The calculated CHF values for the LUT1986 are significantly higher than the experimental results with increased values of about 45 to 118%. The LUT1995 and LUT2006 fit remarkably better to the experimental values compared with the LUT1986 prediction. However, the calculated values were still about 31-51% higher, with an exception of 6% for LUT2006 at  $G=400$  kg/(m<sup>2</sup>s) and  $\Delta h_{in}=250$  kJ/kg because of the length correction step at that point. Generally, the calculated HBM results fit slightly better to the measured values than the DSM results as it was also reported by *Park et al.* [79].

An improved performance of LUT1995 compared with LUT1986 especially for the low pressure and low flow region was also shown by *Chun et al.* [25]. Furthermore, *Groeneveld et al.* [41] reported in the discussion of the LUT2006 accuracy that high errors were primarily found at pressures less than 250 kPa and mass fluxes less than 750 kg/(m<sup>2</sup>s). The authors attributed the very large scatter among the experimental data in the low pressure - low flow region to possible flow instabilities at these conditions. Moreover, only scarce data were available in this parameter region.

### 7.3.3. Doerffer Correlations for Annuli

*Doerffer et al.* [30] developed prediction methods for internally heated annuli based on the 1986 CHF look-up table of *Groeneveld et al.* [42]. Using 1547 CHF data points for internally heated annuli, the authors compared the annuli effects to the CHF in tubes and found out that vapor mass quality, gap size and pressure had the strongest influence. However, the considered CHF data for annuli from the works of *Barnett et al.* [6], [7], *Becker et al.* [8], [9], *Janssen and Kervinen* [48], and *Ahmad and Groeneveld* [2] refer to a higher pressure range of 980 to 14100 kPa (9.8-141 bar). The comparison of *Doerffer et al.* [30] between the CHF for tube and annular geometries is described in section 3.1.

The authors proposed two different correlations for predicting the CHF for internally heated annuli. The first correlation uses three independent factors for correcting the predicted CHF for a 8 mm tube. The second correlation is developed from a rod-centered approach regarding the difference in vapor mass quality between annuli and tubes at CHF. Both correlations and the predicted results are explained in the following.

#### Doerffer Correlation using Correction Factors

The 3-k-factors correlation of *Doerffer et al.* [30] for CHF in internally heated annuli is given by Eqn. (7.10)

$$\dot{q}_{CHF} = \dot{q}_{CHF,8} k_x k_s k_p \quad (7.10)$$

The critical heat flux  $\dot{q}_{CHF,8}$  is the predicted CHF for a tube with 8 mm inner diameter using a LUT. The skeleton look-up table for the development of this correlation was the LUT1986 of *Groeneveld et al.* [42]. The three independent correction factors account for the influences of vapor quality, gap size and pressure on the CHF in annuli.

$k_x$  considers the quality effect with

$$\begin{array}{l|l} x_{th} \leq 0.025 & k_x = 0.81 \\ x_{th} > 0.025 & k_x = 0.859 - 16.179 x_{th}^{1.5} + 15.6 x_{th}^2 - 7.195 x_{th}^2 \ln(x_{th}) \end{array}$$

$k_s$  considers the gap effect with  $s = (d_o - d_i)/2$  in [mm]:

$$\begin{array}{l|l} s < 4.26 & k_s = 0.2872 + 1.209 s^2 - 1.156 s^{2.5} + 0.2873 s^3 \\ 4.26 \leq s \leq 6.27 & k_s = 1.2672 - 0.0298 s \\ 6.27 < s \leq 8.26 & k_s = 0.6663 + 64.374 \exp\left(-\frac{s}{1.242}\right) \\ s > 8.26 & k_s = 0.75 \end{array}$$

$k_p$  considers the pressure effect with p in [MPa]:

$$\begin{array}{l|l} p < 3.30 & k_p = 0.9 \\ 3.3 \leq p \leq 10.5 & k_p = 0.808 + 0.0278 p \\ p > 10.5 & k_p = 1.1 \end{array}$$

The evaluation procedure is the same as for the heat balance method described in section 7.3.2. The CHF for a 8 mm tube is interpolated from the LUT by inserting  $x_{th}$ , G, and p. This value is adapted to annular conditions by multiplying it with the corresponding correction factors according to Eqn. (7.10). The thermodynamic vapor mass quality for the next step is calculated with the resulting CHF value and the procedure is repeated iteratively until reaching a converged result.

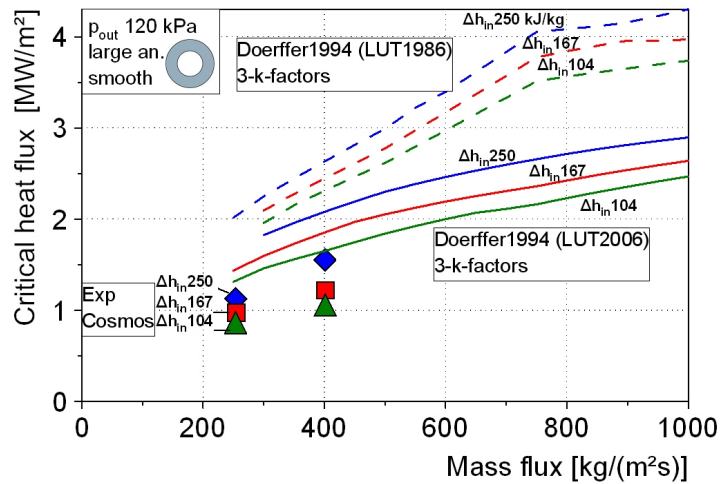


Figure 7.26.: Comparison of results for smooth tube in large annulus at 120 kPa with calculated values of 3-k-factor correlation Eqn. (7.10) of *Doerffer et al.* [30] using LUT1986 and LUT2006

Figure 7.27 shows the comparison between the experimental results of the smooth tube in the large annulus at 120 kPa and the calculated curves with the 3-k-factors correlation using the LUT1986 [42] and LUT2006 [41]. Some values for low mass fluxes are missing in Fig. 7.27 because the iteration was not converging for these specific conditions.

The LUT1986 gives higher over-predicted CHF values than the LUT2006 for this low pressure conditions as it was already shown for the prediction with the look-up tables in Fig. 7.25. The correlated curves using the LUT2006 agree qualitatively with the experimental tendencies, however, the values are 34 to 62% higher than the experimental results which is also similar to the LUT prediction in Fig. 7.25. This similar behavior is not surprising since the values are correlated on base of the different LUTs. In contrast to the LUT prediction curves in Fig. 7.25 the curves of the 3-k-factors correlation of *Doerffer et al.* [30] are continuously increasing. A length effect is not considered in this correlation.

*Park et al.* [79] compared CHF data for internally heated annuli in the low pressure - low mass flux region (100-1000 kPa and 0-500 kg/(m<sup>2</sup>s)) with a correlation of *Bobkov et al.* [14] and the 3-k-factors correlation of *Doerffer et al.* [30]. Both correlations showed unsatisfactory prediction capability for their data in this range.

### Doerffer Correlation using Rod-Centered Approach

*Doerffer et al.* [30] developed a second correlation using a rod-centered subchannel approach. The correlation is based on the observation, that the same CHF value occurs in tubes at higher vapor quality than in annular geometries. This behavior is confirmed in Fig. 7.24 with the shift of the predicted curves from the LUT for tubes to higher vapor qualities in comparison to the experimental annular CHF data. According to the authors the CHF in an internally heated annuli is controlled by phenomena occurring in the vicinity of the heated surface. Any imaginary boundary (with zero shear stress) between the heated inner tube and the unheated outer tube forms a rod-centered annular subchannel. The critical quality for this subchannel is higher than for the entire annular cross section. Consequently, *Doerffer et al.* [30] introduced an additional correlated term for the vapor quality to account for these effects. They assumed that the rod-centered subchannel vapor quality for the CHF in an annulus is

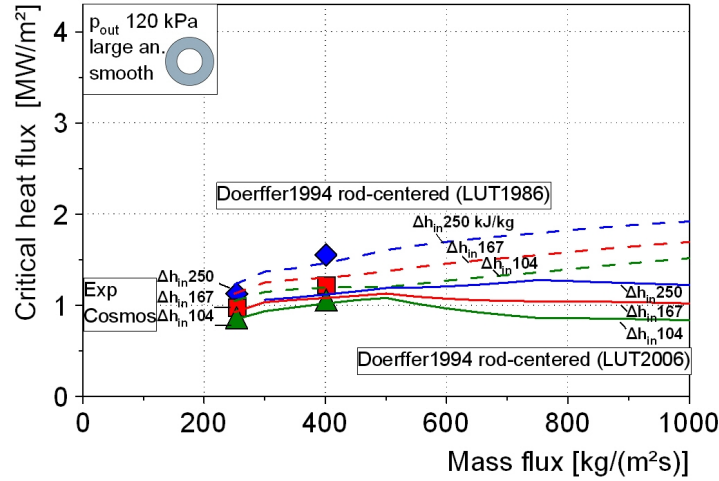


Figure 7.27.: Comparison of results for smooth tube in large annulus at 120 kPa with calculated values of rod-centered approach Eqn. (7.13) of *Doerffer et al.* [30] using LUT1986 [42] and LUT2006 [41]

$$x' = x_{th} + \Delta x' \quad (7.11)$$

where  $x_{th}$  is the thermodynamic vapor mass quality according to Eqn. (2.10) and the additional term  $\Delta x'$  is calculated by following empirical correlation

$$\Delta x' = 0.658 - 0.33 p^{0.428} G^{0.108} s^{-0.453} d_{he}^{0.37} + 0.208 \exp[-18.5(x_{th} - 0.35)^2] \quad (7.12)$$

where  $d_{he}$  is the heated equivalent diameter in [cm], pressure  $p$  in [MPa], mass flux  $G$  in [Mg/m<sup>2</sup>s] and the gap size of the annulus  $s$  in [mm].

The CHF is determined iteratively with the CHF look-up table for 8 mm diameter tubes applying the heat balance method, but the inserted quality is calculated with Eqns. (7.11) and (7.12).

$$\dot{q}_{CHF} = \dot{q}_{CHF,8}(p, G, x') \quad (7.13)$$

Figure 7.27 illustrates the calculated curves of the rod-centered correlation of *Doerffer et al.* [30] using the LUT1986 [42] and LUT2006 [41]. *Doerffer et al.* [30] used the LUT1986 of *Groeneveld et al.* [42] and high pressure CHF measurement data for annuli for correlating the additional vapor quality term in Eqn. (7.12). However, the low pressure behavior of LUT1986 [42] is unsatisfactory as shown for example in Fig. 7.25. Therefore, the good agreement of the rod-centered correlation using the LUT1986 [42] with the experimental data of the large annulus at the applied conditions is quite surprisingly. The relative deviation of the predicted values to the measured values are between -6% and 27%.

Using the improved table of 2006 [41] the calculated values match well with the experimental data for the lower subcoolings of 104 and 167 kJ/kg with relative deviations of -11% to 2%. The calculated CHF values for the higher subcooling of 250 kJ/kg are about -28% smaller.

On the other hand, the curves using the LUT2006 [41] show a decreasing tendency with increasing mass flux. The calculated vapor quality for CHF in annuli with Eqn. (7.11) was  $x' \approx 0.45 - 0.65$  for the complete range of inserted mass fluxes. The CHF curve from the LUT2006 [41] for constant quality of  $x=0.5$  at

constant pressure of 120 kPa gives decreasing CHF values for mass fluxes between 750 and 2500 kg/(m<sup>2</sup>s). Therefore, this behavior is also visible in the rod-centered correlation curves with LUT2006.

This trend is not expected with regard of the measurement results in Fig. 7.4 where the CHF values are still increasing for the higher mass fluxes. The calculated curves with the LUT1986 [42] fit better to the trends of subcooling and mass flux influences in Fig. 7.4. The data in the base table of LUT1986 have no decreasing tendency in the above considered parameter range.

This demonstrates on the one hand, that the behavior of an empirical correlation based on a data bank is not necessarily improved if the data is improved. On the other hand, the approach of predicting CHF for annuli by considering CHF for tubes at higher qualities might not be useful because of possible different characteristics between CHF in annuli at low qualities and CHF in tubes at high qualities.

Moreover, the calculated vapor quality with Eqns. (7.11) and (7.12) can reach values greater than unity for certain conditions. For instance, inserting  $p=0.12$  MPa,  $G=0.4$  Mg/(m<sup>2</sup>s),  $s=4.25$  mm,  $d_{he}=2.46$  cm and  $x_{th} > 0.25$  leads to  $x' > 1$ , and therefore  $\dot{q}_{CHF} = 0$ .

### 7.3.4. Summary of Prediction Methods Comparison

The experimental results of the large annulus measurements at 120 kPa were compared with the predicted results of the *Katto&Ohno* [55] correlation, look-up tables for tubes of *Groeneveld et al.* [42], [40], [41], and two different correlations for annuli of *Doerffer et al.* [30] based on the look-up table of *Groeneveld et al.* [42].

The recommended calculation instructions of *VDI-Wärmeatlas* [94] for applying the *Katto&Ohno* [55] correlation for internally heated annuli by using the outer diameter of the annulus led to more than 500% higher CHF values compared with the measured values. Thus, this prediction method seems to be inappropriate for the given conditions.

The look-up tables for tubes were applied by correcting the predicted tube CHF with a factor depending on the heated equivalent diameter  $d_{he}$  in order to account for the annular geometry. The calculated values with LUT1986 [42] were significantly higher (about 75 to 160%) than the measured results. The experimental data fit remarkably better to the predicted CHF using the updated versions LUT1995 [40] and LUT2006 [41], however, the calculated values were about 31-51% higher. The heat balance method gave slightly better results than the direct substitution method as it was also reported by *Park et al.* [79].

The 3-k-factors correlation of *Doerffer et al.* [30] multiplies the CHF for a 8 mm tube with three correction factors accounting for vapor quality, gap size and pressure effects on CHF in annuli. Since these factors were applied to the CHF values derived from the look-up tables of *Groeneveld et al.* the prediction characteristic were similar to the one of the LUTs described before.

In the rod-centered approach of *Doerffer et al.* [30], the vapor quality for CHF in annuli is expressed by an empirical correlation. The CHF value results from the look-up table for tubes by inserting the correlated vapor quality. The calculated values of the rod-centered correlation were in good agreement with the experimental data in the applied range of low pressure and low mass flux. The predicted CHF values were in a small error range between -6% and 27% using LUT1986 [42] and -28% and 2% using LUT2006 [41]. Thus, the measured results were best described by the rod-centered approach among the presented prediction methods for the applied experimental conditions. However, this correlation showed questionable tendencies in the calculated values regarding higher mass fluxes and higher vapor quality conditions.

An influence of the surface structure is missing in all of the presented prediction methods.



## 8. Critical Heat Flux Measurements with Surface Structured Tubes

The systematic measurement series for the surface structured tubes could only be started after ensuring safe operation conditions. Since the critical heat flux, as the value of interest, is also the upper limit of the system, each individual CHF measurement includes the risk of damaging the test section.

This chapter describes the CHF-results for all surface structured tubes in the large annulus in comparison with the smooth tube results. The experiences with the smooth tube in the small annulus excluded a safe operation. The main difficulty was the variation of the CHF location in the upper half of the heated tube, see section 7.1.3. If the CHF occurred between two temperature measurement positions the temperature jump could cause glowing at the hot spot. Consequently, the surface structure appearance could be changed at this location or the tube could be bend making the tube useless for further comparable measurements. The change to an outer tube with a greater inner diameter ensured an almost fix occurrence at the top end where a temperature measuring head was positioned.

As described in section 7.1.8, the outlet pressure influence on CHF for the smooth tube shows an increasing trend in the higher pressure range between 200 and 300 kPa. For this reason the outlet pressure for the measurements with the surface structured tubes was also varied between 120 and 300 kPa at constant inlet subcooling of 167 kJ/kg. The same two mass fluxes of 250 and 400 kg/(m<sup>2</sup>s) were applied. Thus, the reference values for the comparison with the smooth tube are the ones shown in Fig. 7.19 of section 7.1.8. Table 8.1 lists the experimental parameters of the CHF measurements performed with the surface structured tubes in the large annulus.

Table 8.1.: Experimental parameter range for experiments with surface structures in large annulus

Annulus	Structure	$p_{out}$	$T_{in}$	$\Delta h_{in}(p, T)$	G
-	-	kPa	°C	kJ/kg	kg/(m <sup>2</sup> s)
Large	Micro-channel	120	65	167	250, 400
		150	73	167	250, 400
		200	80	167	250, 400
		250	88	167	250, 400
		300	94	167	250, 400
	Nanoscale-rough, Hemispherical, and Porous-50	120	65	167	250, 400
		200	80	167	250, 400
		300	94	167	250, 400
	Porous-100	120	65	167	250, 400
		200	80	167	250, 400
	Oxidized layer	120	65	167	250, 400
		200	80	167	250, 400
		300	94	167	250

Table 8.2.: Critical heat flux measurements with hemispherical structure tube

Hemispherical structure											
$p_{out}$	$T_{in}$	$\Delta h_{in}$	G	Exp-1	Exp-2	Exp-3	$\dot{Q}_{mean}$	$\Delta \dot{Q}$	$\dot{q}_{CHF}$	$\Delta \dot{q}_{CHF}$	
kPa	°C	kJ/kg	kg/(m <sup>2</sup> s)	kW	kW	kW	kW	kW	MW/m <sup>2</sup>	MW/m <sup>2</sup>	
120	65	167	250	9.1	8.7	8.6	8.8	0.26	0.90	0.027	
200	80.5	167	250	8.9	9.0	9.0	9.0	0.06	0.92	0.006	
300	94	167	250	11.4	11.4	11.2	11.3	0.12	1.16	0.012	
120	65	167	400	11.7	11.7	11.8	11.7	0.06	1.21	0.006	
200	80.5	167	400	11	11.4	11.7	11.4	0.35	1.17	0.036	
300	94	167	400	13.6	14.2	14.6	14.1	0.50	1.45	0.052	

### 8.1. Reproducibility of Measurements with Surface Structured Tubes

Based on the experience with the smooth tube the experiments with the surface structured tubes were conducted as described in section 4.6. Three CHF measurements were examined for each parameter set of inlet temperature, mass flux and outlet pressure. Table 8.2 shows measurements of the hemispherical structure tube as an example for the measurement reproducibility. Taking into account all measurements of the surface structured tubes at the individual parameter sets the standard deviation of the mean CHF values results in  $\Delta \dot{q}_{CHF} \leq 0.06 \text{ MW/m}^2$ . This reproducibility is similar to the smooth tube measurements described in section 7.1.2.

### 8.2. Categorization of Comparison Criteria

With respect to the standard deviation of  $\leq 0.06 \text{ MW/m}^2$  and the maximum deviation of  $\leq 0.1 \text{ MW/m}^2$  (see chapter 7.1.2) from the mean value, the criterion for an enhanced CHF value was defined as  $\dot{q}_{CHF,struct} - \dot{q}_{CHF,smooth} \geq 0.1 \text{ MW/m}^2$ . The difference in CHF between the surface structured tubes and the smooth tube is further categorized according to the criteria given in Tab. 8.3.

Table 8.3.: Criteria for the comparison of CHF-results with the smooth tube results

	Criterion	Symbol	Description
$\Delta \dot{q} = \dot{q}_{CHF,struct} - \dot{q}_{CHF,smooth}$ [MW/m <sup>2</sup> ]	$\Delta \dot{q} \geq 0.1$	+	CHF enhancement
	$0 \leq \Delta \dot{q} < 0.1$	o	Similar range, positive tendency
	$-0.1 < \Delta \dot{q} < 0$	(-)	Similar range, negative tendency
	$\Delta \dot{q} \leq -0.1$	-	CHF deterioration

### 8.3. Results of Micro-channel Structure

The measured CHF-values for the micro-channel structure are depicted with red closed symbols in Fig. 8.1 and furthermore listed in Tab. 8.4. The values for the higher mass flux of 400 kg/(m<sup>2</sup>s) are all above the results of the smooth tube. Contrary to the values of the smooth tube the CHF is continuously increasing with increasing outlet pressure. The values for the lower outlet pressures of 115 and 150 kPa are already higher than the ones to the smooth tube. However the CHF-enhancement is more significant for the higher pressures between 200 and 300 kPa.

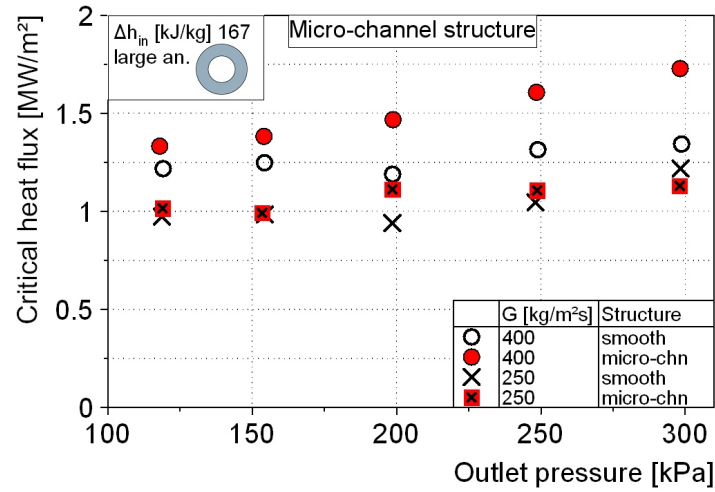


Figure 8.1.: Comparison CHF-results between smooth and micro-channel tube in large annulus for mass fluxes of 250 and 400 kg/(m<sup>2</sup>s)

Table 8.4.: Comparison of CHF-results between smooth and micro-channel tube in large annulus

$G = 250$  kg/(m<sup>2</sup>s),  $\Delta h_{in} = 167$  kJ/kg

	$P_{out}$	kPa	120	150	200	250	300
Smooth	$\dot{q}_{CHF}$	MW/m <sup>2</sup>	0.97	0.98	0.94	1.05	1.22
Micro-channel	$\dot{q}_{CHF}$	MW/m <sup>2</sup>	1.02	0.99	1.11	1.11	1.13
	$\Delta \dot{q}$	MW/m <sup>2</sup>	0.05	0.01	0.17	0.06	-0.09
	Enhancement?	$\Delta \dot{q} > 0.1?$	○	○	+	○	(-)
	rel. Variance	$\Delta \dot{q} / \dot{q}_{smooth} [\%]$	5.2	1.0	18.1	5.7	-7.4

$G = 400$  kg/(m<sup>2</sup>s),  $\Delta h_{in} = 167$  kJ/kg

	$P_{out}$	kPa	120	150	200	250	300
Smooth	$\dot{q}_{CHF}$	MW/m <sup>2</sup>	1.22	1.25	1.19	1.31	1.34
Micro-channel	$\dot{q}_{CHF}$	MW/m <sup>2</sup>	1.33	1.38	1.47	1.61	1.73
	$\Delta \dot{q}$	MW/m <sup>2</sup>	0.11	0.13	0.28	0.30	0.39
	Enhancement?	$\Delta \dot{q} > 0.1?$	+	+	+	+	+
	rel. Variance	$\Delta \dot{q} / \dot{q}_{smooth} [\%]$	9.0	10.4	23.5	22.9	29.1

+ =  $\Delta \dot{q} > 0.1$  / ○ =  $0 < \Delta \dot{q} < 0.1$  / (-) =  $-0.1 < \Delta \dot{q} < 0$  / - =  $\Delta \dot{q} < -0.1$

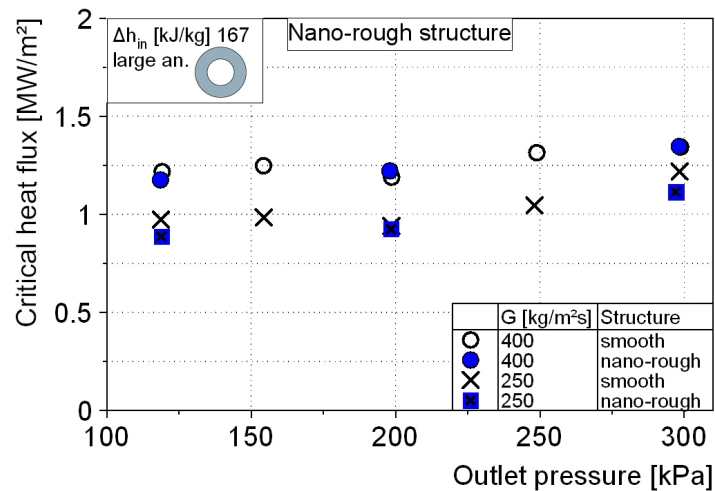


Figure 8.2.: Comparison of CHF-results between smooth and nanoscale rough tube in large annulus for mass fluxes of 250 and 400  $\text{kg}/(\text{m}^2\text{s})$

The CHF-values of the micro-channel tube for the lower mass flux of 250  $\text{kg}/(\text{m}^2\text{s})$  indicate a different behavior. Similar to the higher mass flux, the CHF at 200 kPa is increased in comparison to the smooth tube. However, the measurements of the lower mass flux of 250  $\text{kg}/(\text{m}^2\text{s})$  at the higher pressures of 250 and 300 kPa have been affected by unstable flow conditions. We observed an incipient pulsating flow for the parameter combination of micro-channel structure, inlet subcooling of 167 kJ/kg and a power input of 10.5 kW at outlet pressures at 250 and 300 kPa. At about 10.5 kW it was a stable oscillation, but a further power increase to 10.7-11.0 kW provoked an intensified pulsation causing the critical heat flux. This flow instability phenomena occurred at the same power input in spite of a drastic increase of the inlet throttling. Considering the increasing behavior of CHF with pressure for the higher mass flux 400  $\text{kg}/(\text{m}^2\text{s})$ , the CHF was expected at higher heat fluxes for the higher pressures. Instead, the CHF occurred earlier due to the pulsating flow at these conditions for the low mass flux of 250  $\text{kg}/(\text{m}^2\text{s})$ .

#### 8.4. Results of Nano-rough Structure

Figure 8.2 shows the CHF-results for the nanorough structure. The values for the mass flux of 250  $\text{kg}/(\text{m}^2\text{s})$  are slightly lower than the ones of the smooth tube. The values at 400  $\text{kg}/(\text{m}^2\text{s})$  are similar to the smooth tube results. Considering the pressure dependency both curves for the nano-rough structure indicate the same behavior as for the smooth tube. Table 8.5 contains the comparison of the measured values between the smooth and nano-rough tube.

#### 8.5. Results of Hemispherical Structure

The results of the CHF measurements with the hemispherical structure are depicted in Fig. 8.3. The outlet pressure dependency is similar to the smooth tube results. Moreover, the values are also very similar as it can be seen in Tab. 8.6. The results for the mass flux of 250  $\text{kg}/(\text{m}^2\text{s})$  lie slightly below the smooth tube values for all pressures. The results for the mass flux 400  $\text{kg}/(\text{m}^2\text{s})$  are similar for the pressures at 115 and 200 kPa. For the outlet pressure of 300 kPa can be observed an increased value of 1.46  $\text{MW}/\text{m}^2$  compared to the CHF of 1.34  $\text{MW}/\text{m}^2$  for the smooth tube.

Table 8.5.: Comparison of CHF-results between smooth and nano-rough tube in large annulus

$\Delta h_{in} = 167 \text{ kJ/kg}$			$G = 250 \text{ kg/(m}^2\text{s)}$			$G = 400 \text{ kg/(m}^2\text{s)}$		
	$P_{out}$	kPa	120	200	300	120	200	300
Smooth	$\dot{q}_{CHF}$	MW/m <sup>2</sup>	0.97	0.94	1.22	1.22	1.19	1.34
Nano-rough	$\dot{q}_{CHF}$	MW/m <sup>2</sup>	0.89	0.92	1.11	1.18	1.22	1.35
	$\Delta\dot{q}$	MW/m <sup>2</sup>	-0.08	-0.02	-0.11	-0.04	0.03	0.01
	Enhancement?*)	$\Delta\dot{q} > 0.1?$	(-)	(-)	-	(-)	o	o
	rel. Variance	$\Delta\dot{q}/\dot{q}$ [%]	-8.2	-2.1	-9.0	-3.3	2.5	0.7

\*)  $+$  =  $\Delta\dot{q} > 0.1$  /  $o$  =  $0 < \Delta\dot{q} < 0.1$  /  $(-)$  =  $-0.1 < \Delta\dot{q} < 0$  /  $-$  =  $\Delta\dot{q} < -0.1$

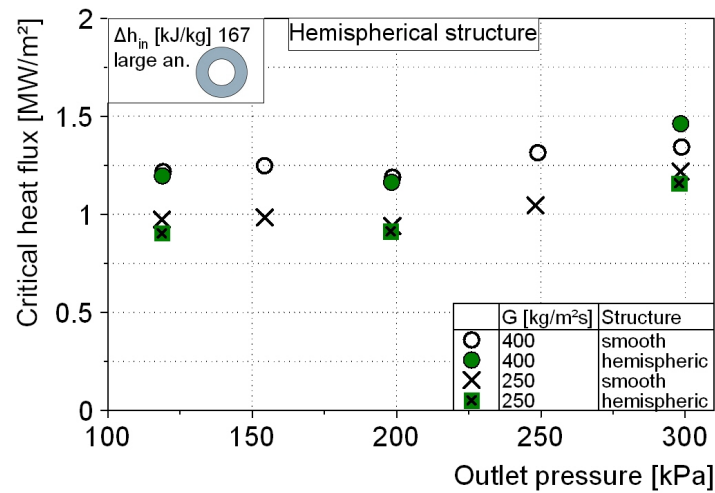
Figure 8.3.: Comparison of CHF-results between smooth and hemispherical structured tube in large annulus for mass fluxes of 250 and 400 kg/(m<sup>2</sup>s)

Table 8.6.: Comparison of CHF-results between smooth and hemispherical structured tube in large annulus

$\Delta h_{in} = 167 \text{ kJ/kg}$			$G = 250 \text{ kg/(m}^2\text{s)}$			$G = 400 \text{ kg/(m}^2\text{s)}$		
	$P_{out}$	kPa	120	200	300	120	200	300
Smooth	$\dot{q}_{CHF}$	MW/m <sup>2</sup>	0.97	0.94	1.22	1.22	1.19	1.34
Hemispherical roughness	$\dot{q}_{CHF}$	MW/m <sup>2</sup>	0.9	0.91	1.16	1.20	1.16	1.46
	$\Delta\dot{q}$	MW/m <sup>2</sup>	-0.07	-0.03	-0.06	-0.02	-0.03	0.12
	Enhancement?*)	$\Delta\dot{q} > 0.1?$	(-)	(-)	(-)	(-)	(-)	+
	rel. Variance	$\Delta\dot{q}/\dot{q}$ [%]	-7.2	-3.2	-4.9	-1.6	-2.5	9.0

\*)  $+$  =  $\Delta\dot{q} > 0.1$  /  $o$  =  $0 < \Delta\dot{q} < 0.1$  /  $(-)$  =  $-0.1 < \Delta\dot{q} < 0$  /  $-$  =  $\Delta\dot{q} < -0.1$

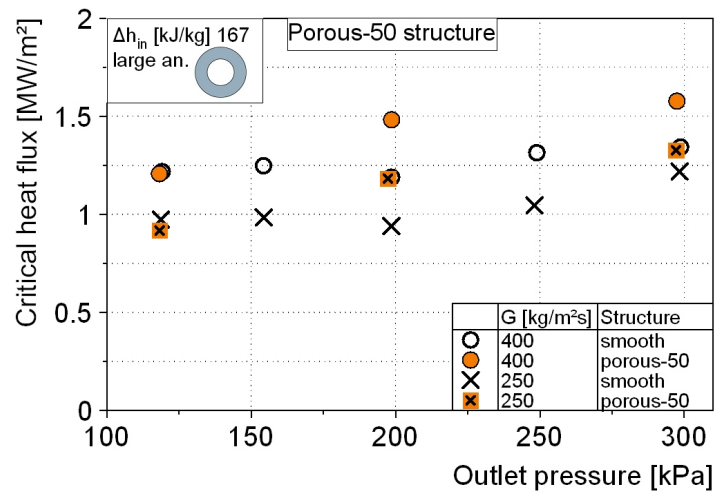


Figure 8.4.: Comparison of CHF-results between tube with smooth and 50  $\mu\text{m}$  porous layer in large annulus for mass fluxes of 250 and 400  $\text{kg}/(\text{m}^2\text{s})$

## 8.6. Results of Porous Structures

Figures 8.4 and 8.5 illustrate the measurement results for the experiments of the tubes with the sintered porous layer on the surface. The same results are shown numerically in Tab. 8.4 and Tab. 8.5 for the porous-50 and porous-100 structure, respectively.

The CHF-values for the tube with a layer thickness of 50  $\mu\text{m}$  in Fig. 8.4 are continuously increasing with increasing outlet pressure. The measured points at 120 kPa are similar to the smooth tube. However, with increasing pressure, the CHF-results are notably higher than the ones of the smooth tube for both applied mass fluxes.

Table 8.7.: Comparison of CHF-results between smooth and porous-50 tube in large annulus

$\Delta h_{in} = 167 \text{ kJ/kg}$			$G = 250 \text{ kg}/(\text{m}^2\text{s})$			$G = 400 \text{ kg}/(\text{m}^2\text{s})$		
	$P_{out}$	kPa	120	200	300	120	200	300
Smooth	$\dot{q}_{CHF}$	MW/m <sup>2</sup>	0.97	0.94	1.22	1.22	1.19	1.34
	$\Delta\dot{q}$	MW/m <sup>2</sup>	-0.05	0.24	0.11	-0.01	0.29	0.24
Porous-50 $\mu\text{m}$	$\dot{q}_{CHF}$	MW/m <sup>2</sup>	0.92	1.18	1.33	1.21	1.48	1.58
	Enhancement?*)	$\Delta\dot{q} > 0.1?$	(-)	+	+	(-)	+	+
	rel. Variance	$\Delta\dot{q}/\dot{q}$ [%]	-5.2	25.5	9.0	-0.8	24.4	17.9

\*) +=  $\Delta\dot{q} > 0.1$  / o =  $0 < \Delta\dot{q} < 0.1$  / (-) =  $-0.1 < \Delta\dot{q} < 0$  / - =  $\Delta\dot{q} < -0.1$

The same behavior as described for the 50  $\mu\text{m}$  can be observed for the layer thickness of 100  $\mu\text{m}$  in Fig. 8.5. However, the CHF at 200 kPa and 400  $\text{kg}/(\text{m}^2\text{s})$  occurred slightly below the top end of the heated section. The CHF-location was between to axial measurement points. In spite of the close positioned measuring heads with a distance of 30 mm the temperature rose to glowing of the material at the hot spot. Afterwards the porous layer showed black tempering color and cracks in the CHF-zone. Furthermore, the tube was slightly bent at the CHF position due to the thermo-mechanical load. Therefore, the measurements for the higher outlet pressure at 300 kPa could not be conducted with this tube.

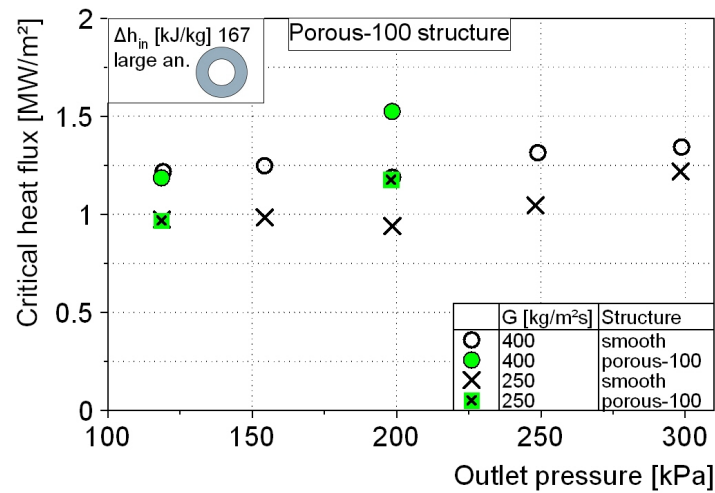


Figure 8.5.: Comparison of CHF-results between tube with smooth and 100  $\mu\text{m}$  porous layer in large annulus for mass fluxes of 250 and 400  $\text{kg}/(\text{m}^2\text{s})$

Table 8.8.: Comparison of CHF-results between smooth and porous-100 tube in large annulus

$\Delta h_{in} = 167 \text{ kJ/kg}$			$G = 250 \text{ kg}/(\text{m}^2\text{s})$			$G = 400 \text{ kg}/(\text{m}^2\text{s})$		
	$P_{out}$	kPa	120	200	300	120	200	300
Smooth	$\dot{q}_{CHF}$	$\text{MW}/\text{m}^2$	0.97	0.94	1.22	1.22	1.19	1.34
Porous-100 $\mu\text{m}$	$\dot{q}_{CHF}$	$\text{MW}/\text{m}^2$	0.97	1.18		1.19	1.53	
	$\Delta\dot{q}$	$\text{MW}/\text{m}^2$	0.00	0.24		-0.03	0.34	
	Enhancement?*)	$\Delta\dot{q} > 0.1?$	o	+		(-)	+	
	rel. Variance	$\Delta\dot{q}/\dot{q} [\%]$	0.0	25.5		-2.5	28.6	

\*)  $+$  =  $\Delta\dot{q} > 0.1$  /  $o$  =  $0 < \Delta\dot{q} < 0.1$  /  $(-)$  =  $-0.1 < \Delta\dot{q} < 0$  /  $-$  =  $\Delta\dot{q} < -0.1$

The porous layers show a similar behavior as the micro-channel structure. At the low pressure of 120 kPa there is no significant difference compared to the smooth tube. With increasing pressure the CHF increases steadily and the values are remarkably higher than the ones of the smooth tube.

## 8.7. Results of Oxidized Layer

Figure 8.6 depicts the measured CHF-results for the oxidized layer structure. The values at the lowest outlet pressure of 115 kPa are notably below the smooth tube results. However, with increasing outlet pressure the CHF-values increase above the values of the smooth tube. Table 8.9 contains the comparison of the measured values between the smooth and oxidized layer tube. The dependency on the outlet pressure is similar to the micro-channel or porous layer structure showing a continuous increase of CHF with increasing pressure.

The experiment at a mass flux of 400  $\text{kg}/(\text{m}^2\text{s})$  and an outlet pressure of 300 kPa could not be conducted. Due to the decreased thermal conductivity of the oxid layer, the tube temperature at the inside of the heated tube is higher than for the measurements of the smooth zircaloy tube. The inner temperature at the high heat input of 400  $\text{kg}/(\text{m}^2\text{s})$  and 300 kPa would rise too high for the PEEK-parts which are used in the temperature measurement module construction (see section 4.3.1).

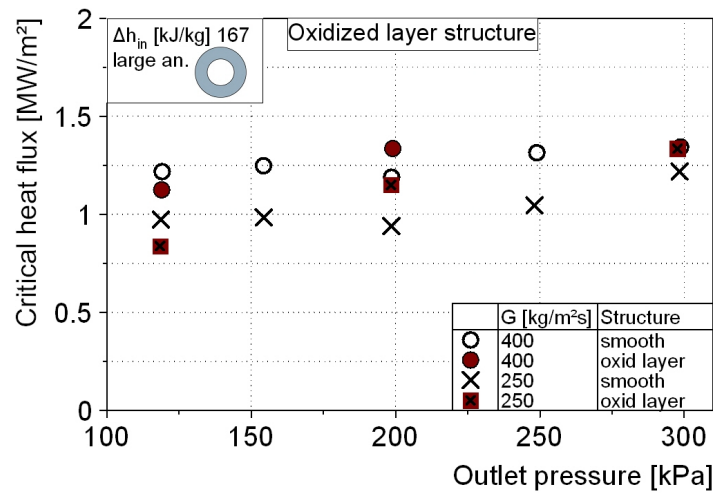


Figure 8.6.: Comparison of CHF-results between smooth and oxidized layer tube in large annulus for mass fluxes of 250 and 400 kg/(m²s)

Table 8.9.: Comparison of CHF-results between smooth and oxidized layer tube in large annulus

$\Delta h_{in} = 167 \text{ kJ/kg}$			$G = 250 \text{ kg/(m}^2\text{s)}$			$G = 400 \text{ kg/(m}^2\text{s)}$		
	$P_{out}$	kPa	120	200	300	120	200	300
Smooth	$\dot{q}_{CHF}$	MW/m²	0.97	0.94	1.22	1.22	1.19	1.34
Oxidized layer	$\dot{q}_{CHF}$	MW/m²	0.84	1.15	1.34	1.13	1.34	
	$\Delta \dot{q}$	MW/m²	-0.13	0.21	0.12	-0.09	0.15	
	Enhancement?*)	$\Delta \dot{q} > 0.1?$	-	+	+	(-)	+	
	rel. Variance	$\Delta \dot{q} / \dot{q} [\%]$	-13.4	22.3	9.8	-7.4	12.6	

\*) +=  $\Delta \dot{q} > 0.1$  / ○ =  $0 < \Delta \dot{q} < 0.1$  / (-) =  $-0.1 < \Delta \dot{q} < 0$  / - =  $\Delta \dot{q} < -0.1$

### 8.8. Comparison of Structured Surface Results

This section summarizes the CHF measurement results of the individual structured surface tubes in comparison to the smooth tube. The relative deviation from the smooth tube result is given in Tab. 8.10 using the symbols of the categories defined in section 8.2.

The nano-rough and the hemispheric structures obviously have no considerable influence on CHF. Furthermore, the CHF is unaffected by surface structures for almost all measurements at the lowest pressure of 120 kPa. Only the micro-channel structure at 400 kg/(m²s) improves the CHF at this pressure condition. The oxidized layer even decreased the CHF at both mass fluxes.

The described behavior at 120 kPa is also visible when plotting the critical heat flux against the thermodynamic vapor mass quality as shown in Fig. 8.7. The dashed lines in Fig. 8.7 show the relationship between heat flux and the thermodynamic vapor mass quality at the test section exit for both mass fluxes of 250 and 400 kg/(m²s). The lines are calculated according to Eqn.(2.11).

The fine error bars indicate the general standard deviation of  $\pm 0.06 \text{ MW/m}^2$ . The error bar in bolt of the smooth tube illustrates the range of  $\pm 0.1 \text{ MW/m}^2$ . Values in this range are considered similar to the smooth tube CHF as defined in Tab. 8.3. The critical heat flux results at the low pressure of 120 kPa are in close proximity to the smooth tube CHF.

A different appearance is visible in the diagrams for the higher pressures of 200 and 300 kPa in Fig. 8.8



Table 8.10.: Percentage deviation of CHF results for surface structured tubes from smooth tube results in large annulus

$\Delta h_{in} = 167 \text{ kJ/kg}$	$G = 250 \text{ kg/(m}^2\text{s)}$			$G = 400 \text{ kg/(m}^2\text{s)}$		
	$P_{out}$ [kPa]	120	200	300	120	200
Nano-rough	(-) 8.2%	(-) 2.1%	- 9.0%	(-) 3.3%	o 2.5%	o 0.7%
Hemispheric	(-) 7.2%	(-) 3.2%	(-) 4.9%	(-) 1.6%	(-) 2.5%	+ 9.0%
Micro-channel	o 5.2%	+ 18.1%	(-) 7.4%	+ 9.0%	+ 23.5%	+ 29.1%
Porous-50	(-) 5.2%	+ 25.5%	+ 9.0%	(-) 0.8%	+ 24.4%	+ 17.9%
Porous-100	o 0.0%	+ 25.5%		(-) 2.5%	+ 28.6%	
Oxidized	- 13.4%	+ 22.3%	+ 9.8%	(-) 7.4%	+ 12.6%	

+ =  $\Delta q > 0.1$  / o =  $0 < \Delta q < 0.1$  / (-) =  $-0.1 < \Delta q < 0$  / - =  $\Delta q < -0.1$

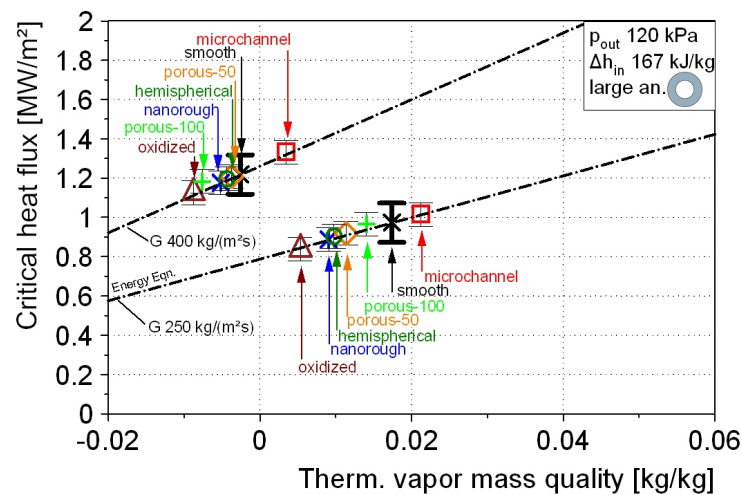


Figure 8.7.: CHF-results for all surface structured tubes at outlet pressure of 120 kPa

and Fig. 8.9. The values for the structures nano-rough and hemispherical remain close to the smooth tube. However, the other structures show an improved CHF behavior compared to the smooth tube. This effect is more remarkable for the higher mass flux. Depending on the structure and conditions the increased values range between 8.3 and 27.8% as indicated in Tab. 8.10. An exception is the value for the micro-channel structure at  $250 \text{ kg/(m}^2\text{s)}$  and 300 kPa. The CHF is lower than the one of the smooth tube because of flow oscillation occurrence for these conditions as described in section 8.3.

An increase in CHF of similar magnitude was observed by *Sarwar et al.* [89] with CHF enhancement up to 25% for flow boiling of water in tubes with porous layers at atmospheric pressure and low mass fluxes of 100-300 kPa. *Ammerman and You* [4] also reported increased CHF values of about 14-36% for flow boiling of FC-87 in a rectangular channel.

In summary, the measurements of the structures micro-channel, porous-50, porous-100, and oxidized layer show generally an improvement of CHF for pressures higher than 120 kPa. This enhancement is more significant for the CHF values of the higher mass flux.

In case of the blank cells in Tab. 8.10 the values could not be measured because of some structure specific events during the systematic measurements of CHF on surface structures. For instance, in an experiment for the  $100 \mu\text{m}$ -porous layer at  $400 \text{ kg/(m}^2\text{s)}$  and 200 kPa the critical heat flux occurred about 50 mm below the top end of the heated section. This position was between two measurement heads and the surface has been

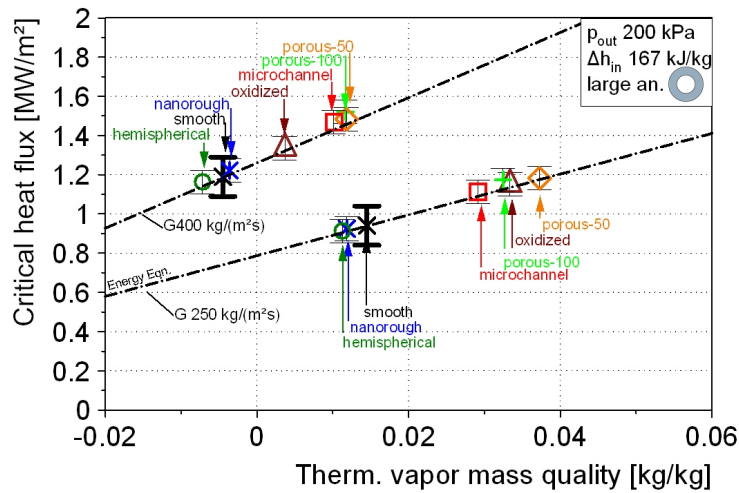


Figure 8.8.: CHF-results for all surface structured tubes at outlet pressure of 200 kPa

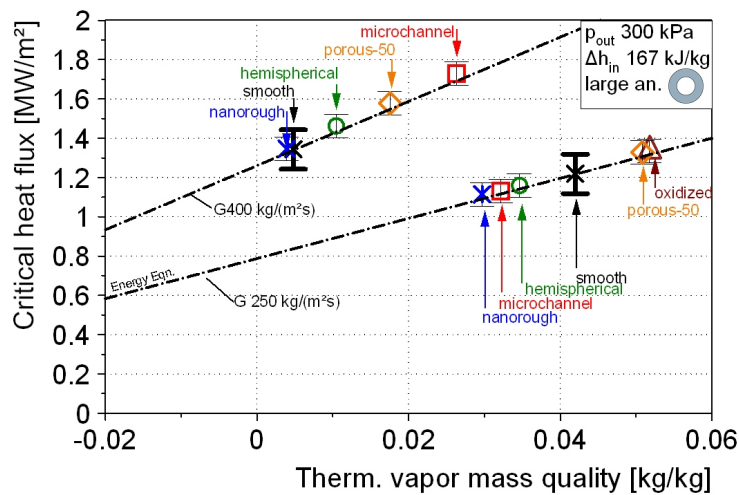


Figure 8.9.: CHF-results for all surface structured tubes at outlet pressure of 300 kPa

glowing at the location before the heating power was shut off. The porous layer was locally oxidized and melted, and the tube was slightly bent. Consequently, the tube was useless for further measurements. Thus, a slight variation of the axial CHF location from the top end remains a risk for the investigations of surface structures in spite of the change to a larger annulus in the present test section design.

Another effect concerning the temperature measurement was observed using the oxidized layer tube. Due to the reduced heat conductivity through the oxidized layer, the inner tube temperature is higher in comparison to the other tubes. For the conditions of the highest applied mass flux and pressure of 400 kg/(m<sup>2</sup>s) and 300 kPa, the inner tube temperature would have become too high for the PEEK-material of the measurement heads. Using a different material like Torlon or ceramics, the working temperature could be increased while maintaining the electrical insulation. Adding more thermocouples at closer distances would increase the safety against damage at CHF, however the small inner diameter of 8.2 mm of the zircaloy tube limits the number of thermocouples.

An incipient flow oscillation occurred for micro-channel structure at the higher outlet pressures of 250 and

300 kPa and the parameter combination of low mass flux of  $250 \text{ kg}/(\text{m}^2\text{s})$ , inlet subcooling of  $167 \text{ kJ}/\text{kg}$  and a heat flux of  $1.08 \text{ MW}/\text{m}^2$ . The pulsating flow induced the occurrence of the critical heat flux. Compared to the increasing behavior of CHF with pressure for the higher mass flux  $400 \text{ kg}/(\text{m}^2\text{s})$  in Fig. 8.1, the CHF was expected at higher heat fluxes for these conditions at low mass flux of  $250 \text{ kg}/(\text{m}^2\text{s})$ . In contrast to the static flow instabilities explained in chapter 6, the pulsating flow occurred in the boiling channel at the same power input of  $10.5 \text{ kW}$  ( $1.08 \text{ MW}/\text{m}^2$ ) independent of a drastic increase of the inlet throttle pressure drop.

This effect of pulsating boiling flow at low flow conditions using the micro-channel structure could not be investigated in more detail in this work. However, this example shows that the complex system of a two-phase boiling system could change its behavior significantly if one of the influencing parameters is varied.

## 8.9. Visualization of Two-phase Flow

The two-phase flow was visualized using a high-speed camera of the type iSpeed3 of Olympus. Detecting the temperature jump at CHF the camera was triggered automatically by the control program. The dynamic buffer was recorded about 1 second before to 0.5 seconds after the CHF event. The frame rate was usually set to 2000 frames per second at full sensor resolution of  $1280 \times 1024$  pixels. After the CHF measurements the two-phase flow behavior was recorded for each parameter set at different selected power inputs as described in section 4.6. The high-speed measurement procedure and the visualization results are also described in the bachelor thesis of *Enderle* [34].

### 8.9.1. Formation of Dry Patch at Critical Heat Flux

The high-speed videos of the porous structured tubes allowed to observe a periodically formation of a dry patch on the surface and subsequent rewetting by a liquid slug at conditions nearly CHF. This phenomenon was visible because the porous layer slightly changed the color to a lighter gray at the dried out patch. Figure 8.10 shows a image series corresponding to conditions just prior to CHF, however, the shown dry patch formation was not directly the one of the detected temperature jump at CHF. The pictures illustrate 80 mm of the upper heated section of the vertical annular test section assembly. The observed light gray spots were subsequently colored by *Enderle* [34] for better illustration. A dry patch about 5 mm long is visible in the picture corresponding to  $t=0\text{s}$ . The second picture after 19 ms shows the upwards elongated patch as well as a second spot at the end of the heated section. Both spots grow together forming an almost 40 mm long patch at  $t=35 \text{ ms}$ .

At the bottom of these pictures rises a liquid slug. Reaching the dried out patch the liquid rewets the surface. Due to the partly evaporation, the continuous liquid phase of the slug breaks up and the liquid parts are accelerated through the channel while the next liquid slug is already rising. The dried out patch is visibly decreased in the picture of  $t=81 \text{ ms}$ .

Remarkably is also the sharply bounded line of the dried out patch at the end of the heated length in the pictures of  $t=27\text{-}53 \text{ ms}$ . The blue line indicates the begin of the fit copper part inside the tube defining the end of the heated section because of the significantly reduced electric resistivity.

The observed dry patch formation agrees with the CHF mechanism description of *Fiori and Bergles* [36] for subcooled flow boiling in internally heated annuli at low pressure: '*...as a large vapor clot passes over the heated surface, nucleating bubbles break the superheated liquid film and cause a stable dry spot. This*

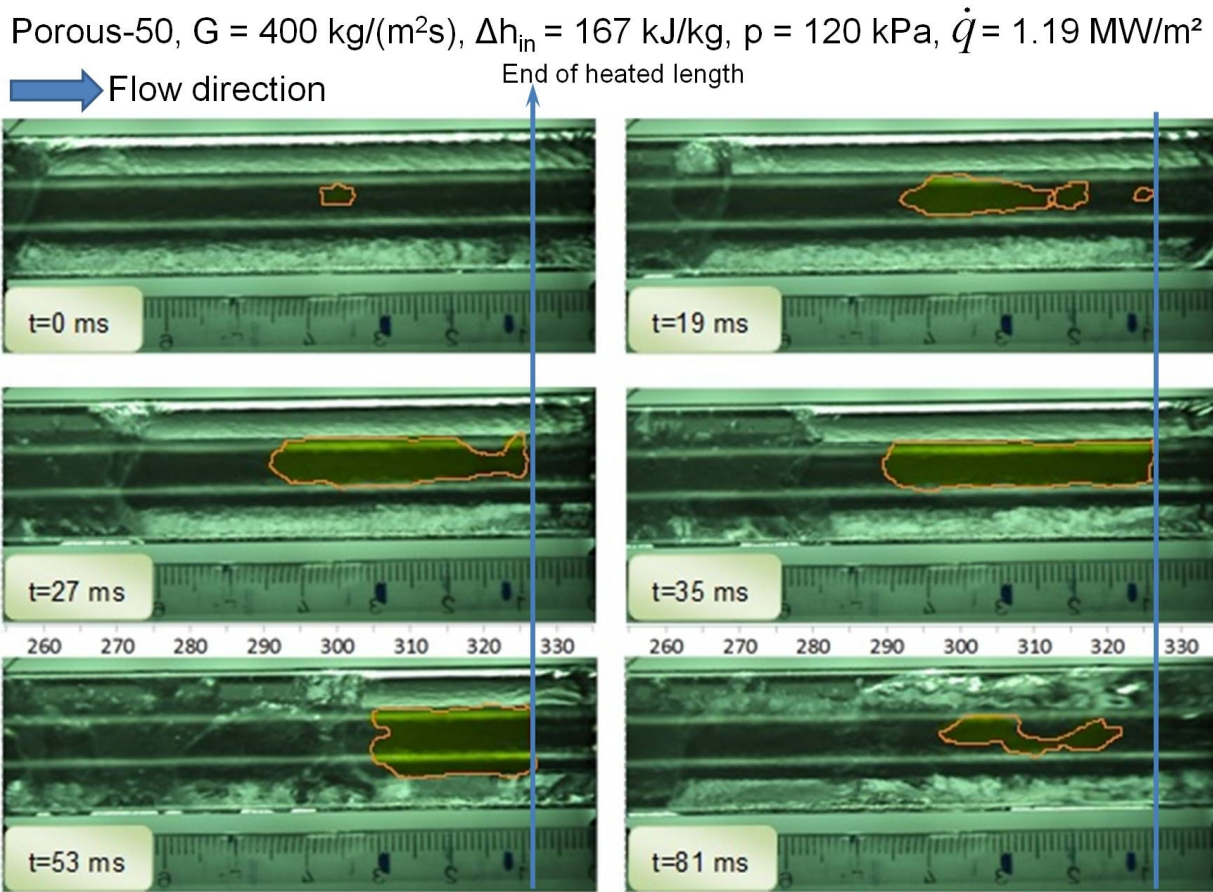


Figure 8.10.: Expanding and rewetting of a dry patch on the porous surface [34]

results in an increasing local surface temperature until the vapor passes the site and the dry spot is quenched by a liquid slug. At CHF, volumetric heat generation, slug frequency, and void fraction are such that the temperature rise resulting from the dry spot is greater than the temperature drop during quenching. An unstable situation results where the temperature of this point continues to rise after each vapor clot passes the site, until the Leidenfrost temperature is reached, at which point quenching is prevented and destruction is generally inevitable. [36]

Figure 8.11 illustrates the two-phase flow regime observed for the different surface structured tubes at the power input of the particular critical heat flux. The pictures show the upper two thirds of the heated tube indicated by a length scale between the pictures of the smooth and nano-rough structured tubes. The black bar at about 250 mm is a cable tie fixing a thermocouple at the outside of the glass tube. The corresponding experimental parameters for the CHF pictures in Fig. 8.11 were mass flux of  $400 \text{ kg}/(\text{m}^2\text{s})$ , outlet pressure of 200 kPa and inlet subcooling of 167 kJ/kg. In spite of showing only a single image of each CHF video sequence, the characteristic flow regimes are recognizable. These observed typical flow regimes are marked for the smooth surface tube on the left side in Fig. 8.11.

The characteristic flow pattern at CHF is bubbly flow in the bottom part followed by a transition to slug flow in the upper part of the heated length. Single bubbles are dispersed in the subcooled liquid in bubbly flow. This flow regime ranged over the first 250 mm of the heated length of 326 mm for the smooth tube at the presented CHF conditions. In the region around 250 mm the vapor volume quantity becomes significant and larger bubbles are formed. This point is called the Onset of Significant Void (OSV) [86]. The bubbles further

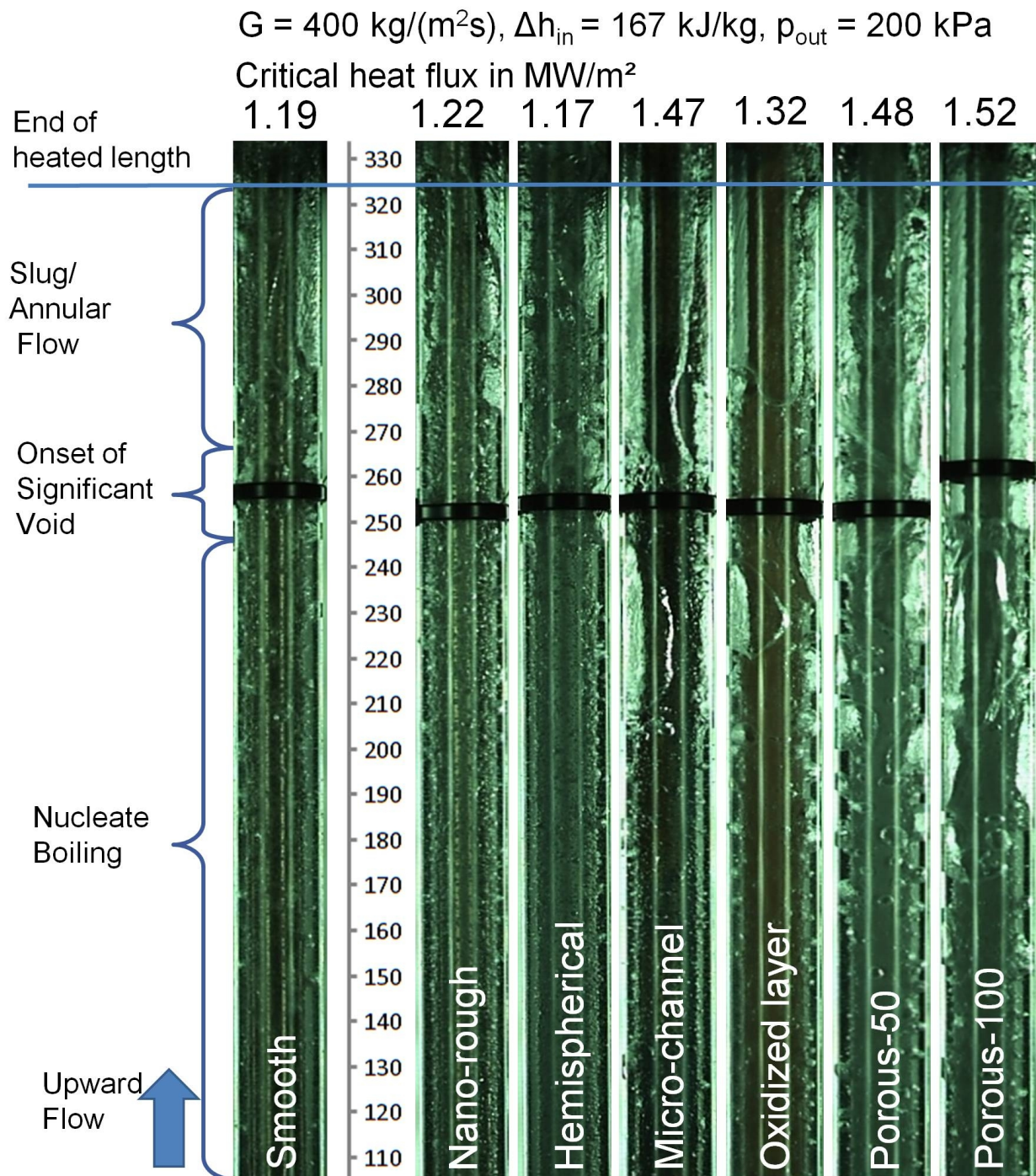


Figure 8.11.: Flow boiling image at heat flux of CHF

coalesce to larger bubbles and vapor slugs which flow through the channel and form temporarily annular flow conditions. These conditions of vapor filling almost the entire cross section are interrupted frequently by liquid slugs rising from the transition region between bubbly and slug flow. The CHF occurred in the slug flow regime for all of the tested tubes and applied experimental conditions. This typical flow pattern at CHF for subcooled flow boiling in annuli at low pressure was also observed by *Fiori and Bergles* [36], *Rogers et al.* [85] and *Schoesse et al.* [90], for instance.

It is visible in Fig. 8.11 that the flow pattern for the nano-rough and hemispherical structures are similar to the smooth tube. The micro-channel structured tube shows also the same characteristic, however, the OSV is shifted upstream. The main reason is simply because the heat flux at CHF was considerably increased from  $1.19 \text{ MW/m}^2$  for the smooth tube to  $1.47 \text{ MW/m}^2$  for the micro-channel structure as indicated above each picture. The similar effect is obvious for the other tubes with oxidized and porous surfaces. However, these structures also show a different behavior in the bubbly flow region. A layer of very small bubbles upon the surface with some larger bubbles still attached to the layer could be observed. These characteristics are also visible when comparing the flow boiling appearance at same heat input as shown in the following section.

### 8.9.2. Flow Regime Comparison at Same Heat Input

In order to compare the flow pattern between the different surface structured tubes high-speed videos were taken at the same heat input and similar parameter conditions. Figures 8.12 and 8.13 show the two-phase flow appearance for a heat flux of  $0.72 \text{ MW/m}^2$ , inlet subcooling of  $167 \text{ kJ/kg}$ , and outlet pressure of  $120 \text{ kPa}$ . The mass flux was set to  $250 \text{ kg/(m}^2\text{s)}$  in Fig. 8.12 and  $400 \text{ kg/(m}^2\text{s)}$  in Fig. 8.13.

Considering the pictures for the mass flux of  $250 \text{ kg/(m}^2\text{s)}$  in Fig. 8.12 it is evident that the four structures on the left side (smooth, nano-rough, hemispherical, and micro-channel) have the same appearance. Single bubbles are visible on the surface and in the liquid flow. The three surface structures on the right side (oxidized layer, porous-50, and porous-100) demonstrate a different behavior in spite of the same conditions. There are many very small bubbles in a hardly noticeable layer covering the surface. These very small bubbles coalesce suddenly to large bubbles or vapor slugs in the upper part. The porous-50 structure shows the formation of single larger diameter bubbles moving upwards with the flow as it was observed in the videos. These bubbles stayed connected to the surface and grew during their passage through the channel. In case of the oxidized and the porous-100 structures a change from very small bubbles to large bubbles or vapor slugs appears quite suddenly in the upper part. Although applying the same conditions these structures already showed slug flow at the end of the heated section, whereas the flow regime of the other structures was still bubbly flow.

Figure 8.13 shows the similar characteristics at the higher mass flux of  $400 \text{ kg/(m}^2\text{s)}$ . Since the mass flux is higher at same heat flux of  $0.72 \text{ MW/m}^2$  the boiling is less intense than in Fig. 8.12. Again the smooth, nano-rough, hemispherical, and micro-channel structured tubes show a similar appearance of single visible bubbles which are growing and condensing in the subcooled liquid. The three tubes with oxidized, porous-50, and porous-100 surfaces at the right side in Fig. 8.13 produce a large number of remarkably smaller bubbles appearing as a layer on the surfaces. From these observations can be concluded that the surface structures of the porous-50, porous-100 and oxidized layer provide an increased number of nucleation sites in comparison to the other structures at the same conditions.

This behavior of the porous layers is consistent with the description of *Tong* [100]. A large number of nucleation sites releasing very small bubbles was observed for a surface with porous deposit. Whereas the

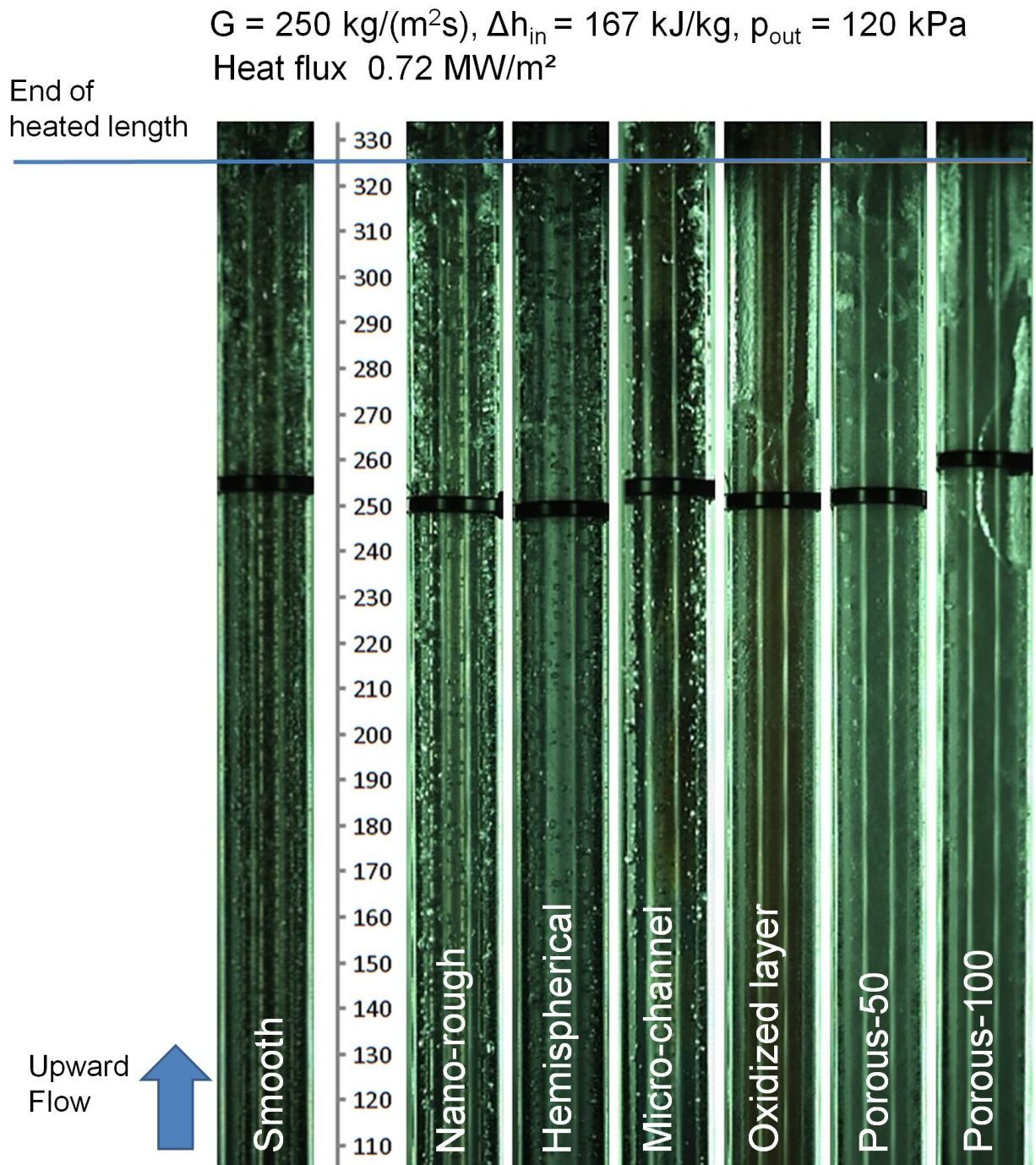


Figure 8.12.: Comparison of flow boiling images between surface structured tubes at  $0.72 \text{ MW}/\text{m}^2$  for  $G=250 \text{ kg}/(\text{m}^2\text{s})$  and  $P=120 \text{ kPa}$

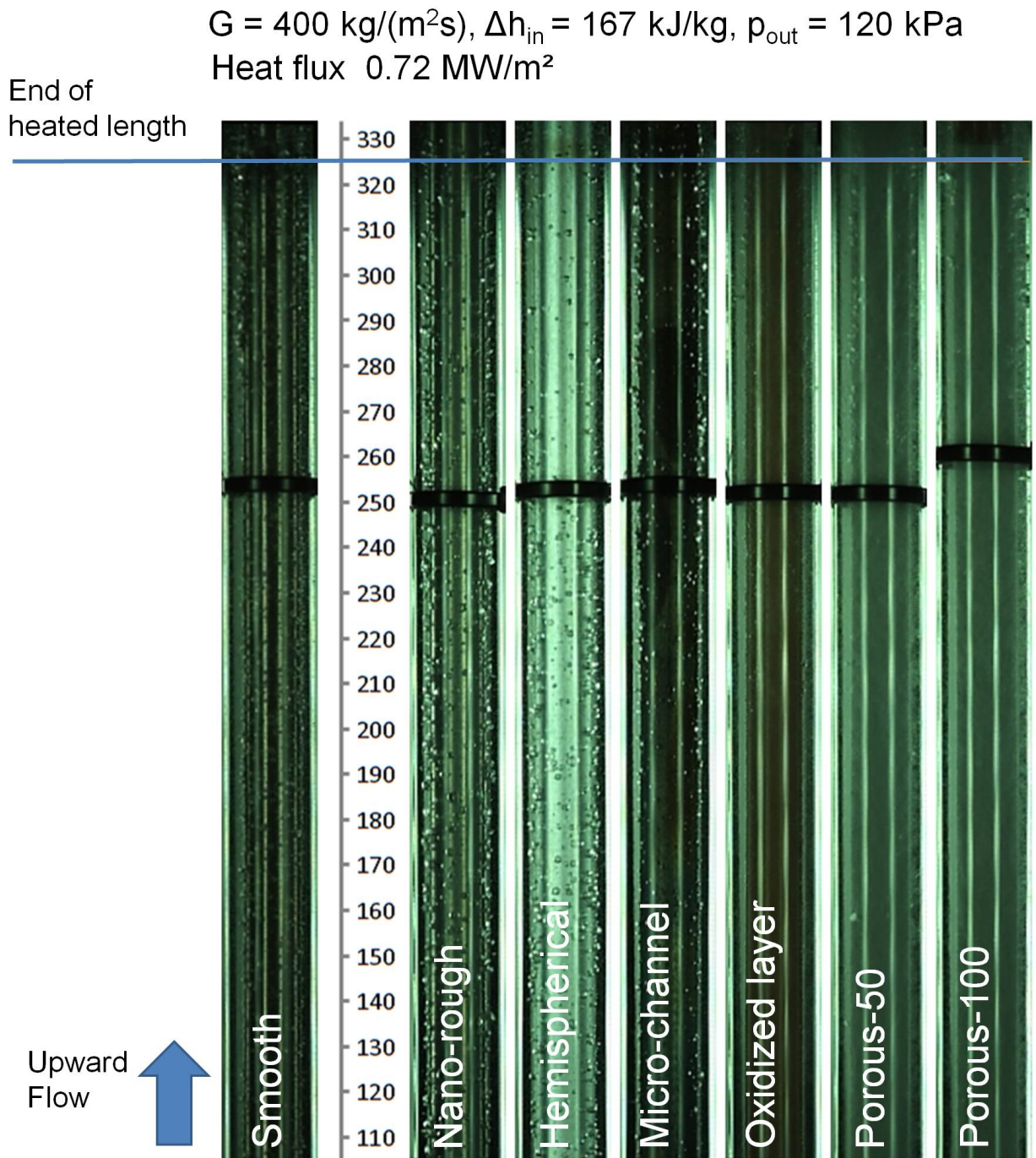


Figure 8.13.: Comparison of flow boiling images between surface structured tubes at  $0.72 \text{ MW}/\text{m}^2$  for  $G=400 \text{ kg}/(\text{m}^2\text{s})$  and  $P=120 \text{ kPa}$



smooth surface produced considerable larger bubbles at relatively small numbers of nucleation sites. This effect was more significant for low pressure (200 kPa) according to *Tong* [100].

It is interesting that the oxidized layer behaves similar to the porous layers. In contrast to the porous layer the oxidized layer has no open porosity. As described in section 5.1.6 the surface is very dense, however there is a structure of connected cracks with a width of about 1 to 2  $\mu\text{m}$  and several microns depth in the oxidized layer. Resulting from the wettability test in section 5.2.5 the oxidized surface showed no remarkable capillary effect. A capability of remaining liquid inside the crack texture could be concluded from a decreased advancing contact angle in the measurements on the rewetted surface. This effect was significantly smaller than for the porous layer, nevertheless, the boiling behavior appears similar to the porous structures.



## 9. Conclusion of Surface Structure Influence

The surface structure influence on CHF was investigated for flow boiling of water in the large annular geometry at mass fluxes of 250 and 400 kg/(m<sup>2</sup>s), constant inlet subcooling of 167 kJ/kg, and outlet pressures between 120 and 300 kPa. The flow boiling appearance was visualized using a high-speed camera. Furthermore, the wettability of the surface structures was characterized by tensiometer measurements. The CHF performance of the investigated surface structures depended on the test boundary conditions and varied between -13% and +29% compared with the smooth surface tests. Increased nucleation site density and/or capillary effects are assumed to influence the CHF performance because of the observed behavior of the structures in flow visualization and wettability characterization:

- The nanorough and hemispherical surface structures were similar in wetting behavior and in boiling appearance compared with the smooth tube. CHF performance was similar, however, most of the values were slightly smaller.
- The oxidized surface with cracks in the layer was similar in wetting behavior but showed an increased number of nucleation sites compared with the smooth tube. CHF was increased at pressures of 200 and 300 kPa and decreased at 120 kPa.
- The micro-channel surface structure was similar in boiling appearance but showed increased wetting forces on the dry and the rewetted surface compared with the smooth tube. CHF was increased for the higher mass flux of 400 kg/(m<sup>2</sup>s) for all tested pressures. On the other hand, the CHF was decreased because of flow instability occurrence for the lower mass flux of 250 kg/(m<sup>2</sup>s) and pressures of 250 and 300 kPa using this surface structure.
- The porous surface structure of 50 μm layer thickness was similar in wetting behavior on the dry surface but had increased wetting forces on the rewetted surface. The number of nucleation sites was increased compared with the smooth tube. CHF was increased at pressures of 200 and 300 kPa and decreased at 120 kPa.
- The porous surface structure of 100 μm layer thickness showed increased wetting forces on the dry and the rewetted surface. The number of nucleation sites was increased compared with the smooth tube. CHF was increased at pressure of 200 kPa and similar and decreased at 120 kPa. CHF at the higher pressure of 300 kPa could not be measured because of local surface destruction during a CHF experiment.

The absence of surface structure influence at the lowest pressure of 120 kPa might be caused by vapor bridging the annular gap at specific void fraction conditions making the surface structure unimportant for the CHF occurrence. The density ratio between liquid and vapor of water decreases significantly with increasing pressure from 1364 at 120 kPa to 835 at 200 kPa and 564 at 300 kPa as shown in Fig. 2.8. This means that the evaporated volume of the same liquid mass amount requires at 120 kPa 2.4 times the volume

as at 300 kPa. As a consequence to the bridging effect, the smaller CHF values at 120 kPa compared to the smooth tube might be caused by the slightly greater outer diameter because of the surface structure thickness. A further enlargement of the annular gap width would possibly lead to an observable surface structure influence on CHF also for pressures near atmospheric conditions. For instance, *Sarwar et al.* [89] reported an increase in CHF for flow boiling of water at atmospheric pressure conditions and similar mass fluxes of 100-300 kg/(m<sup>2</sup>s) in a 10.92 mm diameter and 230 mm long tube with porous coating. On the other hand, this would mean that a minimum channel width depending on the density ratio would be required for an effective surface structure influence. However, these assumptions should be studied by varying the annular gap at constant  $L/d_{he}$  ratio.

The CHF values of the nano-rough and hemispherical structured tubes were similar to the smooth tube results for all applied pressures. Thus, these roughness modifications of elevations in nano- and microscale have no influence on CHF for the applied parameters, however, they confirm the pressure dependency observed in the measurements of the smooth tube. The CHF remained almost constant during the pressure increase from 120 to 200 kPa and showed an increasing trend for pressures between 200 and 300 kPa. Contrary to this behavior, the surface structures with micro-channels, porous layers or oxidized layer already showed an increasing tendency between 120 to 200 kPa. Moreover, the similarity of nano-rough and hemispherical structured tubes to the smooth tube was also observed in the wettability measurements and flow pattern visualization. A slug flow regime in the upper part of the heated section at CHF conditions was generally observable for all surface structured tubes.

From the visualization of the boiling flow resulted that the flow pattern and the number of nucleate boiling sites of the micro-channel structure appeared similar to the surface structures smooth, nano-rough, and hemispherical. However, the CHF values for the micro-channel structure were considerably increased for higher pressures and mass flux. Therefore, the significant effects for CHF enhancement for the micro-channel structure seemed to be independent of the general flow appearance observable from the outside. On the other hand, a negative effect of flow oscillations inducing the critical heat flux could be observed for the low mass flux of 250 kg/(m<sup>2</sup>s) and pressures of 250 and 300 kPa. Both observations gave rise to the assumption that effects caused by the micro-channels in the vicinity of the heated surface were influencing the critical heat flux occurrence and the flow boiling process. However, this region was not visually available by the applied high-speed videos from the outside.

A difference between the micro-channel and the smooth tube could be observed in the wetting behavior. The capillary effect of the micro-channels was noticeable in higher forces measured for the fluid-structure interaction with the Wilhelmy method. The advancing contact angle was already smaller than for the smooth tube in the measurements with the dry surfaces. Moreover, the advancing and the receding wetting forces were similar in the measurements on the rewetted surface indicating that a significant amount of liquid is captured in the surface texture. Therefore, it is assumed that capillary effects due to the micro-channels prevent the local dry out of the surface at CHF conditions of the smooth tube, thus leading to CHF enhancement.

The same effect of similar values in advancing and receding wetting forces was observed for tubes with porous layers. Both, the 50 and 100  $\mu\text{m}$  layer thickness increased the CHF values for applied pressures higher than 120 kPa. Furthermore, these structures showed a different flow boiling appearance. In comparison to the smooth tube a considerable larger amount of nucleation sites producing very small bubbles was observed for the tubes with porous layers. The very local dryout and rewetting mechanism of vapor and

---

liquid slugs at CHF conditions could be observed using the porous layers because of a slight change of the surface color when drying out.

It is interesting that the performance of the oxidized layer was similar to the porous layers. In contrast to the porous layer the oxidized layer has no open porosity. As described in section 5.1.6 the layer surface is generally dense, however, there is a structure of connected cracks with a width of about 1 to 2  $\mu\text{m}$  and several microns depth in the oxidized layer. Resulting from the wettability test the oxidized surface showed no remarkable capillary effect. A capability of remaining liquid inside the crack texture could be concluded from a decreased advancing contact angle in the measurements on the rewetted surface. This effect was significantly smaller compared to the porous layer, nevertheless, the boiling behavior appears similar to the porous structures. The surface texture of cracks provided a considerable increase in nucleation sites. The mixture of cracks with intense small bubble production surrounding areas with limited boiling sites could be the reason for CHF enhancement of the oxidized layer structure.

There was no clear link between the CHF values and the wettability characteristics appropriate to describe the similarities and differences in CHF performance between all measurement results. First, it is questionable if the measurement results of the dynamic wetting behavior using the Wilhelmy method at the applied conditions are appropriate for use in flow boiling situations. Second, other influencing factors such as nucleation site density might not be implicitly covered by the measured wettability quantities. Third, the surface structure influences may also be overlaid by other effects in flow boiling depending on geometry and thermohydraulic conditions.

Nevertheless, a measurable but not exclusively necessary indication for surface structures with increasing CHF effect could be similar advancing and receding forces, i.e. almost no contact angle hysteresis, in the wettability measurements on the rewetted surface by the Wilhelmy method.

The surface structure of major interest could be indeed the micro-channel structure. First, the surface structure can be directly manufactured into the base zircaloy tube meaning that no additional material is necessary. Second, the structure achieved an CHF-enhancement of 22-28% for the mass flux 400  $\text{kg}/(\text{m}^2\text{s})$  and pressures between 200 and 300 kPa. Third, in contrast to the porous layer, the micro-channel surface characteristic remained even if there was glowing of the material at the CHF location before the shut off. Moreover, it is known that the flow in a channel is influenced by periodic vortices originating in axial slots in the wall (*Meyer* [74]). Vortices inside the axial micro-channel flow could have a decreasing effect on the pressure drop in single-phase flow and might also be interesting concerning the prevention of crud deposition on the surface. On the other hand, the above mentioned occurrence of flow oscillations at low mass flux of 250  $\text{kg}/(\text{m}^2\text{s})$  has to be minded as well.



## 10. Summary

The present work contains the investigation of the critical heat flux behavior of smooth and modified surfaces in flow boiling of water in an internally heated vertical annulus at low pressure. A new experimental test facility was designed and installed in order to examine this study. The now existing thermo-hydraulic water/steam loop is applicable for an electrical heated test section with a maximum power of 75 kW in the parameter range of low outlet pressures between 100 and 400 kPa (1-4 bar) and inlet temperatures between 30 and 120 °C. The test section concept for these investigations was a vertical annulus with an inner tube heated over a length of 326 mm and an unheated outer tube of glass. Two annular geometries were used for the investigations, a 1.75 mm wide and a larger 4.25 mm wide gap. The requirement of using genuine zircaloy cladding tubes as used in nuclear reactors was realized for both the test section design and the surface structuring processes. The zircaloy tube of 8.2 mm inner diameter required a special design of a temperature measurement module for detecting the temperature increase at the critical heat flux.

Modifications of the zircaloy cladding surface were realized in cooperation with industry and scientific institutes. The base material zircaloy and the geometry posed quite a challenge for finding suitable manufacturing processes. Nevertheless, six different surface structures, namely *nanoscale roughness*, *hemispherical structure*, *micro-channel*, *50 μm porous layer*, *100 μm porous layer*, and *oxidized layer*, have been successfully manufactured.

Commissioning tests and first critical heat flux measurement series with the technically smooth tubes were conducted for the smaller annular geometry. Since the two phase flow in narrow channels and at low pressures is very susceptible to flow instabilities an experimental stability investigation was examined in order to ensure CHF measurements at stable and reproducible conditions.

Transition from nucleate to film boiling was a very local phenomenon for the CHF in the annulus for the applied conditions. A hot spot was formed by a local dry out leading to the temperature jump at CHF. In the small annulus the CHF position was stochastically distributed in the upper half of the heated section. This variation excluded a safe facility operation for the surface structured tubes due to possible thermo-mechanical damage. As a consequence, a larger annulus was used. For these conditions the CHF occurred always at the top end of the heated section.

CHF values for the smooth tube were measured for inlet subcooling conditions between 100 and 250 kJ/kg, outlet pressures between 115 and 300 kPa and mass fluxes between 250 and 1000 kg/(m<sup>2</sup>s) for the small annular geometry as well as 250 and 400 kg/(m<sup>2</sup>s) for the large annular geometry. The thermodynamic vapor qualities at the exit were generally small with  $-0.02 < x_{th} < 0.02$  for the large annulus and  $0.05 < x_{th} < 0.15$  for the small annulus. Nevertheless, the void fraction was very high because of the enormous difference in density between vapor and liquid for water at low pressure. For technically smooth tube surfaces the pressure influence on CHF between 120 and 300 kPa was similar for both annular geometries investigated. The CHF values remained almost constant between 120 and 200 kPa and showed an increasing trend with pressure between 200 and 300 kPa.

Compared to the literature data of *Rogers et al.* [85] performed for similar experimental parameters and a test section with similar length to heated equivalent diameter ratio, the results of the current work for the larger annulus demonstrated a very good agreement. Moreover, the CHF results were compared with calculated values using the *Katto&Ohno* correlation [55], look-up tables (LUT) of *Groeneveld et al.* [42], [40], [41], and correlations of *Doerffer et al.* [30]. The *Katto&Ohno* [55] correlation was inappropriate for these conditions because of significantly higher calculated CHF values. The LUT1995 and LUT2006 fit remarkably better than LUT1986, but the calculated values were about 31-51% higher than the experimental results. The 3-k-factors correlation for internally heated annuli of *Doerffer et al.* [30] showed similar characteristics as the lookup tables. The experimental values matched best with the calculated values of a rod-centered approach of *Doerffer et al.* [30] using an empirical vapor quality term for CHF in annuli. However, this correlation showed inconsistent behavior for higher vapor qualities and higher mass fluxes.

The results of the technically smooth surface tube were used as a reference to the measurements of the structured tube surfaces. CHF measurements for all surface structures were performed with the larger annular geometry at constant inlet conditions and varied outlet pressures between 120 and 300 kPa. The CHF performance of the investigated surface structures depended on the boundary conditions and varied between -13% and +29% compared with the smooth surface tests.

At the lowest tested pressure of 120 kPa the CHF values for the surface structured tubes were mostly similar or smaller. Vapor bridging the gap of the tested channel geometry could make the underlying surface structure unimportant for CHF occurrence at 120 kPa. For the same vapor mass the volume at 120 kPa is significantly higher than at 200 and 300 kPa. *Nanoscale roughness* and *hemispherical structure* showed a similar CHF performance compared with the smooth surface tube for all tested pressures. The surfaces having micro-channels, porosity and cracks (*micro-channel*, *porous-50*, and *porous-100* and *oxidized layer* structures), showed a tendency of CHF increase with increasing pressure. Depending on the conditions this increase was found to be 10 to 29% compared to the smooth surface tube. An increase of similar magnitude was reported by *Sarwar et al.* [89] for flow boiling of water in vertical tubes with porous coatings at atmospheric pressure and mass fluxes of 100-300 kg/(m<sup>2</sup>s). The micro-channel structure could be the most interesting of the tested surfaces because it is directly produced into the base tube material and the profile is uniform and variable. However, a flow oscillation occurrence was observed for the micro-channel structure for the low mass flux of 250 kg/(m<sup>2</sup>s) and pressures higher than 200 kPa.

The CHF occurrence and the two-phase flow boiling performance at different heating power conditions were observed by high-speed video visualization. The general flow regime at CHF was slug flow in the upper part of the heated section for all tested surface structures. The phenomenon of a periodically local dry out and subsequent quenching of the surface by a liquid slug could be observed for the porous layer because of a slight change in surface color. This CHF mechanism for flow boiling in vertical, internally heated annuli was also reported by *Fiori and Bergles* [36].

Furthermore, the Wilhelmy method was applied as a suitable method for determining the wettability of the surface structures. The fluid-surface interaction was characterized by measuring the wetting forces during immersing and withdrawing the tube into a liquid pool. However, there was no evident link between CHF and wettability measurements to describe the similarities or differences in CHF performance for all measurement results.

The flow boiling appearance of the micro-channel structured tube was similar to the smooth tube, however, a capillary effect of the micro-channels was noticeable in a decreased advancing contact angle. On



the other hand, the oxidized surface had no remarkable capillary effect, but showed an considerable increased number of nucleation sites because of cracks in the layer. The porous layers combined both effects of capillarity and a large number of nucleation sites producing very small bubbles.

Thus, from the comparison of the CHF values with the characteristics of surface wettability and flow boiling performance resulted that CHF might be increased by surface modifications providing capillarity and/or increased number of nucleation sites.

Regarding the application of the nuclear power reactor, it has to be emphasized that the pressure and the mass flux are significantly higher during reactor operating conditions, see Fig. 1.1. The present investigations focused on the realization of surface structures on the zircaloy cladding tube and their behavior in flow boiling at low pressure conditions. Due to the differences in fluid properties a general statement for the behavior at higher pressure conditions is not possible. However, considering the tendencies of the presented results, a positive effect on CHF using the structures with micro-channels, porous or oxidized layers at higher pressure might be assumed.

### 10.1. Proposals for Future Work

As a next step in the CHF studies extension to mass fluxes similar to reactor conditions ( $1000\text{-}4000\text{ kg}/(\text{m}^2\text{s})$ ) at the highest pressure ( $300\text{-}400\text{ kPa}$ ) applicable in COSMOS-test facility is proposed. It should be noted that higher mass fluxes require modifications of the temperature measurement module or an alternative measurement system due to higher temperatures.

Results of the current study indicate that micro-channel, porous layer and oxidized layer structures are of main interest for the future investigations as they provide the highest improvement of the CHF compared to the technically smooth tube. Concerning the structure geometry a variation of the channel geometry and orientation could be interesting, as well as applicability of other structures, e.g. micro-pins, sintered coatings with channels or scratches in the surface similar to the crack texture of the oxidized layer.

The influence of the tube material could be also investigated by using smooth and structured tubes made of inconel or stainless steel, for instance. If the material influence is insignificant, then further investigations of surface structures could be conducted with other materials than zircaloy. The advantage will certainly be a better handling for the combination with other materials thus making the test section design less complex. However, the manufacturing processes of surface modifications shall be still tested for the application on zircaloy cladding tubes.

Unfortunately, a transfer of the structure influence from low to high pressures was not possible in this study due to experimental restrictions. However, the construction of a high pressure test facility at KIT/IKET will allow CHF investigations for fuel rod bundles for pressures up to 150 bar, thus covering the complete range of prototypical reactor conditions and providing a high flexibility by comparing the results from the low pressure and high pressure steam/water loops.



## A. Piping and Instrumentation Diagram

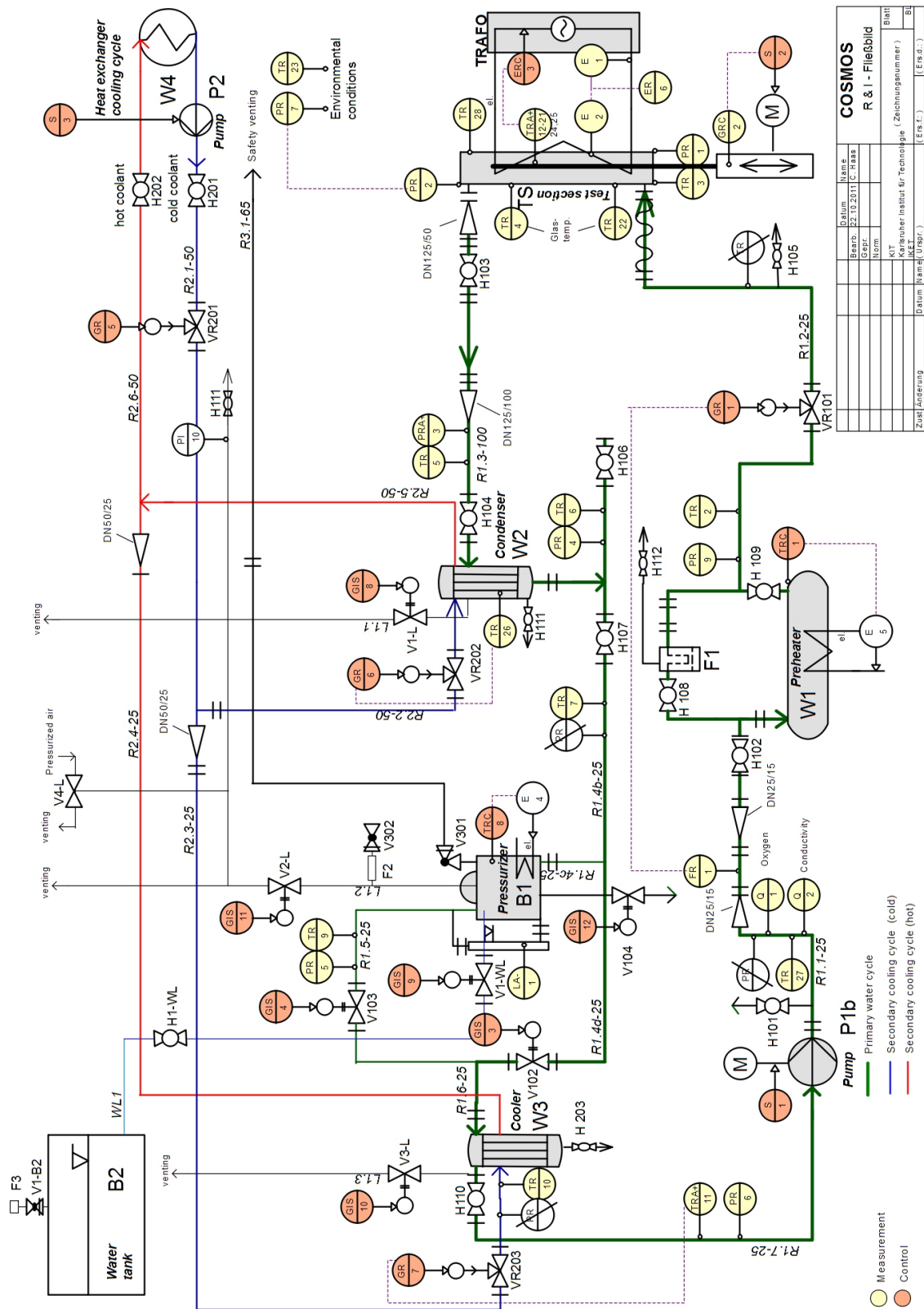


Figure A.1.: Piping and Instrumentation (P&I) diagram for test facility COSMOS

## B. Electric heating of Zircaloy tube

The direct electric heating of the zircaloy tube considering the temperature profile and the power profile was studied in air environment by *Coerdts* in his master thesis [26]. Since the cross sectional area of the heated zircaloy tube is constant over the length, it is assumed to have a uniform axial power profile, meaning that the same heat energy is transferred from every surface location. In other words, the axial heat flux is considered as constant over the length. In order to prove this assumption we made infrared (IR) photographs of the heated test section in air environment and compared the measured temperature profile with calculated results. The complete details of the measurement and calculation are explained in [26]. The main results are shown in the following.

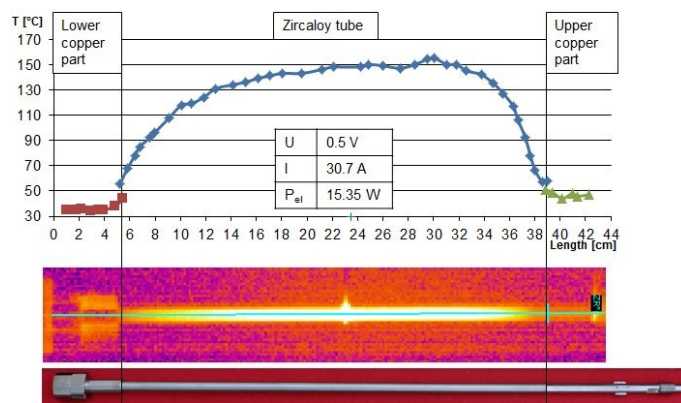


Figure B.1.: Temperature profile of heated zircaloy tube with lower and upper copper part resulting from IR-picture

Figure B.1 shows the IR-picture of the heated test tube and the resulting axial temperature profile. The test tube was in an upright position during the measurement, but is pictured horizontally in Fig. B.1. The outer glass tube and the water in the ring gap are impermeable for infrared radiation, therefore, the temperature profile of the inner heated tube of the annulus could not be measurement via IR during flow boiling.

Instead, the zircaloy test tube with the connected copper parts at both ends was heated and photographed in air environment. Like in the experiments, the tube was heated directly by electric current (AC). However, without the cooling effect of flowing water the temperature of the tube increases already for low voltage and current values. Consequently, we used a transformer for lower AC-power ranges for the heating. The tube temperature was kept below 200 °C , otherwise the zircaloy surface would oxidize at air changing the emission coefficient of the surface which is an important factor for the IR temperature measurement. Indeed, the surface temperature also ranges between 100 and 200 °C for the applied parameters during the flow boiling experiments. As temperature references each one thermocouple was positioned at the surface of the lower copper part, the zircaloy tube, and the upper copper part. For the evaluation of the temperature from the IR picture, the determined emission coefficient had to be considered separately for each material.

Additionally, the axial temperature profile was calculated for the heating condition at air. According to the electric power, the thermal conduction and the heat transfer into the surrounding air environment, the axial

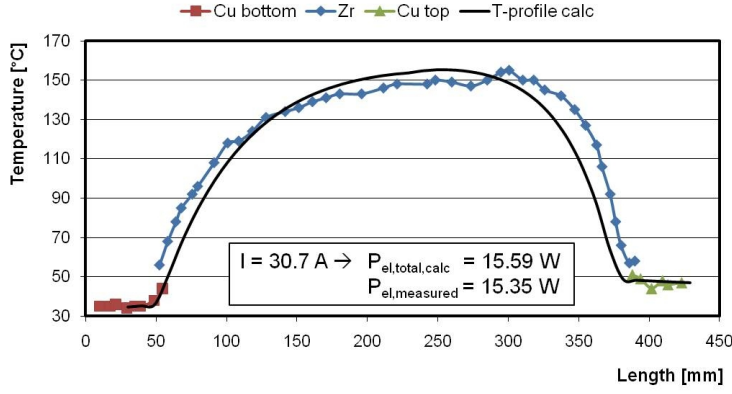


Figure B.2.: Calculated and measured axial temperature profile for an applied electrical current of 30.7 A

surface temperature profile is developed. The given parameters for the calculation were the electric current, the environment temperature and the boundary temperatures of the lower and upper copper part, as well as the material properties like emission coefficient, specific electrical resistance and thermal conductivity. The test tube is partitioned into segments and the axial temperature profile results from solving iteratively the steady state energy equation for each segment, Eqn. (B.1), which includes the electrical heat input  $\dot{Q}_{el,i}$ , the heat dissipation into the environment by convection  $\dot{Q}_{conv,i}$  and radiation  $\dot{Q}_{rad,i}$  and the axial heat conduction  $\dot{Q}_{cond,i}$ .

$$\frac{dH_i}{dt} = 0 = \dot{Q}_{el,i} - \dot{Q}_{conv,i} - \dot{Q}_{rad,i} - \dot{Q}_{cond,i} \quad (\text{B.1})$$

The heat input by the electrical power depends on the resistance of the test section. Equation B.2 describes the proportional relationship between the electric power and the square of the resistance.

$$P_{el} = \dot{Q}_{el} = IU = I^2 R \quad (\text{B.2})$$

The resistance in Eq. (B.3) depends on the electric resistivity  $\rho_{el}$  of the material and the geometry described by the length  $L$  and the cross section  $A$ .

$$R = \rho_{el} \cdot \frac{l}{A} \quad (\text{B.3})$$

Moreover, the resistivity is a function of the temperature with linear relationship given by Eqn. (B.4).

$$\rho(T) = \rho_{el}(T_0) (1 + \alpha_{el} (T - (T_0))) \quad (\text{B.4})$$

where  $\alpha_{el}$  is the temperature coefficient and  $\rho(T_0)$  is the resistivity of any reference temperature  $T_0$ . This linearity is only valid for a limited temperature range. For metals, however, the considered temperatures below 200 °C are covered by the linear range.

Combining the resistivity from Eqn. (B.4) with the electrical power Eqn. (B.2) leads to the following equation (B.5) for the electrical heat input into the segment  $i$  as a function of the local temperature  $T_i$  and the supplied electric current  $I$ .

$$\dot{Q}_{el,i} = I^2 \rho_{el}(T_0) (1 + \alpha_{el} (T_i - (T_0))) \frac{\Delta x_i}{A} \quad (\text{B.5})$$

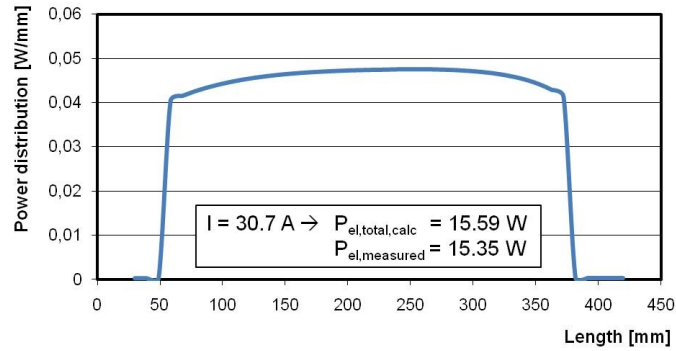


Figure B.3.: Calculated axial power distribution per length for an electrical current of 30.7 A

The resulting temperature profile in Fig B.2 is in agreement with the measured IR profile. The calculated axial power per length profile shows on the one hand the almost constant power input in the heated section. On the other hand, it is evident that the power is mainly released in the zircaloy tube. The power input in the copper parts is insignificant because of the much lower electric resistivity, like it is explained in chapter 4.2.1. Giving an supplied electric current of 30.7 A, the calculated power value of 15.59 W confirms the measured value of 15.35 W. More calculation results are discussed by Coerdts [26].





## **C. Tables of measurements**

Table C.1.: CHF mean values - small annulus - smooth

Tube	L	$d_i$	$d_o$	$d_{he}$	$L/d_{he}$	G	$P_{out}$	$T_m$	$\dot{q}_{CHF}$	$X_{th,out}$	$T_{out}$	$p_{in}$	$\Delta p$
	mm	mm	mm	mm		$\text{kg}/(\text{m}^2\text{-s})$	kPa	$^{\circ}\text{C}$	$\text{MW}/\text{m}^2$		$^{\circ}\text{C}$	kPa	kPa
smooth	326	9.5	13	8.3	39.3	252	114.9	43.9	0.66	0.073	103.2	123.7	8.8
smooth	326	9.5	13	8.3	39.3	246	115.8	64.1	0.84	0.165	104.2	131.1	15.3
smooth	326	9.5	13	8.3	39.3	253	114.7	79.1	0.67	0.138	103.9	127.4	12.7
smooth	326	9.5	13	8.3	39.3	405	113.4	44.4	1.05	0.071	103.7	130.3	16.8
smooth	326	9.5	13	8.3	39.3	409	116.1	64.6	1.31	0.151	104.3	158.0	41.8
smooth	326	9.5	13	8.3	39.3	402	115.9	79.5	1.06	0.140	104.3	139.7	23.7
smooth	326	9.5	13	8.3	39.3	407	143.1	44.1	1.11	0.068	110.6	162.7	19.6
smooth	326	9.5	13	8.3	39.3	405	200.6	59.4	1.08	0.074	121.8	222.3	21.6
smooth	326	9.5	13	8.3	39.3	406	298.2	73.2	1.27	0.109	135.6	331.7	33.5
smooth	326	9.5	13	8.3	39.3	595	111.4	44.4	1.59	0.078	103.1	135.8	24.4
smooth	326	9.5	13	8.3	39.3	595	114.2	64.5	1.93	0.155	103.8	179.0	64.8
smooth	326	9.5	13	8.3	39.3	599	111.4	79.2	1.65	0.149	103.0	178.3	66.9
smooth	326	9.5	13	8.3	39.3	598	141.5	44.2	1.47	0.050	110.1	162.0	20.5
smooth	326	9.5	13	8.3	39.3	1000	114.4	44.4	2.35	0.054	103.9	164.9	50.5
smooth	326	9.5	13	8.3	39.3	976	119.0	64.4	2.83	0.128	105.0	240.6	121.5
smooth	326	9.5	13	8.3	39.3	976	113.2	79.3	2.61	0.143	103.5	246.9	133.8
smooth	326	9.5	13	8.3	39.3	971	198.3	59.9	2.39	0.061	121.6	247.0	48.7
smooth	326	9.5	13	8.3	39.3	970	296.8	73.3	2.39	0.062	135.5	348.9	52.1

Table C.2.: CHF mean values - large annulus - smooth, nanorough, hemispherical

Tube	L	$d_i$	$d_o$	$d_{he}$	$L/d_{he}$	G	$P_{out}$	$T_{in}$	$\dot{q}_{CHF}$	$X_{th,out}$	$T_{out}$	$P_{in}$	$\Delta P$
	mm	mm	mm	mm		kg/(m <sup>2</sup> s)	kPa	°C	MW/m <sup>2</sup>		°C	kPa	kPa
smooth	326	9.5	18	24.6	13.2	254	118.4	44.6	1.13	-0.007	99.8	126.2	7.8
smooth	326	9.5	18	24.6	13.2	255	118.7	64.2	0.97	0.015	105.0	127.8	9.1
smooth	326	9.5	18	24.6	13.2	254	118.4	78.9	0.82	0.029	105.2	127.2	8.8
smooth	326	9.5	18	24.6	13.2	253	154.0	52.4	1.09	-0.010	106.1	163.1	9.0
smooth	326	9.5	18	24.6	13.2	250	154.3	71.9	0.98	0.018	113.0	165.3	11.0
smooth	326	9.5	18	24.6	13.2	252	198.5	79.5	0.94	0.012	120.9	211.2	12.7
smooth	326	9.5	18	24.6	13.2	249	248.1	86.7	1.05	0.024	128.7	265.4	17.3
smooth	326	9.5	18	24.6	13.2	251	298.4	92.7	1.22	0.039	135.5	320.9	22.6
smooth	326	9.5	18	24.6	13.2	401	118.0	45.0	1.55	-0.019	93.5	126.0	8.0
smooth	326	9.5	18	24.6	13.2	402	119.1	64.6	1.22	-0.003	102.5	127.7	8.6
smooth	326	9.5	18	24.6	13.2	401	118.2	79.1	1.02	0.012	104.8	127.8	9.6
smooth	326	9.5	18	24.6	13.2	401	154.2	72.3	1.25	-0.001	110.8	165.7	11.5
smooth	326	9.5	18	24.6	13.2	399	198.6	80.0	1.19	-0.005	116.9	211.1	12.5
smooth	326	9.5	18	24.6	13.2	398	248.9	87.2	1.31	0.003	127.0	263.7	14.8
smooth	326	9.5	18	24.6	13.2	399	298.7	92.7	1.34	0.003	133.2	320.3	21.7
nanorough	326	9.5	18	24.6	13.2	248	118.9	64.3	0.89	0.009	104.6	125.8	6.9
nanorough	326	9.5	18	24.6	13.2	249	198.3	79.5	0.92	0.012	120.5	208.4	10.0
nanorough	326	9.5	18	24.6	13.2	250	297.1	92.6	1.11	0.030	134.8	318.7	21.6
nanorough	326	9.5	18	24.6	13.2	397	118.5	64.3	1.18	-0.005	100.7	126.0	7.5
nanorough	326	9.5	18	24.6	13.2	400	198.0	79.6	1.22	-0.004	117.1	209.7	11.7
nanorough	326	9.5	18	24.6	13.2	398	298.2	93.1	1.35	0.004	132.8	316.5	18.3
hemispherical	326	9.5	18	24.6	13.2	249	118.7	63.9	0.91	0.010	104.7	126.4	7.7
hemispherical	326	9.5	18	24.6	13.2	248	197.9	79.5	0.92	0.012	120.5	210.0	12.1
hemispherical	326	9.5	18	24.6	13.2	249	297.8	92.6	1.17	0.035	135.1	321.4	23.6
hemispherical	326	9.5	18	24.6	13.2	400	118.9	64.4	1.20	-0.004	101.4	127.1	8.2
hemispherical	326	9.5	18	24.6	13.2	398	198.2	79.4	1.17	-0.007	115.1	210.8	12.6
hemispherical	326	9.5	18	24.6	13.2	400	298.4	92.9	1.47	0.011	133.8	318.5	20.1

Table C.3.: CHF mean values - large annulus - micro-channel, porous-50, porous-100, oxidized

Tube	L	$d_i$	$d_o$	$d_{he}$	$L/d_{he}$	G	$P_{out}$	$T_{in}$	$\dot{q}_{CHF}$	$X_{th,out}$	$T_{out}$	$P_{in}$	$\Delta P$
	mm	mm	mm	mm		kg/(m <sup>2</sup> s)	kPa	°C	MW/m <sup>2</sup>		°C	kPa	kPa
micro-channel	326	9.5	18	24.6	13.2	248	118.9	64.2	1.02	0.021	104.8	127.2	8.3
micro-channel	326	9.5	18	24.6	13.2	248	153.4	72.3	0.99	0.020	112.5	163.1	9.7
micro-channel	326	9.5	18	24.6	13.2	250	198.6	79.3	1.11	0.029	121.0	212.8	14.2
micro-channel	326	9.5	18	24.6	13.2	249	248.6	86.8	1.11	0.029	128.1	270.7	22.1
micro-channel	326	9.5	18	24.6	13.2	249	298.0	92.9	1.13	0.032	134.6	322.4	24.5
micro-channel	326	9.5	18	24.6	13.2	400	117.9	64.2	1.33	0.003	103.6	126.4	8.5
micro-channel	326	9.5	18	24.6	13.2	397	154.0	72.0	1.38	0.007	111.8	164.3	10.3
micro-channel	326	9.5	18	24.6	13.2	399	198.7	79.1	1.47	0.010	120.2	212.5	13.8
micro-channel	326	9.5	18	24.6	13.2	400	248.4	87.2	1.61	0.020	128.3	268.4	20.0
micro-channel	326	9.5	18	24.6	13.2	400	298.2	92.8	1.73	0.026	134.7	316.2	18.0
porous-50	326	9.5	18	24.6	13.2	250	118.2	64.1	0.92	0.011	104.5	126.1	7.8
porous-50	326	9.5	18	24.6	13.2	248	197.3	79.4	1.18	0.037	121.2	211.2	13.9
porous-50	326	9.5	18	24.6	13.2	249	297.1	92.4	1.33	0.051	135.2	320.0	22.9
porous-50	326	9.5	18	24.6	13.2	400	118.2	64.3	1.21	-0.004	101.9	126.0	7.8
porous-50	326	9.5	18	24.6	13.2	399	198.6	79.4	1.48	0.012	120.6	212.5	14.0
porous-50	326	9.5	18	24.6	13.2	401	297.4	92.9	1.58	0.018	134.3	318.8	21.4
porous-100	315	9.5	18	24.6	12.8	248	118.6	64.4	0.97	0.014	104.4	126.2	7.6
porous-100	315	9.5	18	24.6	12.8	249	198.1	79.4	1.17	0.032	121.0	212.0	13.9
porous-100	315	9.5	18	24.6	12.8	400	118.6	64.2	1.18	-0.008	99.7	126.3	7.7
porous-100	315	9.5	18	24.6	12.8	398	198.5	79.6	1.52	0.011	120.1	212.1	13.7
oxidized	326	9.5	18	24.6	13.2	247	118.4	64.4	0.84	0.005	103.5	124.8	6.4
oxidized	326	9.5	18	24.6	13.2	248	198.4	79.1	1.15	0.033	121.0	211.1	12.8
oxidized	326	9.5	18	24.6	13.2	249	297.6	92.6	1.34	0.052	135.1	318.7	21.1
oxidized	326	9.5	18	24.6	13.2	398	119.0	64.2	1.13	-0.009	99.9	126.2	7.2
oxidized	326	9.5	18	24.6	13.2	398	199.0	79.8	1.34	0.004	119.3	210.0	11.0

## Abbreviations and Symbols

### Latin letters

$A_{cross}$	$m^2$	Cross-sectional area
$A_{heat}$	$m^2$	Heated area
$A_l$	$m^2$	Cross-sectional area of liquid phase
$A_v$	$m^2$	Cross-sectional area of vapor phase
$C, C_1-C_4$	-	Dimensionless coefficients
$C_{m/s}$	$m/s$	Dimensional coefficient
$d$	$m$	Diameter
$d_{char}$	$m$	Characteristic diameter
$d_{he}$	$m$	Heated equivalent diameter
$d_{hydr}$	$m$	Hydraulic diameter
$d_i$	$m$	Inner diameter of annular cross section
$d_o$	$m$	Outer diameter of annular cross section
$d_{50}$	$m$	Median particle diameter
$D_B$	$m$	Diameter of bubble or vapor blanket
$D_{B,crit}$	$m$	Critical bubble diameter
$f_1, f_4$	-	Correction factors for CHF look-up table
$F_{buoyancy}$	$N$	Buoyancy force
$F_G$	$N$	Gravitational force
$F_M$	$N$	Momentum force
$F_{measured}$	$N$	Measured force of Wilhelmy method
$F_{total}$	$N$	Total force of Wilhelmy method
$F_{wet}$	$N$	Wetting (or Wilhelmy) force
$F_{wet,a}$	$N$	Wetting force for advancing contact angle
$F_{wet,r}$	$N$	Wetting force for receding contact angle
$F_\sigma$	$N$	Surface tension force
$g$	$m^2/s$	Standard gravitational acceleration
$g_{loc}$	$m^2/s$	Local gravitational acceleration
$G$	$kg/m^2s$	Mass flux
$h_l$	$kJ/kg$	Specific enthalpy of liquid
$h_{l,in}$	$kJ/kg$	Specific enthalpy of liquid at inlet
$h_{l,out}$	$kJ/kg$	Specific enthalpy of liquid at outlet
$h_{l,1}, h_{l,2}$	$kJ/kg$	Specific enthalpy of liquid at axial position $z_1$ and $z_2$

C. Tables of measurements

---

$h_v$	$kJ/kg$	Specific enthalpy of vapor
$h'$	$kJ/kg$	Specific enthalpy of saturated liquid
$h'_{out}$	$kJ/kg$	Specific enthalpy of saturated liquid at outlet
$h''$	$kJ/kg$	Specific enthalpy of saturated vapor
$\Delta h_{in}$	$kJ/kg$	Inlet subcooling in terms of enthalpy difference
$\Delta h_v$	$kJ/kg$	Enthalpy of evaporation
$\Delta h_{v,out}$	$kJ/kg$	Enthalpy of evaporation at outlet pressure conditions
$\Delta h_{v,2}$	$kJ/kg$	Enthalpy of evaporation at pressure conditions of axial position $z_2$
$H$	$kJ$	Enthalpy
$H_{magn}$	$A/m$	Magnetic field strength
$H_B$	$m$	Height of vapor bubble or blanket
$I$	$A$	Current intensity
$I_{Fluke}$	$A$	Current intensity measured with Fluke multimeter
$I_{max}$	$A$	Maximum value of current intensity
$k_p$	–	Correction factor for the pressure influence on CHF in annuli
$k_s$	–	Correction factor for the gap size influence on CHF in annuli
$k_x$	–	Correction factor for the vapor mass quality influence on CHF in annuli
$K$	–	Dimensionless coefficient
$K_i$	–	Dimensionless coefficient with counting variable $i$
$l^*$	–	Dimensionless geometry parameter
$L$	$m$	Length of heated channel
$L_{topography}$	$m$	Effective length measured with topographical methods
$L_{wet}$	$m$	Wetted length
$\dot{M}$	$kg/s$	Mass flow rate
$\dot{M}_l$	$kg/s$	Mass flow rate of liquid phase
$\dot{M}_v$	$kg/s$	Mass flow rate of vapor phase
$n$	%	Relative pump rotation speed
$n_{act}$	$1/m^2$	Number of active nucleation sites per surface area
$n_{cav}$	$1/m^2$	Number of micro-cavities per surface area
$p$	$kPa$	Pressure
$p_{in}$	$kPa$	Pressure at inlet
$p_{out}$	$kPa$	Pressure at outlet
$p_{ref}$	$kPa$	Pressure of reference sensor for calibration
$p_1, p_2$	$kPa$	Pressure at axial position $z_1$ and $z_2$
$\Delta p$	$kPa$	Pressure difference
$P_{el}$	$W$	Electrical power
$P_{el,Fluke}$	$W$	Electrical power measured with Fluke multimeters
$P_{el,input}$	$W$	Electrical power signal at wattmeter input

---

$P_{el,output}$	$W$	Electrical power signal at wattmeter output
$P_{el,wattmeter}$	$W$	Electrical power measured wattmeter
$P_{geom}$	$m$	Geometrical perimeter
$P_{heat}$	$m$	Heated perimeter
$P_{max}$	$W$	Maximum value of electrical power
$P_{wet}$	$m$	Wetted perimeter
$\dot{Q}$	$W$	Heat energy
$\dot{Q}_{energy-equ}$	$W$	Heat energy calculated with energy balance
$\dot{Q}_{loss}$	$W$	Dissipated heat
$\dot{q}$	$W/m^2$	Heat flux
$\dot{q}_{CHF}$	$W/m^2$	Critical heat flux
$\dot{q}_{CHF,f1}, \dot{q}_{CHF,f4}$	$W/m^2$	Critical heat flux values corrected with factors $f_1$ and $f_4$
$\dot{q}_{CHF,sat}$	$W/m^2$	Critical heat flux for saturated conditions
$\dot{q}_{CHF,smooth}$	$W/m^2$	Critical heat flux of smooth surface tube
$\dot{q}_{CHF,struct}$	$W/m^2$	Critical heat flux of structured surface tube
$\Delta\dot{q}_{CHF}$	$W/m^2$	Difference in CHF between structured and smooth surface tubes
$\dot{q}_{CHF,8}$	$W/m^2$	Critical heat flux for 8 mm diameter tube
$\dot{q}_{exp}$	$W/m^2$	Experimental critical heat flux result
$\dot{q}_I$	$W/m^2$	Heat flux at vapor-liquid interface
$\dot{q}_{LUT}$	$W/m^2$	Critical heat flux derived from look-up table
$\dot{q}_i^*$	-	Dimensionless critical heat flux with counting variable $i$
$r$	$m$	Radius
$R_{TS}$	$\Omega$	Electrical resistance of heated tube in test section
$s$	$m$	Gap width
$S$	-	Slip velocity ratio between vapor and liquid phase
$t$	$s$	Time
$T$	$^{\circ}C$	Temperature
$T_{f,bulk}$	$^{\circ}C$	Bulk temperature of fluid
$T_{in}$	$^{\circ}C$	Temperature at inlet
$T_{i,tube}$	$^{\circ}C$	Particular wall temperature of heated tube with index $i$
$T_l$	$^{\circ}C$	Temperature of liquid
$T_{l,out}$	$^{\circ}C$	Temperature of liquid at outlet
$T_{l,1}, T_{l,2}$	$^{\circ}C$	Liquid temperature at axial position $z_1$ and $z_2$
$T_{max}$	$^{\circ}C$	Temperature trigger for CHF detection
$T_{ref}$	$^{\circ}C$	Temperature of reference sensor for calibration
$T_{sat}$	$^{\circ}C$	Saturation temperature
$T_v$	$^{\circ}C$	Temperature of vapor
$T_w$	$^{\circ}C$	Wall temperature

### C. Tables of measurements

---

$T_{w,z}$	$^{\circ}\text{C}$	Wall temperature at axial position $z$
$\Delta T$	$K$	Temperature difference
$\Delta T_w$	$K$	Wall superheat
$\Delta T_{sub}$	$K$	Subcooling condition in terms of temperature difference
$u$	$m/s$	Velocity
$U$	$V$	Voltage
$U_A$	$V$	Applied voltage at secondary circuit of power supply
$U_{Fluke}$	$V$	Voltage measured with Fluke multimeter
$U_{max}$	$V$	Maximum value of voltage
$U_{TS}$	$V$	Voltage at test section
$u_l$	$m/s$	Velocity of liquid phase
$u_v$	$m/s$	Velocity of vapor phase
$x_{CHF}$	$kg/kg$	Vapor mass quality at critical heat flux
$x_{th}$	$kg/kg$	Thermodynamic vapor mass quality
$x_{th,i}, x_{th,i+1}$	$kg/kg$	Thermodynamic vapor mass qualities of iteration steps $i$ and $i + 1$
$x_{th,in}$	$kg/kg$	Thermodynamic vapor mass quality at inlet
$x_{th,out}$	$kg/kg$	Thermodynamic vapor mass quality at outlet
$x_2$	$kg/kg$	Vapor mass quality at axial position $z_2$
$x'$	$kg/kg$	Subchannel vapor mass quality
$\Delta x'$	$kg/kg$	Additional vapor mass quality in subchannel approach
$z$	—	Axial coordinate
$z_{in}$	—	Axial coordinate of heated section inlet
$z_{out}$	—	Axial coordinate of heated section outlet
$z_1, z_2$	—	Axial coordinate of position 1 and 2

### Greek letters

$\alpha$	$W/(m^2K)$	Heat transfer coefficient
$\delta$	$m$	Microlayer thickness
$\varepsilon$	$m^3/m^3$	Void fraction
$\varepsilon_{hom}$	$m^3/m^3$	Void fraction for homogeneous two-phase flow (S=1)
$\gamma$	$^{\circ}$	Surface inclination angle
$\theta$	$^{\circ}$	Static contact angle
$\theta_a$	$^{\circ}$	Advancing contact angle
$\theta_r$	$^{\circ}$	Receding contact angle
$\rho_{2ph}$	$kg/m^3$	Two-phase mixture density
$\rho_l$	$kg/m^3$	Density of liquid phase
$\rho_v$	$kg/m^3$	Density of vapor phase
$\rho^*$	—	Dimensionless density parameter: ratio of vapor and liquid density
$\rho'$	$kg/m^3$	Density of saturated liquid phase



---

$\rho''$	$kg/m^3$	Density of saturated vapor phase
$\sigma$	$N/m$	Surface tension
$\sigma^*$	-	Dimensionless surface tension
$\tau_B$	$s$	Passage time of vapor blanket
$\tau_{shear}$	$N/m^2$	Shear stress
$\Delta\tau_d$	$s$	Period to bubble departure
$\Delta\tau_w$	$s$	Period to bubble activation
$\zeta$	-	Friction factor

## Abbreviations

an	Annulus
AC	Alternating current
BWR	Boiling Water Reactor
CAD	Computer-Aided Design
CHF	Critical heat flux
CNC	Computerized Numerical Control
Comp	Comparison
Corr	Correlation
COSMOS	<u>C</u> ritical-heat-flux <u>O</u> n <u>S</u> mooth and <u>M</u> odified <u>S</u> urfaces
CWL	Chromatic white light
DC	Direct current
DSM	Direct substitution method
EFI	Extended Focal Imaging
Exp	Experiment
F	Flow meter
FRT	Fries Research and Technology
H1	Hand valve between pump and preheater
HBM	Heat balance method
IAM-AWP	Institute for Applied Materials, Karlsruhe Institute of Technology
IFAM	Institute for Manufacturing Technology and Advanced Materials, Fraunhofer-Institut Dresden
IKET	Institute for Nuclear and Energy Technologies, Karlsruhe Institute of Technology
IMVT	Institute for Micro Process Engineering, Karlsruhe Institute of Technology
JSME	Japanese Society of Mechanical Engineering
KIT	Karlsruhe Institute of Technology

### C. Tables of measurements

---

LUT	Look-up table
LWR	Light Water Reactor
Max	Maximum
no	Number
OFI	Onset of Flow Instability
ONB	Onset of Nucleate Boiling
PEEK	Polyether ether ketone (thermoplastic)
P&I	Piping and Instrumentation
PVD	Physical Vapor Deposition
PTFE	Polytetrafluoroethylene (thermoplastic)
PWR	Pressurized Water Reactor
rms	root mean square
SEM	Scanning Electron Microscope
Std	Standard
therm	Thermodynamic
TS	Test section
V1	Throttle valve upstream of test section

## List of Figures

1.1	Comparison of the main conditions realized in the current work to typical LWR conditions . . .	2
2.1	Cross section of annular geometry . . . . .	3
2.2	Draft of flow boiling in internally heated annulus . . . . .	5
2.3	Qualitative boiling curve for a heating power controlled system . . . . .	7
2.4	Qualitative boiling curve for a surface temperature controlled system . . . . .	7
2.5	Schematic pressure drop-mass flux curve . . . . .	8
2.6	Two-phase pressure drop curve and pump characteristic . . . . .	10
2.7	Relationship between boiling and pressure drop curve . . . . .	11
2.8	Pressure dependency of density ratio between liquid and vapor phase of saturated water . . .	12
3.1	Single bubble attached to heated surface as basic situation for the model of <i>Kandlikar</i> [51] .	18
3.2	Subcooled core flow with liquid superheated layer as basic situation for model of <i>Celata et al.</i> [20] . . . . .	22
3.3	Industrially manufactured structured surfaces . . . . .	23
3.4	Kinds of boiling inside a porous layer after Malysenko [70] . . . . .	24
4.1	3D-CAD image of the test facility COSMOS . . . . .	30
4.2	Pictures of the COSMOS test facility (left) and the test section (right) . . . . .	30
4.3	Process flow diagram of COSMOS thermo-hydraulic test facility . . . . .	31
4.4	Test section design . . . . .	33
4.5	Test tube with lower and upper interference between the zircaloy tube and nickel-plated copper parts. . . . .	35
4.6	Arrangement for bundle and annular test section . . . . .	36
4.7	Measurement module to determine the wall temperature . . . . .	38
4.8	Design of the measuring head . . . . .	38
4.9	Principle mounting of a thermocouple which is sealed and isolated from sheath . . . . .	39
4.10	Schematic draft of test section power supply . . . . .	40
4.11	Sketch of a cut sinusoidal voltage or current signal . . . . .	40
4.12	Calibration measurement points and approximation curve . . . . .	44
4.13	Control configuration and program scheme . . . . .	45
4.14	Example of important parameters during critical heat flux experiment . . . . .	47
4.15	Time depending power input and oxygen content for a typical operation of a critical heat flux experiment . . . . .	47
5.1	Characteristic pump curves . . . . .	52
5.2	SEM pictures of PVD coated nanorough wafer . . . . .	53

5.3	Light microscope picture of hemispherical structure . . . . .	54
5.4	Micro-channel structure on zircaloy tube . . . . .	56
5.5	Surface appearance of porous layer . . . . .	57
5.6	Surface appearance of porous layer . . . . .	59
5.7	Zircaloy tube with light brown oxidized layer of 90 $\mu\text{m}$ thickness (Pictures from AREVA NP Technical Center) . . . . .	60
5.8	SEM images of oxidized layer surface which is divided into polygonal sections by cracks (Pictures from AREVA NP Technical Center) . . . . .	60
5.9	SEM images of polished cut of oxidized layer (left) and top view on a mechanically spalled area (middle and right) (Pictures from AREVA NP Technical Center) . . . . .	60
5.10	Krüss Tensiometer K100C with mounted smooth tube at balance . . . . .	62
5.11	Schematic draft of receding contact angle measurement with Wilhelmy method . . . . .	62
5.12	Qualitative force measurement over immersion depth for force tensiometry . . . . .	62
5.13	Development from base profile length to effective length . . . . .	63
5.14	Wetted lengths of surface structured tubes compared to smooth tube . . . . .	64
5.15	Test tube in topography apparatus . . . . .	65
5.16	3D topographical images of smooth zircaloy tube determined by chromatic white light sensor technique . . . . .	65
5.17	3D-image of micro-channel structure using chromatic white light sensor technique . . . . .	66
5.18	2D profile of hemispherical structure using light microscope . . . . .	67
5.19	Wetting force for advancing and receding behavior on dry surface in first measurement cycle	68
5.20	Wetting force for advancing and receding behavior on wet surface in second measurement cycle . . . . .	69
5.21	Advancing and receding contact angle of first measurement cycle with dry surface . . . . .	69
5.22	Advancing and receding contact angle of second measurement cycle with wet surface . . . . .	70
6.1	Characteristic pump curves . . . . .	74
6.2	Combined pressure drop curve for decreasing pump rotation speed . . . . .	75
6.3	Combined pressure drop curve for closing throttle valve . . . . .	75
6.4	Two-phase pressure drop across test section . . . . .	76
6.5	Pressure drop across the test section for 16 kW . . . . .	78
6.6	Time dependent curves before CHF at 16 kW for unstable conditions . . . . .	78
6.7	Influence of pressure drop at inlet throttle valve V1 on the CHF . . . . .	78
6.8	Influence of steep pump curve and pressure drop at inlet throttle on two-phase system with constant heat input . . . . .	80
7.1	Heat input at CHF against mass flow rate for smooth tube in small and large annulus at 110-121 kPa . . . . .	83
7.2	All CHF-results at constant outlet pressure (110-121 kPa) for smooth tube in small annulus .	83
7.3	All CHF-results at constant outlet pressure (117-120 kPa) for smooth tube in large annulus .	83
7.4	Comparison of CHF results with literature data . . . . .	84
7.5	CHF measurements for different tubes at the same parameter set . . . . .	85

7.6	Axial position of CHF detection in dependency of mass flux and inlet temperature for outlet pressure of 115 kPa . . . . .	86
7.7	CHF position for all measurements of smooth tube in small and large annulus . . . . .	86
7.8	CHF locations on test tube used in small annulus . . . . .	87
7.9	CHF against inlet temperature at 115 kPa for smooth tube in small annulus . . . . .	88
7.10	CHF against inlet temperature at 119 kPa for smooth tube in large annulus . . . . .	88
7.11	CHF against exit vapor mass quality for small and large annulus at 115-119 kPa . . . . .	90
7.12	CHF against vapor quality at CHF for smooth tube in small annulus . . . . .	91
7.13	CHF against real vapor quality for smooth tube in large annulus . . . . .	91
7.14	Comparison of low pressure (100-600 kPa) and high pressure (980-14100 kPa) CHF behavior for internally heated annuli . . . . .	91
7.15	Void fraction against quality . . . . .	93
7.16	Void fraction against quality . . . . .	93
7.17	Pressure drop across test section against heat input for smooth tube . . . . .	94
7.18	CHF against outlet pressure at subcooling of 250-270 kJ/kg for smooth tube in small annulus	95
7.19	CHF against outlet pressure at subcooling of 167 and 250 kJ/kg for smooth tube in large annulus . . . . .	95
7.20	Comparison of measured values with experimental data of <i>Rogers et al.</i> [85] for similar $L/d_{he}$ of 13.9 (Rogers) and 13.2 (COSMOS) . . . . .	98
7.21	Comparison of CHF measurements between COSMOS and <i>Rogers</i> for similar $d_{he}$ but different $L/d_{he}$ . . . . .	99
7.22	Influence of $L/d_{he}$ variation on CHF for constant inlet subcooling condition of 250-265 kJ/kg	99
7.23	Comparison of results for smooth tube in large annulus at 120 kPa with calculated values of the Katto&Ohno-correlation [55] . . . . .	102
7.24	Comparison of experimental data and results from look-up tables of <i>Groeneveld et al.</i> from 2006 [41] using direct substitution method and correction factors for diameter and length effects . . . . .	103
7.25	Comparison of experimental data and results from look-up tables of <i>Groeneveld et al.</i> from 1986 [42], 1995 [40], and 2006 [41] using the heat balance method . . . . .	104
7.26	Comparison of results for smooth tube in large annulus at 120 kPa with calculated values of 3-k-factor correlation Eqn. (7.10) of <i>Doerffer et al.</i> [30] using LUT1986 and LUT2006 . . . . .	106
7.27	Comparison of results for smooth tube in large annulus at 120 kPa with calculated values of rod-centered approach Eqn. (7.13) of <i>Doerffer et al.</i> [30] using LUT1986 [42] and LUT2006 [41] . . . . .	107
8.1	Comparison CHF-results between smooth and micro-channel tube in large annulus for mass fluxes of 250 and 400 kg/(m <sup>2</sup> s) . . . . .	111
8.2	Comparison of CHF-results between smooth and nanoscale rough tube in large annulus for mass fluxes of 250 and 400 kg/(m <sup>2</sup> s) . . . . .	112
8.3	Comparison of CHF-results between smooth and hemispherical structured tube in large annulus for mass fluxes of 250 and 400 kg/(m <sup>2</sup> s) . . . . .	113
8.4	Comparison of CHF-results between tube with smooth and 50 μm porous layer in large annulus for mass fluxes of 250 and 400 kg/(m <sup>2</sup> s) . . . . .	114

8.5	Comparison of CHF-results between tube with smooth and 100 $\mu m$ porous layer in large annulus for mass fluxes of 250 and 400 $kg/(m^2s)$ . . . . .	115
8.6	Comparison of CHF-results between smooth and oxidized layer tube in large annulus for mass fluxes of 250 and 400 $kg/(m^2s)$ . . . . .	116
8.7	CHF-results for all surface structured tubes at outlet pressure of 120 kPa . . . . .	117
8.8	CHF-results for all surface structured tubes at outlet pressure of 200 kPa . . . . .	118
8.9	CHF-results for all surface structured tubes at outlet pressure of 300 kPa . . . . .	118
8.10	Expanding and rewetting of a dry patch on the porous surface [34] . . . . .	120
8.11	Flow boiling image at heat flux of CHF . . . . .	121
8.12	Comparison of flow boiling images between surface structured tubes at 0.72 $MW/m^2$ for $G=250 kg/(m^2s)$ and $P=120 kPa$ . . . . .	123
8.13	Comparison of flow boiling images between surface structured tubes at 0.72 $MW/m^2$ for $G=400 kg/(m^2s)$ and $P=120 kPa$ . . . . .	124
A.1	Piping and Instrumentation (P&I) diagram for test facility COSMOS . . . . .	136
B.1	Temperature profile of heated zircaloy tube with lower and upper copper part resulting from IR-picture . . . . .	137
B.2	Calculated and measured axial temperature profile for an applied electrical current of 30.7 A . . . . .	138
B.3	Calculated axial power distribution per length for an electrical current of 30.7 A . . . . .	139

## List of Tables

2.1	Classification on dynamic instabilities . . . . .	10
3.1	Literature for CHF in annuli at low pressure and experimental parameter range . . . . .	17
4.1	General process parameters of test facility COSMOS . . . . .	31
4.2	Basic requirements for the test section concept . . . . .	32
4.3	Accuracy of measurements . . . . .	37
4.4	Comparison of different power measurement methods . . . . .	42
5.1	Overview on surface structures . . . . .	52
5.2	Zircaloy tube with technically smooth surface . . . . .	53
5.3	Nanoscale roughness on zircaloy tube . . . . .	54
5.4	Hemispherical structure on zircaloy tube . . . . .	55
5.5	Micro-channel structure on zircaloy tube . . . . .	56
5.6	Porous structure on zircaloy tube . . . . .	58
5.7	Determination of porous coated layer thickness . . . . .	58
5.8	Oxidized layer structure on zircaloy tube . . . . .	59
5.9	Comparison of perimeter results between tensiometer and topographical measurements . . . . .	67
5.10	Conditions of tensiometer measurements . . . . .	67
5.11	Differences in boundary conditions between flow boiling system and applied tensiometer measurements . . . . .	72
7.1	Comparison of the geometry details between the small and large annulus . . . . .	81
7.2	Experimental parameter range for smooth tube in small annular geometry . . . . .	82
7.3	Experimental parameter range for smooth tube in large annular geometry . . . . .	82
7.4	Deviations of experimental parameters for all conducted experiments . . . . .	85
7.5	Inlet subcooling conditions for the three different inlet temperatures at 120 kPa . . . . .	88
7.6	Comparison of experimental conditions between <i>Rogers et al.</i> [85] and present work (COSMOS) . . . . .	96
7.7	Comparison of geometry sizes between test sections of <i>Rogers et al.</i> [85] and present work (COSMOS) . . . . .	97
7.8	Empirical coefficients and parameter range for correlation of <i>Rogers et al.</i> [85] in Eqn. (7.1) . . . . .	97
7.9	Comparison of experimental data and results from look-up tables of <i>Groeneveld et al.</i> from 1986 [42], 1995 [40], and 2006 [41] using the direct substitution method . . . . .	103
8.1	Experimental parameter range for experiments with surface structures in large annulus . . . . .	109
8.2	Critical heat flux measurements with hemispherical structure tube . . . . .	110
8.3	Criteria for the comparison of CHF-results with the smooth tube results . . . . .	110

8.4	Comparison of CHF-results between smooth and micro-channel tube in large annulus . . . . .	111
8.5	Comparison of CHF-results between smooth and nano-rough tube in large annulus . . . . .	113
8.6	Comparison of CHF-results between smooth and hemispherical structured tube in large annulus . . . . .	113
8.7	Comparison of CHF-results between smooth and porous-50 tube in large annulus . . . . .	114
8.8	Comparison of CHF-results between smooth and porous-100 tube in large annulus . . . . .	115
8.9	Comparison of CHF-results between smooth and oxidized layer tube in large annulus . . . . .	116
8.10	Percentage deviation of CHF results for surface structured tubes from smooth tube results in large annulus . . . . .	117
C.1	CHF mean values - small annulus - smooth . . . . .	142
C.2	CHF mean values - large annulus - smooth, nanorough, hemispherical . . . . .	143
C.3	CHF mean values - large annulus - micro-channel, porous-50, porous-100, oxidized . . . . .	144



## Bibliography

- [1] A. Adamson. Potential distortion model for contact angle and spreading ii. temperature dependent effects. *Journal of Colloid Interface Science*, 44:273–281, 1973.
- [2] S. Ahmad and D. Groeneveld. Fluid modelling of critical heat flux in uniformly heated annuli. Report AECL-4070, Chalk River Laboratories, 1972.
- [3] H. S. Ahn, C. Lee, H. Kim, H. Jo, S. Kang, J. Kim, J. Shin, and M. Kim. Pool boiling CHF enhancement by micro/nanoscale modification of zircaloy-4 surface. *Nuclear Engineering and Design*, 240:3350–3360, 2010.
- [4] C. Ammerman and S. You. Enhancing small-channel convective boiling performance using a micro-porous surface coating. *Journal of Heat Transfer*, 123:976–983, 2001.
- [5] H. D. Baehr and K. Stephan. *Wärme- und Stoffübertragung*. Springer Verlag, 2006.
- [6] P. Barnett. A correlation of burnout data for uniformly heated annuli and its use for predicting burnout in uniformly heated rod bundles. Report AEEW-R-463, Atomic Energy Establishment Winfrith, 1966.
- [7] P. G. Barnett. A comparison of the accuracy of some correlations for burnout in annuli and rod bundles. Report AEEW-R-558, Atomic Energy Establishment Winfrith, 1968.
- [8] K. Becker, G. Hernborg, M. Bode, and O. Eriksson. Burnout data of boiling water in vertical round ducts, annuli and rod clusters. Report AE-177, Aktiebolaget Atomenergi, Sweden, 1965.
- [9] K. Becker and A. Letzter. Burnout measurements for flow of water in annulus with two-sided heating. In *European Two-Phase Flow Group Meeting*, Haifa, Israel, 1975.
- [10] J. C. Berg, editor. *Wettability*. Marcel Dekker, Inc., 1993.
- [11] A. Bergles, J. Lienhard V, G. Kendall, and P. Griffith. Boiling and evaporation in small diameter channels. *Heat Transfer Engineering*, 24(1):18–40, 2003.
- [12] A. E. Bergles. Subcooled burnout of tubes of small diameter. Paper 63-WA-182, ASME, 1963.
- [13] J. D. Bernardin, I. Mudawar, C. B. Walsh, and E. I. Franses. Contact angle temperature dependence for water droplets on practical aluminum surfaces. *International Journal of Heat and Mass Transfer*, 40(5):1017 – 1033, 1997.
- [14] V. Bobkov, N. Kozina, V. V.N., and O. Zyatnina. New model for burnout prediction in channels of various cross-section. In *The 7th International Topical Meeting on Nuclear Reactor Thermal Hydraulics (NURETH-7)*, volume 4, pages 2539–2557, 1995.

- [15] J. A. Bouré. *Two-phase Flows and Heat Transfer with Application to Nuclear Reactor Design Problems*, chapter Oscillatory Two-Phase Flows, pages 211–239. Hemisphere Publishing Corporation, 1978.
- [16] J. A. Bouré, A. E. Bergles, and L. S. Tong. Review of two-phase flow instability. *Nuclear Engineering and Design*, 25:165–192, 1973.
- [17] R. Bowring. *Heat and Fluid Flow in Water Reactor Safety*, chapter A new mixed flow cluster dryout correlation for pressure in the range 0.6-15.5 MN/m<sup>2</sup> (90-2250 psia)-for use in transient blowdown code, pages 175–182. Institute of Mechanical Engineers, 1977.
- [18] S. Braun. Planung eines versuchsstands zur untersuchung der kritischen heizflächenbelastung bei zwangskonvektion mit wasser unter hohem druck. Masterarbeit 06/03, Hochschule Karlsruhe-Technik und Wirtschaft, 2006.
- [19] G. Celata, M. Cumo, and A. Mariani. Assessment of correlations and models for the prediction of chf in water subcooled flow boiling. *International Journal of Heat and Mass Transfer*, 37(2):237 – 255, 1994.
- [20] G. Celata, M. Cumo, A. Mariani, M. Simoncini, and G. Zummo. Rationalization of existing mechanistic models for the prediction of water subcooled flow boiling critical heat flux. *International Journal of Heat and Mass Transfer*, 37, Supplement 1(0):347 – 360, 1994.
- [21] J. Chang and S. You. Enhanced boiling heat transfer from micro-porous cylindrical surfaces in saturated fc-87 and r123. *Journal of Heat Transfer*, 119:319–325, 1997.
- [22] S. Chang and W.-P. Baek. Understanding, predicting, and enhancing critical heat flux. In *Nuclear Reactor Thermal Hydraulics (NURETH-10)*, Seoul, Korea, 2003.
- [23] Y. Chang. An analysis of the critical conditions and burnout in boiling heat transfer. Report TID-14004, USAEC, Washington DC, 1961.
- [24] X. Cheng and U. Mueller. Review on critical heat flux in water cooled reactors. Wissenschaftliche Berichte FZKA 6825, Forschungszentrum Karlsruhe, 2003.
- [25] S.-Y. Chun, H.-J. Chung, S.-K. Moon, S.-K. Yang, M.-K. Chung, T. Schoesse, and M. Aritomi. Effect of pressure on critical heat flux in uniformly heated vertical annulus under low flow conditions. *Nuclear Engineering and Design*, 203(2-3):159 – 174, 2001.
- [26] F. Coerdts. Inbetriebnahme einer versuchsanlage mit niederdruckwasserkreislauf zur untersuchung der siedecharakteristik und der kritischen wärmestromdichte am überströmten beheizten rohr. Master's thesis, Karlsruhe Institute of Technology (KIT), 2010.
- [27] J. Collier and J. Thome. *Convective Boiling and Condensation*. Oxford University Press, 3rd edition, 1994.
- [28] P.-G. de Gennes, F. Brochard-Wyart, and D. Quéré. *Capillarity and Wetting Phenomena: drops, bubbles, pearls, waves*. Springer Verlag, 2004.

- [29] T. Diesselhorst, U. Grigull, and H. E. *Heat transfer in boiling*, chapter Hydrodynamic and surface effects on the peak heat flux in pool boiling, pages 99–135. Academic Press, New York, 1977.
- [30] S. Doerffer, D. C. Groeneveld, S. Cheng, and K. Rudzinski. A comparison of critical heat flux in tubes and annuli. *Nuclear Engineering and Design*, 149:167–175, 1994.
- [31] V. Doroshchuk, L. Levitan, and F. Lantsmann. Recommendations for calculating burnout in a round tube with uniform heat release. *Teploenergetika*, 22(12):66–70, 1975.
- [32] R. Duffey and E. Hughes. Static flow instability onset in tubes, channels, annuli, and rod bundles. *International Journal of Heat and Mass Transfer*, 34(10):2483–2496, 1991.
- [33] M. S. El-Genk, S. Haynes, and S. Kim. Experimental studies of critical heat flux for low flow of water in vertical annuli at near atmospheric pressure. *International Journal of Heat and Mass Transfer*, 31(11):2291–2304, 1988.
- [34] P. Enderle. Experimentelle untersuchung der siedecharakteristik an überströmten beheizten rohren mit mikrostrukturierten oberflächen. Bachelor thesis, Karlsruhe Institute of Technology, 2011.
- [35] R. Evangelisti and P. Lupoli. The void fraction in an annular channel at atmospheric pressure. *International Journal of Heat and Mass Transfer*, 12:699–711, 1969.
- [36] M. Fiori and A. Bergles. Model of critical heat flux in subcooled flow boiling. Technical Report DSR 70281-56, Massachusetts Institute of Technology, 1968.
- [37] R. Fong, G. McRae, C. Coleman, T. Nitheanandan, and D. Sanderson. Correlation between the critical heat flux and the fractal surface roughness of zirconium alloy tubes. In *Ninth International Topical Meeting on Nuclear Reactor Thermal Hydraulics (NURETH-9)*, San Francisco, California, 1999.
- [38] R. Goldschmidt. *Experimentelle Untersuchung des Einflusses von porös beschichteten Heizflächen auf vollständige Siedekennlinien von aufwärts strömendem Wasser im einseitig beheizten Rechteckkanal*. PhD thesis, Technische Universität Berlin, 2004.
- [39] D. Groeneveld. On the definition of critical heat flux margin. *Nuclear Engineering and Design*, 163:245–247, 1996.
- [40] D. Groeneveld, L. Leung, P. Kirillov, V. Bobkov, I. Smogalev, V. Vinogradov, X. Huang, and E. Royer. The 1995 look-up table for critical heat flux in tubes. *Nuclear Engineering and Design*, 163:1–23, 1996.
- [41] D. Groeneveld, J. Shan, A. Vasic, L. Leung, A. Durmayaz, J. Yang, S. Cheng, and A. Tanase. The 2006 chf look-up table. *Nuclear Engineering and Design*, 237:1909–1922, 2007.
- [42] D. C. Groeneveld, S. C. Cheng, and D. T. 1986 aecl-uo critical heat flux lookup table. *Heat Transfer Engineering*, 7(1-2):46–62, 1986.
- [43] D. C. Groeneveld, L. Leung, N. Aksan, A. Badulescu, J. Cleveland, W. P. Baek, M. Chung, F. D’Auria, X. Cheng, P. Kirillov, and J. Macek. A general method of predicting critical heat flux in

- advanced water-cooled reactors. In *Ninth International Topical Meeting on Nuclear Reactor Thermal Hydraulics (NURETH-9)*, San Francisco, California, 1999.
- [44] C. Haas, L. Meyer, and T. Schulenberg. Flow instability and critical heat flux for flow boiling of water in a vertical annulus at low pressure. In *ASME/JSME 2011 8th Thermal Engineering Joint Conference (AJTEC2011)*, number AJTEC2011-44292, March 2011.
- [45] C. Han and P. Griffith. The mechanisms of heat transfer in nucleate pool boiling, part i, bubble initiation, growth and departure. *International Journal of Heat and Mass Transfer*, 8(6):887–904, 1965.
- [46] Y. Haramura and Y. Katto. New hydrodynamic model of critical heat flux applicable widely to both pool and forced convection boiling on submerged bodies in saturated liquids. *International Journal of Heat and Mass Transfer*, 26:379–399, 1983.
- [47] G. Hetsroni, editor. *Handbook of Multiphase Systems*. Hemisphere Publishing Corporation, 1982.
- [48] E. Janssen and J. Kervinen. The critical boiling heat flux at high flows and high qualities. Report APED-4554, General Electric, 1964.
- [49] S. Kakac and H. Bon. A review of two-phase flow dynamic instabilities in tube boiling systems. *International Journal of Heat and Mass Transfer*, 51:399–433, 2008.
- [50] A. Kamura, Y. Takata, T. Hazuku, Y. Fukuhara, and T. T. Temperature dependence of surface wettability before and after  $\gamma$ -ray irradiation. In *Proceedings of The 13th International Topical Meeting on Nuclear Reactor Thermal Hydraulics*, 2009.
- [51] S. G. Kandlikar. A theoretical model to predict pool boiling chf incorporating effects of contact angle and orientation. *Journal of Heat Transfer*, 123:1071–1079, 2001.
- [52] Y. Katto. Generalized correlations of critical heat flux for the forced convection boiling in vertical uniformly heated annuli. *International Journal of Heat and Mass Transfer*, 22:575–584, 1979.
- [53] Y. Katto. A prediction model of subcooled water flow boiling chf for pressure in the range 0.1-20 mpa. *International Journal of Heat and Mass Transfer*, 35(5):1115 – 1123, 1992.
- [54] Y. Katto. Critical heat flux. *International Journal of Multiphase Flow*, 20(Supplement 1):53–90, Aug. 1994.
- [55] Y. Katto and H. Ohno. An improved version of the generalized correlation of critical heat flux for the forced convective boiling in uniformly heated round tubes. *International Journal of Heat and Mass Transfer*, 27(9):1641–1648, 1984.
- [56] S. Kim, I. Bang, J. Buongiorno, and L. Hu. Surface wettability change during pool boiling of nanofluids and its effect on critical heat flux. *International Journal of Heat and Mass Transfer*, 50(19-20):4105 – 4116, 2007.
- [57] S. Kim, B. Truong, J. Buongiorno, L. Hu, and I. Bang. Study of two-phase heat transfer in nanofluids for nuclear applications. In *International Conference on the Advances in Nuclear Power Plants*, pages 1573–1580, 2006.

- [58] R. Knobloch. Teststrecke im wasser-/dampf-kreislauf. Technical report, Karlsruhe Institute of Technology (KIT), Duale Hochschule Baden-Württemberg (DHBW), 2009. german.
- [59] D. Knoebel, S. Harris, and B. Crain. Forced convection sub-cooled critical heat flux. Report DP-1306, USAEC, 1973.
- [60] N. Kolev. *Multiphase Flow Dynamics 2*, chapter How accurately can we predict nucleate boiling?, pages 339–469. Springer Verlag, 3 edition, 2007.
- [61] A. Kon'kov. Experimental study of the conditions under which heat exchange deteriorates when a steam-water mixture flows in heated tubes. *Teploenergetika*, 13(12):53–57, 1966.
- [62] V. T. W. Kulmbach, editor. *Handbuch Wasser*. Vulkan-Verlag Essen, 9. auflage edition, 2000.
- [63] S. Kutadeladze. On the transition to film boiling under natural convection. *Kotloturbostroenie*, 3:10–12, 1948.
- [64] R. Lahey and F. Moody, editors. *The Thermal Hydraulics of a Boiling Water Nuclear Reactor*. American Nuclear Society, 1977.
- [65] C. Lee and I. Mudawar. A mechanistic critical heat flux model for subcooled flow boiling based on local bulk flow conditions. *International Journal of Multiphase Flow*, 14:711–728, 1988.
- [66] S. Liaw and V. Dhir. Effect of surface wettability on transition boiling heat transfer from a vertical surface. In T. C.L., V. Carey, and F. J.K., editors, *Proceedings of the 8th International Heat Transfer Conference*, volume 4, pages 2031–2036, San Francisco, CA U.S.A., 1986. Hemisphere Publishing Corporation.
- [67] J. Lienhard and V. Dhir. Extended hydrodynamic theory of the peak and minimum pool boiling heat fluxes. Technical Report CR-2270, NASA, 1973.
- [68] J. Lim and J. Weisman. A phenomenologically based prediction of the critical heat flux in channels containing an unheated wall. *International Journal of Heat and Mass Transfer*, 33:203–205, 1990.
- [69] W. Lowdermilk, C. Lanzo, and B. Siegel. Investigation of boiling burnout and flow stability for water flowing in tubes. Technical Report TN 4382, National Advisory Committee for Aeronautics (NACA), 1958.
- [70] S. Malysenko and M. Styrikovich. Heat transfer at pool boiling on surfaces with porous coating. In *International Symposium of Multiphase Flow and Heat Transfer*, volume 1, pages 269–284, Xi'an, China, 1989.
- [71] J. Maulbetsch and P. Griffith. Prediction on the onset of system-induced instabilities in subcooled boiling. In *Proceedings of Symposium on Two Phase Flow Dynamics*, volume 1, pages 799–825. Commission of the European Communities, 1967.
- [72] W. McAdams, W. Kennel, C. Minden, R. Carl, P. Picornell, and J. Dew. Heat transfer at high rates to water with surface boiling. *Ind. Eng. Chem.*, 41, 1949.

- [73] R. Menegus. Burnout of heating surfaces in water. Report DP-363, USAEC, 1959.
- [74] L. Meyer. From discovery to recognition of periodic large scale vortices in rod bundles as source of natural mixing between subchannels—a review. *Nuclear Engineering and Design*, 240(6):1575 – 1588, 2010.
- [75] K. Mishima and H. Nishihara. Effect of channel geometry on critical heat flux for low pressure water. *International Journal of Heat and Mass Transfer*, 30(6):1169 – 1182, 1987.
- [76] K. Mishima, H. Nishihara, and I. Michiyoshi. Boiling burnout and flow instabilities for water flow in a round tube under atmospheric pressure. *International Journal of Heat and Mass Transfer*, 28(6):1115–1129, 1985.
- [77] I. Mudawar. Two-phase micro-channel heat sinks: Theory, applications and limitations. In *ASME/JSME 2011 8th Thermal Engineering Joint Conference (AJTEC2011)*, number AJTEC2011-44005, March 2011.
- [78] S. Nukiyama. The maximum and minimum values of the heat  $q$  transmitted from metal to boiling water under atmospheric pressure. *International Journal of Heat and Mass Transfer*, 9:1419–1433, 1966.
- [79] J.-W. Park, W.-P. Baek, and S. H. Chang. Assessment of chf correlations for internally heated concentric annulus channels. *International Communications in Heat and Mass Transfer*, 23(8):1077 – 1086, 1996.
- [80] J.-W. Park, W.-P. Baek, and S. H. Chang. Critical heat flux and flow pattern for water flow in annular geometry. *Nuclear Engineering and Design*, 172:137–155, 1997.
- [81] R. Parthier. *Messtechnik*. Vieweg Verlag, 4 edition, 2008.
- [82] F. D. Petke and B. Ray. Temperature dependence of contact angles of liquids on polymeric solids. *Journal of Colloid Interface Science*, 31:216–227, 1969.
- [83] F. Philipps. Charakterisierung der oberflächeneigenschaften mikrostrukturierter rohre. Studienarbeit, Institute of Thermal Process Engineering (TVT), Karlsruhe Institute of Technology (KIT), June 2011. German.
- [84] M. E. Poniewski and J. Thome. *Nucleate Boiling on Micro-Structured Surfaces*. Heat Transfer Research, Inc. (HTRI), 2008.
- [85] J. Rogers, S. M., and A. Tahir. Flow boiling critical heat fluxes for water in a vertical annulus at low pressure and velocities. In *Proceedings of The Seventh International Heat Transfer Conference*, pages 339–344, 1982.
- [86] J. Rogers, M. Salcudean, Z. Abdullah, D. McLeod, and D. Poirier. The onset of significant void in up-flow boiling of water at low pressure and velocities. *International Journal of Heat and Mass Transfer*, 30(11):2247 – 2260, 1987.

- [87] W. Rohsenow and P. Griffith. Correlation of maximum heat transfer data for boiling of saturated liquids. *Chemical Engineering Progress*, 52:47–49, 1956.
- [88] P. Sadisavan, C. Unal, and R. Nelson. Perspective: Issues in chf modeling - the need for new experiments. *Journal of Heat Transfer*, 117:558–567, 1995.
- [89] M. Sarwar, Y. Jeong, and S. Chang. Subcooled flow boiling chf enhancement with porous surface coatings. *International Journal of Heat and Mass Transfer*, 50:3649–3657, 2007.
- [90] T. Schoesse, M. Aritomi, Y. Kataoka, S.-R. Lee, Y. Yoshioka, and M. K. Chung. Critical heat flux in a vertical annulus under low upward flow near atmospheric pressure. *Journal of Nuclear Science and Technology*, 34(6):559–570, 1997.
- [91] D. Schroeder-Richter, S. Yildiz, and G. Bartsch. Effect of porous coating on critical heat flux. *International Communications in Heat and Mass Transfer*, 23(4):463–471, 1996.
- [92] B. Shin and S. Chang. The effects of swirl flow on chf by various spacer grids in 2\*2 rod bundle with r-134a. In *International Conference on the Advances in Nuclear Power Plants*, pages 1520–1526, Pittsburgh, USA, 2004.
- [93] D. Spori, T. Drobek, S. Zürcher, M. Ochsner, C. Specher, A. Mühlebach, and N. D. Spencer. Beyond the lotus effect: Roughness influences on wetting over a wide surface-energy range. *Langmuir*, 24:5411–5417, 2008.
- [94] Springer-Verlag, editor. *VDI-Wärmeatlas*. Verein Deutscher Ingenieure; VDI-Gesellschaft Verfahrenstechnik und Chemieingenieurwesen, 10 edition, 2006.
- [95] F. Staub. The void fraction in subcooled boiling - prediction of the initial point of net vapour generation. *Journal of Heat Transfer*, 90:151–157, 1968.
- [96] M. Stein. *Systematische Untersuchung der kritischen Wärmestromdichte beim Strömungssieden von Wasser in lotrechten Kreisrohren mit und ohne poröser Beschichtung*. PhD thesis, Technische Universität Berlin, 2004.
- [97] R. Stoddard, A. Blasick, S. Ghiaasiaan, S. Abdel-Khalik, S. Jeter, and M. Dowling. Onset of flow instability and critical heat flux in thin horizontal annuli. *Experimental Thermal and Fluid Science*, 26:1–14, 2002.
- [98] F. Tachibana et al. Report on burnout mechanism: 1965 research for peaceful uses of atomic energy. Report, Japanese Society of Mechanical Engineers, June 1967. In Japanese.
- [99] T. Theofanous, T. Dinh, J. Tu, and A. Dinh. The boiling crisis phenomenon: Part ii: dryout dynamics and burnout. *Experimental Thermal and Fluid Science*, 26(6-7):793 – 810, 2002.
- [100] L. S. Tong. Heat-transfer mechanisms in nucleate and film boiling. *Nuclear Engineering and Design*, 21:1–25, 1972.
- [101] G. B. Wallis. *One-dimensional Two-phase Flow*. McGraw-Hill Book Company, 1969.

- [102] C. Wang and V. Dhir. Effect of surface wettability on active nucleation site density during pool boiling of water on a vertical surface. *Journal of Heat Transfer*, 115:659–669, 1993.
- [103] J. Weisman and S. Ileslamlou. A phenomenological model for prediction of critical heat flux under highly subcooled conditions. *Fusion Technology*, 13:654–659, 1988. (Corrigendum in *Fusion Technology*, vol. 15, p. 1463, 1989).
- [104] J. Weisman and B. Pei. Prediction of critical heat flux in flow burnout at low qualities. *International Journal of Heat and Mass Transfer*, 36:1463–1477, 1983.
- [105] R. Whittle and F. R. A correlation for the minima in pressure drop versus flow rate curves for subcooled water flowing in narrow heated channels. *Nuclear Engineering and Design*, 6:89–99, 1967.
- [106] S. Ying and J. Weisman. Prediction of the critical heat flux in flow boiling at intermediate qualities. *International Journal of Heat and Mass Transfer*, 29:1639–1648, 1986.
- [107] S. You, K. Rainey, and C. Ammerman. *Advances in Heat Transfer*, volume 38, chapter A New Microporous Surface Coating for Enhancement of Pool and Flow Boiling Heat Transfer, pages 73–142. Elsevier Inc., 2004.
- [108] T. Zhang, T. Tong, J.-Y. Chang, Y. Peles, R. Prasher, M. Jensen, J. Wen, and P. Phelan. Ledinegg instability in microchannels. *International Journal of Heat and Mass Transfer*, 52:5661–5674, 2009.
- [109] P. Zinn. Umsetzung von verbesserungsmaßnahmen zur strömungsstabilisierung. Technical report, Karlsruhe Institute of Technology (KIT), Duale Hochschule Baden-Württemberg (DHBW), 2010. german.
- [110] N. Zuber. *Hydrodynamic Aspects of Boiling Heat Transfer*. PhD thesis, University of California, Los Angeles, 1959.







ISSN 1869-9669  
ISBN 978-3-86644-923-7

